

Indian J. pure appl. Phys., Vol. 18 No. 12 pp. 933-1034

December 1980

CODEN : IJOPAU ISSN: 0019-5596

18 (12) 933-1034 (1980)

964

20.1.81.

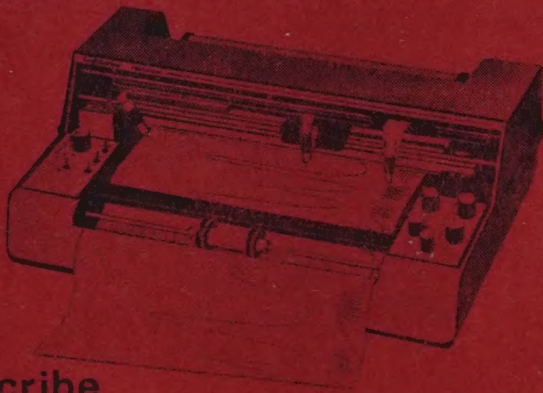
INDIAN JOURNAL OF PURE & APPLIED PHYSICS

Please renew subscription
for 1981
Renewal form enclosed



Published by
PUBLICATIONS & INFORMATION DIRECTORATE, CSIR, NEW DELHI
in association with
THE INDIAN NATIONAL SCIENCE ACADEMY, NEW DELHI

a quantum leap in recorder technology now available to the discriminating research scientist a range of reliable 'state of the art' recording instruments



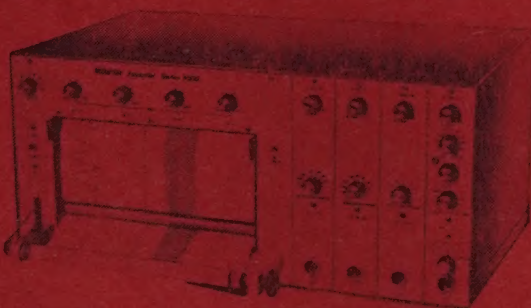
DigiScribe

Strip Chart Recorders One to Four Pens,
0.5 mV full scale and up, 0.5 sec response



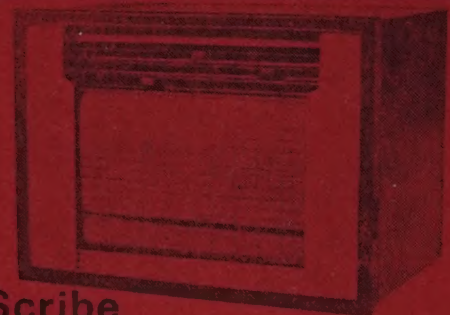
DigiGraphic

XY/t Recorders with plug-in modules to give
wide ranges of sensitivity, time base facility
and log recording.



HiScribe Oscillographic

Oscillographic Recorders DC to 80 Hz, One
to eight channels, Heat or ink writing. Plug in
modules to give wide range of sensitivities



MultiScribe

One to Three Pen and 6, 12 and 24 point
Recorders. Rack mounting with alarm
contacts, cold junction compensation, and
other features.

APPLICATIONS IN THE FIELDS OF

- METEOROLOGY • MATERIAL SCIENCES
- LIFE SCIENCES • PHYSICAL SCIENCES
- CHEMICAL AND ELECTROCHEMICAL SCIENCES
- BIOLOGICAL SCIENCES • PHYSIOLOGICAL AND
BEHAVIOURAL SCIENCES • COMPUTER SCIENCES
- ENVIRONMENTAL AND POLLUTION STUDIES
- ENERGY STUDIES • PHARMACOLOGY
- MECHANICAL/ELECTRICAL ENGINEERING
- METALLURGY/METALLURGICAL ENGINEERING
- AERODYNAMICS/AERONAUTICAL ENGINEERING
- BIO-MEDICAL ENGINEERING
- QUALITY CONTROL APPLICATIONS

MANUFACTURED BY:

DIGITAL ELECTRONICS LIMITED

A Company in collaboration with

**houston
instrument**

DIVN OF **BAUSCH & LOMB** 

Office & Factory:

Digilog House, 74/II, C, Cross Road, Marol Industrial Area, MIDC,
Andheri (East), Bombay-400 093. Phone: 577676, Gram: 'DIGILOG'

NOTICE TO AUTHORS

From January 1981

The abbreviations of journals and other serial titles in the 'References' section of papers published in the *Indian Journal of Pure & Applied Physics* (IJPAP) will be in conformity with those followed by the *Physics Abstracts* (PA) published by the INSPEC, U K. This change is being effected to ensure alignment with international usage of wide scientific following in this regard, since PA is the most widely consulted abstracting periodical by physicists all over the world and is easily accessible. Journals not covered by PA will be abbreviated according to the *Bibliographic Guide for Editors & Authors* (BGEA), 1974, published by the American Chemical Society, Washington DC. The *Chemical Abstracts* follows the abbreviations as given in BGEA.

Therefore, authors submitting papers for publication in IJPAP are requested to consult recent numbers of PA and BGEA (or the "Chemical Abstracts Service Source Index") for abbreviation of names of journals cited in the 'References' section. In the case of journals not covered by PA, the name of the country from which the journal is issued is to be included in parenthesis immediately after the abbreviated title, to maintain uniformity of presentation. Also, the full stops after the abbreviated words in titles will be deleted.

Authors may please note this change in the presentation of journal title abbreviations, with effect from January 1981, and ensure that the abbreviations are made conforming to the style outlined above, before despatching the manuscripts for the editor's consideration.

For convenient ready reference, the title abbreviations according to the new style, for some frequently cited journals are given on the reverse.

The Indian Journal of Pure & Applied Physics

is regularly covered by the following abstracting and current awareness services, as well as ICSU AB Member Services :

- | | |
|----------------------------------|--|
| 1. Physics Abstracts | 9. BIOSIS |
| 2. Physics Briefs | 10. Bulletin Signalétique |
| 3. Solid State Abstracts | Bibliographie des Sciences de la Terre |
| 4. Atom Index | 11. Informascience—Centre National |
| 5. Chemical Abstracts | de la Recherche Scientifique |
| 6. Current Contents | 12. Japan Information Centre |
| 7. Engineering Index | of Science and Technology |
| 8. American Geological Institute | 13. Referativnyi Zhurnal |

Abbreviations of Journals

Acta Cienc Indica
Acta Crystallogr Sect A (Denmark)
Acta Electron (France)
Acta Phys Acad Sci Hung (Hungary)
Acta Phys Austriaca
Acta Phys Pol A (Poland)
Acta Phys Slovaca (Czechoslovakia)
Acustica (Germany)
Adv Phys (GB)
AIP Conf Proc (USA)
Akust Zh (USSR)
Am J Phys (USA)
Ann Nucl Energy (GB)
Ann Phys (France)
Ann Phys (USA)
Appl Acoust (GB)
Appl Opt (USA)
Appl Phys (Germany)
Appl Phys Lett (USA)
Appl Spectrosc (USA)
Astrofizika (USSR)
Astron J (USA)
Astrophys & Space Sci (Netherlands)
Astrophys J (USA)
Astrophys J Lett Ed (USA)
Astrophys Lett (GB)
Astrophysics (USA)
Aust J Phys (Australia)
Bell System Tech J (USA)
C R Hebd Seances Acad Sci Ser A
 (France)
Can J Phys (Canada)
Chem Phys (Netherlands)
Chem Phys Lett (Netherlands)
Crystal Lattice Defects (GB)
Curr Sci (India)
Czech J Phys Sect A (Czechoslovakia)
Discuss Faraday Soc (USA)
Dokl Akad Nauk SSSR
Earth & Planet Sci Lett (Netherlands)
Electron Lett (GB)
Elektronika (Poland)
Exp Tech Phys (Germany)
Ferroelectrics (GB)
Fiz Nizk Temp (USSR)
Fiz Plazmy (USSR)
Fizika (Yugoslavia)
Found Phys (USA)
Gen Relativity & Gravitation (GB)
Geophys Res Lett (USA)
High Temp Sci (USA)
Hitachi Rev (Japan)
IEE J Electron Circuits & Syst (GB)
IEE J Microwaves Opt & Acoust (GB)
IEE J Solid-State & Electron Devices (GB)
IEEE J Solid-State Circuits (USA)
IEEE Trans Antennas & Propag
 (USA)
IEEE Trans Microwave Theory & Tech (USA)
IEEE Trans Plasma Sci (USA)
IEEE Trans Sonics & Ultrason (USA)
Indian J Blochem & Biophys
Indian J Chem A
Indian J Mar Sci
Indian J Meteorol & Geophys

Indian J Meteorol Hydrol & Geophysics
Indian J Phys Part A
Indian J Pure & Appl Math
Indian J Pure & Appl Phys
Indian J Radio & Space Phys
Indian J Technol
Indian J Textile Res
Indian J Theor Phys
Indian Sci Abstr
Indian Sci Congr Assoc Proc
Infrared Phys (GB)
Int J Electron (GB)
Int J Quantum Chem (USA)
Int J Solids & Struct (GB)
Int J Theor Phys (USA)
Izv Akad Nauk SSSR Ser Fiz
Izv VUZ Fiz (USSR)
Izv VUZ Radioelectron (USSR)
J Acoust Soc Am (USA)
J Am Ceram Soc (USA)
J Appl Crystallogr (Denmark)
J Appl Phys (USA)
J Atmos Sci (USA)
J Atmos & Terr Phys (GB)
J Cryst Growth (Netherlands)
J Chem Phys (USA)
J Geophys (Germany)
J Geophys Res (USA)
J Geomagn & Geoelectr (Japan)
J Low Temp Phys (USA)
J Mater Sci (GB)
J Math Phys (USA)
J Mol Spectrosc (USA)
J Non-Cryst Solids (Netherlands)
J Nucl Mater (Netherlands)
J Opt (France)
J Opt (India)
J Opt Soc Am (USA)
J Phys (France)
J Phys A (GB)
J Phys & Chem Ref Data (USA)
J Phys & Chem Solids (GB)
J Phys Lett (France)
J Phys Soc Jpn (Japan)
J Plasma Phys (GB)
J Raman Spectrosc (GB)
J Res Natl Bur Stand (USA)
J Sci & Ind Res (India)
J Soc Mater Sci Jpn (Japan)
J Solid State Chem (USA)
Jpn J Appl Phys (Japan)
Lett Nuovo Cimento (Italy)
Magn Lett (GB)
Microwave J (USA)
Met Sci (GB)
Microelectron & Reliable (GB)
Mol Phys (GB)
Mon-Not R Astron Soc (GB)
Nature (GB)
Nucl Fusion (Austria)
Nucl Instrum & Methods (Netherlands)
Nucl Phys A (Netherlands)
Nuovo Cimento A (Italy)
Opt & Quantum Electron (GB)
Opt & Spectrosc (USA)

Opt Acta (GB)
Opt Commun (Netherlands)
Opt Lett (USA)
Philos Mag A (GB)
Phys Fluids (USA)
Phys Lett A (Netherlands)
Phys Rep (Netherlands)
Phys Rev A (USA)
Phys Rev Lett (USA)
Phys Ser (Sweden)
Phys Status Solidi a (Germany)
Physica a (Netherlands)
Pis'ma V Astron Zh (USSR)
Pis'ma V Zh Eksp & Teor Fiz
 (USSR)
Planet & Space Sci (GB)
Plasma Phys (GB)
Pramana (India)
Proc IEEE (USA)
Proc IRE (Australia)
Proc Indian Acad Sci Sec A
Proc Indian Assoc Cultiv Sci
Proc Inst Elect Eng (GB)
Proc Indian Natl Sci Acad Part A
Proc Inst Radio Eng (Australia)
Proc Phys Soc (GB)
Proc R Soc London Ser A (GB)
Prog Theor Phys (Japan)
Q J R Astron Soc (GB)
Q J R Meteorol Soc (GB)
Radio & Electron Eng (GB)
Radio Sci (USA)
Rep Ionos & Space Res Jpn (Japan)
Rep Prog Phys (GB)
Res Ind (India)
Rev Mex Fis (Mexico)
Rev Mod Phys (USA)
Rev Phys Appl (France)
Rev Roum Phys (Rumania)
Rev Sci Instrum (USA)
Rev Geophys Space Phys. (USA)
Sol Phys (Netherlands)
Solid-State Commun (USA)
Solid-State Electron (GB)
Sov Astron (USA)
Sov J Quantum Electron (USA)
Sov Phys J (USA)
Sov Phys Acoust (USA)
Sov Phys Crystallogr (USA)
Sov Phys Dokl (USA)
Sov Phys Lebedev Inst Rep (USA)
Sov Phys Semicond (USA)
Sov Phys Solid-State (USA)
Sov Phys Tech Phys (USA)
Sov Tech Phys Lett (USA)
Space Sci Rev (Netherlands)
Thin Solid Films (Switzerland)
Trans ASAE (USA)
Trans Am Crystallogr Assoc (USA)
Trans Am Nucl Soc (USA)
Ukr Fiz Zh (USSR)
Weather (GB)
Yad Fiz (USSR)
Z Naturforsch a (Germany)
Z Phys A (Germany)
Zh Eksp & Teor Fiz (Germany)

Renewal Notice

Your subscription which expires with the despatch of the December 1980 issue of the Journal, stands for renewal. We request you to be so good as to return the enclosed order form duly filled in early, so as to ensure continuity in despatch. Please note the revised subscription rates effective from 1 January 1981.

Sales & Distribution Officer

DATED

THE SALES & DISTRIBUTION OFFICER
PUBLICATIONS & INFORMATION DIRECTORATE (CSIR)
HILLSIDE ROAD, NEW DELHI 110 012 (INDIA)

Dear Sir,

Please renew my subscription/enrol me as subscriber to :

	Rs	£	\$
1. Journal of Scientific & Industrial Research (Monthly)	100.00	17.00	38.00
2. Indian Journal of Chemistry Sec. A (Inorganic, Physical, Theoretical and Analytical Chemistry) (Monthly)	125.00	21.00	47.00
3. Indian Journal of Chemistry, Sec. B (Organic and Medicinal Chemistry) (Monthly)	125.00	21.00	47.00
4. Indian Journal of Technology (Monthly)	90.00	15.00	34.00
5. Indian Journal of Pure & Applied Physics (Monthly)	120.00	20.00	45.00
6. Indian Journal of Experimental Biology (Monthly)	180.00	30.00	68.00
7. Indian Journal of Biochemistry & Biophysics (Bimonthly)	60.00	10.00	23.00
8. Indian Journal of Radio & Space Physics (Bimonthly)	90.00	15.00	34.00
9. Indian Journal of Marine Sciences (Quarterly)	75.00	13.00	28.00
10. Research & Industry (Quarterly)	45.00	8.00	17.00
11. Indian Journal of Textile Research (Quarterly)	45.00	8.00	17.00
12. Current Literature on Science of Science (Monthly)	50.00	6.00	15.00
13. Medicinal & Aromatic Plants Abstracts (Bimonthly)	40.00	7.00	17.00
14. Industrial News Digest (Monthly)	20.00	4.00	8.00

(Please tick off the periodicals you would like to subscribe)

for one year from January 1981 for which I/we have remitted a sum of Rs.....
£...../\$.....by Cheque/Demand Draft No.....
dated.....in favour of PUBLICATIONS & INFORMATION DIRECTORATE

COMPLETE MAILING ADDRESS

Name.....
Address.....
Country/State.....

(Signature)

- Note :
1. Subscribers at annual rates for all the periodicals are enlisted for the full volumes, i.e. for the period from January to December only.
 2. The Cheque/Demand Draft may please be drawn in favour of "PUBLICATIONS & INFORMATION DIRECTORATE, NEW DELHI". Banking charges shall be borne by the subscriber. For inland outstation cheques please add Rs. 3.50. For foreign cheques please add \$ 1.00 or £ 0.45.
 3. Supply will commence on receipt of subscription in advance.

Indian Journal of Pure & Applied Physics

VOLUME 18

No. 12

DECEMBER 1980

EDITORIAL BOARD

Dr B A Dasannacharya
Bhabha Atomic Research Centre
Bombay

Prof. B M Deb
Indian Institute of Technology
Bombay

Prof. P Krishna
Banaras Hindu University
Varanasi

Prof. Krishnaji
Allahabad University
Allahabad

Prof. K V Ramanathan
Tata Institute of Fundamental Research
Bombay

Dr S Chandrasekhar
Indian National Science Academy
New Delhi/Raman Research
Institute Bangalore

Prof. A K Saha
Saha Institute of Nuclear Physics
Calcutta

Prof. N C Sil
Indian Association for
Cultivation of Science
Calcutta

Prof. R Srinivasan
Indian Institute of Science
Bangalore

Prof. K Venkata Ramiah
Osmania University
Hyderabad

Dr K L Chopra
Indian National Science Academy
New Delhi/Indian Institute of
Technology New Delhi

Shri Y R Chadha, *Ex-officio* Secretary & Chief Editor

EDITORIAL STAFF

Editors

D S Sastry & K S Rangarajan

Assistant Editors

G N Sarma, J B Dhawan & Tarun Banerjee

Published by the Publications & Information Directorate, CSIR, Hillside Road, New Delhi 110 012

Chief Editor : Y R Chadha

The Indian Journal of Pure & Applied Physics is issued monthly. The Directorate assumes no responsibility for the statements and opinions advanced by contributors. The editorial staff in its work of examining papers received for publication is assisted, in an honorary capacity, by a large number of distinguished scientists, working in various parts of India.

Communications regarding contributions for publication in the journal should be addressed to the Editor, Indian Journal of Pure & Applied Physics, Publications & Information Directorate, Hillside Road, New Delhi 110 012.

Correspondence regarding subscriptions and advertisements should be addressed to the Sales & Distribution Officer, Publications & Information Directorate, New Delhi 110 012.

Annual Subscription
Rs. 100.00 £ 16.50 \$ 42.00

Single Copy
Rs. 10.00 £ 1.80 \$ 4.50

50% Discount is admissible to research workers and students and 25 % discount to non-research individuals, on annual subscription. Payments in respect of subscriptions and advertisements may be sent by cheque, bank draft, money order or postal order marked payable *only* to Publications & Information Directorate, New Delhi 110 012. Claims for missing numbers of the journal will be allowed only if received within 3 months of the date of issue of the journal plus the time normally required for postal delivery of the journal and the claim.

CSIR SCIENTIFIC PERIODICALS

(Revised subscription rate effective from 1 Jan. 1981)

JOURNAL OF SCIENTIFIC & INDUSTRIAL RESEARCH (monthly)

With a fine record of over 35 years' service to the scientific community, this Journal has grown into India's leading general science periodical. Intended to fulfil the responsibility of helping the research workers to keep themselves abreast of current developments in various fields of science and technology, the Journal carries editorial features highlighting important scientific events in India and abroad; articles on science policy and management of science; review articles on topics of current research interest; technical reports on international and national conferences; reviews of scientific and technical publications; and notes on major advances in various fields.

Annual subscription	Rs 100.00	£ 17.00	\$ 38.00
Single copy	10.00	1.70	3.80

INDIAN JOURNAL OF CHEMISTRY (monthly)

This Journal which is running the 19th year of its publication, Consists of the following two sections.

Section A: This section is devoted to papers in Inorganic, Physical, Theoretical and Analytical Chemistry.

Annual subscription	Rs 125.00	£ 21.00	\$ 47.00
Single copy	12.50	2.10	4.70

Section B: This section is devoted to papers in Organic Chemistry including Medicinal Chemistry.

Annual subscription	Rs 125.00	£ 21.00	\$ 47.00
Single copy	12.50	2.10	4.70

INDIAN JOURNAL OF PURE & APPLIED PHYSICS (monthly)

This Journal, which is running the 19th year of its publication, is devoted to original research communications (full papers and short communications) in all conventional branches of physics (except radio and space physics).

Annual subscription	Rs 120.00	£ 20.00	\$ 45.00
Single copy	12.00	2.00	4.50

INDIAN JOURNAL OF RADIO & SPACE PHYSICS (bimonthly)

This Journal serves as a medium for the publication of original research work (full papers and communications) in various areas of radio and space physics.

Annual subscription	Rs 90.00	£ 15.00	\$ 34.00
Single copy	12.00	3.00	6.80

INDIAN JOURNAL OF TECHNOLOGY (INCLUDING ENGINEERING) (monthly)

This Journal publishes papers reporting results of original research of applied nature pertaining to unit operations, heat and mass transfer, products, processes, instruments, and appliances, etc. The Journal is of special interest to research workers in the departments of applied sciences in

universities, institutes of higher technology, commodity research laboratories, industrial cooperative research institutes, and industrial research laboratories.

Annual subscription	Rs 90.00	£ 15.00	\$ 34.00
Single copy	9.00	1.50	3.40

INDIAN JOURNAL OF EXPERIMENTAL BIOLOGY (monthly)

This Journal, devoted to the publication of research communications in the fields of experimental botany, zoology, microbiology, pharmacology, endocrinology, nutrition, etc., is the only one in India with such a wide coverage and scope.

Annual subscription	Rs 180.00	£ 30.00	\$ 68.00
Single copy	18.00	3.00	6.80

INDIAN JOURNAL OF BIOCHEMISTRY & BIOPHYSICS (bimonthly)

This Journal, published in association with the Society of Biological Chemists (India), Bangalore, is the only research Journal in India devoted exclusively to original research communications in biochemistry and biophysics.

Annual subscription	Rs 60.00	£ 10.00	\$ 23.00
Single copy	12.00	2.00	4.60

INDIAN JOURNAL OF MARINE SCIENCES (quarterly)

Commencing publication from June 1972, this Journal is devoted to research communications (full papers and short communications) pertaining to various facets of marine research, viz. biological, physical, geological and chemical oceanography.

Annual subscription	Rs 75.00	£ 13.00	\$ 28.00
Single copy	22.00	4.00	8.40

RESEARCH & INDUSTRY (quarterly)

Intended to serve as a link between science and industry, this Journal is addressed primarily to technologists, engineers, executives and others in industry and trade. It publishes informative original articles containing practical details of processes and products developed in India, which show promise of ready utilization, and technical digests on new processes, products, instruments and testing methods which are of interest to industry. Developments in Indian industry are regularly reported.

Annual subscription	Rs 45.00	£ 8.00	\$ 17.00
Single copy	13.00	2.50	5.00

INDIAN JOURNAL OF TEXTILE RESEARCH (quarterly)

Commencing publication from March 1976, this Journal is devoted to the publication of papers reporting results of fundamental and applied researches in the field of textiles.

Annual subscription	Rs 45.00	£ 8.00	\$ 17.00
Single copy	13.50	2.50	5.10

Please contact

THE SALES & DISTRIBUTION OFFICER
PUBLICATIONS & INFORMATION DIRECTORATE, CSIR
HILLSIDE ROAD, NEW DELHI 110 012

CONTENTS

Solid State Physics

- Temperature Dependence of Internal Friction in Polycrystalline Ferrites 933

S RAMANA MURTY & T SESHAGIRI RAO

- Temperature Dependence of Magnetic Susceptibility of $\text{CaSO}_4 : \text{Dy}$ Phosphors ... 936

M R MULLA & S H PAWAR

- An Empirical Generalized Relation on Decay of CaS Phosphors 940

A S MEHTA, M C TIWARI & V G MACHWE

- Determination of Preferred Sites of Fe^{2+} in the Lattices of W-Hexaferrite Crystal of $\text{Ba}^{2+} \text{Fe}_{2+} \text{F}_{16}^{3+} \text{O}_{27}$ from Mössbauer Spectral Study ... 942

M K FAYEK & A A BAGHAT

- Structure & Growth of MnSe & MnTe Films ... 950

PRABHAT SINGH

- Compression of Sodium Chloride Single Crystals along [001] Direction ... 953

L C JAIN & T S MURTY

- Electret Properties of Electrically Charged Silicone Rubber 957

RUDRA KANT SRIVASTATA, M S QURESHI & C S BHATNAGAR

- Electronic Polarizabilities & Radii of Ions in Rutile-type Crystals ... 961

JAI SHANKER, S C AGRAWAL & V K JAIN

Chemical Physics

- On the Isotopic Invariants of Polyatomic Molecules ... 964

R JAGANNATHAN, V A CHINNAPPAN & G A SAVARI RAJ

- Temperature Dependence of Rotational Relaxation in o-&-n Hydrogen ... 970

PRABHURAM & M P SAKSENA

(Contd)

CONTENTS (Contd)

Magneto & Spectral Studies on Rare Earth Chelates of β -BenzidinyI 2 : 4-Dihydroxy Propiophenone	973
V K RASTOGI, B S TYAGI, A N PANDEY & R C SAXENA	
Dielectrics & Microwaves	
Radio Frequency Conductivity of Opalescent Binary Liquid Mixtures ...	977
S N SEN & A K GHOSH	
Temperature & Frequency Dependence of Dielectric Properties of CoSiF ₆ . 6H ₂ O around Its Structural Phase Transition Temperature	981
S K DUTTA ROY, S S MITRA & S K GHORAI	
General Physics	
Prediction of Effective Thermal Conductivity of Two-phase Porous Materials Using Resistor Model	984
VEERENDRA KUMAR & D R CHAUDHARY	
Mathematical & Theoretical Physics	
Reduction & Second Quantization of Generalized Electromagnetic Fields for Non-zero Mass System	988
D C JOSHI & B S RAJPUT	
Plasma Physics	
An Investigation of the Electron Cyclotron Resonance Line Shape in Transient Afterglow Plasmas of Neon & Argon	993
A P KABILAN	
COMMUNICATIONS	
Broad Line Proton Magnetic Resonance Investigations on Solid Semi-carbazide Hydrochloride	997
PUSHPA KHARE, S S ASHUTOSH MISHRA, PURNIMA BHARTI & R C GUPTA	
Pulse Height Analyzer for High Counting Rate in Mössbauer Work	999
ANJALI KRISHNAMURTY, RAMESH CHANDRA & S LOKANATHAN	
NOTES	
After-effect of Heat & Magnetic Field on the Dielectric Permittivity of Sulphur	1002
VIJAY K SHRIVASTAVA, M L KHARE & C S BHATNAGAR	
Variable Frequency Interference Filter	1004
J ASHOK & D VASANTHA	

(Contd)

CONTENTS (Contd)

90° Growth Twins in Float-Zone Silicon Crystals	1005
R K BAGAI & W N BORLE				
Study of Surface Distortion around Dynamic Impacts on Cleavages of Sodium Bromide Single Crystals	1008
M H ANSARI & S C DATT				
Stability of Intramolecular Hydrogen Bond of 8-Hydroxy Quinoline in Different Solvents : IR Spectroscopic Study	1010
I SURYANARAYANA & S K SAIKIA				
Elastic Constants of Phloroglucinal Dihydrate by X-Ray Diffuse Scattering	...			1012
SURESH CHANDRA				
Sputtered Molybdenum Film Resistors	1014
AWATAR SINGH				
Slater-Condon & Spin-Orbit Parameters for Tm^{3+} in Thulium Sulphate, Thulium Ethyl Sulphate & Zinc Sulphide	1015
S V J LAKSHMAN & C K JAYA SANKAR				
PMR Study of Intramolecular Motion in Solid 2, 4-Dinitrophenyl Hydrazine	...			1017
ALPANA ROY & R C GUPTA				
Relative Permittivity of the Acetates of Potassium, Lithium, Rubidium & Cesium				1019
J HATIBARUA				
Influence of Dielectric Constant on Cationic Mobilities of Electrolytic Solution in Relation to Eigen Mechanism	1021
V BRAHMAJI RAO, T SATYANARAYANA RAO & N CHOWDARY BABU				
Temperature Dependence of Pressure-broadened Microwave Line-widths of Some Rotational Lines of Carbonyl Sulphide	1023
G K JOHRI, S GUPTA, B CHANDRA & R P RISHISHWAR				

(Contd)

CONTENTS (Contd)

An Assembly for Measuring the dc Conductivity of Organic Solids	1026
S C DUTT			
Motional Impedance of a Rigid, Conducting, Diamagnetic Prolate			
Plasma Spheroid	1028
B N MARIHAL & B G JYOTI			
X-ray <i>K</i> -Absorption Discontinuity in Crystalline & Amorphous			
Arsenic	1029
Y L RAO & C MANDE			
Electronic Simulation of Acoustic Emission	1031
SANJEEV CHADDA & S P MALLIKARJUN RAO			
Infrared Spectra of the Biological Molecule 4,6-Dihydroxy-2-Methyl			
Pyrimidine	1032
NITISH K SANYAL, R K GOEL, K P KANSAL & S N SHARMA			

Temperature Dependence of Internal Friction in Polycrystalline Ferrites*

S RAMANA MURTY & T SESHAGIRI RAO

Department of Physics, University College of Science, Osmania University, Hyderabad 500 007

Received 1 September 1979; revised received 30 November 1979

The 'composite oscillator' method has been used to study the dependence of the internal friction of nickel and nickel-zinc ferrites on temperature. It is observed that the internal friction increases with increase of temperature and shows a peak at a temperature below the Curie temperature. The temperature at which the peak is observed in each case is almost coincident with the temperature at which the velocities of the longitudinal ultrasonic wave (and hence the Young's modulus) have shown minimum values. The occurrence of the internal friction peaks has been explained in terms of the magnetic anisotropy energy and the domain wall motion.

1. Introduction

The mechanical energy of a vibrating body is converted into heat even when the body is completely isolated from its surroundings. As a result, the vibrations of the body are damped quickly. This energy transfer and the consequent damping of the vibrations are attributed to the presence of internal friction. The internal friction makes it possible to evaluate the tendency of a material to elastic lag, creep and grain boundary relaxation. In the case of metals and alloys, processes such as recrystallization, annealing, quenching and tempering, plastic deformation, strain aging are successfully studied by the internal friction method. Besides, measurements of internal friction provide valuable information about the structure of the solid state and a wide variety of work has been carried out in this direction. Although the internal friction in metals has been extensively investigated, there is only meagre literature available regarding the polycrystalline ferrites. As such, a study of the internal friction of pure and mixed ferrites has been undertaken and the results obtained in the case of nickel and nickel-zinc ferrites are presented in this paper.

2. Experimental Method

The method adopted in the present investigation is that of the composite piezo-electric oscillator.¹⁻⁴ Several X-cut quartz bars provided with silver electrodes on its X faces with resonant frequencies of 90 and 120 kHz and a cross-section of $3 \times 3 \text{ mm}^2$, have been employed to excite the longitudinal vibrations. The quartz bar is cemented to the test specimen of identical cross-section using

phenyl salicylate for room temperature measurements.

The experimental method consists of adjusting the length of the specimen by trial and error such that the resonant frequency of the composite system lies within 5% of that of the quartz bar. A constant alternating voltage is applied to the quartz bar and its frequency is varied over a range of 50 Hz on either side of its resonant frequency. The electric current through the electrodes is measured at different frequencies and a plot of the current versus frequency gives the resonance curve (Fig. 1). If the maximum and minimum currents are denoted by I_m and I_n and the corresponding frequencies by f_m and f_n respectively, then the resonant frequency (f_0) of the composite oscillator is given by

$$f_0 = f_m + (f_n - f_m) \frac{I_n}{I_m + I_n} \quad \dots(1)$$

If m_q and m_s are the masses of the quartz and the specimen respectively, then the internal friction (Q_s^{-1}) of the sample is given by

$$Q_s^{-1} = \left(1 + \frac{m_q}{m_s} \right) 2 \left(\frac{f_n - f_m}{f_0} \right) \frac{\sqrt{I_m I_n}}{I_m + I_n} \quad \dots(2)$$

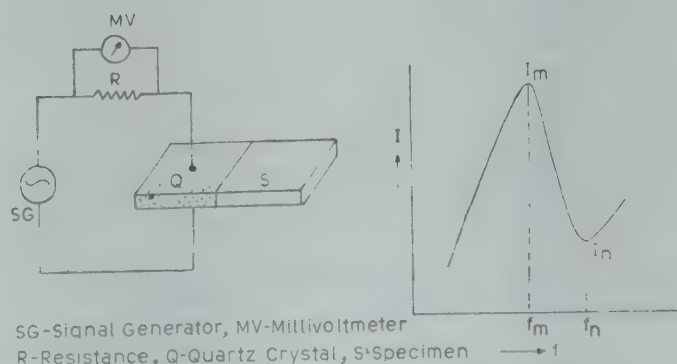


Fig. 1—Experimental set-up and typical resonance curve

*Paper presented at the National Seminar on 'Applications of Acoustics and Ultrasonics' held at Baroda, 1978.

In the present investigation, the composite bar and a small resistance R in series are connected to a standard signal generator (Marconi, Type TF 144 G). The electrical current is obtained by measuring the voltage across the resistance R with an ac millivoltmeter. The frequency is measured by a Beckmann counter and timer having an accuracy of 1 in 10^6 .

The internal friction has been measured at high temperatures by suspending the composite system in an electric furnace which can go up to 600°C . The temperature of the furnace is controlled by stabilized power supply and a variac. The temperature of the system is measured with Cr/Al thermocouple to an accuracy of $\pm 1^\circ\text{C}$. For high temperature work, the adhesive used consists of two parts of barium sulphate mixed with a drop of water glass. The composite system works satisfactorily after it is kept under pressure for about 72 hr at room temperature, before starting the high temperature work.

3. Results and Discussion

Room temperature studies—Fig. 2 shows the resonance curve obtained in the case of nickel ferrite at room temperature. Similar resonance curves have been obtained in the case of nickel-zinc ferrites from which the internal friction has been calculated using the relation (2). The values thus obtained are presented in Table 1.

As far as the present authors are aware, no internal friction data are available in the literature for polycrystalline ferrites for comparing the results obtained in the present investigation. However, Gibbons⁵ studied the variation of internal friction with temperature for single crystals of manganese, manganese-zinc and nickel-iron ferrites at low temperatures. The value obtained by him for nickel

Table 1—Values of Internal Friction for Nickel and Nickel-Zinc Ferrites at Room Temperature

Ferrite	Internal friction $Q^{-1} \times 10^4$
Ni Fe ₂ O ₄	3.06
Ni _{0.9} Zn _{0.1} Fe ₂ O ₄	5.54
Ni _{0.5} Zn _{0.5} Fe ₂ O ₄	0.80
Ni _{0.1} Zn _{0.9} Fe ₂ O ₄	0.06

iron ferrite at 140 K is 0.3×10^{-4} . It can be seen from Table 1 that on the addition of 0.1 mole of zinc to nickel ferrite, the value of Q^{-1} has increased from 3.06×10^{-4} to 5.54×10^{-4} . Further addition of zinc, however, has resulted in a decrease of the value of Q^{-1} . This result is in agreement with the observation recorded in Ref. 6, according to which on the addition of zinc ferrite (non-magnetic) to nickel ferrite (magnetic), the value of saturation magnetization first increases and attains a maximum at about 0.7 mole of zinc ferrite and decreases with further increase of zinc content.

High temperature study—Fig. 3 gives the plots of Q^{-1} versus temperature for different nickel-zinc ferrites. In all the cases, the value of Q^{-1} increases with increase of temperature, attains a maximum value at a certain temperature and thereafter decreases with further increase of temperature. In the case of Ni_{0.1} Zn_{0.9} Fe₂ O₄, Q^{-1} increases steeply with increase of temperature and the decrease after the peak is also quite steep in the temperature range 190 to 270°C . It can be seen from Fig. 3 that when the composition of zinc ferrite is increased, sharpness of the peak decreases till the composition Ni_{0.9} Zn_{0.1} Fe₂ O₄ and increases thereafter.

Table 2 lists the temperatures (T_1) at which the internal friction attains a maximum value and the temperatures (T_2) at which Young's modulus becomes a minimum, for all the nickel-zinc ferrites. It can

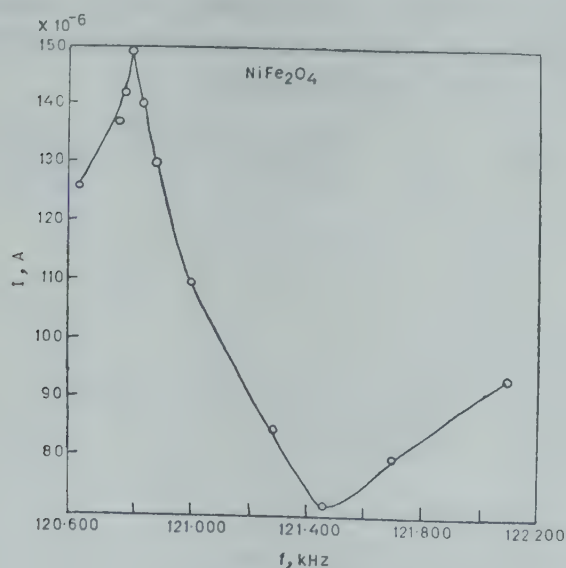


Fig. 2—Resonance curve for nickel ferrite

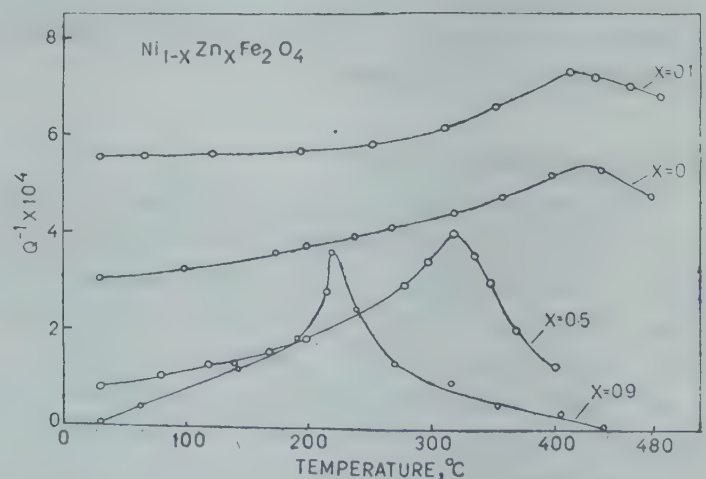


Fig. 3—Plot of internal friction versus temperature for nickel-zinc ferrites

Table 2—Temperature Data for Nickel-Zinc Ferrites

Ferrite	T_1 (°C)	T_2 (°C)
Ni Fe ₂ O ₄	420	420
Ni _{0.9} Zn _{0.1} Fe ₂ O ₄	416	415
Ni _{0.5} Zn _{0.5} Fe ₂ O ₄	320	330
Ni _{0.1} Zn _{0.9} Fe ₂ O ₄	220	155

be seen from Table 2 that the two temperatures are nearly the same for a ferrite of the given composition. It is observed that the temperatures corresponding to Q_s^{-1} maximum of this work closely follows the variation of Curie temperatures with zinc content in mixed nickel-zinc ferrite system.

The minimum in the Young's modulus (E) versus temperature curve has been explained^{7,8} to occur at a temperature at which the magnetic anisotropy constant (K_1), which can be considered as a measure of the magnetic energy barrier to the movement of domains in a magnetic material, becomes zero.

As such, the domains will be free to move at a temperature at which K_1 becomes zero. At this temperature where $K_1 = 0$, the substance undergoes a maximum strain for a given stress and E becomes a minimum. Thus the substance exhibits maximum ΔE -effect at this temperature. As the

peak in the internal friction-temperature curve is occurring at almost the same temperature as E_{\min} , the same explanation holds good for the occurrence of the peak as well.

Quimby¹ has studied the elastic behaviour and internal friction of nickel at different temperatures and at various magnetic fields up to the saturation field. He has observed that the values of temperature at which E_{\min} occurs coincide with the internal friction peak temperatures. Koster⁹ also has studied the variation of internal friction with temperature for nickel and observed a maximum at 150-200°C which was attributed by him to the disappearance of crystal anisotropy at that temperature. Thus the explanation offered in the present investigation for the internal friction peak is in conformity with the results of Quimby and Koster.

References

1. Quimby S L, *Phys. Rev.*, **25** (1925), 558.
2. Balamuth L, *Phys. Rev.*, **45** (1934), 715.
3. Rose F C, *Phys. Rev.*, **49** (1936), 50.
4. Cooke W T, *Phys. Rev.*, **50** (1936), 1158.
5. Gibbons D F, *J. appl. Phys.*, **28** (1957), 810.
6. *Handbook of microwave ferrite materials*, edited by H Von Aulock (Academic Press, New York), 1965, 381.
7. Seshagiri Rao T & Ramana Murty S, *J. acoust. Soc. India*, **5** (1977), 72.
8. Ramana Murty S & Seshagiri Rao T, *J. acoust. Soc. India*, **5** (1977), 105.
9. Koster W, *Z. Metalkunde*, **35** (1943), 246.

Temperature Dependence of Magnetic Susceptibility of CaSO_4 : Dy Phosphors

M R MULLA & S H PAWAR

Materials Research Laboratory, Department of Physics, Shivaji University, Kolhapur 416 004

Received 30 July 1979; revised received 22 October 1979

Dysprosium-doped calcium sulphate phosphors of varying activator concentrations have been prepared with and without addition of flux. Their temperature (T) dependence of magnetic susceptibilities (K_s) has been studied in the range 300-452 K. The observed linearity between K_s and $1/T$, obeys Curie's law. The K_s of the host CaSO_4 , is found practically temperature independent. However, K_s of Dy-added phosphors is found to be temperature dependent. The flux-added phosphors show even greater degree of temperature dependence. The estimation of paramagnetic impurity incorporated in the host, is made on the basis of Langevin's quantum theory of paramagnetism. The effects of flux and activator concentration are explained on the basis of temperature dependence studies.

1. Introduction

There is a revival of interest in CaSO_4 phosphors due to their application in thermoluminescence dosimeters. Extensive work has been done, in the last few years, on the thermoluminescence and emission spectra of these phosphors.¹⁻⁴ Relatively little is known about the magnetic behaviour of these phosphors. The host, CaSO_4 , is diamagnetic,⁵ and the paramagnetic impurities are embedded in it as the luminescence centres. The effect of photo-excitation on the magnetic susceptibility is found to be interesting and the present authors have recently reported this phenomenon as the photomagnetic effect (PME).⁶ The nature of paramagnetic impurity in the diamagnetic host may be understood with the help of electron paramagnetic resonance⁷ and temperature dependence of magnetic susceptibility. Bowers and Melamed⁸ have reported the temperature dependence of magnetic susceptibility of Cu- and/or Cl-activated ZnS phosphors. Johnson and Williams^{9,10} have done similar studies in case of Mn-activated ZnF_2 phosphors. Studies on magnetic susceptibility and the temperature dependence of CaSO_4 : Dy phosphors are few to date to the best of the knowledge of the authors. In the present investigation, calcium sulphate phosphors doped with dysprosium (Dy) have been prepared from an Indian mineral and temperature dependence of their magnetic susceptibilities has been investigated. The effect of Dy concentration and the role of flux have also been studied. On the basis of Langevin's quantum

theory of paramagnetism, an attempt has been made to estimate the paramagnetic ion impurity in the host.

2. Experimental Details

Calcium sulphate phosphors activated with dysprosium, with various weight percentage compositions were prepared from the Indian mineral gypsum, as reported earlier.⁶ In brief, purified gypsum powder was dissolved in concentrated H_2SO_4 and a pre-determined quantity of Dy_2O_3 solution was added. The charge was kept at 300°C for evaporation and further heated to 600°C for 2 hr and then quenched suddenly to room temperature. The dysprosium weight percentage was varied from 0.005 to 0.5. Some phosphors were prepared by adding Na_2SO_4 as a flux. X-ray diffraction powder photographs were taken with Debye-Scherrer camera. The phosphor was found to be crystalline in nature, and the structure analyzed was found to be orthorhombic.

The magnetic susceptibilities of these polycrystalline phosphors were measured in the temperature range 300-452 K, using the standard Gouy method. A semi-micro balance capable of measuring $1 \times 10^{-5}\text{g}$ was used to measure the force on the phosphor contained in a thin walled pyrex sample tube of 5 mm in diameter and 15 cm in length. Finely ground powder was used to minimize the packing correction. The ramming method was adopted as it facilitates a maximum filling and minimizes the chances of preferential orientation of the particles in the field.

In this method, small and nearly equal portions of the powder were introduced in the tube and were packed by pounding, after each addition, with the flat end of a ramrod that snugly fits the tube. An electric cylindrical furnace, with coil wound non-inductively to prevent stray magnetic field, was used to attain high temperature. The temperature measurement was made with chromel-alumel thermocouple. In order to achieve thermal equilibrium between the sample and surroundings, the sample was made to stand at a fixed temperature for about 10 to 15 min. A magnetic field of the order of 7.5 kOe was applied. The magnetic susceptibility was measured at different intervals of temperature. The experimental procedure eliminated the observed forces on pyrex sample tube arising from certain paramagnetic impurities,¹¹ as well as the effect of change in buoyancy of air with temperature.

3. Results and Discussion

The magnetic susceptibilities (K_s) have been measured for CaSO_4 :Dy phosphors, at and above room temperature. The values of K_s at room temperature have been listed in Table 1, for the phosphors studied. It is worth noting that the undoped phosphor (PM61) is diamagnetic, as its constituents Ca^{2+} and SO_4^{2-} are diamagnetic. In the case of phosphors without flux, it may be noted from Table 1 that the addition of Dy makes the phosphor less diamagnetic (PM24) and paramagnetic for higher concentration (PM59). This can be understood as follows.

Table 1—Compositions, and Values of K_s and N for CaSO_4 :Dy Phosphors

Phosphor No	Composition	$K_s \times 10^{-6}$ at room temperature	$N \times 10^{-16}$
PM61	CaSO_4	-0.30	—
PM24	CaSO_4 :0.075 Dy wt % (without flux)	-0.15	1134
PM59	CaSO_4 :0.5 Dy wt % (without flux)	+0.30	4377
PM26	CaSO_4 :0.025 Dy wt % (with flux)	-0.25	451.7
PM28	CaSO_4 :0.075 Dy wt % (with flux)	-0.02	4404
PM30	CaSO_4 :0.125 Dy wt % (with flux)	+0.08	5177
PM32	CaSO_4 :0.5 Dy wt % (with flux)	+1.12	9891

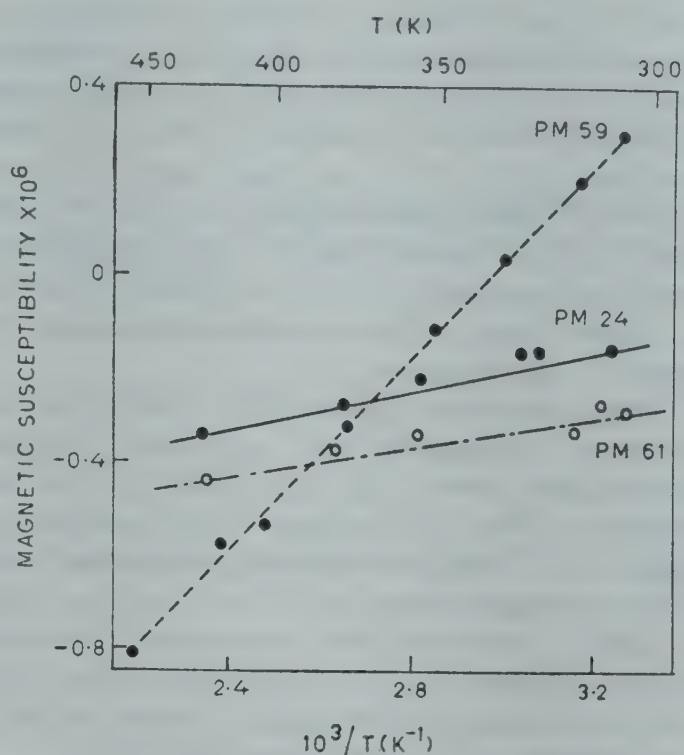


Fig. 1—Variation in magnetic susceptibility versus reciprocal of temperature for undoped and Dy-doped phosphors

The magnetic susceptibilities for gram-ion for Ca^{2+} , SO_4^{2-} and Dy^{3+} , are -8×10^{-6} , -40×10^{-6} and $+19 \times 10^{-6}$ respectively. Under the equilibrium condition of charge balancing, two Dy^{3+} ions may be incorporated at the substitutional positions (as the ionic radii for Ca^{2+} and Dy^{3+} ions are nearly the same, 0.99 Å) by removing three Ca^{2+} ions. This gives rise to the change in magnetic susceptibility of CaSO_4 phosphor towards the paramagnetism.

For the further confirmation of the entry of paramagnetic Dy^{3+} ions in the diamagnetic host, the variation of K_s with temperature is studied. The typical plots of K_s versus $1/T$ are shown in Fig. 1, for phosphors without flux. In case of Dy-activated phosphors (PM24 and PM59) the plots are linear obeying Curie's law. In case of undoped phosphor (PM61), the results are rather inconsistent with the Langevin's theory of diamagnetism. This can be attributed to the host crystalline defects formed during the preparation of phosphor. A similar observation has been reported by Bowers and Melamed,⁸ in the case of undoped ZnS phosphor.

The quantitative estimation of paramagnetic impurities in the diamagnetic host can be made on the basis of Langevin's quantum theory of paramagnetism. Accordingly, the number of paramagnetic ions per unit volume is given by

$$N = \frac{3K(K_s, T)}{g^2 [J(J+1)] \mu_B^2} \quad \dots(1)$$

where K is the Boltzmann's constant, (K/T) corresponds to the slope of K , versus $1/T$ graph, g denotes the spectroscopic splitting factor and J is the total angular quantum number, and μ_B stands for Bohr magneton. The factor $g[J(J+1)]^{1/2}$ corresponds to the effective number of Bohr magnetons (P_{eff}), and has the value 10.66 for Dy. The calculated values of N for different percentage compositions of Dy are listed in Table 1. It is seen that as Dy-concentration increases, the value of N also increases.

The typical plots (PM26, PM30, PM32) for the flux-added phosphors with increasing activator concentration from 0.025% to 0.5% Dy are depicted in Fig. 2. The plots are linear obeying Curie's law. From the slopes of the plots the values of N are evaluated using Eq. (1) and they are listed in Table 1. It is noted that the value of N increases with Dy-concentration. This gives rise to the phosphor as a whole a paramagnetic nature, at higher concentrations of Dy (PM 30 and PM 32).

A small quantity of flux, Na_2SO_4 , added during the preparation of $\text{CaSO}_4:\text{Dy}$ phosphors, has played

an important role in luminescence and photomagnetic effect.⁶ In order to understand its role in the magnetic behaviour, the plots for phosphors with and without flux having the same concentration of Dy (PM59 and PM32) are shown in Fig. 2. At room temperature, the flux-added phosphor is more paramagnetic than that without flux. As the degree of paramagnetism is related to the number of paramagnetic ions in the host, the observed increase in paramagnetism leads to the entry of more number of Dy^{3+} ions in the host. The quantitative value of N for phosphors with and without flux are shown in Table 1. A similar conclusion has been drawn by the present authors, from the studies of luminescence, for the large entry of Dy^{3+} ions in the host due to the addition of flux. This has been explained on the basis of charge compensation theory of Kroger and Hellingmann.¹²

4. Conclusions

1. The magnetic susceptibility of the host CaSO_4 shows slight temperature dependence, which is rather inconsistent with the Langevin's theory of diamagnetism. This is attributed to the host crystalline defects.
2. The addition of dysprosium in the diamagnetic host CaSO_4 , makes the phosphor less diamagnetic and it becomes even paramagnetic for higher concentration of Dy.
3. The dysprosium activated phosphors obey Curie's law.
4. The estimation of paramagnetic ions per unit volume N , has been made on the basis of Langevin's quantum theory of paramagnetism. It is found that N increases with increase of Dy concentration.
5. Phosphors with flux are more paramagnetic than those without flux. This is attributed to the large entry of Dy^{3+} ions in the host by the charge compensation due to flux.

Acknowledgement

The authors are grateful to Mr R M Raverkar, Principal, Science College, Karad, for his constant encouragement and they are also thankful to Mr S G Sabnis for his help in carrying out the experimental work.

References

1. Nambi K S V, Bapat V N & Ganguly A K, *J. Phys.*, 7C (1974), 4403.
2. Draai W T & Blasse G, *Phys. Status Solidi (a)*, 21 (1974), 569.
3. Luthra J M, Gupta N M, Nambi K S V & Bapat V N, *Proc. natn. Symp. on TL and Its Applications, India*, 1975, 147.

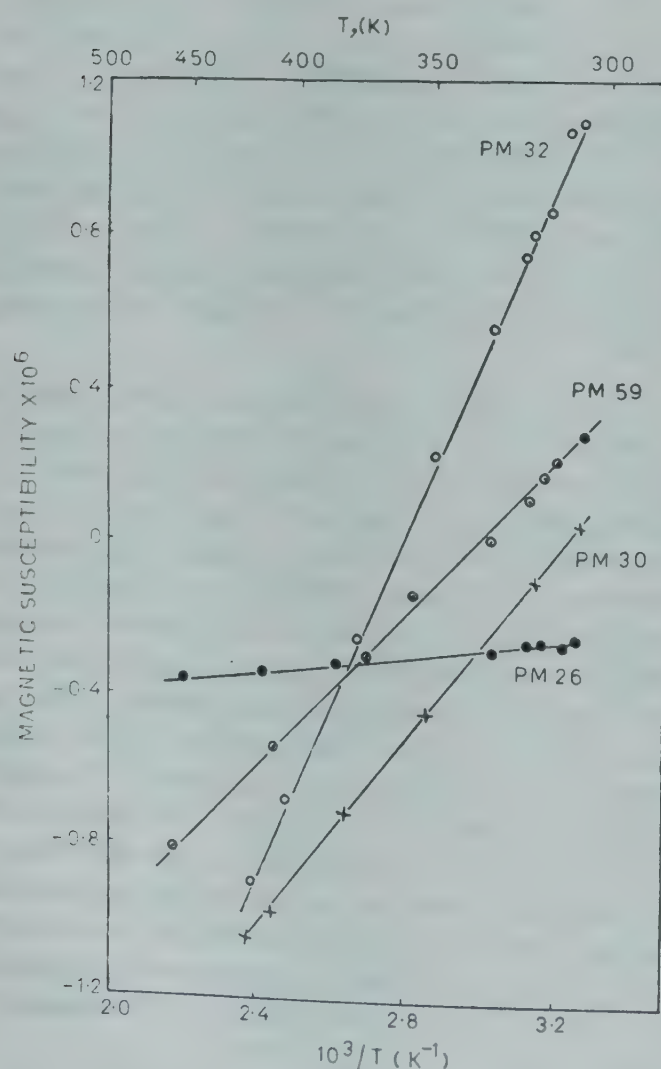


Fig. 2—Variation in magnetic susceptibility versus reciprocal of temperature for the Dy-doped phosphors, with and without flux

MULLA & PAWAR : MAGNETIC SUSCEPTIBILITY OF CaSO_4 : Dy PHOSPHORS

4. Pawar S H, Jagadale S H & Gaikwad N B, *Indian J. pure appl. Phys.*, **15** (1977), 365.
5. Pawar S H, Mulla M R & Sabnis S G, *Proc. Nucl. Phys. & Solid St. Phys. Symp.*, (Department of Atomic Energy, Govt of India, Bombay) **20 C** (1977), 500.
6. Mulla M R & Pawar S H, *Mater. Res. Bull.*, **12** (1977), 929.
7. Paul H Kasai & Yoshira Ottomo, *Phys. Rev. Lett.*, **7** (1961), 17.
8. Bowers R & Melamed N T, *Phys. Rev.*, **99** (1955), 1781.
9. Johnson P D & Williams F E, *J. chem. Phys.*, **17** (1949), 435.
10. Johnson P C & Williams F E, *J. chem. Phys.*, **18** (1950), 323.
11. Heer C V & Rausch C, *Phys. Rev.*, **90** (1953), 530.
12. Kroger F A & Hellingmann J E, *J. electrochem. Soc.*, **95** (1949), 68.

An Empirical Generalized Relation On Decay of CaS Phosphors

A S MEHTA, M C TIWARI & V G MACHWE

Department of Physics, S A Technological Institute, Vidisha

Received 30 January 1978; revised received 10 April 1980

Considering the reported results of decay of various CaS phosphors, a generalized decay relation (GDL): $I = I_0 \exp \{ \alpha - (t/t_0)^{1/4} \}$ is obtained empirically. A model has also been proposed on the basis of trap density (N_t), relative emission rate per unit trap $\{[(dN_{t-1}/dt) (dN_t/dt)] \cdot 1/r\}$ and time ratio $[(t/t_0)]$. The above relation is in good agreement with the proposed model.

1. Introduction

Common as well as infrared-sensitive alkaline earth sulphide phosphors have been extensively studied by various workers.¹⁻³ These phosphors in spite of great care taken in their synthesis have failed to observe in strict accordance any particular decay law.^{3,4} It has also become difficult to assign a fixed order of kinetics^{4,5} to the luminescence process of this type of phosphors. Such an indefiniteness, therefore, reduced the possibility of declaring the reproducibility of this class of phosphors which have not been probably grown in the form of single workable crystals. Recently it is shown by Delosh *et al.*⁶ that the decay of phosphors doped with certain rare earths and transition ions (Tb^{3+} , Eu^{3+} and Mn^{2+}) in inorganic solid phosphors exhibits unusual characteristics. The decay becomes faster under certain photo-excitation. It is also dependent on excitation pulse duration. Interestingly ESR studies on most sulphide phosphors⁷ have revealed the presence of Mn^{2+} as an inherent impurity in most of them. Impurity analysis of $CaSO_4$ —the starting material of CaS phosphors in the present case—is reported by Rawat and Ranade⁸ and Nambi *et al.*⁹ They have shown that transition metals and rare earths of the order of several parts per million are present. The situation inspired the authors to investigate empirically a modified decay law by curve fitting analogy that could accommodate the complex nature of practically all types of calcium sulphide phosphors (short, medium and long after-glow type of CaS phosphors, e.g. $CaS:Nd$, $CaS:Mn$, Cu , Sm and $CaS:Bi$ respectively). Further a model is also proposed.

2. Various Decay Relations

Many workers¹⁰⁻¹⁴ have proposed the following relations for the isothermal phosphorescence decay

characteristics (PDC) of CaS phosphors:

$$I_t = I_0 t^{-1} \quad \dots(1)$$

$$I_t = I_0 (1 + At)^{-2} \quad \dots(2)$$

$$I_t = I_0 \exp(-pt) \quad \dots(3)$$

Since none of these could explain the total observed decay, Coldman and Romaneko¹⁴ proposed the relation

$$I_t = A_1 \exp(-b_1 t) + A_2 (1 + b_2 t)^{-2} \quad \dots(4)$$

while studying $SrS:Cu$, Eu phosphors. This relation suggests that the earlier part of the decay is exponential and the rest is hyperbolic. The power law expression which is being used by many workers in the field is

$$I_t = \text{constant}/t^{(0.8T+1)} \quad \dots(5)$$

It is obtained from a model which emphasized the existence of 'metastable state' and assumed that the number of electrons in this state is just sufficient to saturate after which the decay starts. This number is given by an exponential distribution function $C \exp(-\beta E)$. This relation holds good only when t is large. Another form of power law is

$$I_t = I_0 (t/t_0)^{-b} \quad \dots(6)$$

Further, if $t_0 = 1$ sec, then

$$I_t = I_0 t^{-b} \quad \dots(7)$$

In Eqs. (1)-(7), the various terms stand for: I_t = intensity at time t , I_0 = intensity at time t_0 , p = probability per second of finding the electrons in trap, b = decay constant, and, A , A_1 , A_2 , b_1 , b_2 , β and C are all constants. Eq. (7) fits in well with the experimental results in comparison to other relations. The value of b is calculated¹³ by a statistical relation

$$b = \frac{\sum x \sum y - m \sum xy}{(\sum x)^2 - m \sum x^2} \quad \dots(8)$$

where x and y stand for $\log I$ and $\log t$ and m for the number of sets of (x, y) , which should be large. In support of the validity of Eq. (7), these workers have calculated the degree of linearity in terms of 'correlation coefficient' r , from the relation

$$r = \frac{m \sum x \cdot y - \sum x \cdot \sum y}{[\{m \sum x^2 - (\sum x)^2\} \{m \sum y^2 - (\sum y)^2\}]^{1/2}} \quad \dots(9)$$

The condition to test the validity of the linearity is that the value of r should be $(-1 \leq r \leq 1)$.

3. Results

The authors noted from the reported work¹¹⁻¹⁵ and also from the samples under study that the values of b and r fluctuate appreciably. The range of fluctuation of b is between 0.4 and 1.2 and that of r is between 0.98 and 1.12. On further investigation it is found that $\log I_t - \log t$ plots which should have been straight lines, according to Eq. (7), and which are deliberately reported so by almost all workers in the field, showed upward convexity. For long decay, the PDCs show more clear deviation. When earlier and initial decay is taken into account together with the delayed decay, the convexity becomes pronounced. The authors have dealt the 'initial decay mechanism' separately in a recent communication.¹⁶ What is important here is the deviation of the long tail of the PDC also from the established Eq. (5). In the light of work mentioned earlier,⁶ such a deviation should occur and therefore the $\log I_t - \log t$ curves are approximated to straight lines. The slopes of such lines are reported to lie between -2 and -1.25 . Though such a variation is assigned to the 'quasi-uniform distribution'¹² of electron traps in the proximity region below conduction band, yet this interpretation has a weak basis. We conclude therefore, that both theoretical considerations and experimental observations indicate that CaS phosphors deviate largely from the power law relation mentioned above, except in the intermediate region of the PDC.

Keeping this in view, an attempt is made to remove, empirically, the convexity of $\log I_t - \log t$ curve as well as the concavity of $\log I_t - t$ curve by straightening the former curve along the time axis. The straight line so obtained can be represented by a simple hyperbolic relation.

$$\left[\log \frac{I_0}{I_t} \right]^d = \phi t \quad \dots(10)$$

where ϕ and d are constants.

The experimental values of I_t , I_0 and t from the prepared samples are taken and the numerical value

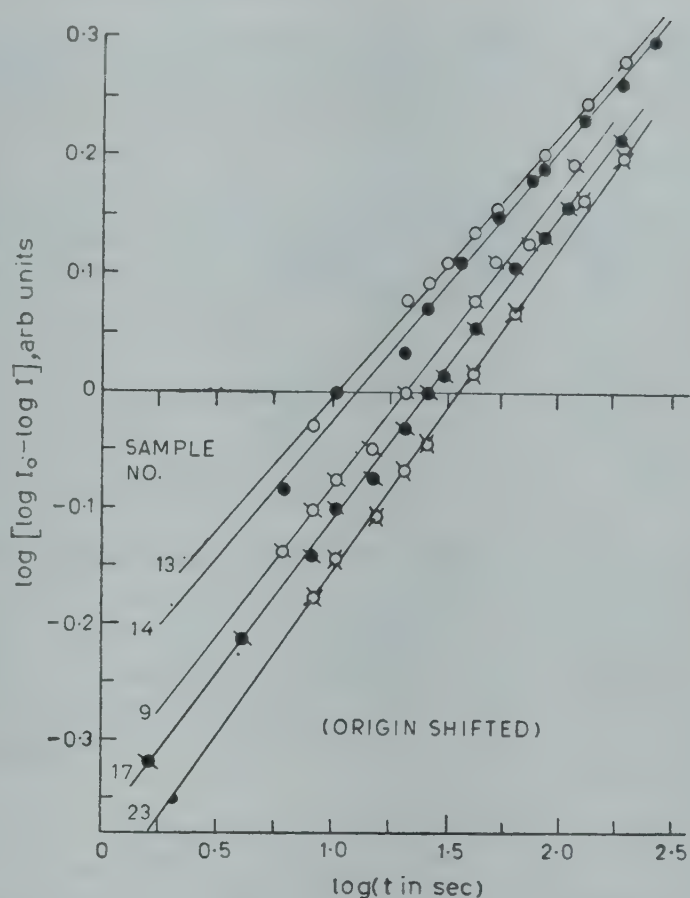


Fig. 1—Log ($\log I_0 - \log I$) versus $\log t$ plot of CaS:Nd phosphors

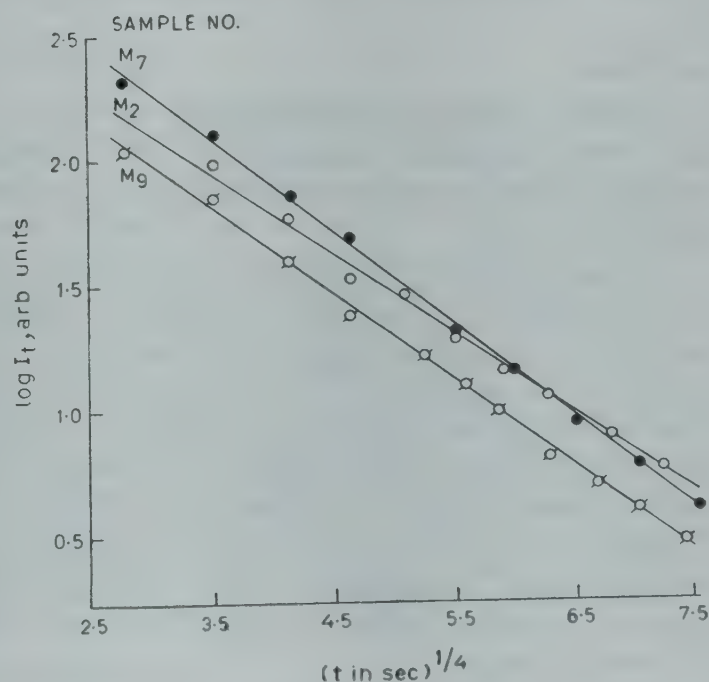


Fig. 2—Log I_t versus $t^{1/4}$ plots of CaS:Bi phosphors

of d is obtained which comes out to be 4. A representative diagram for the estimation of d is illustrated in Fig. 1 (CaS:Nd samples). With $d = 4$ Eq. (10) implies that $\log I_t$ versus $t^{1/4}$ curves should result in straight lines. Such straight lines are obtained for various samples of CaS activated with single, double and triple activators (Figs. 2, 3 and 4 and Table 1), which confirm the validity of Eq. (10).

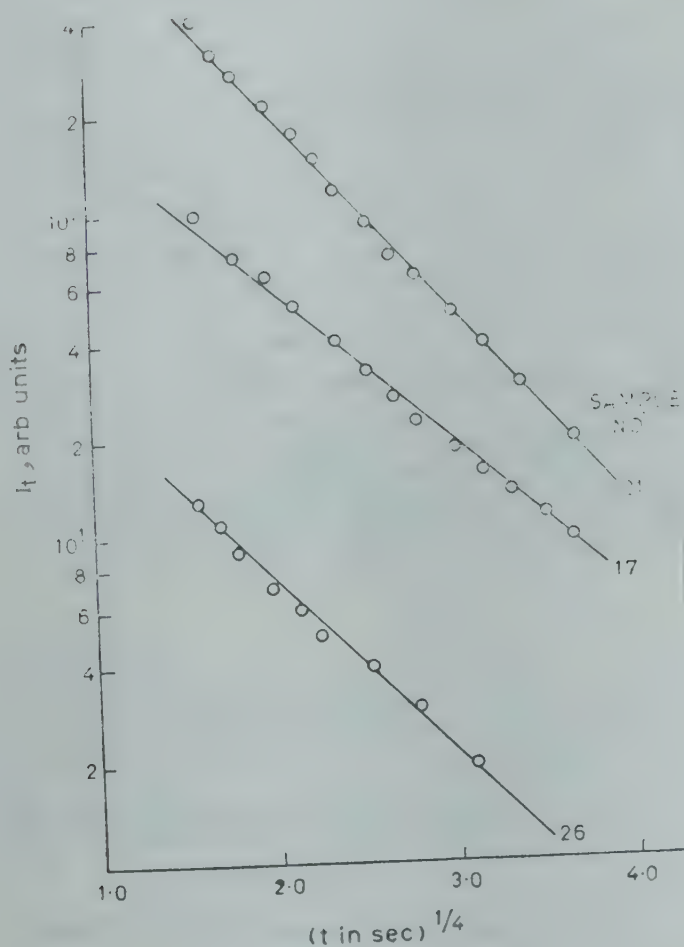


Fig. 3—Log I_t versus $t^{1/4}$ plots of CaS:Nd phosphors

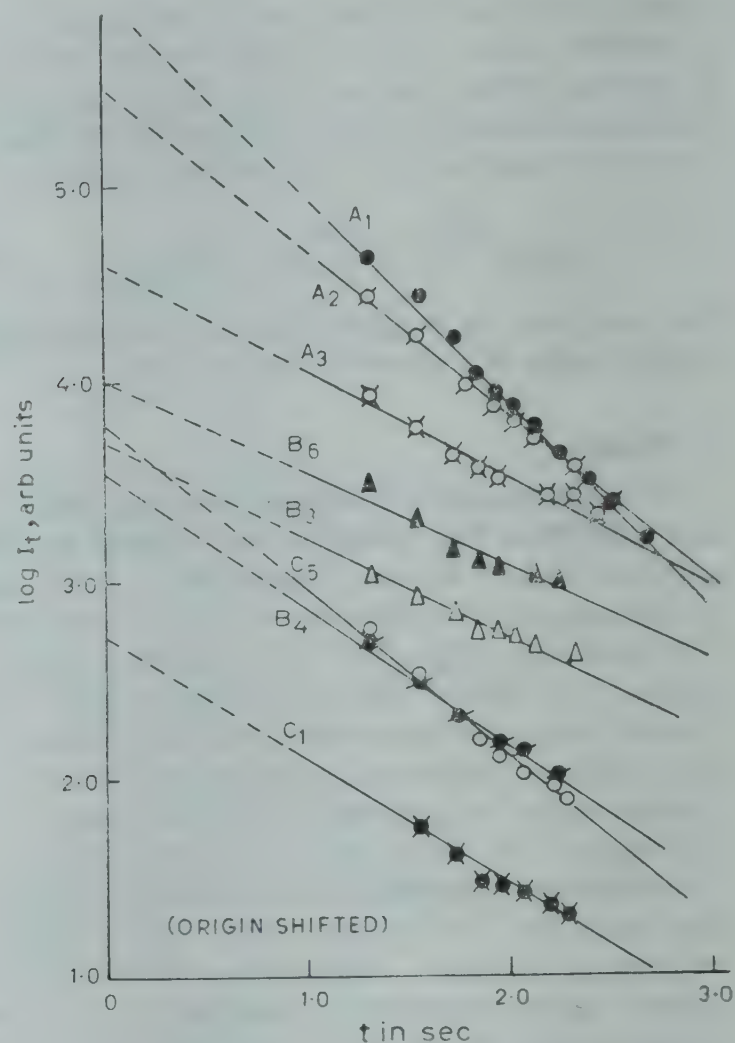


Fig. 4—Log I_t versus $t^{1/4}$ plots of CaS:Mn, Sm, Ce phosphors

4. Model

In order to give a theoretical basis to arrive at the above empirical relation (10), we make an attempt to give a simple model for the decay process discussed above.

A very significant change in conventional thermoluminescence (TL) model is proposed by Bosacchi *et al.*,¹⁷ who on the suggestion of Simmons and co-workers^{18,21} extended the continuous distribution of traps in the TL model originally suggested for semiconductors. However, when such a TL mode is taken into account along with exponential distribution function: $C \exp(-\beta E)$, the mathematical expression becomes much complicated. Thus departing with original statistical model for decay, we make the following assumptions:

- (i) The electron traps of different energies are distributed throughout the meta-stable state of the phosphor below the conduction band.

- (ii) The density of the electrons in all the traps can be given by a simple relation

$$N = N_1 + N_2 + N_3 + \dots + N_r \quad \dots(11)$$

where $N_1, N_2, N_3, \dots, N_r$ are the electron densities in 1st, 2nd, 3rd, \dots, r th trap levels respectively.

Table 1—Activator Concentration of Different Samples in Figs. 1-4

S.No.	Sample Code	Activator Concentration ($\times 10^{-3}$ g in 10 g of CaSO_4)	
1.	A ₁	Mn _{0.2} · Sm _{0.2} · Ce ₄₀	Ref. 13
2.	A ₂	Mn _{0.2} · Sm _{0.8} · Ce ₄₀	
3.	A ₃	Mn _{0.2} · Sm _{2.2} · Ce ₄₀	
4.	B ₃	Mn _{3.2} · Sm ₃₀ · Ce _{0.08}	
5.	B ₄	Mn _{0.2} · Sm ₃₀ · Ce _{0.2}	
6.	B ₆	Mn _{0.2} · Sm ₃₀ · Ce _{0.8}	
7.	C ₁	Mn _{0.02} · Sm ₃₂ · Ce _{0.02}	Ref. 13
8.	C ₂	Mn _{2.0} · Sm ₃₂ · Ce _{0.03}	
9.	M ₂	Bi _{0.8} — —	
10.	M ₇	Bi _{3.0} — —	Author's work
11.	M ₉	Bi _{8.0} — —	
			Machwe V G, PhD thesis, Saugar University, Saugar, MP, (1969)
12.	9	Nd _{0.2} — —	Ref. 10
13.	13	Nd _{0.8} — —	
14.	14	Nd _{0.9} — —	
15.	17	Nd _{10.0} — —	
16.	21	Nd _{3.21} — —	
17.	23	Nd _{10.0} — —	
18.	26	Nd _{80.0} — —	Tiwari M C <i>et al.</i> Conf. Lumin. Allied, Phenomena' IIT, Kharagpur, 25th Dec. 1979
19.	M ₉	Cu _{1.3} · Tb _{10.0} —	
20.	P ₇	Tb _{52.5} · Cu _{0.64} —	

(iii) The electrons reach the emission centre to combine with the hole, via successive intermediate trap levels which interact mutually. The process can be taken analogous to the process of radioactive decay as has been suggested by Curie²² for ZnS:Cu and CaS:Bi phosphors.

Let t' be the time an electron takes to recombine with a hole from emission centre and t_b is the time to travel between any two successive intermediate trap levels.

Writing (dN_r/dt) as the rate of emission of electrons from r th trap level and (dN_{r-1}/dt) from $(r-1)$ th trap level where $t = t' + r \cdot t_b$. Therefore,

$$\frac{(dN_{r-1}/dt)}{(dN_r/dt)} \cdot \frac{1}{r}$$

is the relative emission rate of electrons per unit trap between r th and $(r-1)$ th trap levels. Generally, in decay process it can be understood that such relative emission rate per unit trap would be proportional to same power of a time ratio. Hence,

$$\frac{(dN_{r-1}/dt)}{(dN_r/dt)} \cdot \frac{1}{r} = K (t_b/t)^\delta \quad \dots(12)$$

where K is a constant and δ is some power of 'time ratio'. The validity of this assumption rests on the fact that the above relation (12) is a power law, already discussed in Eq. (6). As the process of decay means fall of intensity with increase of time, the constant K is replaced by $(-1/\alpha)$ where α is a positive number. Therefore,

$$(t_b/t)^\delta = -\alpha \left\{ \frac{(dN_{r-1}/dt)}{(dN_r/dt)} \cdot \frac{1}{r} \right\}$$

$$\text{or } dN_r/dt = -\frac{\alpha}{r} (dN_{r-1}/dt) (t/t_b)^\delta. \quad (13)$$

The standard form of intensity of light is given as

$$dN_r/dt = I_r, dN_{r-1}/dt = I_{r-1} \text{ \& } c \quad \dots(14)$$

The total sum of intensities due to different trap levels, say I_D will be:

$$I_D = (dN/dt)$$

$$\text{or } I_D = d/dt (N_1 + N_2 + N_3 + \dots N_r + \dots) \text{ from Eq. (11),}$$

$$= dN_1/dt + dN_2/dt + \dots dN_r/dt + \dots \quad \dots(15)$$

From Eqs. (14) and (15), we obtain

$$I_D = I_1 + I_2 + I_3 + \dots + I_r + \dots \quad \dots(16)$$

Here it is to be noted that some of the electrons may already be lying at active emission centres before the decay starts, which means that intensity at any time t is given by

$$I_t = I_0 + I_D \quad \dots(17)$$

where I_0 is the intensity due to electrons at active emission centres at $t = 0$. Thus

$$I_t = I_0 + I_1 + I_2 + \dots + I_r + \dots \quad \dots(18)$$

The value of intensities corresponding to various trap levels is obtained by putting $r = 1, 2, 3, \dots$ in Eq. (13). Substituting these values of intensities in Eq. (18) we get:

$$I_t = I_0 \left[1 - \frac{\alpha (t/t_b)^\delta}{1!} + \frac{\alpha^2 (t/t_b)^{2\delta}}{2!} - \dots \right] \\ = I_0 \exp \left\{ -\alpha (t/t_b)^\delta \right\} \quad \dots(19)$$

Comparing Eq. (19) with Eq. (10), it is seen that $\delta = 1/d = 1/4$ and $\phi = (-\alpha^{1/\delta}/t_b)$. Eq. (19) suggests that $\log I_t$ versus $t^{1/4}$ plot should be a straight line. This is verified for the samples of CaS under study and shown in Figs. 2, 3 and 4. Finally Eq. (19) becomes

$$I_t = I_0 \exp \left\{ -\alpha \left(\frac{t}{t_b} \right)^{1/4} \right\} \quad \dots(20)$$

This expression gives a decay which can represent the complete decay of phosphors of CaS, weak or strong. Therefore, it is termed as 'Generalized Decay Law' (GDL).

5. Conclusion

The model suggested above accords with the empirically derived Eq. (10). Since a good number of phosphors of CaS doped with single and mixed activators belonging to transition and rare-earth ions, exhibit decay in accordance with Eq. (20), it can be accepted as a modified GDL over other existing relations. Lastly, the present work does not contradict the various well known decay laws for sulphide phosphors, but suggests simply an improvement to accommodate the practical situations. However, the elementary model discussed above can be further improved in the light of studies on dependence of decay on temperature, kinetics and the mode of excitation, etc. and also the nature of ϕ .

Acknowledgement

The authors are thankful to Prof. MD Abhyankar for his valued suggestions and Prof. S C Jain for providing results of his studies.

References

1. Lehmann W, *J. Lumin.*, 5 (1972), 87.
2. Keller S P, *J. chem. Phys.*, 29 (1958), 180.
3. Ellikson R T & Parker W L, Cornell Symposium, (John Wiley, New York), 1948, 327.
4. Randall J T & Wilkin's M H F, *Proc. R. Soc.*, A184 (1948), 347, 373.
5. Chen R, *J. Electrochem. Soc.*, 116 (1969), 1254.

6. Delosh R G, Gibson E F, Tien T Y & Stadler H L, Paper presented in the Spring Meeting of Electro-chem. Soc., DC, USA, 9th to 13th May, 1971.
7. Nair P G, Lingam K V & Machwe V G, *Proc. Indian Acad. Sci.*, **70** (No. 2) (1969), 53.
8. Rawat B L & Ranade J D, *J. Lumin.*, **14** (1976), 417.
9. Nambi K S V, *J. Phys.*, **C7** (1974), 4403.
10. Mehta A S, Machwe V G & Saxena R C, *Indian J. Phys.*, **49** (1975), 761.
11. Mor S L & Bhawalkar D R, *Indian J. pure appl. Phys.*, **8** (1970), 320.
12. Lawanger R D & Narlikar A V, *Indian J. pure appl. Phys.*, **10** (1972), 617.
13. Jain S C & Bhawalkar D R, *Indian J. pure appl. Phys.*, **13** (1975), 74.
14. Agnihotri V B & Ranade J D, *Indian J. pure appl. Phys.*, **16** (1978), 71.
15. Coldman A G & Romaneko I L, *Optics and spectroscopy*, **27** (1970), 269.
16. Tiwari M C, Mehta A S & Machwe V G, 'Initial decay mechanism in CaS: Phosphors', Paper accepted for publication in '*Proc. natn. Acad. Sci.*'
17. Bosacchi A, Franchi S & Bosacchi B, *Phys. Rev.*, **B12** (1974), 5234.
18. Simmons J G & Taylor G W, *Phys. Rev.*, **B4** (1971), 502.
19. Simmons J G & Taylor G W, *Phys. Rev.*, **B5** (1972), 1619.
20. Simmons J G & Tam M C, *Phys. Rev.*, **B7** (1973), 3706.
21. Simmons J G, Taylor G W & Tam M C, *Phys. Rev.*, **B7** (1973), 3714.
22. Curie D, *Phys. Rev.*, **90** (1953), 154.

Determination of Preferred Sites of Fe^{2+} in the Lattices of W-Hexaferrite Crystal of $\text{Ba}^{2+} \text{Fe}_2^{2+} \text{Fe}_{16}^{3+} \text{O}_{27}^{2-}$ from Mossbauer Spectral Study

M K FAYEK & A A BAHGAT

Atomic Energy Establishment and Faculty of Science, Al Azhr University, Cairo

Received 16 July 1979

Mössbauer effect measurements are carried out in the temperature range (78-750 K) for the hexagonal ferrite $\text{Ba}^{2+} \text{Fe}_2^{2+} \text{Fe}_{16}^{3+} \text{O}_{27}^{2-}$. The different iron sublattices of this complicated structure are detected. The Néel magnetic transition and the Debye temperatures are determined.

1. Introduction

The magnetic properties of hexaferrites have recently received a great deal of attention. This is a result of the search for new magnetic materials and their potential technological applications. One of the typical representatives of the above class of materials is the so called W-type hexaferrite which appeared as a promising material for technological application in the fields of permanent magnets and microwave devices. The crystallographic and magnetic properties of the stoichiometric and mixed W-type hexaferrites have already been studied using different techniques.

Kimich *et al.*¹ at first carried out Mössbauer effect (ME) studies on the compound $\text{Ba Fe}_{18} \text{O}_{27}$. They later repeated their investigation on the same compound and extended their measurements² to the cobalt-substituted hexagonal ferrite, $\text{Ba}^{2+} \text{Co}_x^{2+} \text{Fe}_{2-x}^{2+} \text{Fe}_{16}^{3+} \text{O}_{27}^{2-}$ with ($x=1$ and 1.75) at room temperature. The Mössbauer spectra for these compounds showed complex structures resulting from the overlap of Zeeman splitting patterns of the iron nuclei occupying different crystallographic positions in the lattice. For the Co^{2+} substituted hexaferrites, the Fe^{2+} Mössbauer spectra was reduced in intensity. This reduction in the intensity was explained on the basis of some cobalt ions occupying Fe^{2+} positions in the lattice at the tetrahedral sites while the rest were supposed to occupy randomly other positions in the spinel lattice which were occupied originally by the Fe^{2+} . It is of interest to mention here that X-ray diffraction investigations of Fe_2 -W ferrites failed to establish the positions of the divalent iron ions in the calcite because of the similarity of the scattering factors of the Fe^{2+} and the Fe^{3+} ions. On the other hand, Braun³ applied the condition of charge neutrality and assumed that the Fe^{2+} ions exist in the hexa-

ferrite spinel lattice without specifying their crystallographic positions.

Unfortunately the lack of reliable experimental data in the literature does not allow a detailed analysis of the intrinsic properties of these ferri-magnetic compound on a microscopic scale. For this reason, it seemed interesting to reinvestigate the W-hexaferrite $\text{Ba}^{2+} \text{Fe}_2^{2+} \text{Fe}_{16}^{3+} \text{O}_{27}^{2-}$ using ME measurements over a wide range of temperatures (77-750 K). These studies were expected to provide information on distribution of the iron ions among the different crystallographic sites.

2. Experimental Procedure

Polycrystalline specimens of the hexaferrite $\text{Ba}^{2+} \text{Fe}_2^{2+} \text{Fe}_{16}^{3+} \text{O}_{27}^{2-}$ were prepared by wet grinding into intimate mixtures, of carefully weighted powders of BaO , FeO and $\alpha\text{-Fe}_2\text{O}_3$ in proportions appropriate to the desired compositions. The mixture was pressed into pellets and calcined at 1000°C for 24 hr. The pellets were cooled slowly, ground into fine powders, repelletized and fired at $1300\text{-}1350^\circ\text{C}$ for 24 hr and then allowed to cool slowly.

X-ray powder diffraction pattern of the prepared sample was taken at 20°C using Cu K_α radiation. It showed a single phase of the W-structure with no evidence of impurities or unreacted constituents. The lattice parameters of this hexaferrite are found to be $a = 5.8811 \text{ \AA}$ and $c = 32.8801 \text{ \AA}$.

The Mössbauer effect measurements were carried out for these hexaferrites over a wide range of temperatures (80-750 K) after checking and choosing the optimum absorber thickness which gives best ME spectra. ^{57}Co source embedded in chromium lattice was used as source which was prepared at room temperature. Velocity drive was calibrated

using the quadrupole splitting of the polycrystalline sample of sodium nitroprusside. The measurements were repeated twice for every spectrum. The sample temperature was kept at the desired value with in ± 0.5 K. The resonant absorption spectra at different temperatures are shown in Figs. 1 and 2. The relative area A under resonance was determined at every temperature. The curve $\ln A$ versus T is shown in Fig. 3. The Debye temperature was determined from the variation of $\ln A$ versus T curves for iron nuclei occupying different lattice sites, and found to be $\theta_B = 351 \pm 5$ K.

3. Results and Discussion

On the analysis of ME spectrum of $\text{Fe}_2\text{-W}$ hexaferrite at 293 K, the spectrum can be resolved into twenty-two lines (Fig 2). The line number 3 is slightly broadened and has a lower intensity than the second line, which has a higher intensity making it possible to assume a superposition of not less than

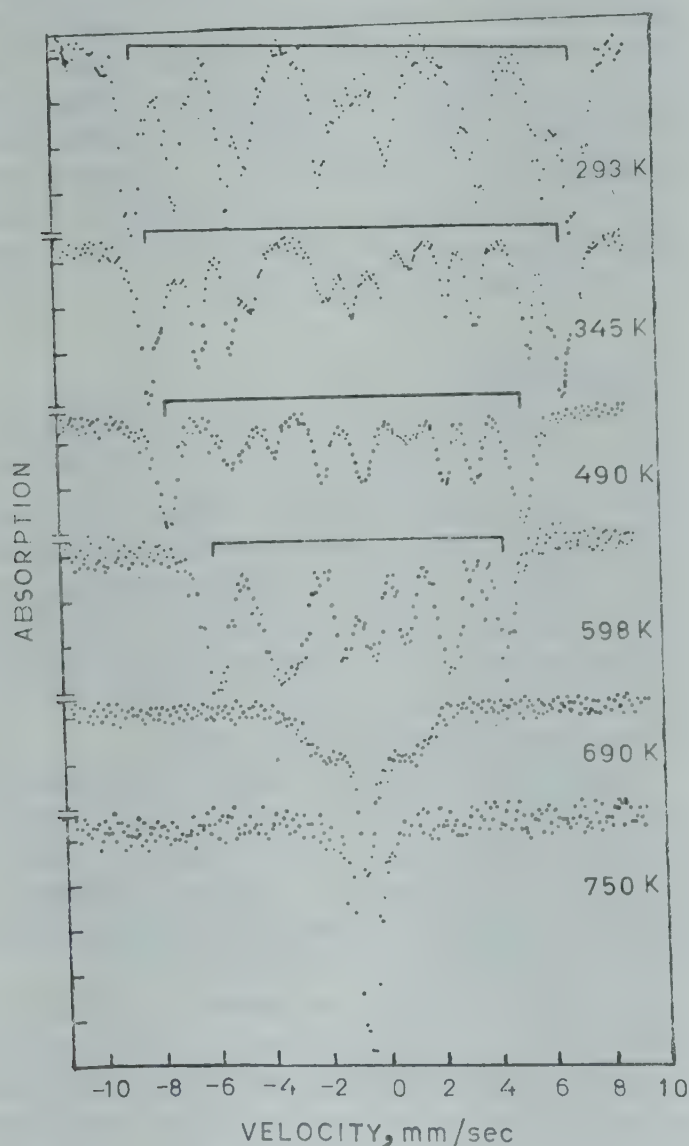


Fig. 1—Mössbauer effect spectra for the compound $\text{Ba}^{2+} \text{Fe}_2^{2+} \text{Fe}_{16}^{3+} \text{O}_{27}^{2-}$ at the temperature range 293 to 750 K

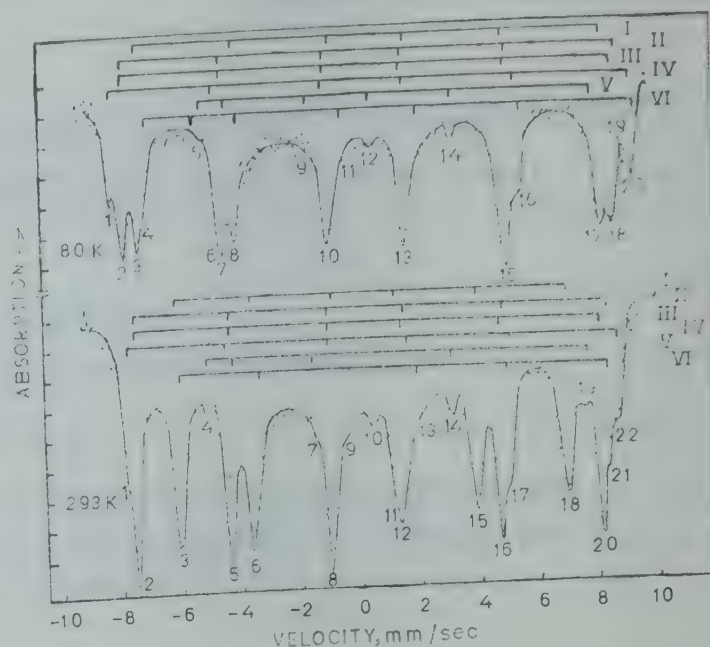


Fig. 2—Mössbauer effect spectra of $\text{Ba}^{2+} \text{Fe}_2^{2+} \text{Fe}_{10}^{3+} \text{O}_{27}^{2-}$ at 80 and 293 K

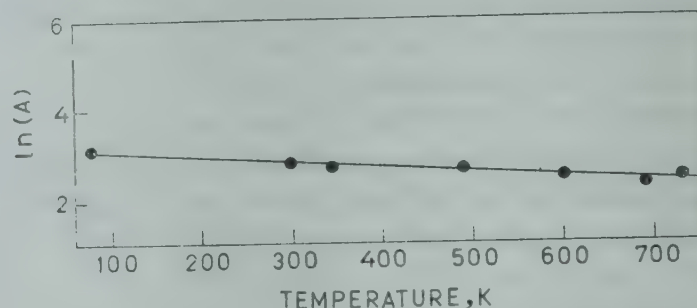


Fig. 3—Variation of the relative ME area $\ln(A)$ with temperature (T) for $\text{Ba}^{2+} \text{Fe}_2^{2+} \text{Fe}_{16}^{3+} \text{O}_{27}^{2-}$

two lines. The spectrum in general, has a complex structure resulting from the overlap of Zeeman splitting patterns from iron nuclei occupying different crystallographic positions. The analysis for the left and right hand peaks of $\text{Fe}_2\text{-W}$ ME spectrum are performed at the room temperature, on the basis of location and intensity of the individual lines (Fig. 4). This is done in the light of previous reported data on the W-hexaferrite compounds.

The obtained spectrum $\text{Fe}_2\text{-W}$ was resolved by trial and error into 6 subspectra and could be then interpreted to six different Zeeman sextets.

For drawing correlations between the sextets (labelled I, II, III, IV, V and VI) and the magnetic sublattices, we have taken advantage to a certain extent of the analogy between M- and W-type compounds reported by different authors⁴⁻⁹ (see Table 1). The intensity of each Zeeman pattern has been established by taking into account the spin orientation relative to the various sextets and the proportionality between the intensity of the sextets and the sublattice population. Comparing the spectra at 80

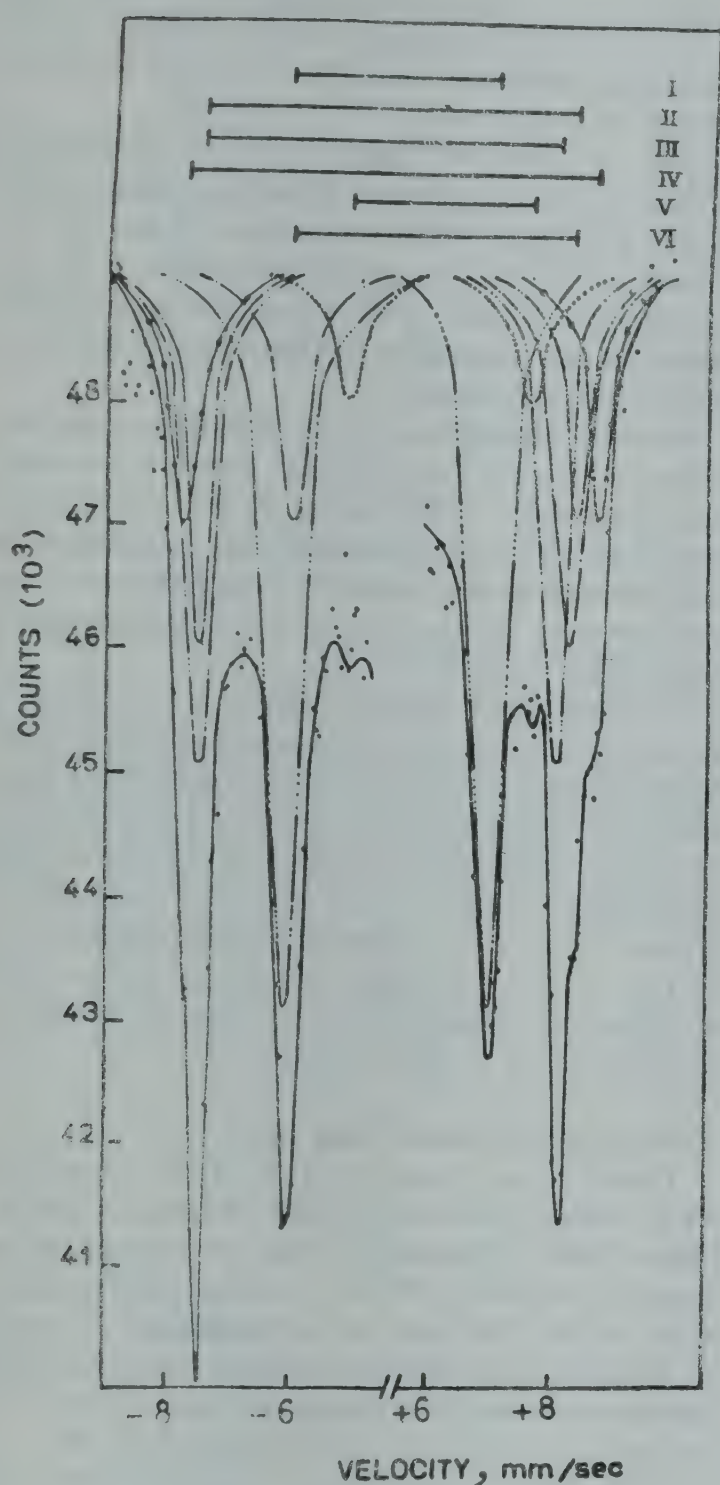


Fig. 4—Analysis of the two outer peaks of the Mössbauer effect spectra for $\text{Ba}^{2+} \text{Fe}_2^{2+} \text{Fe}_{16}^{3+} \text{O}_{27}^{2-}$ at 293 K

and 293 K (Fig. 2), it is seen that the effect of reducing the temperature is seen to increase the intensity of the lines as a result of layer hyperfine fields at the nuclei of the various iron sites. It was also noticed that the line number 3 which appeared as broadened at the room temperature (Fig. 2) was resolved at 80 K into two clear tets with numbers 3 and 4. This is due to the high ordering of the iron spin moment at the low temperature where the magnetization nearly approached saturation. The excess tet number 4 appearing on the spectrum at 80 K probably belongs to the sextet of the ferrous sublattice.

The crystal structure for the compound $\text{Ba}^{2+} \text{Fe}_2^{2+} \text{Fe}_{16}^{3+} \text{O}_{27}^{2-}$ consists of two spinel blocks and one hexagonal R-block.³ In each spinel block for the two compounds there are two molecules of $\text{Fe}_2^{2+} \text{Fe}_2^{3+} \text{O}_4^{2-}$ respectively. The metal ions are located in the interspaces of the oxygen lattices, as in the case of the spinel structure. Thus it can be expected, for this compound, that the mechanism responsible for the magnetic behaviour of the spinel blocks of these oxides will be analogous to that which prevails for the ferrocube materials like $\text{Me}^{2+} \text{Fe}_2^{3+} \text{O}_4^{2-}$ where Me^{2+} represents the divalent metal ions.

In the light of the preceding comparison, the Mössbauer effect parameters [the isomer shift (δ), the hyperfine magnetic field at the ^{57}Fe nuclei, (H_{eff}) and the quadrupole splitting (Δs)] calculated for the investigated compound are reported in Table 2 and the implications are discussed in what follows.

3.1 The Isomer Shift (δ)

The isomer shift values of the different sublattices at both room and liquid nitrogen temperatures for the $\text{Ba}^{2+} \text{Fe}_2^{2+} \text{Fe}_{16}^{3+} \text{O}_{27}^{2-}$ hexaferrite are listed in Table 1. For the spinel block, there is an observed increase in the isomer shift value of ferric ions located at the octahedral site (II) than that at the tetrahedral site (III), which may in the first place be due to the covalency effects through 4s- elec

Table 1—Mössbauer Effect Notations, Coordination, Proposed Ionic Distribution and Spin Direction for the Various Cation Sublattices of W-type Hexaferrite

Mössbauer line notation	Crystallographic position	Coordination number	Proposed ionic distribution	No of ions per formula unit	Block type	Spin direction
I	12 (K)	octahedral	Fe^{3+}	6	R-S	\uparrow
II	6 (9)	octahedral	Fe^{3+}	3	S-S	\uparrow
III	4 (e)	tetrahedral	Fe^{3+}	4	S	\downarrow
	4 (f_1)IV					
IV	4 (f_2)VI	octahedral	Fe^{3+}	2	R	\downarrow
V	2 (d)	hexahedral	Fe^{3+}	1	R	\uparrow
VI	4 (f_3)	octahedral	Fe^{2+}	2	S	\uparrow

Table 2—Mössbauer Effect Parameters of $\text{Ba}^{2+} \text{Fe}_2^{3+} \text{F}_{16}^{3+}$

Sublattice	O_{27}^{2-} Hexaferrites					
	at 293 K			at 78 K		
	δ mm/sec	Δs mm/sec	H_{eff} kOe	δ mm/sec	Δs mm/sec	H_{eff} kOe
I	0.13	0.13	408	0.46	0.01	483
II	0.34	0.08	491	0.39	0.10	415
III	0.25	0.04	485	0.33	0.07	510
IV	0.41	0.09	514	0.42	0.10	541
V	0.38	0.93	397	0.43	0.98	406
VI	1.04	0.17	446	1.02	0.18	508
Dev.	± 0.0817	± 0.0204	± 2.5	± 0.0817	± 0.0204	± 2.5

trons.¹⁹ It could be also interpreted as a compression of the *s*-electron wave functions due to the fact that the volume available to the iron ion at the tetrahedral site is smaller than that at the octahedral site.

A rather large value of the isomer shift is obtained for the sublattice VI (1.04 mm/sec) indicating the presence of the Fe^{2+} iron ion in this sublattice.

This large value of the isomer shift for Fe^{2+} ions with respect to that of Fe^{3+} ions arises from the following causes:

- An excess 3*d*-electron in the Fe^{2+} ions than for Fe^{3+} ions, which can be considered as a shielding for 3*s*-orbitals and thus the 3*s*-electron density decreases, which in turn tends to increase the isomer shift.
- A transfer of an electron from 4*s* to 3*d*-orbits, reduces the electronic contribution to the isomer shift given by the total *s*-electron density at the nucleus, and thus the isomer shift of Fe^{2+} is increased rather than that of Fe^{3+} .

On the other hand, for the R-block, the isomer shift of the octahedral ferric ions at site I is seen to be reduced relative to that at the octahedral sites IV and II. This is due to the distortion in the octahedron of oxygen ions¹¹ about the site I. This fact leads to the inference that the covalency could be entirely responsible for the low isomer shift of this site.

The large isomer shift value of Fe^{3+} at the octahedral site IV is the result of the strong superexchange interactions with the iron ions on site V.

3.2 The Quadrupole Interaction (Δs)

The greatest quadrupole splitting (0.93 mm/sec) is exhibited by the Fe^{3+} ions characterized by the fivefold coordination (sublattice V) because the main contribution to the EFG at the nuclei of the Mössbauer atoms comes from the low-lying shells of the Fe^{3+} ion (3 *p* electrons). This is due to the

significant elongation of the bipyramids, which leads to a significant anisotropy in the overlap of the electronic orbitals of the Fe^{3+} ions as the electronic orbitals of the ligands.

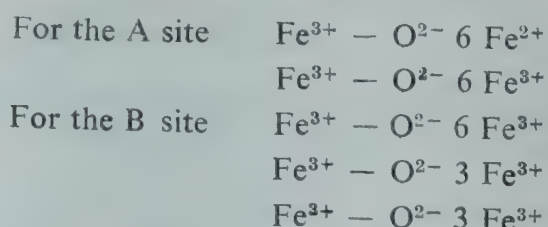
The Fe^{3+} ions are located at the pentahedron formed by nodes of chains of exchange interactions of the iron ions in the sublattices IV and I. The orientation of the magnetic moments of the iron ions in the sublattice V evidently has a strong influence on the orientation of the magnetic moments in the other sublattices.

Since the trigonal axis of the fivefold coordination of the Fe^{3+} ions in $\text{Fe}_2\text{-W}$ is the principle symmetry axis of the tensor of the electric field gradient and if it coincides with the hexagonal axis, a strong spin-orbit interaction may arise.¹² As a result the magnetic moments of the iron ions in the sublattice V orient along the *c*-axis.

The quadrupole splitting values for the site V of the sample are increased as the temperature is lowered while a contraction of the lattice takes place upon cooling. This can occur as a result of a change in the position of equilibrium of the ^{57}Fe nucleus relative to the surrounding ion, i.e. the 2(*d*) iron ion is trapped in one of the potential minima which results in the effective equalization of the mean-square displacements along the *c*-axis and in the plane perpendicular to it (basal plane).

3.3 The Hyperfine Magnetic Field (H_{eff})

Table 2 shows that the H_{eff} of the octahedral site II is larger than that of the tetrahedral site III. This could be explained as due to the existence of largest number of Fe^{3+} ions as the nearest neighbours for the O^{2-} atom at the octahedral site than for the same atom at the tetrahedral site as indicated from the following ferrimagnetic bonds:¹³



On the other hand, the magnetic hyperfine field due to the Fe^{2+} ions placed at the octahedral site VI, which appeared in the present study of the ME spectrum, is smaller than that for the ferric ions lying in the tetrahedral site III.

The hyperfine magnetic field value obtained in the present study for the ferric ions at the octahedral site I is less than that for iron ions on both octahedral sites IV and II. This may be a result of the distortion in the octahedron of oxygen ions about the site I, so that two of them are at a distance smaller

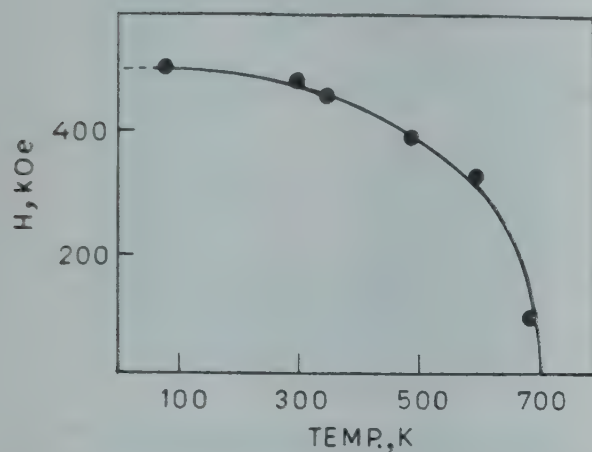


Fig. 5—The magnetic hyperfine field of the tetrahedral sublattice (III) at different temperatures

than that for this site. Consequently the covalency could be entirely responsible for the low hyperfine field of this site.

The value of the magnetic hyperfine field for the octahedral site IV is the largest one. This could be attributed to the presence of strong exchange interactions with iron ions on the pentahedral site V, where the bond angle $\text{Fe}^{3+}(\text{IV}) - \text{O}^{2-} - \text{Fe}^{3+}(\text{V})$ is large.^{8,9}

Site V has a lower hyperfine field than others. This site is coordinated with five O^{2-} ions. Such a configuration suggests much covalency in the $\text{Fe}^{3+} - \text{O}^{2-}$ bond and thus a smaller hyperfine field at the Fe^{3+} iron nucleus.

Fig. 5 shows the temperature dependence of the magnetic hyperfine fields for the $\text{Ba}^{2+} \text{Fe}_2^{2+} \text{Fe}_{16}^{3+} \text{O}_{27}^{2-}$ compound relative to the strongest observed sextet III. Because of the complexity of the ME spectrum at high temperatures there is a rapid fall in hyperfine fields beyond $T=500$ K. The intersection of the curve with the magnetic hyperfine field axis gives $H_{\text{eff}}(0)$ while the intersection of the curve with the temperature axes gives the Néel temperature (Néel transition point T_N) where $T_N = 728$ K. This value is found to be in a good agreement with the previously published data of the magnetization measurements, obtained by Gorter.¹⁴

The relative magnetic hyperfine fields $H(T)/H(0)$ are plotted versus $(1 - T/T_N)$ on a double logarithmic

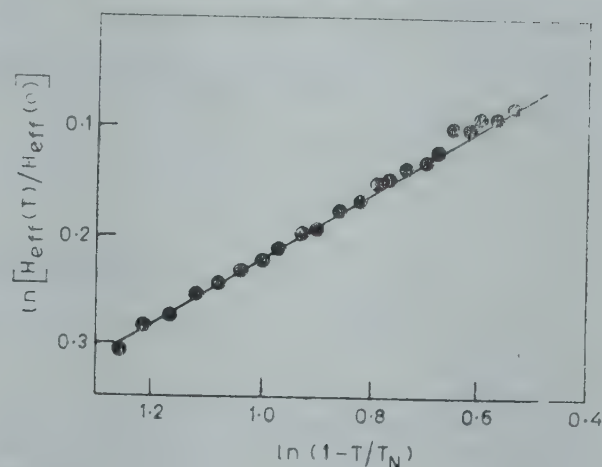


Fig. 6—The relation between reduced hyperfine magnetic fields and reduced temperature for $\text{Fe}_2\text{-W}$ hexaferrite

scale (Fig. 6). The variation of $H_{\text{eff}}(T)/H_{\text{eff}}(0)$ with $(1 - T/T_N)$ follows a $1/3$ power law according to the relation:

$$H_{\text{eff}}(T)/H_{\text{eff}}(0) = D(1 - T/T_N)^B$$

The values of constants are found to be $D = 1.0949 \pm 0.0044$ and $B = 0.3124 \pm 0.0214$.

References

1. Kimich T A, Belov V F, Shipko M N & Korneev E V, *Soviet Phys. Solid St.*, 11 (1970), 1960.
2. Belov V F, Kimich T A, Shipko M N, Zheludev I S, Korneev E V & Ovanesyan N S, *Soviet Phys. JETP*, 37 (1973), 1089.
3. Braun P B, *Philips Res. Rep.*, 12 (1957), 491.
4. Albanese G, Carbucchio M & Asti G, *Appl. Phys.*, 11 (1976), 81.
5. Sizov R A & Zaitsev K N, *Soviet Phys. JETP*, 39 (1974), 1.
6. Bahgat A A, Fayek M K & Eissa N A, *Arab. J. Nucl. Sci.*, 226 (1978), 226.
7. Oleszkowski, Fayek M K & Yamzin I I, *Crystallography*, 14 (1969), 447.
8. Streever R L, *Phys. Rev.*, 186 (1969), 2.
9. Petrov M P & Kunevich A V, *Soviet Phys. JETP*, 36 (1972), 6.
10. Walker J, *Phys. Rev. Lett.*, 6 (1961), 98.
11. Smit J & Wijn H J P, *Ferrites*, (Philips Technical Library, Holland) 1959.
12. Bongers P F, *Philips Tech. Rev.*, 28 (1967), 13.
13. Eissa N A, Bahgat A A & Fayek M K, *Hyperfine interactions*, 5 (1977), 137.
14. Gorter E W, *Philips Res. Rep.*, 9 (1954), 321.

Structure & Growth of MnSe & MnTe Films*

PRABHAT SINGH

National Chemical Laboratory, Pune 411 008

Received 3 October 1979

Electron diffraction study on vapour phase deposits of MnSe and MnTe films formed at different temperatures on different faces of rock salt and glass has been made. Deposits of MnSe retain cubic structure (α -MnSe, $a = 5.45 \text{ \AA}$) at all temperatures. Deposits of MnTe consist entirely of tellurium at lower substrate temperatures but at the intermediate temperatures ($\approx 350^\circ\text{C}$) MnTe films having NiAs-type structure ($a = 4.16 \text{ \AA}$, $c = 6.82 \text{ \AA}$, $c/a = 1.63$) are formed; at higher temperatures ($\approx 400^\circ\text{C}$) the deposits develop cubic- and hexagonal-type structures, the higher temperatures, however, favouring epitaxial growth.

1. Introduction

Chalcogenides of manganese have attracted considerable attention because of their magnetic behaviour. While bulk MnSe is anti-ferromagnetic¹ between -196 and 70°C , MnTe though anti-ferromagnetic undergoes a change to paramagnetic state above its Neel point² ($\approx 50^\circ\text{C}$). Diselenide and ditelluride of manganese are also anti-ferromagnetic.³

Solubility limits of tellurium and selenium in manganese are narrow.⁴ X-ray diffraction reveals that Mn and Te form two phases, namely MnTe having a hexagonal structure ($a = 4.146 \text{ \AA}$, $c = 6.709 \pm 5 \text{ \AA}$) and MnTe_2 a cubic one (C_2 type structure, $a = 6.951 \pm 2 \text{ \AA}$).

Selenium forms two types of compounds, namely MnSe and MnSe_2 . MnSe exists in three modifications,⁵ viz. α , β and γ , where α and β are cubic having B_1 and B_3 types of structure respectively, while γ phase, which is very stable, is hexagonal (B_4 type, $a = 4.12 \text{ \AA}$, $c = 6.72 \text{ \AA}$, $c/a = 1.63$, $M = 2$, P_{63mc}). MnSe_2 has a cubic structure (C_2 type, $a = 6.417 \pm 5 \text{ \AA}$). While studies on the bulk structure of MnSe and MnTe films have been exhaustive, no structural studies on their vapour phase deposits and also on their magnetic properties have been made. In the present paper, a detailed investigation has been made on the structures, phase transitions, orientation, etc. of the vapour phase deposits formed on single crystal substrates, especially at higher substrate temperatures (t_s).

2. Experimental Details

Spec pure quality of Mn and Te or Se (purity 99.99% or more) were mixed together in powdered form and reacted together in vacuum-sealed silica

tube. The detailed procedure was similar to that described earlier.⁶

The compounds thus prepared were examined by the X-ray powder method. Small amounts of the compounds were separately vacuum deposited on collodion, glass and also on (100), (110) and (111) faces of rock salt crystals in the temperature range from about room temperature to 400°C . These were then examined both by reflection and transmission techniques in the electron diffraction and camera (HEED) in the usual way.

3. Results

3.1 MnSe Films

On NaCl polycrystalline tablets—Deposits of MnSe formed between the room temperature and 200°C were amorphous in nature or had a fine grain structure. With the increase of t_s , the deposits became crystalline and sharp diffraction patterns were obtained conforming to the cubic structure of α -MnSe ($a = 5.45 \text{ \AA}$).

On NaCl (100) faces—Deposits formed up to about 350°C were having properties similar to those observed on the polycrystalline tablets. At higher t_s ($\approx 400^\circ\text{C}$), these deposits consisted of α -MnSe developing a $2\text{-}d\{100\}$ orientation on these substrates (Fig. 1).

On NaCl (110) faces—MnSe films on NaCl (110) faces at temperatures $350\text{--}400^\circ\text{C}$ also developed with $2\text{-}d\{100\}$ orientation. However, the diffraction pattern showed four additional strong spots lying on 200, 220, etc. reflections which suggested that the $2\text{-}d\{100\}$ orientated deposits were mutually rotated by 45° .

*NCL Communication No. 2504.

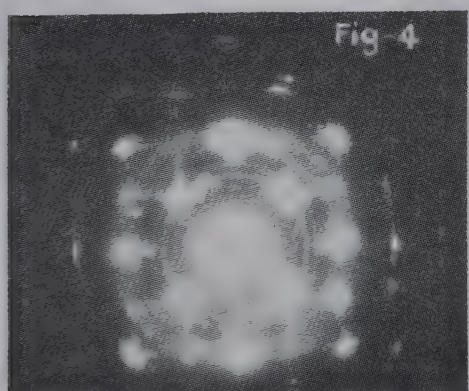
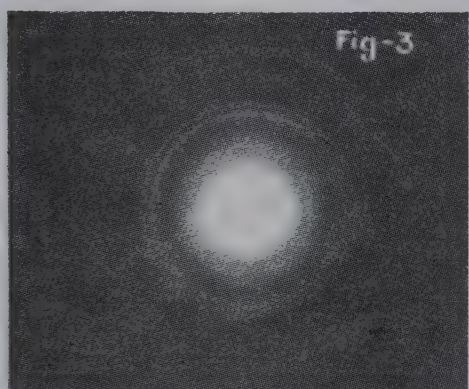
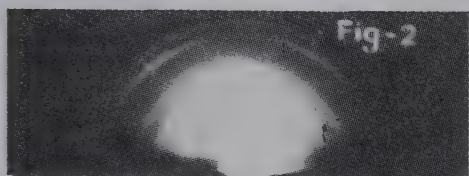
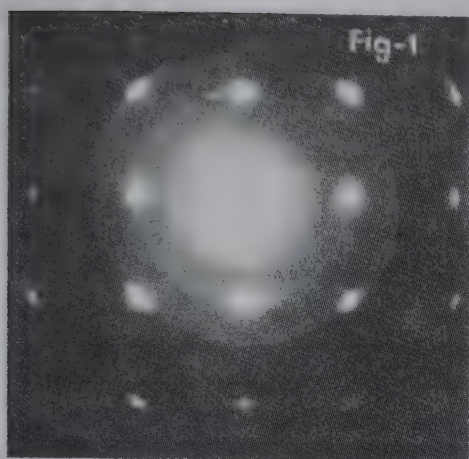


Fig. 1—Electron diffraction pattern of 2- d {100} orientation of MnSe on (100) (cubic) face of NaCl at 400°C

Fig. 2—Electron diffraction patterns of 1- d {111} orientation of MnSe on glass substrate at 300°C

Fig. 3—Electron diffraction patterns of MnTe on NaCl polycrystalline tablets at $\approx 350^\circ\text{C}$

Fig. 4—Electron diffraction patterns of 2- d {100} orientation of C-phase coupled with 2- d {30·5} orientation of H-phase of MnTe films on NaCl (100) face at 300-400°C

From the disposition of the spot patterns with respect to the substrate face, it was concluded that these films grew epitaxially in such a way that

$\langle 100 \rangle$ and $\langle 110 \rangle$ of MnSe were parallel to $\langle 100 \rangle$ of NaCl.

On NaCl (111) faces—These deposits were again amorphous or fine-grained in structure at $t_s < 350^\circ\text{C}$. At 400°C, these deposits consisted of α -MnSe developing both 2- d {111} and 2- d {211} orientations.

On glass substrates—At higher t_s (300°C), the deposits were polycrystalline developing 1- d {111} orientation (Fig. 2).

3.2 MnTe films

On NaCl polycrystalline tablets—Deposits of bulk MnTe formed at temperatures below 200°C yielded patterns primarily due to some tellurium. However, when t_s was raised to about 350°C, the films were polycrystalline and yielded patterns conforming to the hexagonal structure of MnTe ($a = 4.16 \text{ \AA}$, $c = 6.82 \text{ \AA}$, $c/a = 1.63$) (Fig. 3; Table 1).

On NaCl (100) faces—Deposits formed at temperatures below 300°C contained mainly tellurium as observed in the case of deposits on polycrystalline NaCl substrates. At higher t_s (300-400°C), the film yielded patterns consisting of spots and rings and their sharpness increased with the rise of t_s (Fig. 4). On analysis, they were found to be a mixture of hexagonal (H)- and cubic (C)- phases with lattice parameters such that $d_{11.0}$ of H-phase corresponded to d_{220} of the C-phase. It was further seen, that there were numerous streaks passing through the diffraction patterns, i.e. spots arising from the intersection of

Table 1—Analysis of the Patterns of MnTe on NaCl Polycrystalline Tablets at $\approx 350^\circ\text{C}$ ($a = 4.16 \text{ \AA}$, $c = 6.82 \text{ \AA}$, $c/a = 1.63$) (Ref. Fig. 3)

I/I_0	$d, \text{ \AA}$	hkl
W	3.41	00·2
S	3.15	10·1
S	2.86	—
M	2.51	10·2
M	2.23	00·3
S	2.08	11·0
W	1.95	11·1
M	1.90	10·3
W	1.78	20·0
MS	1.53	20·2
M	1.50	11·3
M	1.33	21·1
W	1.28	11·4
W	1.24	21·2
W	1.13	21·3

W, weak; M, medium; MS, medium strong; S strong

two perpendicular streaks suggested the development of a 2-*d* {100} orientation of the C-phase. Further, each of the 200 reflections was surrounded by four spots arising probably from two types of fractional indices, such as 2/3, 4/3, 1/3 and 1/3, 7/3, 1/3 of the C-phase which are equivalent to 10·0 and 10·2 reflections of the H-form. The disposition corresponded exactly to H- and C-phases of CrTe.⁷ This disposition of spots may be ascribed to the formation of {111} twinned structures of 2-*d* {100} oriented cubic phase, double diffraction process or due to curvature of the deposited film. The other features of the diffraction patterns correspond to the presence of a mixture of H- and C-phases similar to those obtained in CrTe films.

The disposition to 10·1 spots also suggests that the beam was along the $\langle 211 \rangle$ direction of the deposits, nearly corresponding to the {30·5} orientation of the H-form crystallites but rotated by 90°.

On NaCl (110) faces—The deposits in this case also became epitaxial at higher *t_s* (about 350°C) developing primarily 2-*d* {10·4} + {30·5} + {12·5} orientations.

On NaCl (111) faces—These deposits were epitaxial at higher *t_s* (350-400°C), developing a 2-*d* {00·1} orientation.

4. Discussion

It has been observed during the present study of selenide films that the deposits developed an fcc (NaCl type) structure (*a* = 5·45 Å, α-MnSe) at all temperatures on polycrystalline as well as single crystal substrates. The deposits were polycrystalline at lower *t_s* but became 2-*d* oriented on single crystal

substrates with the increase in *t_s*. The deposits had a tendency to become polycrystalline and developing a 1-*d* {111} orientation with the increase in film thickness. This is clearly shown in the case of thick films on glass substrates at about 250°C. MnTe films obtained from vapour phase contain mostly tellurium at lower *t_s*, but at higher *t_s* they are composed of MnTe as the bulk. This appears to be due to the ease of dissociation of MnTe to its constituents in vapour phase, which when condensed still retains dissociated phases, but at higher *t_s* the dissociated phases, even though condensed as individual species, react at the substrate surface to form the MnTe phase. Similar dissociation has been produced at lower temperatures for CoTe but the formation of the main species has also been observed.⁸

Acknowledgement

Thanks are due to Dr A Goswami for his interest in this work.

References

1. Lindsay R, *Phys. Rev.*, **84** (1951), 569.
2. Willis B T M & Rooksby H P, *Proc. phys. Soc. Lond.*, **B57** (1954), 290.
3. Hastings J M, Elliott N & Corliss L M, *Phys. Rev.*, **115** (1959), 13.
4. Furberg S, *Acta Chem. scand.*, **7** (1953), 693.
5. Baroni A, *Z. Kristallogr.*, **99** (1938), 336.
6. Goswami A & Mandale A B, *Japan J. appl. Phys.*, **17** (1978), 473.
7. Goswami A & Nikam P S, *Thin Solid Films*, **11** (1972), 353.
8. Goswami A & Prabhat Singh, *Indian J. pure appl. Phys.*, **11** (1973), 373.

Compression of Sodium Chloride Single Crystals Along [001] Direction

L C JAIN

Department of Physics, Government Engineering College, Rewa
and

T S MURTY

Department of Physics, University of Jabalpur, Jabalpur

Received 1 February 1980

Sodium chloride single crystals were compressed at room temperature along [001] direction and a large number of stress-strain curves were obtained with a view to studying the elastic and plastic deformations. Yield strengths and work-hardening coefficients (measured in terms of angles) were found to vary within a wide range. The elasto-plastic deformation was further studied using etch technique. The mechanisms of dislocation multiplication, which causes variation in dislocation density and glide band formation, are explained.

1. Introduction

Schmid and Boas¹ and many others^{2,3} reported the studies of stress-strain curves of NaCl crystals, but their work was performed before the dislocation theory came into existence. In recent years, Pratt⁴ and Davidge and Pratt⁵ have investigated the compressional curves of NaCl crystals, but the scope of their work is confined to study the role of gliding as a predominant process in the deformation of such crystals and to develop a theory of work-hardening. So far none seems to have fully investigated the yield point limits of NaCl crystals with the help of compressional stress-strain curves. The present work was undertaken with a view to studying the variations in the yield points and work-hardening coefficients (measured in terms of angles). The elasto-plastic deformation was further studied using etch technique.

2. Experimental Details

Single crystals of NaCl were grown from melt by Kyropoulos technique using rotation and water cooling device. Specimens of various lengths and cross-sectional areas were prepared by cleaving the lower half of these crystals, to ensure uniform dislocation density.⁶ The exact dimensions of such samples are given in Tables 1 and 2. These were, then, annealed at 600°C for a period of 18 hr and then cooled at a rate of 8°C/hr. The details of such annealing are given elsewhere.⁷ These samples were compressed along their lengths by the self-recording testing machine which has already been described

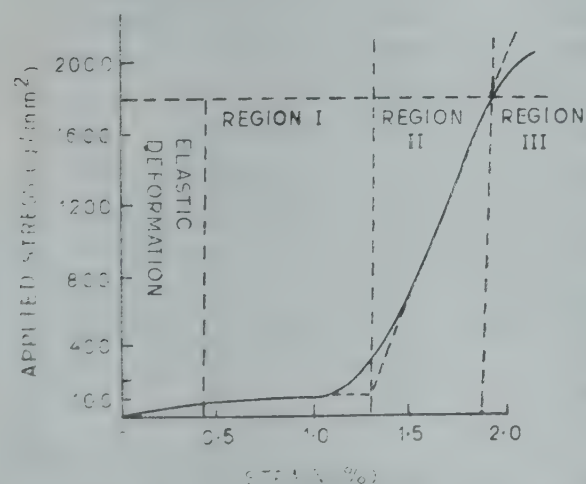


Fig. 1—Stress-strain curve showing the three regions of plastic deformation

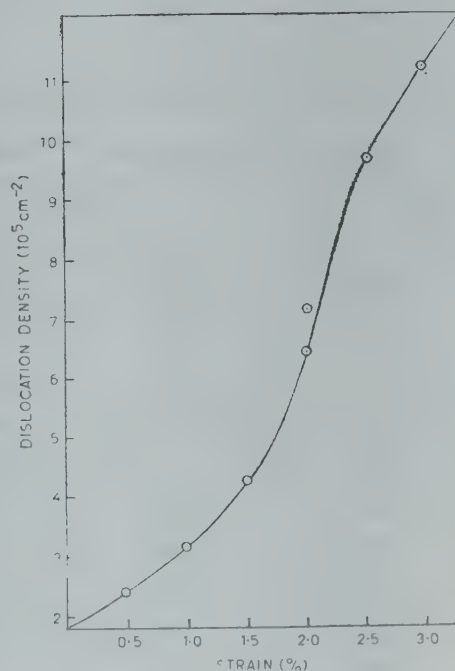


Fig. 2—Plot of dislocation density versus strain

earlier.⁸ The cross-head speed used for deformation was 0.125 mm/min.

3. Results and Discussion

3.1 Stress-Strain Curves

Stress-strain curves were obtained for a large number of samples. One such curve is shown in Fig. 1. The following information is obtained from these curves:

- (1) Every curve has a typical elastic region, followed by three regions of plastic deformation similar to an fcc metal crystal.⁹

- (2) The yield point values vary within wide limits, the minimum value being 33 g/mm² and the maximum 110 g/mm².

- (3) The extension and work-hardening coefficients (measured in terms of angles) were different for regions I and II (also known as easy glide region and linear work-hardening region respectively) for all the samples. The calculated values of yield stress and the work-hardening coefficients are given in Table 1.

Gilman and Johnston¹⁰ found a large drop in stress at the yield point for LiF, but no such drop

Table 1—Details of Compression of NaCl Samples along [001] Direction (For such compression, specimens of various dimensions were selected)

Specimen No.	Length mm	Breadth mm	Thickness mm	Area of cross-section mm ²	Yield strength g/mm ²	Work-hardening coefficient	
						θ_I	θ_{II}
1	14.3	4.6	3.6	16.56	100	3°	69°
2	15.0	4.3	4.0	17.20	100	4°	63°
3	13.8	4.2	3.9	16.38	100	5°	65°
4	12.2	8.8	4.8	42.24	50	1°	74°
5	10.0	4.0	4.0	16.00	90	4°	69°
6	10.4	9.7	4.7	45.59	33	4°	70°
7	15.0	4.0	4.0	16.00	110	2°	74°
8	15.0	4.0	4.0	16.00	100	1°	70°
9	15.0	4.0	4.0	16.00	75	—	—
10	11.6	4.9	4.6	22.54	65	3°	67°
11	20.0	5.0	5.0	25.00	50	1°	62°
12	20.0	6.0	6.0	36.00	100	6°	65°
13	14.0	4.0	3.0	12.00	60	6°	57°
14	11.5	4.6	4.7	21.62	70	3°	40°
15	15.0	5.0	5.0	25.00	70	3°	78°

Table 2—Size Effect on the Compression of NaCl Samples Along [001] Direction

Specimen No	Length in mm	Breadth in mm	Thickness in mm	Area of cross-section in mm ²	Value of yield strength g/mm ²	Work-hardening coefficients	
						θ_I	θ_{II}
1	18.0	8.0	3.0	24.00	80	2°	76°
2	18.0	10.0	5.0	50.00	28	3°	75°
3	18.0	4.0	4.0	16.00	100	—	—
4	18.0	4.0	4.0	16.00	80	—	—
5	18.0	5.0	5.0	25.00	50	—	—
6	12.0	5.0	5.0	25.00	140	2°	65°
7	15.0	5.0	5.0	25.00	80	2°	64°
8	12.0	5.0	5.0	25.00	66	4°	66°
9	13.3	5.0	5.0	25.00	80	—	—
10	20.0	5.0	5.0	25.00	40	—	—

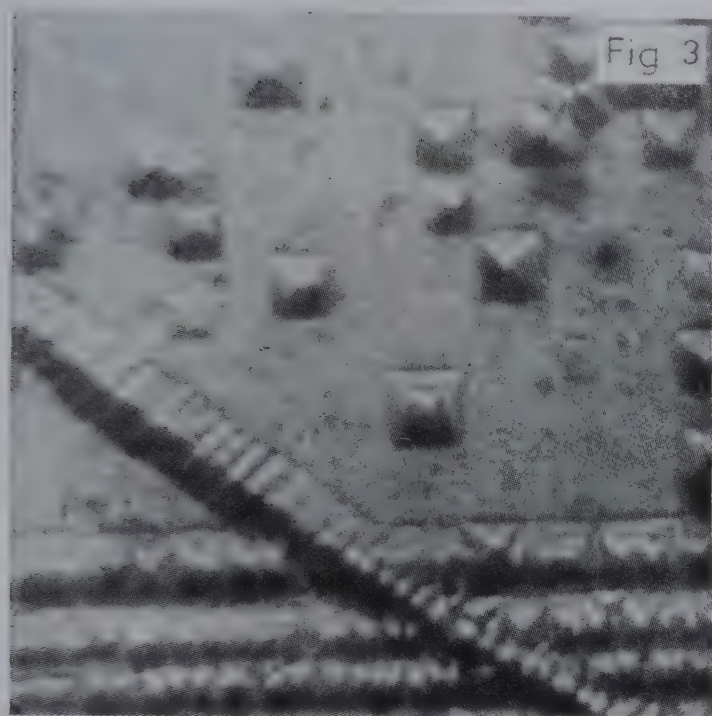


Fig. 3—Etch pattern on a (001) surface showing low dislocation density [specimen was compressed by a small amount, cleaved in a direction perpendicular to the compression axis and the freshly cleaved (001) surface was etched ($\times 200$)]

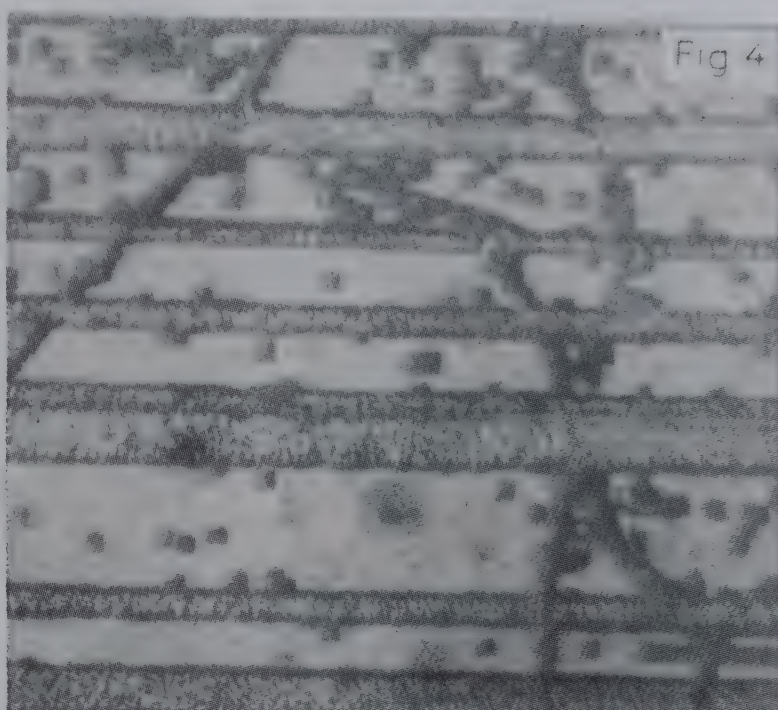


Fig. 4—Formation of screw dislocation glide bands of various widths [the specimen was compressed 1%, cleaved in a direction perpendicular to the compression axis and then etched ($\times 150$)]

was observed for NaCl. Inder Schmitt and Hassen¹¹ too have not reported such a yield instability. This may be due to the fact that NaCl has a lower yield stress than LiF. A notable feature of these investigations was that some of the samples cleaved along the compressional direction even before the generation of appreciable plastic flow. Hayden *et al.*¹² have reported a similar behaviour for bcc metal crystals. Such a feature was not observed when X-irradiated samples of NaCl single crystals were compressed along the [001] direction.¹³

3.2 Size Effect

The effect of size of crystals on the stress-strain curves was studied by preparing samples in the following two ways: (i) specimens with same lengths, but of different areas of cross-section and (ii) specimens with equal areas of cross-section, but of different lengths. These were then compressed using a cross-head motion of 0.125 mm/min. The yield stress values and work-hardening coefficients for both categories of samples are given in Table 2. The values of yield strength for specimens with smaller lengths and smaller areas of cross-section are found to be more.

Boas,¹⁴ Nabbarro¹⁵ and Kochendorfer¹⁶ have reported similar results for metal crystals.

3.3 Dislocation Density

Each specimen was compressed to a different percentage of strain and then cleaved into half in a

direction perpendicular to the compression axis. The cleaved faces were then etched by the method mentioned elsewhere.¹⁷ Dislocation densities were calculated from the count of the etch pits. Fig. 2 shows a plot of dislocation density versus corresponding percentage strain. The dislocation density is very low in the initial regions and then increases enormously in stages II and III of plastic deformation. Fig. 3 shows a (001) surface of a crystal that has undergone only a little amount of plastic deformation. A few screw dislocation glide bands are seen in Fig. 3 along with the dislocation etch pits. When the deformation was high enough, it was found that the slip was developing fast and the number of glide bands was increasing. Fig. 4 shows such typical screw dislocation glide bands of various widths, obtained after cleaving the (001) face of a crystal which was compressed to nearly 1%.

The entire mechanism of strain-hardening responsible for the plastic deformation of NaCl crystals has already been described.⁸

References

1. Schmid E & Boas W, *Plasticity of crystals* (F A Hughes, London), 1950.
2. Brilliantow N A & Obreimon I W, *Phys. Z. Soujet*, 6 (1934), 587.
3. Blank F, *Z. Phys.*, 61 (1930), 727.
4. Pratt P L, *Acta Metall.*, 1 (1953), 103.
5. Davidge R W, Pratt P L, *Phys. Status Solidi*, 6 (1964), 759.

6. Naidu S M R & Murty T S, *Proc. nuclear and solid state physics symposium, Madras* (Bhabha Atomic Research Centre, Bombay), 1968, 405.
7. Jain L C, *Investigations of elastic and plastic properties of materials*, Ph D thesis, Jabalpur University, Jabalpur, 1971.
8. Jain L C & Murty T S, *Indian J. pure appl. Phys.*, **9** (1971), 87.
9. Jain L C & Murty T S, *Proc. nuclear & solid state physics symposium, Bombay* (Bhabha Atomic Research Centre, Bombay), 1968, 275.
10. Gilman J J & Johnston W G, *Solid state physics*, Vol. 13 (Academic Press, New York), 1962, 165.
11. Inder Schmitt W & Haasen P, *J. appl. Phys.*, **32** (1961), 1790.
12. Hayden W H, Mofatt W F & Wulff J, *The structure and Properties of materials*, Vol. III (John Wiley, New York), 1966, 191.
13. Jain L C & Murty T S, *Journal of Science Research*, (Jabalpur University, Jabalpur), 1974, 8.
14. Boas W, *Helv. phys. Acta*, **23** (1950), 159.
15. Nabarro F R N, *Some recent developments in rheology* (British Rheologists Club, London), 1950.
16. Kochendorfer A, *Plasticshe eigenschaften von kristallen* (Springer, Berlin), 1941.
17. Jain L C & Murty T S, *Indian J. pure appl. Phys.*, **14** (1976), 67.

Electret Properties of Electrically Charged Silicone Rubber

RUDRA KANT SRIVASTAVA, M S QURESHI & C S BHATNAGAR

Department of Physics, M A College of Technology, Bhopal 462 007

Received 9 August 1979; revised received 11 February 1980

The electret properties like depth of penetration of charge δ , initial trap density n_{t0} , mobility-free lifetime product $\mu\tau$, dipolar concentration, etc. have been obtained from a single measurement (thermally stimulated discharge current TSDC) of thermoelectrically charged electrets of silicone rubber (medical grade). The thermal current spectra of these electrets show two current peaks one at 336 K and the second at 405 K.

1. Introduction

In order to develop the right kind of vascular prosthesis, the authors have, for the first time, developed a technique for the production of charged polymer tubes¹ by giving them a thermo-magnetic treatment. They have also studied²⁻⁵ the basic properties like the effect of temperature, magnetic field, storage time, heating rate, charge-decay, thermally stimulated discharge current (TSDC) of these tubes of silicone rubber (medical grade) and polymethylmethacrylate. A theory has been developed⁶ previously to describe the TSDC of magnetically polarized dielectrics with the help of which it has been possible to explain the peaks observed and to obtain their kinetics for magnetically polarized polymer tubes.

The present paper reports the various electret properties as studied from TSDC analysis of electrically modified silicone rubber—the substance which is gaining importance in prosthetic work.⁴

2. Theory

The expressions given here and used in the calculations have been derived by Perlman and Creswell.⁷⁻⁹ The basic expression, describing the peaks in TSDC obtained from near surface charged insulators, heated at a constant rate, is:

$$j(T) = A \exp \left[-E/kT - B \int_{T_0}^T \exp(-E/kT) dT \right] \quad \dots(1)$$

Perlman advocated that both types of mechanisms, dipole orientation and trapping of charges, must be used to describe the TSDC of a dielectric. Consequently, the values of constants, A , B and E have different significances.

If we explain a TSDC peak in terms of dipole orientation, the constant E is called activation energy and the values of A and B are

$$A = \frac{N \mu^2 E_p}{3k T_p \tau_0}; \quad B = \frac{1}{\beta \tau_0} \quad \dots(2)$$

where N is the dipolar concentration, μ the dipole moment, T_p the polarizing temperature, τ_0 the pre-exponential factor of time-constant, β the uniform heating rate.

On the other hand, when the peak is supposed to be due to charge trapping, E is called charge trap depth and the values of A and B are given by

$$A = \frac{(n_{t0} e \delta)^2 \mu \tau}{2 \epsilon \cdot d \cdot \tau_0}; \quad B = \frac{1}{\beta \tau_0} \quad \dots(3)$$

where n_{t0} is the initial trap density, e the electronic charge, δ the depth of penetration of charge, $\mu\tau$ the charge mobility-free lifetime product, ϵ the dielectric permittivity, d the sample thickness and τ_0 the inverse of trap escape frequency.

The current released initially, just above T_0 [Eq. (1)], can be shown to have the form:¹⁰

$$\ln j \approx \text{constant} - E/kT \quad \dots(4)$$

The activation energy E for the discharge process, responsible for a peak, can be obtained from a plot of $\ln j$ vs $1/T$.

Eq. (1) can be written in the form

$$j(T) = A \exp \left[-x + B' \int_{x_0}^x \exp(-x) x^{-2} dx \right] \quad \dots(5)$$

where $x = E/kT$ and $B' = BE/k$. The above equation can be written as

$$j(T) = A \exp [-x - B \exp(-x) \cdot x^{-2}]_{x_0}^x \quad \dots(6)$$

if we ignore all but the first term in the series, obtained from the expression of the integral in Eq. (5), by integrating by parts.

Again if x_0 is greater than all values of x within the TSD span, the bottom limit of Eq. (6) can be ignored and therefore, dropping it, Eq. (1) takes the form

$$j(T) = A \exp[-x - B' \exp(-x) \cdot x^{-2}] \quad \dots(7)$$

Using the Cowell and Woods curve fitting technique¹¹ with an initial low guess of E , then increasing it in small steps, it is possible to determine E and τ_0 . An advantage of this technique is that the value of constant A in Eqs. (2) and (3) is also obtained from it.

An attempt can be made to calculate depth of penetration of charge δ following the method described earlier.³ The values of n_{i0} and $\mu\tau$ can be obtained from the expressions:¹²

$$n_{i0} = \frac{Q}{e \delta S} \cdot \frac{2d}{\delta} \quad \dots(8)$$

$$\mu_{i0} = \epsilon \cdot \frac{\delta}{d} \cdot \frac{\delta S}{Q} \quad \dots(9)$$

where Q is the charge released from a trap and S is the surface area of the sample. Attempt-to-escape frequency ν_D and capture cross-section σ_D , the important parameters of a dielectric which are likely to affect its properties, can be estimated from the formula^{13,14}

$$\nu_D = \frac{3 T' \beta}{2 (T_m - T') T_m} \exp\left(\frac{E}{k T_m}\right) \text{ sec}^{-1} \quad \dots(10)$$

$$\sigma_D = \frac{\nu_D}{2.1 \times 10^{24} T_m^2} \text{ m}^2 \quad \dots(11)$$

where T' is the half-width temperature on the lower temperature side of the TSDC curve and T_m is the temperature corresponding to current maximum.

3. Experimental Details

The method of preparation of electret was the same used earlier by the authors,³ with the difference that as in the previous study electric field is used in place of magnetic field. The discs of silicone rubber used were 11 mm in diameter and 2.0 mm in thickness. Samples were prepared by putting the disc in between two well polished copper electrodes (Fig. 1). The electrodes have a diameter of 12 mm and cover the whole area of the sample. The distance between the electrodes can be varied by a spring loaded slot on the upper electrode, which also keeps the electrodes pressed in contact with the samples during its

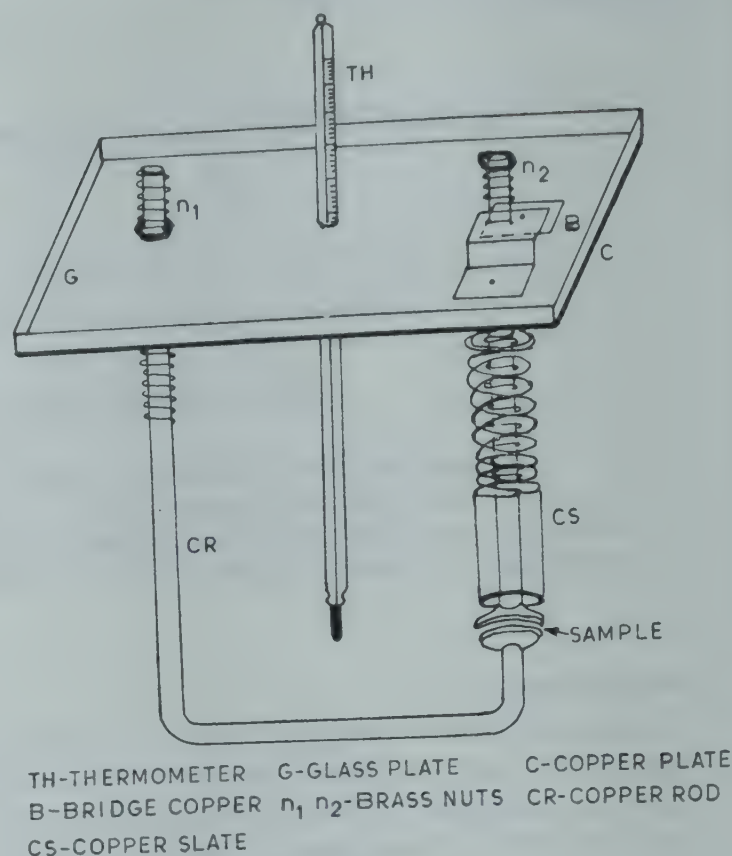


Fig. 1—Copper sample holder for TSDC analysis

heating. Time taken to reach the final constant temperature (polarizing temperature) was 45 min. The electric field was maintained for 2 hr, including 1 hr at the elevated constant temperature, and 1 hr during cooling. Samples were prepared at T_p 140°C and at different electric fields viz. 6.6, 10.0, 13.4 and 16.7 kV/cm. After polarization, the sample assembly was placed in a high temperature chamber. The temperature of this can be regulated with a variac so that a linear heating rate of $\sim 1^\circ\text{C}/\text{min}$ was obtained. A Keithley electrometer (610 C) was used to measure the discharge current. Peak cleaning and partial heating seemed to be unnecessary as peaks observed in Fig. 2 were already well separated. All calculations were performed with the aid of a mini-computer MOSCAL 1080.

4. Results and Discussion

Fig. 2 shows curves for thermo-induced currents from electrically charged silicone rubber. Most of the curves show discharge currents in both directions to the temperature axis, except the curves (a) and (e). Two current peaks are discernible in each of the curves (a), (b), (c) and (d) which correspond to samples polarized with electric field of 6.6, 10.0, 13.4 and 16.7 kV/cm, respectively. The two peak temperatures are 62°C and 132°C and are designated as α' and ρ' peaks. For the samples prepared at 140°C; 6.6 kV/cm [curve (a)] and 140°C, 10.0 kV/cm

Table 1—Summary of Electret Properties from TSDC Analysis of Electrically Charged Silicone Rubber

E_p kV/cm	TSDC 10^{-10} A	E eV	A cm	τ_0 sec	τ_{300} sec	N dipoles cm^{-3}	ν_D sec^{-1}	σ_D m^2	δ cm	n_{t0} cm^{-3} 10^{20}	$\mu \tau$ $\text{cm}^2 \text{V}^{-1}$ 10^{-18}
α' peak; $T_m = 336 \text{ K}$; $T_p = 413$											
6.6	1.5	1.20	3.71×10^8	6.4×10^{-13}	9.6×10^7	4.06×10^{27}	1.52×10^{13}	4.5×10^{-18}	—	—	—
10.0	1.0	1.17	1.01×10^8	1.5×10^{-12}	7.1×10^7	1.72×10^{27}	6.30×10^{11}	1.8×10^{-18}	—	—	—
13.4	0.3	1.30	1.77×10^9	3.3×10^{-14}	2.4×10^8	4.99×10^{26}	3.00×10^{13}	8.8×10^{-17}	—	—	—
16.7	0.8	1.11	7.59×10^6	9.3×10^{-12}	4.3×10^7	6.83×10^{26}	1.00×10^{11}	3.1×10^{-19}	—	—	—
ρ' peak; $T_m = 405$; $T_p = 413$											
6.6	3.9	2.20	4.71×10^{18}	3.0×10^{-31}	3.1×10^6	—	3.00×10^{30}	—	5.65	0.88	0.25
10.0	3.3	2.00	4.72×10^{15}	2.5×10^{-28}	1.1×10^6	—	3.9×10^{27}	—	6.19	1.32	7.79
13.4	2.7	2.10	2.98×10^{17}	7.1×10^{-30}	1.4×10^6	—	1.3×10^{27}	—	6.27	1.98	4.01
16.7	1.8	1.90	2.47×10^{14}	8.5×10^{-27}	0.8×10^6	—	1.1×10^{26}	—	6.54	2.11	3.85

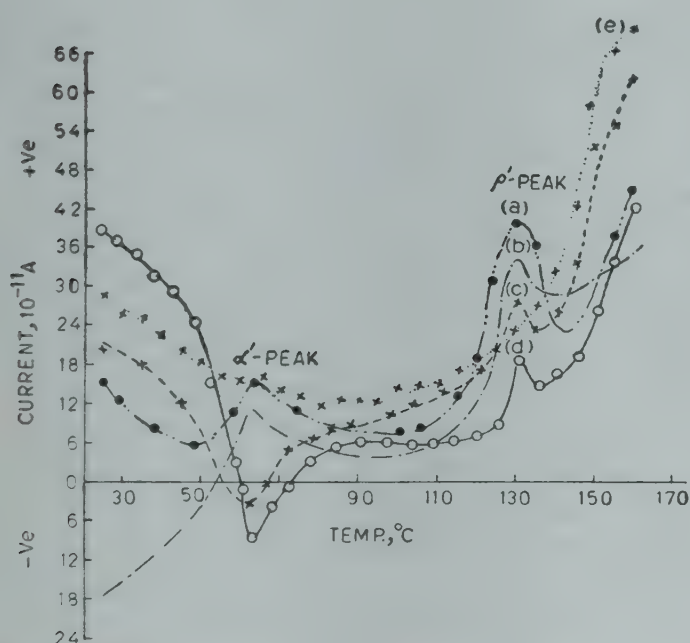


Fig. 2—TSDC spectrum of electrically charged silicone rubber [Poling Conditions: (a) 140°C, 6.6 kV/cm; (b) 140°C, 10.0 kV/cm; (c) 140°C, 13.4 kV/cm; (d) 140°C, 16.7 kV/cm; and (e) 140°C, 0.0 kV/cm.]

[curve (b)] both the peaks are positive in nature. As we increase the value of polarizing field further, [curve (c) and (d)], α' peak becomes negative while ρ' peak still remains positive. There is no regular variation of the height of α' peak with the polarizing field while ρ' peak diminishes as E_p increases. After the formation of ρ' peak, discharge current goes on increasing as we further increase the temperature. Curve (e) shows TSDC of blank sample which does not show any current peak at this T_p .

The kinetics calculations carried out on the TSDC peaks obtained from electrically charged silicone rubber disc are summarized in Table 1. In general,

the activation energy E , associated with the discharge processes, lies between 1 and 2 eV and is of the same order as is associated with molecular motion.

The ρ' peak yields mobility-free lifetime products of the order of $10^{-18} \text{ cm}^2/\text{V}$. The attempt-to-escape frequency (ν_D) for α' peak is 10^{13} sec^{-1} while it is comparatively large (10^{27} sec^{-1}) for the ρ' peak, thus showing that the second peak is more stable and hence discharging at higher temperature (405 K). The values of n_{t0} and δ show an increase as we increase the polarizing field, thereby indicating that at higher fields more strong and stable electrets can be made from silicone rubber (medical grade). The values of dipolar concentration do not show any systematic variation with the polarizing field showing that the field does not have pronounced effects on these electrets at lower forming temperatures.

Acknowledgement

The authors wish to thank Dr B L Mehrotra, Principal, M A College of Technology, for permitting to do the work and Dr Roy C Gunter of USA for supplying the silicone rubber sheet (medical grade). The study was supported in part by financial assistance from the National Science Foundation, USA.

References

1. Srivastava Rudra Kant, Ph D thesis, Bhopal University, Bhopal 1979, II-5.
2. Srivastava Rudra Kant, Qureshi M S & Bhatnagar C S, *Japan J. appl. Phys.*, 17 (1978), 1537.
3. Srivastava Rudra Kant, Khare M L, Qureshi M S & Bhatnagar C S, *Indian J. pure appl. Phys.*, 18 (1980), 20.
4. Srivastava Rudra Kant & Bhatnagar C S, *Indian J. pure appl. Phys.*, 15 (1977), 875.

5. Srivastava Rudra Kant, Khare M L, Qureshi M S, Khare M L & Bhatnagar C S, *Indian J. pure appl. Phys.*, 18 (1980), In press, Sep-2657.
6. Qureshi M S & Bhatnagar C S, Paper presented at the *International Conference of Electrical Polymers*, Institute of Chemical & Physical Research, Tokyo, Japan, Oct. 1978.
7. Creswell R A & Perlman M M, *J. appl. Phys.*, 41 (1970), 2365.
8. Perlman M M & Creswell R A, *J. appl. Phys.*, 42 (1971), 531.
9. Perlman M M & Creswell R A, Paper presented at the *International Conference on Electrical Insulation and Dielectric Phenomena*, NAS & NRC, Pennsylvania, Oct. 1970.
10. Garlick G F J & Gibson A F, *Proc. phys. Soc.*, 60 (1948), 574.
11. Cowell T A T & Woods J, *Br. J. appl. Phys.*, 18 (1967), 1045.
12. Creswell R A, Perlman M M & Kabayama M A, *Dielectric properties of polymers*, edited by Karasz (Plenum, New York), 1972, 295.
13. Grossweiner L I, *J. appl. Phys.*, 24 (1953), 1306.
14. Kendall E J M, Haslett J W & Scholdz F Z, In *Electrets charge storage and transport in dielectrics*, edited by M M Perlman (Electrochemical Society, New York), 1973, 96.

Electronic Polarizabilities & Radii of Ions in Rutile-type Crystals

JAI SHANKER, S C AGRAWAL* & V K JAIN*

Department of Physics, Agra College, Agra 282 002

Received 30 November 1979

The electronic polarizabilities and radii of ions in crystals with rutile structure have been calculated using the model developed by Jai Shanker and M P Verma [*J. Phys. Chem. Solids*, **37** (1976), 883]. The results obtained agree well with those obtained by earlier investigators.

1. Introduction

Electronic polarizabilities and radii of ions are important parameters for understanding the nature of chemical bond, crystalline interactions, crystal structure and many other physical and chemical properties of ionic crystals.^{1,2} The present knowledge of these parameters in respect of crystals having rutile structure is not very satisfactory. In the case of highly ionic crystals like alkali halides, the additivity rule works well.^{3,4} However, in the case of triatomic crystals with rutile structure, the additivity rule does not hold so well because of their partial covalent character;⁵ thus we cannot use this rule for determining the crystalline electronic polarizabilities and radii of ions in these crystals. It is, therefore, desirable to have an alternative approach for calculating these parameters in rutile-type solids. In the present paper, we have calculated the crystalline polarizabilities and radii of ions in fourteen oxides and fluorides crystallizing in rutile structure,⁶ adopting the model developed by Shanker and Verma.⁷

2. Method of Analysis

The electronic polarizability and radius of a positive ion increase and those of a negative ion decrease in going from the free state to a crystal.^{8,9} The radii¹⁰ and polarizabilities¹¹ derived by Pauling correspond to free state for the reasons discussed at length by Fumi and Tosi.¹² The free state implies that ions do not overlap and, in fact, it was shown by Maslen¹³ that the criterion of minimum overlap for two ions separated by a distance equal to that as observed in the crystal leads to ionic radii which are very nearly the same as those of Pauling.¹⁰ Recently Deb and Ghosh¹⁴ demonstrated, by an analysis of the electronic charge distributions corres-

ponding to free ion wavefunctions, that Pauling's radii are nearly equal to those in free state. The polarizability (α) and radius (r) of a given ion are related by the following expressions^{7,15}

$$\alpha_c = k r_c^n \quad \dots(1)$$

and

$$\alpha_f = k r_f^n \quad \dots(2)$$

where subscripts c and f represent the crystalline and free state values respectively. It has been assumed that k and n remain constant for a given ion in going from free state to a crystal. Eqs. (1) and (2) lead to the following relations between crystalline state and free state data for cations (+) and anions (—)

$$\alpha_{c+}/\alpha_{f+} = (r_{c+}/r_{f+})^{n_1} \quad \dots(3)$$

and

$$\alpha_{c-}/\alpha_{f-} = (r_{c-}/r_{f-})^{n_2} \quad \dots(4)$$

Eqs. (3) and (4) lead to

$$\frac{n_2}{n_1} \frac{\log(\alpha_{c+}/\alpha_{f+})}{\log(\alpha_{c-}/\alpha_{f-})} = \frac{\log(r_{c+}/r_{f+})}{\log(r_{c-}/r_{f-})} \quad \dots(5)$$

Eq. (5) can also be expressed as

$$r_{c+}/r_{f+} = (r_{c-}/r_{f-})^\beta \quad \dots(6)$$

where

$$\beta = \frac{n_2}{n_1} \frac{\log(\alpha_{c+}/\alpha_{f+})}{\log(\alpha_{c-}/\alpha_{f-})} \quad \dots(7)$$

It is evident from the studies on ionic radii by Fumi and Tosi¹² and by Maslen¹³ that the free ion radii and crystal radii are related such that

$$r_{f+} + r_{f-} = r_{c+} + r_{c-} = R \quad \dots(8)$$

where R is the observed interionic separation in the crystals. From the accepted property of ionic radii we can write⁹

$$\delta r = r_{c+} - r_{f+} = r_{f-} - r_{c-} \quad \dots(9)$$

Using Eq. (9), Eq. (6) can be written as

$$\left(1 + \frac{\delta r}{r_{f+}}\right) = \left(1 - \frac{\delta r}{r_{f-}}\right)^\beta$$

*Present address: Department of Physics, C L Jain College, Firozabad (UP)

$$= 1 - \beta \left(\frac{\delta r}{r_{f-}} \right) + \frac{\beta(\beta-1)}{2} \left(\frac{\delta r}{r_{f-}} \right)^2 \dots(10)$$

It is evident from studies on ionic radii¹² that $\delta r \sim 0.2 \text{ \AA}$ and $r_{f-} \sim 2 \text{ \AA}$ which lead to $\left(\frac{\delta r}{r_{f-}} \right)^2 \simeq 10^{-2}$.

Hence retaining only the first order term in $(\delta r/r_{f-})$ we get

$$\beta \simeq - \left(\frac{r_{f-}}{r_{f+}} \right) \dots(11)$$

Values of β obtained from Eq. (11) are used to calculate the crystalline state radii r_{c+} and r_{c-} from Eqs. (6) and (8) in 14 crystals with rutile structure. Input data on r_{f+} , r_{f-} and R used in calculations along with the values of β based on Eq. (11) are given in Table 1. Values of r_{c+} and r_{c-} , calculated from Eqs. (6) and (8), are reported in Table 2.

The previous methods^{3,4} of calculating the electronic polarizabilities of ions are not applicable to the crystals under study for two reasons. First, the data on dielectric constant or refractive index for these crystals are not available. Second, the additivity rule is not supposed to work so well for rutile type crystals as for alkali halides. We have, therefore, used the polarizability-radius cube relation

$$\frac{\alpha_c}{\alpha_f} = \left(\frac{r_c}{r_f} \right)^3 \dots(12)$$

which has been found to be a good approximation for the rutile (TiO_2) crystal.¹⁶ Values of α_f have

been taken from literature^{11,17-19} and are given in Table 3. Values of α_{c+} and α_{c-} calculated from Eq. (12) are also reported in Table 3.

3. Results and Discussion

The crystal radii r_{c+} and r_{c-} calculated in the present study are compared with those obtained by Shannon and Prewitt,²⁰ using the techniques similar to those used by Goldschmidt²¹ (Table 2). In fact, the radii reported by Shannon and Prewitt are quite

Table 2—Values of Crystalline State Radii of Ions

Crystal	$r_{c+}, \text{\AA}$		$r_{c-}, \text{\AA}$	
	Present study	Ref. 20	Present study	Ref. 20
SiO_2	0.448	0.40	1.309	1.24
TiO_2	0.661	0.67	1.284	1.24
GeO_2	0.582	0.54	1.290	1.24
SnO_2	0.773	—	1.279	—
CrO_2	0.591	0.58	1.289	1.24
RuO_2	0.665	—	1.277	—
OsO_2	0.681	—	1.281	—
PbO_2	0.892	0.92	1.268	1.24
MgF_2	0.740	—	1.219	—
MnF_2	0.875	—	1.229	—
FeF_2	0.762	0.77	1.236	1.17
CoF_2	0.793	0.79	1.234	1.17
NiF_2	0.744	—	1.237	—
ZnF_2	0.777	0.74	1.235	1.17

Table 1—Values of Input Data

Crystal	$r_{f+}, \text{\AA}$ (Ref. 10)	$r_{f-}, \text{\AA}$ (Ref. 10)	β	$R, \text{\AA}$ (Ref. 23)
SiO_2	0.357	1.40	-3.922	1.757
TiO_2	0.545	1.40	-2.569	1.945
GeO_2	0.472	1.40	-2.966	1.872
SnO_2	0.652	1.40	-2.147	2.052
CrO_2	0.480	1.40	-2.917	1.880
RuO_2	0.542	1.40	-2.583	1.942
OsO_2	0.562	1.40	-2.491	1.962
PbO_2	0.760	1.40	-1.842	2.160
MgF_2	0.619	1.36	-2.197	1.979
MnF_2	0.744	1.36	-1.828	2.104
FeF_2	0.638	1.36	-2.132	1.998
CoF_2	0.667	1.36	-2.039	2.027
NiF_2	0.621	1.36	-2.190	1.981
ZnF_2	0.652	1.36	-2.086	2.012

Table 3—Electronic Polarizabilities of Ions (in \AA^3)

Crystal	α_{f+}	α_{f-}	α_{c+}	α_{c-}
SiO_2	0.03 ¹¹	2.75 ¹⁷	0.06	2.25
TiO_2	0.19 ¹¹	2.75 ¹⁷	0.34	2.12
GeO_2	0.14 ¹¹	2.75 ¹⁷	0.26	2.15
SnO_2	0.50 ¹¹	2.75 ¹⁷	0.83	2.10
CrO_2	0.15 ¹⁹	2.75 ¹⁷	0.28	2.15
RuO_2	0.38 ¹⁹	2.75 ¹⁷	0.70	2.09
OsO_2	0.76 ¹⁹	2.75 ¹⁷	1.35	2.11
PbO_2	0.61 ¹¹	2.75 ¹⁷	0.99	2.04
MgF_2	0.09 ¹¹	1.20 ¹⁸	0.15	0.86
MnF_2	0.23 ¹⁹	1.20 ¹⁸	0.37	0.89
FeF_2	0.24 ¹⁹	1.20 ¹⁸	0.41	0.90
CoF_2	0.25 ¹⁹	1.20 ¹⁸	0.42	0.90
NiF_2	0.26 ¹⁹	1.20 ¹⁸	0.45	0.90
ZnF_2	0.28 ¹¹	1.20 ¹⁸	0.47	0.90

Note—In columns 2 and 3, superscripts refer to the respective literature reference.

accurate and reliable because they have been derived from: (1) 1000 experimental interatomic distances, and (2) an approximately linear relationship between ionic volume and unit cell volume of over 60 isotypic series of oxides and fluorides; these radii take into account the electronic spin state and the coordination of both cations and anions and have been found to reproduce closely the experimental inter-ionic distances in the crystals of oxides and fluorides. The fact that r_{c+} and r_{c-} calculated in the present study agree closely with those of Shannon and Prewitt²⁰ demonstrates the validity of the approach adopted by us.

It should be mentioned that the electronic polarizabilities α_{c+} and α_{c-} calculated in the present study differ considerably from those based on the additivity rule.³ The failure of the additivity rule is evident from the fact that Tessman *et al.*³ obtained the negative values for the polarizabilities of Mg^{2+} , Fe^{2+} and Si^{4+} ions which have no physical significance. On the other hand, we obtained positive and reasonable values for the electronic polarizabilities of ions in rutile-type compounds. Our polarizabilities for oxygen and fluorine ions agree well with those reported by previous workers.^{4,15}

The results obtained in the present study are expected to be useful in studying the cohesive elastic and dielectric properties of rutile-type crystals.²²

References

1. Born M & Huang K, *Dynamical theory of crystal lattices*, (Oxford University Press, London), 1954.
2. Mott N F & Gurney R W, *Electronic processes in ionic crystals* (Oxford University Press, London and New York), 1948.
3. Tessman J R, Kahn A H & Shockley W, *Phys. Rev.*, **92** (1953), 890.
4. Pirenne J & Kartheuser E, *Physica*, **30** (1964), 2005.
5. Wackman P H, Hirthe W M & Frounfolker R E, *J. Phys. Chem. Solids*, **28** (1967), 1525.
6. Baur W H & Kahn A H, *Acta crystallogr.*, **27** (1971), 2133.
7. Shankar J & Verma M P, *J. Phys. Chem. Solids*, **37** (1976), 883.
8. Ruffa A R, *Phys. Rev.*, **130** (1963), 1412; **133** (1964), 1418.
9. Tosi M P, *Solid St. Phys.*, **16** (1964), 1.
10. Pauling L, *The nature of the chemical bond* (Cornell University Press, Ithaca), 1960.
11. Pauling L, *Proc. R. Soc.*, **A114** (1927), 181.
12. Fumi F G & Tosi M P, *J. Phys. Chem. Solids*, **25** (1964), 31, 45.
13. Maslen V W, *Proc. phys. Soc. Lond.*, **91** (1967), 259.
14. Deb S C & Ghosh A K, *Indian J. Phys.*, **49** (1975), 528.
15. Sharma O P, Bhardwaj M & Shanker J, *J. inorg. nucl. Chem.*, **39** (1977), 763.
16. Shanker J & Verma M P, *Phys. Rev.*, **B12** (1975), 3449.
17. Fajans K & Joos G, *Z. Phys.*, **23** (1924), 23.
18. Donath W E, *IBM Res. Rep.*, RW-27, 1961.
19. Shanker J, Jain V K & Agrawal S C, *J. chem. Phys.*, **72** (1980), 4458.
20. Shannon R D & Prewitt C T, *Acta Crystallogr.*, **B25** (1969), 525.
21. Goldschmidt V M, *Skr. Norske Vid Akad. Oslo, Math-Nat. Kl*, No. 2, (1926).
22. Striefler M E & Barsch G R, *Phys. Status Solidi (b)*, **59** (1973), 205; **64** (1974), 613; **67** (1975), 143.
23. Ladd M F C, *J. chem. Phys.*, **60** (1974), 1954.

On the Isotopic Invariants of Polyatomic Molecules

R JAGANNATHAN, V A CHINNAPPAN & G A SAVARI RAJ

Department of Physics, St Joseph's College (Autonomous), Tiruchirapalli 620 002

Received 16 July 1979

The methods of construction of certain isotopic invariants developed earlier for a few XY_n -type molecules [V A Chinnappan, R Jagannathan & G A Savari Raj, *Indian J. pure appl. Phys.*, 16 (1978), 668.] are put in a general framework so as to be applicable to any X_mY_n -type molecule having the G -matrix in a mass-independent internal symmetry coordinate system with only one-dimensional and two-dimensional blocks. Applications of the theory to the cases of symmetrical linear X_2Y_2 -type molecule and symmetrical XY_n -type molecules are discussed generally and briefly. These isotopic invariants are ready-made expressions in terms of experimental quantities, useful mainly for relatively easy estimation of the various vibrational-rotational constants of several isotopically related molecules of known geometry and the same symmetry, directly from the corresponding constants of one or two of these isotopically related molecules.

1. Introduction

Extending the work of Parker,¹ we constructed recently^{2,3} for bent symmetrical XY_2 and planar symmetrical XY_3 molecules certain expressions which contain only observable quantities like frequencies, Coriolis constants and centrifugal distortion constants, and which remain unchanged in numerical values under any symmetrical isotopic substitution. The study of these isotopic invariants of polyatomic molecules of known geometry can be used: (i) to verify the assumption that molecular geometry and force-field are invariant under any symmetry preserving isotopic substitution; (ii) to choose the most reliable set of data, when several sets of data on the required molecular constants are available, based on the assumption of validity of invariance of molecular geometry and force-field under symmetrical isotopic substitutions; and (iii) to estimate in a relatively easy manner the various vibrational-rotational constants of isotopically related molecules of the same symmetry directly from the corresponding constants of one or two of these isotopically related molecules, assuming the invariance of geometry and force-field for them. The parameters of common geometry of the isotopically related molecules of the same known symmetry may also be estimated in some cases utilizing these invariants.

In this paper, we have developed a general method for the construction of isotopic invariants for any X_mY_n -type molecule, provided its G -matrix in a symmetry-adapted mass-independent internal coordinate system has only one-dimensional and two-dimensional blocks. The theory has been applied to

symmetrical linear X_2Y_2 -type molecule and symmetrical XY_n -type molecules. Detailed investigations including numerical calculations will be reported later for specific molecules of each of these types.

2. General Theory of Isotopic Invariants

Firstly the meanings and applications of the desired isotopic invariants will be studied thoroughly using a general approach than has been done earlier.² Let the basic eigenvalue equation for the harmonic frequencies be written as

$$GFL = L\Lambda \quad \dots(1)$$

using the well known FG -matrix formalism of Wilson,⁴ where the diagonal matrix Λ contains the frequency parameters $\{\lambda = 4\pi^2 c^2 \omega^2\}$ and the symmetric matrices G and F are related to the kinetic and potential energies of the molecule as

$$T = 1/2 \dot{S}^\dagger G^{-1} \dot{S} \quad \dots(2)$$

$$V = 1/2 S^\dagger FS \quad \dots(3)$$

with S denoting the column vector of mass-independent internal symmetry coordinates. Throughout this paper, all the symbols used will have the usual meanings as given by Cyvin⁵ unless otherwise specified. Let us now take

$$G = TT^\dagger \quad \dots(4)$$

and rewrite Eq. (1) as

$$T^\dagger FTT^{-1}L = T^{-1}L\Lambda \quad \dots(5)$$

Let

$$T^{-1} = \Gamma \quad \dots(6)$$

$$T^\dagger FT = H \quad \dots(7)$$

It follows that since H is symmetric, Γ must be an orthogonal matrix, so that

$$H = \Gamma \Lambda \Gamma^{-1} = \Gamma \Lambda \Gamma^\dagger \quad \dots(8)$$

Then the force-constant matrix F is given by

$$F = T^{-1\dagger} H T^{-1} = T^{-1\dagger} \Gamma \Lambda \Gamma^\dagger T^{-1} \quad \dots(9)$$

in the mass-independent symmetry-adapted internal coordinate system specified by S .

Let the matrix T of Eq. (4) be given by

$$T = g d \quad \dots(10)$$

where the matrix g is mass-independent with the same block structure as G and d is a diagonal matrix, i.e. we require blockwise

$$G = g d^2 g^\dagger$$

$$\frac{dg_{kl}}{dm_i} = 0, i = 1, 2, \dots, N$$

$$d_{kl} = \delta_{kl} d_{kk} \quad \dots(11)$$

where m_i denotes the mass of the i -th atom of the N -atomic molecule and (k, l) are the matrix indices. Substitution of Eq. (10) in Eq. (9) gives

$$F = g^{-1\dagger} d^{-1} \Gamma \Lambda \Gamma^\dagger d^{-1} g^{-1} \quad \dots(12)$$

If we now define a new mass-independent internal symmetry coordinate system by

$$S' = g^{-1} S \quad \dots(13)$$

then the force-constant matrix F' in S' -system is given by

$$S'^\dagger F' S' = S^\dagger F S \quad \dots(14)$$

or

$$F' = d^{-1} \Gamma \Lambda \Gamma^\dagger d^{-1} \quad \dots(15)$$

Invariance of the molecular geometry and force-field under symmetry-preserving isotopic substitutions implies the invariance of the elements of F and F' since they are given in mass-independent internal coordinate systems. In the S' -coordinate system the G -matrix becomes diagonal as

$$G' = g^{-1} G g^{-1\dagger} = d^2 \quad \dots(16)$$

Hence from Eqs. (12), (15) and (16), we expect the elements of the isotopically invariant force-constant matrix F' in the S' -coordinate system to have simpler forms than the corresponding elements of the matrix F in the initial S -coordinate system when these are expressed in terms of purely observable quantities like frequencies, Coriolis constants and centrifugal distortion constants. Only this simple and general theory is behind the study of isotopic invariants; actually the elements of F' were first obtained by Parker¹ for the special case of bent symmetrical XY_2 molecules and later by us^{2,3} for the cases of a few symmetrical XY_n -type molecules using a somewhat different approach.

Let us now consider the case of a molecule for which the G -matrix in a suitable mass-independent internal symmetry coordinate system contains only 1×1 and 2×2 blocks. The elements of F' can then be expressed purely in terms of experimental quantities. We shall denote the k th 1×1 element of G by G_k and the j th symmetric 2×2 block of G by

$$G(j) = \begin{bmatrix} G(j)_{11} & G(j)_{12} \\ G(j)_{21} & G(j)_{22} \end{bmatrix} \quad \dots(17)$$

The corresponding 1×1 and 2×2 blocks of g , d , Λ , Γ and symmetric F' can then be taken as

$$g_k = 1, d_k = G_k^{1/2}$$

$$\Gamma_k = 1, \Lambda_k = \lambda_k$$

$$F'_k = \lambda_k / G_k \quad \dots(18)$$

$$g(j) = \begin{bmatrix} g(j)_{11} & g(j)_{12} \\ g(j)_{21} & g(j)_{22} \end{bmatrix}$$

$$d(j) = \begin{bmatrix} d(j)_1 & 0 \\ 0 & d(j)_2 \end{bmatrix}$$

$$\Gamma(j) = \begin{bmatrix} \cos \theta(j) & -\sin \theta(j) \\ \sin \theta(j) & \cos \theta(j) \end{bmatrix}$$

$$\Lambda(j) = \begin{bmatrix} \lambda(j)_1 & 0 \\ 0 & \lambda(j)_2 \end{bmatrix}$$

$$F'(j) = \begin{bmatrix} F'(j)_{11} & F'(j)_{12} \\ F'(j)_{12} & F'(j)_{22} \end{bmatrix} \quad \dots(19)$$

Now denoting the desired invariant matrix F' by I for the sake of notational continuity with our earlier papers^{2,3} we find that the elements of I are given by

$$I_k = \lambda_k / G_k \quad \dots(20)$$

$$I(j)_{11} = d(j)_1^{-2} \{ \lambda(j)_1 \cos^2 \theta(j) + \lambda(j)_2 \sin^2 \theta(j) \} \quad \dots(21)$$

$$I(j)_{12} = [2d(j)_1 d(j)_2]^{-1} \{ [\lambda(j)_1 - \lambda(j)_2] \sin 2\theta(j) \} \quad \dots(22)$$

$$I(j)_{22} = d(j)_2^{-2} \{ \lambda(j)_1 \sin^2 \theta(j) + \lambda(j)_2 \cos^2 \theta(j) \} \quad \dots(23)$$

Using the relation

$$L = T \Gamma = g d \Gamma \quad \dots(24)$$

obtained from Eqs. (6) and (10), and the expressions⁵

$$\zeta^\alpha = L^{-1} C^\alpha L^{-1\dagger}, \quad \alpha = x, y, z \quad \dots(25)$$

the parameters $\{\theta(j)\}$ in Eqs. (21)-(23) can be expressed in terms of various observable Coriolis constants, which are the elements of the ζ^α -matrices. Similarly the parameters $\{\theta(j)\}$ can also be related to the centrifugal distortion constants using their relation with the L -matrix (Ref. 6). Thus the elements of $\{I(j)\}$ given by Eqs. (21)-(23) and the desired isotopic invariants are obtained in terms of the various observable quantities, viz. frequencies, Coriolis constants, centrifugal distortion constants, etc.

The practical applications of the isotopic invariants, mentioned in section 1, are to be accomplished as follows:

(i) When reliably accurate experimental data on the values of the quantities involved in the elements of I are available for several isotopically related molecules of known geometry and of the same symmetry, the extent of invariance of the molecular geometry and force-field under symmetrical isotopic substitutions can be estimated from the extent of variations in I (cf. Table 1 of Ref. 2).

(ii) If we assume the validity of the invariance of the molecular geometry and force field under symmetrical isotopic substitution then among the several different sets of experimental data on the quantities involved in I the most reliable set of data should be the one which fits the invariance of I in the best manner (cf. Table 2 of Ref. 2).

(iii) (a) We observe from Eqs. (20)-(23) that

$$\lambda_k = I_k G_k \quad \dots(26)$$

$$\lambda(j)_1 = 1/2 \left\{ [I(j)_{11} d(j)_1^2 + I(j)_{22} d(j)_2^2] - [I(j)_{11} d(j)_1^2 - I(j)_{22} d(j)_2^2]^2 + 4 I(j)_{12}^2 d(j)_1^2 d(j)_2^2]^{1/2} \right\} \quad \dots(27)$$

$$\lambda(j)_2 = 1/2 \left\{ [I(j)_{11} d(j)_1^2 + I(j)_{22} d(j)_2^2] - [I(j)_{11} d(j)_1^2 - I(j)_{22} d(j)_2^2]^2 + 4 I(j)_{12}^2 d(j)_1^2 d(j)_2^2]^{1/2} \right\} \quad \dots(28)$$

$$\theta(j) = 1/2 \tan^{-1} \left\{ \frac{2I(j)_{12} d(j)_1 d(j)_2}{I(j)_{11} d(j)_1^2 - I(j)_{22} d(j)_2^2} \right\} \quad \dots(29)$$

Hence due to the isotopic invariance of I we have for the symmetrically substituted isotopic variant of the given molecule,

$$\lambda(j)_{1s} = \frac{1}{2} \left\{ [I(j)_{11} d(j)_{1s}^2 + I(j)_{22} d(j)_{2s}^2] - [I(j)_{11} d(j)_{1s}^2 - I(j)_{22} d(j)_{2s}^2]^2 + 4 I(j)_{12}^2 d(j)_{1s}^2 d(j)_{2s}^2]^{1/2} \right\} \quad \dots(30)$$

$$\lambda(j)_{2s} = \frac{1}{2} \left\{ [I(j)_{11} d(j)_{1s}^2 + I(j)_{22} d(j)_{2s}^2] - [I(j)_{11} d(j)_{1s}^2 - I(j)_{22} d(j)_{2s}^2]^2 + 4 I(j)_{12}^2 d(j)_{1s}^2 d(j)_{2s}^2]^{1/2} \right\} \quad \dots(31)$$

$$\theta(j)_s = \frac{1}{2} \tan^{-1} \left\{ \frac{2I(j)_{12} d(j)_{1s} d(j)_{2s}}{I(j)_{11} d(j)_{1s}^2 - I(j)_{22} d(j)_{2s}^2} \right\} \quad \dots(32)$$

along with the well known relation

$$\lambda_{ks} = I_k G_{ks} = \lambda_k G_{ks}/G_k \quad \dots(33)$$

The additional subscript s is used to indicate quantities of the molecule obtained by symmetric isotopic substitution. Thus while calculating the invariant matrix I from the knowledge of the observables involved for a given molecule, the frequencies and other vibrational-rotational constants of a symmetrical isotopic variant of it can be estimated using Eqs. (30)-(33).

(iii) (b) If the frequencies of two isotopically related molecules of the same symmetry are known, their various vibrational-rotational constants and other isotopic variants can be estimated from the relation,

$$\theta(j) = \frac{1}{2} \cos^{-1}$$

$$\left[\frac{\{\lambda(j)_1 + \lambda(j)_2\} \{d(j)_1^2 d(j)_{2s}^2 + d(j)_2^2 d(j)_{1s}^2\} - 2\{\lambda(j)_{1s} + \lambda(j)_{2s}\} d(j)_1^2 d(j)_2^2}{\{\lambda(j)_1 - \lambda(j)_2\} \{d(j)_1^2 d(j)_{2s}^2 - d(j)_2^2 d(j)_{1s}^2\}} \right] \quad \dots(34)$$

This relation is obtained by solving the equation,

$$I(j) = I(j)_s \quad \dots(35)$$

expressing the invariance of I under symmetric isotopic substitutions (cf. Table 3 of Ref. 2).

Since $\tan(\theta + \pi) = \tan \theta$ and $\cos(-\theta) = \cos(\theta)$, Eqs. (32) and (34) will lead to two values of $\theta(j)$ and hence to two sets of values for the quantities calculated using them. The choice of correct set of data will depend on further physical arguments.

Sometimes the equation, $I = I_s$, may lead to very simple and direct proportionality relations among certain observables of isotopic variants of the molecule. For example, it can be noted that for bent symmetrical XY_2 molecules the isotopic invariants given under section 4 lead to simple proportionality relations between the centrifugal distortion constants of symmetrical isotopic substituents. Infact, it has been the main aim of Parker¹ to obtain such simple and direct relations among the observables of isotopic substituents of a molecule.

(iii) (c) The study of these isotopic invariants may also be useful to obtain data on the common geometry parameters of the isotopically related molecules of known identical symmetry from the values of the

vibrational-rotational constants and mass parameters. Here we shall not consider this case in detail since each model of molecule has to be treated separately. As an example let us consider the case of bent symmetrical XY_2 molecules. Solving Eqs. (27), (28) and (30) of Ref. 2, we can see easily that

$$A = \tan^{-1} \left[\frac{m_X^{1/2} (\zeta_2 \cos \theta - \zeta_1 \sin \theta)}{M^{1/2} (\zeta_1 \cos \theta + \zeta_2 \sin \theta)} \right]$$

$$R = \left[\frac{M^{1/2} [\zeta_1 \zeta_2 \cos 2\theta + \frac{1}{2} (\zeta_2^2 - \zeta_1^2) \sin 2\theta]}{m_X^{1/2} m_Y \sin 2A} \right]^{1/2} \quad \dots(36)$$

with

$$M = m_X + 2m_Y$$

$$\theta = \frac{1}{2} \cos^{-1}$$

$$\left[\frac{(\lambda_1 + \lambda_2)[m_Y(M, m_X + Mm_{X_s}) - 2(\lambda_{1s} + \lambda_{2s})Mm_{X_s}m_Y]}{(\lambda_1 - \lambda_2)[m_Y(M, m_X - Mm_{X_s})]} \right] \quad \dots(37)$$

where $2A$ is the equilibrium YXY angle, R the equilibrium XY distance, m_X and m_Y are the masses of X and Y atoms respectively, λ_1 and λ_2 belong to the symmetry species A_1 and ζ_1 and ζ_2 are the two non-vanishing elements of ζ^Y -matrix belonging to A_1XB_1 type of coupling.

3. Factorization of G -matrix

In Refs. 2 and 3, the study of isotopic invariants of bent symmetrical XY_2 and planar symmetrical XY_3 molecules is based on intuitively derived factorizations of the G -matrices in valence-force coordinate systems as required by Eq. (11). In this section, we shall give a general method of obtaining the factorization according to Eq. (11) of symmetry-adapted G -matrices of X_mY_n -type molecules with only 1×1 and 2×2 blocks.

The factorization of any 1×1 block element of a G -matrix as required is given by Eq. (18). We shall now observe that we can write, in general, any 2×2 block of the G -matrix for a X_mY_n -type molecule in a mass-independent internal symmetry coordinate system as

$$\begin{bmatrix} G_{11} & G_{12} \\ G_{12} & G_{22} \end{bmatrix} = \begin{bmatrix} a_{11X}\mu_X + a_{11Y}\mu_Y & a_{12X}\mu_X + a_{12Y}\mu_Y \\ a_{12X}\mu_X + a_{12Y}\mu_Y & a_{22X}\mu_X + a_{22Y}\mu_Y \end{bmatrix} \quad \dots(38)$$

where the coefficients $\{a\}$ are independent of μ_X and μ_Y . We can then write Eq. (11) for the above 2×2 block of G explicitly as

$$\begin{bmatrix} G_{11} & G_{12} \\ G_{12} & G_{22} \end{bmatrix} = \begin{bmatrix} g_{11} & g_{12} \\ g_{12} & g_{22} \end{bmatrix} \begin{bmatrix} d_1^2 & 0 \\ 0 & d_1^2 \end{bmatrix} \begin{bmatrix} g_{11} & g_{12} \\ g_{12} & g_{22} \end{bmatrix} \quad \dots(39)$$

where we have taken g as symmetric and require

$$d_1^2 = C_{1X}\mu_X + C_{1Y}\mu_Y$$

$$d_2^2 = C_{2X}\mu_X + C_{2Y}\mu_Y \quad \dots(40)$$

From Eqs. (38)-(40) it follows that if we take all the coefficients $\{a\}$, $\{g\}$ and $\{C\}$ of G , g and d^2 respectively to be mass-independent, then we get

$$\begin{bmatrix} a_{11X} & a_{12X} & a_{22X} \\ a_{11Y} & a_{12Y} & a_{22Y} \\ 0 & 0 & 1 \end{bmatrix} = \begin{bmatrix} C_{1X} & C_{2X} & 0 \\ C_{1Y} & C_{2Y} & 0 \\ 0 & 0 & 1 \end{bmatrix} \begin{bmatrix} g_{11}^2 & g_{11}g_{12} & g_{12}^2 \\ g_{12}^2 & g_{12}g_{22} & g_{22}^2 \\ 0 & 0 & 1 \end{bmatrix} \quad \dots(41)$$

or symbolically

$$a = C_Y \quad \dots(42)$$

Assuming that

$$g_{11} = 1 \quad \dots(43)$$

and expressing the equation

$$C = a_Y^{-1} \quad \dots(44)$$

obtained from Eq. (42) explicitly in terms of matrix elements we have

$$C_{1X} = \epsilon^{-1} (g_{12} g_{22} a_{11X} - g_{12}^2 a_{12X})$$

$$C_{1Y} = \epsilon^{-1} (g_{12} g_{22} a_{11Y} - g_{12}^2 a_{12Y})$$

$$C_{2X} = \epsilon^{-1} (a_{12X} - g_{12} a_{11X})$$

$$C_{2Y} = \epsilon^{-2} (a_{12Y} - g_{12} a_{11Y})$$

$$\epsilon = g_{12} (g_{22} - g_{12}^2) \quad \dots(45)$$

$$g_{12}^2 - a_{12X}^{-1} (a_{22X} + g_{22} a_{11X}) g_{12} + g_{22} = 0 \quad \dots(46)$$

$$g_{12}^2 - a_{12Y}^{-1} (a_{22Y} + g_{22} a_{11Y}) g_{12} + g_{22} = 0 \quad \dots(47)$$

On equating the coefficients of g_{12} in Eqs. (46) and (47), we get

$$g_{22} = \frac{a_{12X} a_{22Y} - a_{12Y} a_{22X}}{a_{11X} a_{12Y} - a_{11Y} a_{12X}} \quad \dots(48)$$

Substituting Eq. (48) in Eq. (46) or Eq. (47) and solving the resulting equation for g_{12} we have two solutions given by

$$g_{12}(+) = \frac{1}{2} \{b + (b^2 - 4g_{22})^{1/2}\} \quad \dots(49)$$

$$g_{12}(-) = \frac{1}{2} \{b - (b^2 - 4g_{22})^{1/2}\} \quad \dots(50)$$

where

$$b = \frac{a_{11X} a_{22Y} - a_{11Y} a_{22X}}{a_{11X} a_{12Y} - a_{11Y} a_{12X}} \quad \dots(51)$$

Since

$$g_{12}(+) g_{12}(-) = g_{22} \quad \dots(52)$$

the two possible g -matrices are given by

$$g(+) = \begin{bmatrix} 1 & g_{12}(+) \\ g_{12}(+) & g_{22} \end{bmatrix} \quad \dots(53)$$

and

$$g(-) = \begin{bmatrix} 1 & g_{12}(-) \\ g_{12}(-) & g_{22} \end{bmatrix} = \begin{bmatrix} 1 & g_{22}/g_{12}(+) \\ g_{22}/g_{12}(+) & g_{22} \end{bmatrix} = g(+)h$$

where

$$h = g(+)^{-1} g(-) \begin{bmatrix} 0 & g_{22}/g_{12}(+) \\ 1/g_{12}(+) & 0 \end{bmatrix} \quad \dots(55)$$

If we denote by $I(+)$ and $I(-)$ the invariant matrix blocks obtained using the two solutions $g(+)$ and $g(-)$ respectively, then due to Eqs.(12) and (15) the relevant 2×2 block of the force-constant matrix in the initial S -coordinate system, is given by

$$F = g(+)^{-1} I(+) g(+)^{-1} \quad \dots(56)$$

$$= g(-)^{-1} I(-) g(-)^{-1}$$

Using Eqs. (54) and (56) it is found that

$$I(-) = h^\dagger I(+) h \quad \dots(57)$$

Hence it is enough to consider one of the two solutions for g_{12} given by Eqs. (49) and (50) in constructing the desired invariants since the usage of the other solution also leads to the same invariants apart from multiplications by isotopically invariant geometrical parameters as seen from Eqs. (55) and (57).

In the following we shall use only the solution $g_{12}(+)$ given by Eq. (49) and denote it simply by g_{12} . It is then evident that Eqs. (38)-(40), (43), (45), (48), (49) and (51) solve the problem of splitting any 2×2 block of the G -matrix of an $X_m Y_n$ -type molecule according to the prescription in Eq. (11). Thus using this process of factorization of G according to Eq. (11), the isotopic invariants of Sec. 2 can be obtained for any $X_m Y_n$ -type molecule having its G -matrix in a mass-independent internal symmetry coordinate system with only 1×1 and 2×2 blocks.

4. Applications to Some $X_m Y_n$ -type Molecules

We shall now list the factorizations as in Eq. (11) of the 2×2 blocks of G -matrices in symmetry-adapted internal valence-force coordinate systems for some $X_m Y_n$ -type molecules obtained using the method described in Sec. 3. The index j of Eq. (19) specifying the 2×2 block within the complete G -matrix is replaced in the following by the symbol for the appropriate species of irreducible representation of the corresponding symmetry group and the diagonal elements of d have been taken to be the positive square roots of the corresponding elements of d^2 obtained in the above process of factorization.

(a) For symmetrical linear $X_2 Y_2$ molecule:

$$g(\Sigma_g^+) = \begin{bmatrix} 1 & -\sqrt{2} \\ -\sqrt{2} & 0 \end{bmatrix},$$

$$d(\Sigma_g^+) = \begin{bmatrix} \mu_X^{1/2} & 0 \\ 0 & (\mu_Y/2)^{1/2} \end{bmatrix} \quad \dots(58)$$

(b) For bent symmetrical XY_2 molecule:

$$g(A_1) = \begin{bmatrix} 1 & \sqrt{2} \cot A \\ \sqrt{2} \cot A & -2 \end{bmatrix},$$

$$d(A_1) = \begin{bmatrix} \mu_Y^{1/2} \sin A & 0 \\ 0 & (\mu_X + \frac{1}{2} \mu_Y)^{1/2} \sin A \end{bmatrix} \quad \dots(59)$$

where $2A$ denotes the XYX angle. In Ref. 2 we have used essentially this factorization of $G(A_1)$ except that $\sin A$, an isotopic invariant, has been transferred from $d(A_1)$ to $g(A_1)$ leading to

$$g(A_1) = \begin{bmatrix} \sin A & \sqrt{2} \cos A \\ \sqrt{2} \cos A & -2 \sin A \end{bmatrix},$$

$$d(A_1) = \begin{bmatrix} \mu_Y^{1/2} & 0 \\ 0 & (\mu_X + \frac{1}{2} \mu_Y)^{1/2} \end{bmatrix} \quad \dots(60)$$

Some of the isotopic invariants obtained as a result of Eq. (60) for this molecule, as given already in Refs. 2 and 3, are as follows:

$$I(A_1)_{11} = m_Y \{A^2 (\lambda_1 \zeta_1^2 + \lambda_2 \zeta_2^2) + B^2 (\lambda_1 \zeta_2^2 + \lambda_2 \zeta_1^2) + 2AB (\lambda_1 - \lambda_2) \zeta_1 \zeta_2\}$$

$$= \frac{\lambda_1 \lambda_2 M t_{XXXX}}{8m_X R^2 \cos^2 A}$$

$$I(A_1)_{12} = m_Y^{1/2} \mu^{1/2} \{(\lambda_1 - \lambda_2) [(B^2 - A^2) \zeta_1 \zeta_2 - AB (\zeta_2^2 - \zeta_1^2)]\}$$

$$= - \frac{\lambda_1 \lambda_2 t_{XXYY}}{2\sqrt{2} R^2 \sin 2A}$$

$$I(A_1)_{22} = \mu \{A^2 (\lambda_1 \zeta_2^2 + \lambda_2 \zeta_1^2) + B^2 (\lambda_1 \zeta_1^2 + \lambda_2 \zeta_2^2) - 2AB (\lambda_1 - \lambda_2) \zeta_1 \zeta_2\}$$

$$= \frac{\lambda_1 \lambda_2 \mu t_{YYYY}}{8m_Y R^2 \sin^2 A} \quad \dots(61)$$

where

$$M = m_X + 2m_Y$$

$$\mu = [2m_X m_Y] / (m_X + 2m_Y)$$

$$A = (I_X / I_Z)^{1/2}$$

$$B = (I_Y / I_Z)^{1/2}$$

$$I_X = \mu R^2 \cos^2 A$$

$$I_Y = 2m_Y R^2 \sin^2 A$$

$$I_Z = I_X + I_Y \quad \dots(62)$$

and t_s are the centrifugal distortion constants (Ref. 6) and the meanings of other quantities are the same as given in Section 2 in connection with Eqs. (36) and (37).

(c) For planar symmetrical XY_3 molecule:

$$g(E') = \begin{bmatrix} 1 & \sqrt{3} \\ \sqrt{3} & -3 \end{bmatrix},$$

$$d(E') = \begin{bmatrix} [\frac{1}{2}(3\mu_X + \mu_Y)]^{1/2} & 0 \\ 0 & (\mu_Y/6)^{1/2} \end{bmatrix} \quad \dots(63)$$

Some of the isotopic invariants derived as a result of Eq. (63) for this type of molecule, as given already in Ref. 2, are as follows:

$$I(E')_{11} = [2m_X m_Y / M] [\lambda_1 (\zeta_{2,1a}^y)^2 + \lambda_2 (\zeta_{2,2a}^y)^2]$$

$$= [m_X m_Y / M] [(\lambda_1 + \lambda_2) + (\lambda_1 - \lambda_2) \zeta_{1a,1b}^x]$$

$$I(E')_{12} = [12m_X m_Y^2 / M]^{1/2} [(\lambda_2 - \lambda_1) \zeta_{2,1a}^y \zeta_{2,2a}^y]$$

$$= [3m_X m_Y^2 / M]^{1/2} [(\lambda_2 - \lambda_1) \zeta_{1a,2b}^x]$$

$$I(E')_{22} = 6m_Y [(\lambda_1 (\zeta_{2,2a}^y)^2 + \lambda_2 (\zeta_{2,1a}^y)^2)]$$

$$= 3m_Y [(\lambda_1 + \lambda_2) - (\lambda_1 - \lambda_2) \zeta_{1a,1b}^x] \quad \dots(64)$$

where $M = m_X + 3m_Y$, (λ_1, λ_2) belonging to E' -species are doubly degenerate, (ζ^x, ζ^y) matrices are of the type $A' \times E'$ and ζ^z -matrix is of the type $E' \times E'$ (for details, see Ref. 2),

(d) For regular pyramidal XY_3 molecule:

$$g(A) = \begin{bmatrix} 1 & -2 \tan A \\ -\tan A & \sec^2 A - 4 \end{bmatrix}$$

$$d(A) = \begin{bmatrix} [(4 \cos^2 A - 1) (\mu_X + \frac{1}{3}\mu_Y)]^{1/2} & 0 \\ 0 & (\frac{1}{3} \cos^2 A \mu_Y)^{1/2} \end{bmatrix} \quad \dots(65)$$

$$g(E) = \begin{bmatrix} 1 & \tan A \\ \tan A & -\frac{1}{2}(2 + \sec^2 A) \end{bmatrix}$$

$$d(E) = \begin{bmatrix} [2\sin^2 A \mu_X + \frac{1}{3}(2\cos^2 A + 1)\mu_Y]^{1/2} & 0 \\ 0 & (\frac{3}{2}\cos^2 A \mu_Y)^{1/2} \end{bmatrix} \quad \dots(66)$$

where $2A$ is the equilibrium YXY angle.

(e) For planar symmetrical XY_4 molecule:

$$g(E_u) = \begin{bmatrix} 1 & \sqrt{2} \\ \sqrt{2} & -2 \end{bmatrix}$$

$$d(E_u) = \begin{bmatrix} (\frac{1}{2}\mu_Y)^{1/2} & 0 \\ 0 & (\mu_X + \frac{1}{4}\mu_Y)^{1/2} \end{bmatrix} \quad \dots(67)$$

(f) For tetrahedral XY_4 molecule:

$$g(F_2) = \begin{bmatrix} 1 & 2 \\ 2 & -2 \end{bmatrix}$$

$$d(F_2) = \begin{bmatrix} \frac{1}{3}(4\mu_X + \mu_Y)^{1/2} & 0 \\ 0 & (\frac{1}{6}\mu_Y)^{1/2} \end{bmatrix} \quad \dots(68)$$

(g) For octahedral XY_6 molecule:

$$g(F_{1u}) = \begin{bmatrix} 1 & 2 \\ 2 & -2 \end{bmatrix}$$

$$d(F_{1u}) = \begin{bmatrix} (2\mu_X + \frac{1}{3}\mu_Y)^{1/2} & 0 \\ 0 & (\frac{1}{6}\mu_Y)^{1/2} \end{bmatrix} \quad \dots(69)$$

(h) For planar regular hexagonal Z_6 molecules:

$$g(E_{2g}) = \begin{bmatrix} 1 & \sqrt{3} \\ \sqrt{3} & -3 \end{bmatrix},$$

$$d(E_{2g}) = \begin{bmatrix} (\frac{1}{2}\mu_Z)^{1/2} & 0 \\ 0 & (\frac{2}{3}\mu_Z)^{1/2} \end{bmatrix} \quad \dots(70)$$

Work is in progress to obtain all possible isotopic invariants of the types considered in this paper for all the above types of molecules.

References

1. Parker P M, *J. molec. Spectrosc.*, 58 (1975), 344.
2. Chinnappan V A, Jagannathan R & Savari Raj G A, *Indian J. pure appl. Phys.*, 16 (1978), 668.
3. Chinnappan V A & Savari Raj G A, *Indian J. pure appl. Phys.*, 17 (1979), 423.
4. Wilson (Jr) B B, Decius J C & Cross P C, *Molecular vibrations* (McGraw-Hill, New York), 1955.
5. Cyvin S J, *Molecular vibrations and mean square amplitudes* (Elsevier, Amsterdam), 1968.
6. Cyvin S J, cited in *Molecular structures and vibrations*, edited by S J Cyvin (Elsevier, Amsterdam), 1972, Ch. 1.

Temperature Dependence of Rotational Relaxation in o- & n-Normal Hydrogen

PRABHURAM & M P SAKSENA

Department of Physics, University of Rajasthan, Jaipur 302 004

Received 28 February 1980; revised received 20 June 1980

Treating the molecules in various rotational states as the components of a hypothetical multicomponent gas mixture, the effective rotational relaxation numbers have been calculated for ortho-hydrogen and its temperature dependence has been investigated. Further, applying the theory of mixtures the rotational relaxation numbers for normal hydrogen have been obtained. The calculated values are in good agreement with the available experimental data.

1. Introduction

Recently, Prabhuram and Saksena¹ have suggested a method for obtaining the effective rotational relaxation number from the knowledge of Z_{rot} values for the transitions between two specific levels. These studies are useful in understanding the role of higher energy states which have significant population at temperatures higher than the room temperature. These authors have also shown that the decrease in Z_{rot} with temperature is arrested by involvement of higher energy modes and there is a possibility that after a particular temperature, the Z_{rot} values may even show an increasing trend. In the present paper, we present the calculated effective Z_{rot} values for ortho hydrogen, and using the earlier results¹ for para-hydrogen, the rotational relaxation numbers for normal hydrogen have been predicted.

2. Theory : Calculation of Effective Z_{rot} Values

For large spacing between the rotational energy states, Prabhuram and Saksena¹ have shown that the Brout's² relation for the cross-section σ_{jj-2} can be written as

$$\sigma_{jj-2} = C\lambda^2 \pi \frac{\alpha^2 k_i \left(k_i^2 + \frac{2\mu\Delta\epsilon}{\hbar^2} \right)^{3/2}}{\left[\alpha^4 + 2\alpha^2 \left(2k_i^2 + \frac{2\mu\Delta\epsilon}{\hbar^2} \right) + \left(\frac{2\mu\Delta\epsilon}{\hbar^2} \right)^2 \right]^2} \times \left(\frac{9}{4} \right) \frac{j^2 (j-1)^2}{(4j^2-1)^2} \quad \dots(1)$$

where, C is a constant and λ is a parameter expressing the deviation of potential from spherical symmetry and its value for hydrogen is 0.45.

$$\alpha = 4A^{-1},$$

$$k_i = (2\mu kT/\hbar^2)^{1/2},$$

$$k_f = [2\mu(kT + \Delta\epsilon)/\hbar^2]^{1/2}$$

$\Delta\epsilon$ = energy difference between rotational levels j and $j-2$ and μ is the reduced mass.

This relation then can be used to obtain rotational relaxation number $(Z_{\text{rot}})_{jj-2}$ as

$$(Z_{\text{rot}})_{jj-2} = \frac{\pi \sigma_0^2}{\sigma_{jj-2} \left[1 + \frac{1}{(2j+1)} \exp \left\{ (E_j - E_{j-2})/kT \right\} \right]} \quad \dots(2)$$

where σ_0 represents the hard sphere diameter.

Further, if x_j represents the relative population in j th level, then treating it as the fraction of j th component in hypothetical mixture the effective rotational relaxation number is given by

$$\frac{1}{(Z_{\text{rot}})_{\text{eff}}} = \frac{x_1}{(Z_{\text{rot}})_{13}} + \frac{x_3}{(Z_{\text{rot}})_{35}} + \frac{x_5}{(Z_{\text{rot}})_{57}} + \dots \quad \dots(3)$$

3. Results

The relative population in different levels at various temperatures for ortho-hydrogen is given in Table 1. The relative population has been obtained using the Boltzmann distribution law.³ While using Eq. (1), the value of the constant C has been adjusted to fit the smoothened experimental data at a given temperature. For ortho-hydrogen, $C = 291$ has been used which yields $Z_{\text{rot}} = 510$ at 250 K. The Z_{rot} values for different transitions as a function of temperature calculated according to Eqs. (1) and (2), are also listed in Table 1. The effective Z_{rot} values obtained through Eq. (3) are plotted against temperature in Fig. 1. The only available experimental data of Prangma *et al.*⁴ are also shown in Fig. 1.

Normal hydrogen being a mixture of para and ortho components involves para-para, ortho-ortho and para-ortho collisions. Assuming these reactions

Table 1—Relative Population and $(Z_{\text{rot}})_{j,j-2}$ at Different Temperatures for ortho-hydrogen

Energy level	Temp., K															Z_{rot}
	100	150	200	250	300	400	500	700	900	1200	1500	1800	2100	2400	3000	
$j = 1$	0.999	0.992	0.967	0.927	0.878	0.775	0.685	0.548	0.455	0.362	0.302	0.261	0.232	0.210	0.181	
$j = 3$	—	0.007	0.032	0.072	0.121	0.217	0.292	0.380	0.413	0.416	0.401	0.380	0.362	0.346	0.319	
$j = 5$	—	—	—	—	0.001	0.007	0.022	0.068	0.118	0.182	0.226	0.255	0.274	0.287	0.302	
$j = 7$	—	—	—	—	—	—	—	0.003	0.013	0.039	0.070	0.103	0.131	0.156	0.177	
Transitions $j =$																
$1 \rightarrow 3$	758	634	561	511	477	426	393	350	324	299	283	273	264	259	250	
$3 \rightarrow 5$	1230	1013	885	798	735	646	587	508	459	411	380	358	341	328	309	
$5 \rightarrow 7$	1958	1600	1387	1242	1136	987	885	752	667	583	528	487	457	433	397	

to be in parallel, we can define two relaxation numbers Z_1 and Z_2 as⁵

$$\frac{1}{Z_1} = \frac{x_p}{Z_{pp}} + \frac{x_o}{Z_{po}} \quad \dots(4)$$

and

$$\frac{1}{Z_2} = \frac{x_o}{Z_{oo}} + \frac{x_p}{Z_{op}} \quad \dots(5)$$

where x_p is the mole fraction of para-hydrogen in the mixture, Z_{pp} the effective rotational relaxation number for para-para collisions and Z_{po} the rotational relaxation number for para-ortho collisions. x_o , Z_{oo} and Z_{op} are defined in a similar way.

These two relaxation processes can be combined to give the effective relaxation number for the normal hydrogen as

$$\begin{aligned} \frac{1}{Z_n} &= \frac{x_p}{Z_1} + \frac{x_o}{Z_2} \\ &= \frac{x_p^2}{Z_{pp}} + x_p x_o \left(\frac{1}{Z_{po}} + \frac{1}{Z_{op}} \right) + \frac{x_o^2}{Z_{oo}} \quad \dots(6) \end{aligned}$$

Jonkman *et al.*⁶ have given the value of $Z_{po}=394$ at 77 K. At other temperatures there are no data either theoretical or experimental. Assuming $Z_{po}=Z_{op}$ we have empirically obtained the value of Z_{po} as 196 at 300 K. Using the experimental value of Z_{po} at 77 K and the empirical values around the room temperature and above, we have obtained the effective rotational relaxation number Z_n for normal hydrogen. These values are plotted in Fig. 1 as a function of temperature. At temperatures above 273 K, the relative proportion of para- and ortho-hydrogen remains 1 : 3. However, at lower temperatures the proportion of para-hydrogen increases. We have used the values of the relative proportion given by Glasstone³ in this study.

4. Discussion

From Table 1 it is evident that $(Z_{\text{rot}})_{j,j-2}$ values decrease as temperature rises but increase for tran-

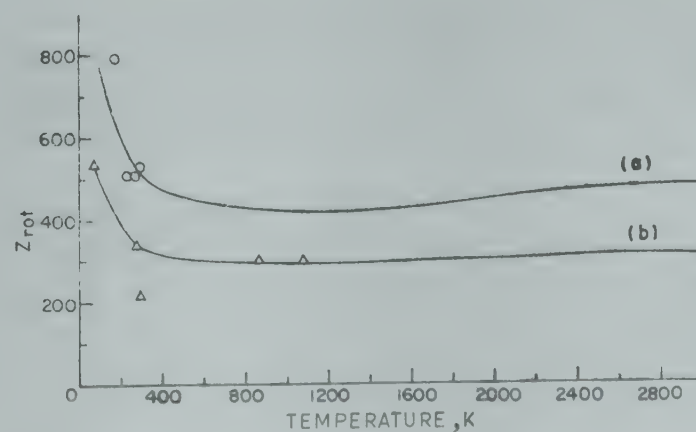


Fig. 1—Plot of Z_{rot} versus Temperature [curve (a) ortho-hydrogen and curve (b) normal hydrogen o, Δ experimental points from Ref. 4]

sitions involving higher j values. The increase with higher j values is due to the larger spacing between the levels involved in the transition. The effective Z_{rot} values for ortho-hydrogen rapidly decrease with temperature in the lower temperature range but at temperatures above room temperature the $(Z_{\text{rot}})_{\text{eff}}$ values remain almost constant. The $Z_{\text{rot}}-T$ curve [Fig. 1, curve (a)] shows a shallow minimum around 1200 K. This behaviour is in accordance with the observations of Lambert⁷ and Agrawal and Saksena.^{8,9} The theory is in satisfactory agreement with the experimental data of Prangma *et al.*⁴ which covers only a limited range 170 to 293 K. These data are also expected to have some error due to the presence of p-H₂. The authors have claimed the purity of ortho-hydrogen used in the experiment to be 95-96%. The presence of p-H₂ will induce para-ortho collisions which can drastically change the relaxation behaviour.

For n-H₂ the comparison of theoretical $(Z_{\text{rot}})_{\text{eff}}$ values with experimental data¹⁰⁻¹² is shown in Fig. 1, curve (b). It is obvious that this comparison is limited by the approximations involved in the determination of a single effective relaxation number for n-H₂ and a considerable scatter in the experimental data. The variation of $(Z_{\text{rot}})_{\text{eff}}$ with temperature has the same trend as obtained for ortho-hydrogen and para-hydrogen. One can, however, conclude from these studies that at lower temperatures below 200 K both ortho- and para-hydrogen behave as two-level systems, at higher temperatures as the higher rotational states get populated, the gas can be

treated as a hypothetical multicomponent mixture and a single effective relaxation number can be obtained.

Acknowledgement

One of the authors (Prabhuram) is grateful to the University Grants Commission, New Delhi, for the grant of a teacher fellowship. The authors are grateful to the referee for valuable suggestions.

References

1. Prabhuram & Saksena M P, *Indian J. pure appl. Phys.*, **19** (1981), in press.
2. Brout R, *J. chem. Phys.*, **22** (1954), 1189, Erratum p. 1791.
3. Glasstone S, *Theoretical chemistry* (D Van Nostrand, New York), 1944.
4. Prangma G J, Borsboom L J M, Knaap H F P, Vanden Meijdenberg C J N & Beenakker J J M, *Physica*, **61** (1972), 527.
5. Herzfeld K F & Litovitz T A, *Absorption and dispersion of ultrasonic waves* (Academic Press, New York), 1959, 137.
6. Jonkman R M, Prangma G J, Ertas I, Knaap H F P & Beenakker J J M, *Physica*, **38** (1968), 441.
7. Lambert J D, *Vibrational rotational relaxation in gases* (Clarendon Press, Oxford), 1977.
8. Agrawal P M & Saksena M P, *J. Phys.*, **B8** (1975), 1575.
9. Agrawal P M & Saksena M P, *Chem. Phys. Lett.*, **32** (1975), 123.
10. Narayana H & Woods S B, *Can. J. Phys.*, **48** (1970), 305.
11. Stewart J L & Stewart E S, *J. acoust. Soc. Am.*, **24** (1952), 194.
12. Winter T G & Hill G L, *J. acoust. Soc. Am.*, **42** (1967), 848.

Magneto & Spectral Studies on Rare Earth Chelates of β -Benzidinyl 2 : 4-Dihydroxy Propiophenone

V K RASTOGI, B S TYAGI* & A N PANDEY†

Department of Physics, Lajpat Rai College, Sahibabad 201 005

and

R C SAXENA

Department of Chemistry M M (P G) College, Modinagar 201 204

Received 23 November 1979

Some new complexes of lanthanide chlorides of the composition $[M(C_{21}H_{18}N_2O_3)_2]Cl.nH_2O$, where $M = Ce^{+3}$, Pr^{+3} , Sm^{+3} , Gd^{+3} and Dy^{+3} , $n=1$ and 2 , with β -Benzidinyl, 2:4-Dihydroxy propiophenone have been isolated in solid state for the first time. These compounds are characterized on the basis of infrared, analytical and magnetic studies and it has been concluded that (1) they possess octahedral (O_h) symmetry around the central metal ion, and (2) strong covalent bonding exists between lanthanions and the ligand. (M—O) and (M—N) stretching force constants have also been calculated and the results are briefly discussed.

1. Introduction

The spectroscopic studies on rare earth chelates, because of their use as laser materials,¹ have assumed considerable attention in recent years. The study of infrared spectra and magnetic properties give valuable information regarding the structure of chelates.² With the help of infrared studies, the metal ligand frequencies and the number of groups of complexing agent, which are coordinated can be known. Liang³ has made a systematic study of the infrared spectrum of europium acetonates and established the metal-ligand frequencies. Garg *et al.*⁴ have identified the different vibrational frequencies and the metal-ligand frequencies in the infrared spectra of some rare earth chelates of 2-hydroxy-5-methyl acetophenone. Recently lanthanide complexes with some nitrogen donor molecules, having varying coordination number have been prepared⁵⁻⁸ in a non-aqueous medium. In these compounds, the coordination number of rare earths varies from 6 to 10 or even more, which indicates more strong interaction between Ln and N, than previously assumed. In the present paper, we describe the synthesis and characterization of rare earth complexes of cerium, praseodymium, samarium, gadolinium and dysprosium with β -Benzidinyl 2:4-Dihydroxy propiophenone.

2. Experimental Procedure

2.1 Preparation of Organic Ligand

The ligand β -benzidinyl 2:4-dihydroxy propiophenone has been prepared by condensing 2:4-dihydroxy acetophenone with ice-cooled formaldehyde containing the β -benzidine. On keeping the ice-cooled mixture for about 3 hr, brick red coloured crystals precipitated out and these were washed repeatedly with water, recrystallized with ethanol and dried over P_2O_5 . Chemical analysis indicated a molecular formula $C_{21}H_{20}N_2O_3$ with m.p. $149^\circ C$ and the percentage weights of the components as follows:

	C%	H%	N%
Found	72.20	5.73	7.92
Calc.	72.41	5.75	8.05

The solutions of specpure lanthanide chlorides were prepared in a mixture of alcohol and water and the lanthanide content was determined gravimetrically by the oxalate oxide method.⁹

2.2 Preparation of the Complexes

Lanthanide chloride (1 mmole) and Mannich base (2.5 mmole) were dissolved separately in ethanol and acetone respectively and then mixed together. The precipitate formed was refluxed for about an hour, over steam bath to ensure the completion of the reaction. The solid product thus obtained was washed repeatedly with water, dried and stored in a vacuum desiccator.

* Principal, Lajpat Rai Postgraduate College, Sahibabad.

† Molecular Spectroscopy Research Laboratory, Department of Physics, Meerut College, Meerut.

The infrared spectra (KBr) of all the complexes along with the ligand have been measured in the region 200-4000 cm^{-1} . The (M—O) and (M—N) stretching frequencies obtained from the infrared absorption spectra of the complexes have been used to calculate K (M—O) and K (M—N) stretching force constants. The magnetic susceptibility measurements were made at room temperature by Guoy's method,¹⁰ using $\text{Hg} [\text{Co}(\text{NCS})_4]$ as the calibrant. The effective Bohr magneton numbers were calculated using the relation $\mu_{\text{eff}} = 2.827 \sqrt{\chi_m T}$, where χ_m is the gram-mole corrected diamagnetics susceptibility and T the absolute temperature. The values obtained are recorded in Table 1.

3. Results and Discussion

The compounds have been characterized on the basis of chemical analysis, magnetic measurements and IR spectral data. The experimental findings show that the ligand functions as monobasic and tridentate containing nitrogen and oxygen as donor atoms. The complexes are of 1:2 stoichiometry and each being associated with water molecules. The analytical data (Table 1) show that these complexes have the general formula $[\text{Ln}(\text{L})_2] \text{Cl} \cdot n\text{H}_2\text{O}$, where $n = 1$ and 2. The presence of Cl^- outside the coordination sphere is confirmed by alcoholic silver nitrate test.

3.1 Magnetic Studies

All the chelates were found paramagnetic in nature. It is apparent from Table 1 that the magnetic moment values obtained closely resemble the theoretical values obtained for the lanthanide salts and there is little difference between theoretical and experimental values of the magnetic moment. The difference is due to the shielding effect of $4f$ electrons, of rare earth ions which prevent interaction of

the ligand with the lanthanons. The Bohr magneton values suggest the octahedral geometry for these complexes. Further support to this geometry comes from spectral data.

3.2 Spectral Studies

From the analysis of the spectra, the vibrational frequencies and metal ligand frequencies are established. The assignments proposed for chief bands observed in the IR spectrum of the ligand and complexes are given in Table 2. The infrared spectra of all the complexes have many similar features indicating the similarity in the structures of the complexes under present investigation. On scrutinizing the observations it is found, that the ligand β -benzidiny 2:4-dihydroxypropiophenone functions as a tridentate ligand. A study of the IR spectra indicates the characteristic aromatic (C—H) frequency at $\sim 3020 \text{ cm}^{-1}$, out-of-plane (C—H) band around 950 cm^{-1} , (C=C) frequency at 1570 cm^{-1} , out-of-plane (C—C) band at 680 cm^{-1} , phenolic (C—O) stretching peak at about $1270\text{--}1300 \text{ cm}^{-1}$ and the —OH stretching at 3340 cm^{-1} .

The structures of all the complexes have been arrived at by comparing the IR spectra of the ligand with the IR spectra of the complexes. The IR spectra of the ligand shows a sharp band $\sim 3340 \text{ cm}^{-1}$ due to free hydroxy group,^{11,12} which disappears on complexation, showing thereby the hydrogen of the —OH group is replaced by the metal ion. The ν (N—H) frequency in ligand occurs at 3400 cm^{-1} , which gets lowered on complexation. The considerable shift of the ν (N—H) band (from 3400 to $3310\text{--}3380 \text{ cm}^{-1}$), indicates coordination of the secondary —N to the metal atom. The presence of the sharp absorption peak $\sim 570 \text{ cm}^{-1}$ by —NH₂ group indicates that —N[−] of NH₂ does not involve in complex forma-

Table 1—Colour, Analytical and Magnetic Data of Complexes Studied

Complex	Colour	Found/Calc. (%)				M	μ_{eff}	
		C	H	N	Cl		Obs. BM	Calc. BM
$[\text{Ce} (\text{C}_{21}\text{H}_{18}\text{N}_2\text{O}_3)_2] \text{Cl} \cdot 2\text{H}_2\text{O}$	Dark yellow	55.68	3.99	6.00	3.85	15.43	2.18	2.39
		55.77	4.42	6.19	3.92	15.50		
$[\text{Pr} (\text{C}_{21}\text{H}_{18}\text{N}_2\text{O}_3)_2] \text{Cl} \cdot \text{H}_2\text{O}$	Whitish yellow	56.53	4.19	6.25	3.98	15.88	3.54	3.62
		56.58	4.26	6.31	4.00	15.89		
$[\text{Sm} (\text{C}_{21}\text{H}_{18}\text{N}_2\text{O}_3)_2] \text{Cl} \cdot 2\text{H}_2\text{O}$	Brown	55.00	4.30	6.00	3.78	16.39	1.59	1.65
		55.15	4.37	6.12	3.88	16.45		
$[\text{Gd} (\text{C}_{21}\text{H}_{18}\text{N}_2\text{O}_3)_2] \text{Cl} \cdot 2\text{H}_2\text{O}$	Brown	54.70	4.31	6.13	3.80	17.03	7.85	7.91
		54.73	4.34	6.08	3.85	17.13		
$[\text{Dy} (\text{C}_{21}\text{H}_{18}\text{N}_2\text{O}_3)_2] \text{Cl} \cdot \text{H}_2\text{O}$	Brown	55.47	4.07	6.10	3.84	17.85	10.52	10.60
		55.50	4.18	6.16	3.90	17.89		

Table 2—Infrared Absorption Bands of the Ligand and Rare Earth Chelates (Values are in cm^{-1})

Ligand	Ce	Pr	Sm	Gd	Dy	Tentative assignment (Ref. 18-19)
3340(sh)	—	—	—	—	—	ν (O—H) phenolic
3400(m)	3380(m)	3370(m)	3300(m)	3300(m)	3310(m)	ν (N—H)
—	3180 } (w, b) 3320 }	3200 } (w, b) 3330 }	3240(w, b)	3280(w, b)	3290(w, b)	ν (OH) of water molecule
3020(w)	3000(w)	3000(w)	3020(w)	3010(w)	3020(w)	ν (C—H) Stretch.
1680(s)	1657(s)	1659(s)	1664(s)	1667(s)	1670(s)	(>C=O)
—	1640	1640	1630	1635	1640	Bending modes of water
1620	1610	1620	1610	1615	1620	δ (NH_2)
1600	1590	1580	1570	1580	1590	(C=C) aromatic
1585	1560	1560	1550	1560	1560	Aromatic ring
1240(s)	1200(s)	1240(s)	1220(s)	1200(s)	1230(s)	Plane deformation (OH)
1090	1020	1080	1060	1070	1080	Aromatic (C—O)
970(s)	960(s)	960(s)	950(s)	960(s)	970(s)	(C—H) Out-of-plane
920	880	880	870	910	900	Meta substituted
860(s)	800(s)	850(s)	840(s)	820(s)	820(s)	Para substituted
630(w)	600(w)	600(w)	610(w)	610(w)	620(w)	τ (NH_2)
590	580	570	580	570	570	γ (NH_2)
—	530 str	530 str	520 str	500 str	510	ν (M—N)
—	460(m)	460(m)	470(m)	474(m)	477(m)	ν (M—O)

sh, sharp; w, weak; s, strong; m, medium; b, broad; δ , bend; τ , torsion; γ , rock

tion.^{13,14} The strong band appearing at 1680 cm^{-1} in the ligand spectra, has been assigned to the carbonyl group >C=O . On chelation of the ligand with the metals, the frequency of this group gets shifted to the negative side. This shift might be due to back donation of d electrons of the metal ion. The lowering in frequency of >C=O group indicates the involvement of the carbonyl oxygen in coordination and formation of C—O—M bonding.

Further, the shift in >C=O frequency of the ligand on chelation gives the most important information regarding the structural change. By plotting a graph between the shift in >C=O frequencies and Ln^{3+} radii (Table 3), a straight line was obtained, which indicates that (M—O) bond strength increases with increasing ionic radii. A similar result was also obtained earlier by Parris and Long.¹⁵

On comparing the spectra of the ligand and its rare earth chelates it has also been observed that the bands observed at 460 and 530 cm^{-1} in Ce (III) complex, 460 and 530 cm^{-1} in Pr (III) complex, 470 and 520 cm^{-1} in Sm (III) complex, 474 and 500 cm^{-1} in Gd (III) complex and 477 and 500 cm^{-1} in Dy (III)

Table 3—Radius of Rare Earth Metal Ions and Shift in >C=O Stretching Frequency in Rare Earth Complexes

Particular	Complexes				
	Ce (III)	Pr (III)	Sm (III)	Gd (III)	Dy (III)
Ionic radii (\AA)	1.034	1.013	0.967	0.938	0.908
Change in >C=O frequency (cm^{-1})	23	21	16	13	10

complex are non-ligand bands and absent in the ligand spectra. These bands may tentatively be assigned to ν (M—O) and ν (M—N) vibration modes respectively. Such bands have been observed in infrared spectra of benzoates by Taylor *et al.*,¹⁶ in acetyl acetonates by Liang³ and in the rare earth complexes of 2-hydroxy-5-methyl acetophenone by Garg *et al.*⁴

It is evident from Table 2 that ν (M—O) stretching frequency increases in the order Ce (III) < Pr (III) < Sm (III) < Gd (III) < Dy (III), i.e. ν (M—O) stretching frequency increases with the increasing

Table 4 - Force Constants of Rare Earth Complexes

Complex	Force Constant (10 ⁵ dyne/cm)	
	K(M—O)	K(M—N)
[Ce (C ₂₁ H ₁₈ N ₂ O ₃) ₂] Cl·2H ₂ O	1·789	2·107
[Pr (C ₂₁ H ₁₈ N ₂ O ₃) ₂] Cl·H ₂ O	1·790	2·108
[Sm (C ₉₁ H ₁₈ N ₂ O ₃) ₂] Cl·2H ₂ O	1·881	2·040
[Gd (C ₂₁ H ₁₈ N ₂ O ₃) ₂] Cl·2H ₂ O	1·922	1·894
[Dy (C ₂₁ H ₁₈ N ₂ O ₃) ₂] Cl·H ₂ O	1·952	1·976

atomic number of rare earth metal, whereas ν (M—N) stretching frequencies in respective complexes do not show such a behaviour. K (M—O) and K (M—N) stretching force constants are presented in Table 4. An inspection of the results further shows that with the increase in the (M—O) stretching frequency, the (M—O) stretching force constant also increases. The other force constants do not show marked variation.

Coordinated water is reported to give bands in the region¹⁹ (880-640 cm⁻¹) whereas in the present complexes we get bands around 3300 cm⁻¹, indicating the presence of a water molecule outside the coordination sphere.

The shift in >C=O and N—H frequencies as well as complete disappearance of phenolic —OH frequency indicate that these three are the coordinating sites to the rare earth metal ion.

Thus, the analytical data, magnetic measurements, position and intensities of absorption bands suggest that the rare earth complexes studied here are cationic in nature, having octahedral environment around the central metal ion.

Acknowledgement

The authors are grateful to Drs S L Gupta and V Kumar of the Department of Physics, M M College, Modi Nagar, and (Miss) Anita Singh for continued interest, encouragement and helpful discussions.

References

1. Schimitschek E J & Schwartz E G K, *Nature, Lond.*, **196** (1962), 832.
2. Nakamoto K & McCarthy P J, *Spectroscopy and structure of metal chelate compounds*, (John Wiley, New York), 1968.
3. Liang C Y, *Proc. Int. Conf. Spectroscopy India*, Vol. 2 (1967), 302.
4. Garg C L, Narasimham K C & Tripathi B N, *J. inorg. nucl. Chem.*, **33** (1971), 387.
5. Moeller T & Forsberg J H, *J. Am. chem. Soc.*, **90** (1968), 1932.
6. Moeller T & Forsberg J H, *Inorg. Chem.*, **8** (1969), 883.
7. Moeller T & Charpentier L J, *J. Inorg. nucl. Chem.*, **32** (1970), 3575.
8. Forsberg J H & Wathen C A, *Inorg. Chem.*, **10** (1971), 1379.
9. Kolthoff I M & Elving P J, *Treatise on analytical chemistry* (Interscience, New York), 1963, Part II, Vol. 8.
10. Lewis J & Wilkins R G, *Modern coordination chemistry*, (Interscience Publishers, New York), 1967, 409.
11. Kuhn L P, *J. Am. chem. Soc.*, **74** (1952), 2492.
12. Ingrahm L L, Corse J, Bailey G F & Still F, *J. Am. chem. Soc.*, **74** (1952), 2292.
13. Nagano K, Kinoshita H & Hirakawa A, *Chem. Pharm. Bull.*, **12** (1964), 1198.
14. Braibanti A, Dallavalle F, Peltinghelli M A & Leporati E, *Inorg. Chem.*, **7** (1968), 1430.
15. Parris G S & Long G G, *J. inorg. nucl. Chem.*, **32** (1970), 1593.
16. Taylor M D, Cartex C P & Wynter C I, *J. inorg. nucl. Chem.*, **30** (1968), 1503.
17. Gamo I, *Bull. Chem. Soc. Japan*, **34** (1961), 760.
18. Silverstein R M & Bassler C C, *Spectrometric identification of organic compounds*, (John Wiley, New York), 1967.
19. Bellamy L J, *The infrared spectra of complex molecules*, (Methuen, London), 1969.

Radio Frequency Conductivity of Opalescent Binary Liquid Mixtures

S N SEN & A K GHOSH

Department of Physics, North Bengal University, Darjeeling 734 430

Received 3 December 1979

The radio frequency conductivity of three opalescent binary mixtures (methyl alcohol + n-hexane, methyl alcohol + carbon disulphide, methyl alcohol + cyclohexane) have been measured under a radio frequency field of 400 kHz. It has been shown from the simultaneous measurement of rf conductivity of the polar component and that of the binary mixture in the same proportion as is necessary to make an opalescent mixture but at a temperature slightly above the critical temperature, that there is no evidence of cluster formation in the critical state. From the abrupt increase of relaxation time at the critical temperature, the increase of viscosity has been obtained and the value of internal friction constant has been calculated utilizing Fixman's theory. It is shown that the internal friction constant depends upon the nature of the non-polar component of the opalescent mixture.

1. Introduction

Recently much effort has been made both theoretically and experimentally to study the dielectrical behaviour such as the relaxation process and transport phenomena near the critical temperature of binary liquid mixtures. Although Semenchenko's¹ treatment on the basis of thermodynamical considerations predicts a large increase of ϵ' , the real part of the dielectric constant at the critical solution temperature, the experimental evidence is meagre and frequently contradictory. Arkhangelskei and Semenchenko² examined a number of polar-non-polar systems and found that dielectric constant ϵ' and dielectric loss ϵ'' show a maximum at the critical temperature region. Similar results have been reported by Quinn and Smyth.³ Piekara⁴ observed that in case of nitrobenzene-hexane system at the critical temperature, ϵ' increased with decreasing temperature and the derivative $d\epsilon'/dt$ was not constant near the critical temperature. Similar results have been reported by Konecki⁵ recently. Although there are some contradictory results regarding the sharp increase of ϵ' in the opalescent state it has, however, been conclusively shown by different workers⁶⁻⁹ experimentally that there is a sharp rise in the coefficient of viscosity and ultrasonic absorption near the critical temperature. Fixman¹⁰ explained theoretically the increase of viscosity of critical mixtures near the critical region on the basis of density fluctuations. His method involves calculation of the entropy production through diffusion which

results when a mixture in a state of composition fluctuation is caused to have a velocity gradient. The long wavelength part of the spectrum of composition fluctuation is intense and very easily distorted by a velocity gradient in the critical region. The return to uniform composition through diffusion dissipates energy, and the loss is interpreted as an excess viscosity. It was shown by Krishnan¹¹ that the depolarization factor observed in the light scattered transversely by opalescent binary liquid mixtures is different from unity although in case of clear solutions, the value is unity. The discrepancy was explained by Krishnan on the hypothesis that in the clear solution the scattering is due to single molecules whereas in case of opalescent mixtures it is due to cluster of molecules. Sen and Ghosh¹² have measured the rf conductivity in case of two opalescent mixtures (nitrobenzene + n-hexane, aniline + cyclohexane) and found a large increase of rf conductivity at the critical temperature. From the calculated value of time of relaxation and radius of the rotating unit, it has been shown that the intense density fluctuation at the critical stage is not due to formation of cluster of molecules as proposed by Krishnan. The same conclusion has been arrived at by Lubezky and McIntosh¹³ though on different grounds. Sen and Ghosh¹² have also applied Fixman's theory in order to calculate the internal frictional constant β and found a good agreement with the literature value. Though Fixman's theory has been applied only in two systems by Sen and Ghosh, more investigation is necessary to verify the

theory in explaining the experimental results in the rf conductivity measurement. Hence it was considered desirable to extend the investigations to a number of other binary opalescent mixtures with the following aims in view:

- To observe whether the intense density fluctuation is due to formation of clusters of molecules in the critical state,
- To verify Fixman's theory in case of other opalescent mixtures and
- To observe whether the internal frictional term β changes for a particular polar solute in different non-polar solvents, since this may throw some light regarding the nature of β , the internal friction constant introduced by Fixman.

For this purpose, the measurement of rf conductivity was carried out in case of three opalescent binary mixtures, viz. methyl alcohol + n-hexane, methyl alcohol + carbon disulphide and methyl alcohol + cyclohexane under the application of a rf field of 400 kHz.

2. Experimental Arrangement

The method of determining the rf conductivity has been described in detail in a previous communication by Sen and Ghosh.¹² The dielectric cell used is a cylindrical glass tube of diameter 2.62 cm fitted with two circular gold electrodes 1.08 cm apart. Each gold plate is connected with a platinum wire which is sealed with the glass tube. A constant temperature bath was used to keep the mixtures at the desired temperatures. Following the theory of Murphy and Morgan,¹⁴ we have

$$K' = \frac{\epsilon'' \omega}{4\pi} \quad \dots(1)$$

where K' the real part of the rf conductivity, ϵ'' the loss factor and ω the angular frequency of the applied field. In case of polar liquid, K' is given by

$$K' = \frac{1}{4\pi} \frac{(\epsilon_0 - \epsilon_\infty)}{1 + \omega^2 \tau^2} \omega^2 \tau$$

where ϵ_0 and ϵ_∞ are the static and high frequency dielectric constants of the liquid and τ is the time of relaxation. As the frequency at which the rf conductivity has been measured is 400 kHz, $\omega^2 \tau^2 \ll 1$ and hence

$$K' = \frac{1}{4\pi} (\epsilon_0 - \epsilon_\infty) \omega^2 \tau \quad \dots(2)$$

In case of a polar-non-polar liquid mixture having N_2 number of polar solutes per cc where

$N_2 = (N d_{12}/M_2) \omega_2$, loss factor ϵ'' is given by Smyth¹⁵

$$\epsilon'' = \frac{4\pi N d_{12} w_2 \mu^2 (\epsilon_0 + 2)(\epsilon_\infty + 2)}{27 M_2 kT (1 + \omega^2 \tau^2)} \omega \tau \quad \dots(3)$$

where d_{12} is the density of the solution of weight fraction w_2 of polar solute having its molecular weight M_2 and dipole moment μ . The terms ϵ_0 and ϵ_∞ represent the static and high frequency dielectric constants of the mixture, τ is the time of relaxation, N the Avogadro's number, k the Boltzmann's constant and T the temperature in absolute scale. Value of ϵ_∞ may be taken as the square of the refractive index (n). Considering $\omega^2 \tau^2 \ll 1$ we have from Eqs. (1) and (3)

$$K' = \frac{4\pi^2 f^2 N \tau \mu^2 d_{12} (\epsilon_0 + 2)(n^2 + 2)}{27 M_2 kT} w_2 \quad \dots(4)$$

where $\omega = 2\pi f$. Eqs. (2) and (4) have been utilized for the determination of time of relaxation in case of pure polar liquid and the solution respectively.

3. Results and Discussion

Three sets of measurements were made in case of mixtures as follows:

- Measurement of K' for the pure polar liquid at a temperature at which the mixture becomes opalescent.
- Measurement of K' of the clear solution of the mixture containing appropriate proportion of polar-non-polar components necessary to make an opalescent mixture at the critical temperature; but at a temperature slightly higher than the temperature of opalescence.
- Measurement of K' when the mixture is opalescent.

The experimental values of K' thus measured are given in the third column of Table 1. The time of relaxation for pure liquid and clear solution of the mixture in appropriate proportion but at a temperature 1°C above the opalescent temperature, has been calculated from Eqs. (2) and (4) respectively. The dielectric constant of the pure liquid and the mixture have been measured by the same apparatus by the resonance method. The refractive indices of the solution have been calculated from the relation

$$n = x_1 n_{01} + x_2 n_{02} \quad (\text{Glasstone}^{16})$$

where x_s and n_s are the mole fraction and refractive indices of the pure solvent and solute respectively. The mole fraction x_2 of the solute is related to w_2 by

$$x_2 = \frac{w_2 M_1}{w_2 M_1 + w_1 M_2}$$

Table 1—Values of Parameters Calculated for Binary Liquid Mixtures

Liquid mixture system	rf conduc- tivity 10^{-3} esu	Relaxa- tion time 10^{-11} sec	Viscosity of the mixture (η_{12}) 1°C above opalescent temperature cP	Value of η_c/η_{12}	Value of $[m_1 m_2 \phi_2]$ $[\rho V_1^2 V_2]$ $\phi_1 (n_1 + n_2)]$	Value of $a^{1/2}/K$ $\times 10^{12}$	Value of $\beta \times 10^{-15}$	Value of $\beta =$ $e/\mu_1 m_2$ $\times 10^{-15}$	$\beta \times \eta_c/\eta_{12}$ $\times 10^{-15}$
Methyl alcohol at 29.5°C	0.6376	4.159							
Methyl alcohol 30% by wt + n-hexane 70% by wt at 30.5°C	0.0821	2.727	0.38469	1.6725	0.1695	4.8323	1.264		2.114
Opalescent mixture at 29.5°C	0.1373	4.561							
Methyl alcohol at 40.5°C	0.7778	5.073							
Methyl alcohol 20% by wt + carbon disulphide 80% by wt at 41.5°C	0.0667	1.829	0.35978	2.4220	0.3066	6.8019	0.981	4.407	2.376
Opalescent mixture at 40.5°C	0.1616	4.429							
Methyl alcohol at 45°C	0.8287	5.506							
Methyl alcohol 26.14% by wt + cyclohexane 73.86% by wt at 46°C	0.0903	3.862	0.53865	1.6181	0.1895	5.3135	1.323		2.141
Opalescent mixture at 45°C	0.1462	6.249							

The value of η_{12} , the viscosity of the clear solution of the binary mixture has been calculated from the relation $\log \eta_{12} = x_1 \log \eta_1 + x_2 \log \eta_2$ where x s and η s are the mole fraction and the coefficient of viscosity of the solvent and solute respectively.

It is known that the equation $\tau = 4 \pi \eta a^3/kT$ can be utilized for calculating the radius of the rotating unit when the value of τ is extrapolated to infinite dilution. However, the relative change in the value of a can be estimated if we measure τ at two different concentrations. As in this case, we have calculated τ from experimental determination of rf conductivity in case of the pure liquid as well as when methyl alcohol is dissolved in different non-polar solvents in the same proportion as is necessary in case of opalescent mixture but at a temperature 1°C above the critical temperature we get

$$\frac{a^3}{a_{12}^3} = \frac{T}{T+1} \cdot \frac{\eta_{12}}{\eta} \cdot \frac{\tau}{\tau_{12}}$$

where a and a_{12} are the radii of the rotating unit for the polar solute and solution respectively. Substituting the values in the right hand side of the above equation, we get in case of methyl alcohol and methyl alcohol-n-hexane mixture $a/a_{12} = 1.001$.

In case of methyl alcohol- CS_2 mixture, the ratio a/a_{12} is of the order of 1.303 and for methyl alcohol-cyclohexane, the ratio is 1.202. Hence it is clear that there is a slight change in the value of the radius of the rotating unit and even at a temperature 1°C

higher than that at which opalescence takes place there is no evidence of cluster formation. If it is further assumed that for a change of temperature of 1°C , the viscosity of the mixture is the same as that in the critical state, from the relation:

$$\frac{\tau_{\text{clear}}}{\tau_{\text{crit}}} = \frac{a^3 T}{a_c^3 (T+1)}$$

it is found by substituting the value of τ_{clear} and τ_{crit}

$$a/a_c = 0.8433$$

where a and a_c are the radii of the rotating unit when the solution is clear and opalescent respectively.

Hence it can be argued that there is no appreciable change in the radius of the rotating unit; otherwise, there is no evidence of cluster formation as the temperature of critical opalescence is approached. Similar results have been reported earlier by Sen and Ghosh¹² in case of nitrobenzene + n-hexane and aniline + cyclohexane mixtures. As the abrupt change of relaxation time when the mixture passes into opalescent stage cannot be explained by the change in the value of radius of the rotating unit, we have to assume that there is a sudden change of viscosity.

We have then from the ratio of relaxation times

$$\frac{\eta_c}{\eta_{12}} = \frac{\tau_c T}{\tau_{12} (T+1)}$$

where η_c and η_{12} are the viscosities at the critical opalescent state and that of mixture which is not

opalescent but at a temperature higher by 1°C respectively, τ_c and τ_{12} are the times of relaxation under similar conditions as mentioned above. The values of η_c/η_{12} are listed in the sixth column of Table 1. From Table 1 col. 6 it is evident that in case of all the mixtures there is an abrupt change of viscosity as the critical temperature is approached. From the theory of Fixman,¹² the increase in viscosity is given by

$$\Delta \eta = \left\{ \frac{m_1 m_2 \phi_2}{e V_1^2 V_2 \phi_1 (n_1 + n_2)} \right\} \left\{ \frac{a^{1/2}}{K} \right\} \frac{1}{40} (\beta a^{1/2})$$

where the symbols have the same significance as in Fixman's paper and

$$\frac{a^{1/2}}{K} = \left\{ \frac{V_1}{4 \pi \phi_2} \right\}^{1/2} \left[\left\{ \phi_1^{-1} - (1 - m^{-1}) - \frac{T_c}{T} \right. \right. \\ \left. \left. (1 + m^{-1/2})^2 \phi_2 \right\}^{-1} - \frac{V_2}{V_1} \right]^{1/2}$$

The values of $\frac{m_1 m_2 \phi_2}{e V_1^2 V_2 \phi_1 (n_1 + n_2)}$ and $a^{1/2}/K$ have been calculated and are given in 7th and 8th columns

of Table 1. Since $\frac{\Delta \eta}{\eta_{12}} = \left[\frac{\eta_c}{\eta_{12}} - 1 \right]$, putting the ex-

perimental values of η_c/η_{12} the value of $\Delta \eta$ has been calculated and finally assuming $a=1 \text{ \AA}$ as in Fixman's paper, the internal frictional term β has been calculated and entered in the 9th column of Table 1. When β is calculated from the alternative formula $\beta = e/\mu_1 m_2$ as has been suggested by Sen and Ghosh,¹² the value becomes equal to 4.407×10^{15} where μ_1 is the mobility of the hydroxyl ion and in this case is taken as $20.5 \times 10^{-4} \text{ cm/sec.}$ (Glasstone¹⁶) and $m_2 = M_2/N$ where N is the Avogadro's number. It is observed that the value of β calculated by an independent procedure is of the same order of magnitude as obtained from Fixman's calculation from the experimental results obtained in the present investigation.

It is observed from Table 1 col. 9 that β varies with the nature of the non-polar solvent and we get different values of β when the opalescent mixture is made with methyl alcohol as one of the components and hexane, carbon disulphide and cyclohexane as non-polar components. Fixman in his paper has introduced β as a measure of internal frictional constant.

From col. 11 of Table 1 it is, however, noted that the product $\beta \times \eta_c/\eta_{12}$ is almost a constant for all the three opalescent mixtures studied in the present investigation. Evidently η_c/η_{12} can be taken as a measure of the screening effect of the surrounding molecules on the resultant internal friction constant.

This method of measuring the rf conductivity enables us to calculate the sharp increase of viscosity when the critical temperature is approached as has been observed by direct experimental measurement of Reed and Taylor⁶ in case of iso octane perfluoroheptane and that of Yang and Meeks⁹ in case of cyclohexane-aniline binary liquid system.

The analysis of the experimental results thus indicates that there is a sharp increase of viscosity as the critical temperature is approached and there is no evidence of cluster formation in the critical opalescent state. The experimental results thus lend support to the theory of Fixman regarding the sudden increase of viscosity in the critical state.

References

1. Semchenko V K, *Zh. Fiz. Khim.*, **25** (1951), 121.
2. Arkhangelskii K V & Semchenko V K, *Zh. Fiz. Khim.*, **41** (1967), 1303; English Transl. *Russ. J. Phys., Chem.*, **41** (1967), 692.
3. Quinn R G & Smyth C P, *J. chem. Phys.*, **39** (1963), 3285.
4. Piekara A, *Phys. Rev.*, **42** (1932), 448.
5. Konecki M, *Chem. Phys. Lett.*, **57** (1978), 90.
6. Reed T M & Taylor T E, *J. phys. Chem.*, **63** (1959), 58.
7. Chynoweth A G & Schenieder W G, *J. chem. Phys.*, **19** (1951), 1566.
8. Schemidt H, Jura G & Hidebrand J H, *J. phys. Chem.*, **63** (1959), 297.
9. Yang C C & Meeks F R, *J. phys. Chem.*, **75** (1971), 2619.
10. Fixman M, *J. chem. Phys.*, **36** (1962), 310.
11. Krishnan R S, *Proc. Indian Acad. Sci.*, **A1** (1935), 915.
12. Sen S N & Ghosh R, *J. phys. Soc. Japan*, **33** (1972), 838.
13. Lubezky L & McIntosh R, *Can. J. Chem.*, **51** (1974), 3176.
14. Murphy E J & Morgan S C, *Bell. Syst. Tech. J.*, **18** (1939), 502.
15. Smyth C P, *Dielectric behaviour and structure* (McGraw-Hill, New York), 1955.
16. Glasstone S, *Physical chemistry* (McMillan, London), 1968; *An Introduction to electrochemistry* (D Van Nostrand, New York), 1962.

Temperature & Frequency Dependence of Dielectric Properties of $\text{CoSiF}_6 \cdot 6\text{H}_2\text{O}$ around Its Structural Phase Transition Temperature

S K DUTTA ROY, S S MITRA & S K GHORAI

Cryogenic Engineering Centre, Indian Institute of Technology, Kharagpur 721 302

Received 24 December 1979

Dielectric constant (ϵ'), dielectric loss ($\tan \delta$) and ac conductivity of $\text{CoSiF}_6 \cdot 6\text{H}_2\text{O}$ single crystal have been measured as a function of frequency within the range 100 Hz - 0.1 MHz at room temperature and as a function of temperature within the range of 200-300 K at two fixed frequencies, viz. 1 kHz and 10 kHz. The frequency dependence of ϵ' shows space charge effect at lower frequencies and dipolar characteristics at high frequencies; $\tan \delta$ vs frequency curve shows a maximum around 66.07 kHz and the corresponding dipolar relaxation time has been calculated. Thermal variations of ϵ' , $\tan \delta$ and ac conductivity show anomalous increase at the structural transition temperature ($T_c = 246$ K) of the crystal during cooling. During heating, the discontinuity has been obtained at a higher temperature ($T_h = 261$ K), confirming the hysteresis of the transition temperature. The height of the peak for ϵ' , etc. near transition is smaller for higher frequencies. The jump becomes less pronounced in the second run.

1. Introduction

$\text{CoSiF}_6 \cdot 6\text{H}_2\text{O}$ (CFSH) crystals exhibit a phase transition from rhombohedral to monoclinic structure at about 246 K. The transition is accompanied by a thermal hysteresis in the structural transition temperature during cooling (T_c) of about 14 K in the heating cycle.^{1,2} An unnatural feature of this crystal as revealed by the X-ray data at room temperature is a disorder in the position of one of the six fluorine atoms (hydrogen bonded with the water octahedra) between two sites unrelated by any symmetry element with unequal occupancy number.³ The occupancy number of the minority site increases as the temperature comes down near T_c .⁴ Another X-ray study by Watanabe⁵ in the low temperature phase of CFSH shows that below T_c , there are two kinds of $\text{Co}^{2+}(\text{H}_2\text{O})_6$ octahedra with a different orientation and a doubling of the unit cell takes place. Study on $\text{CoSiF}_6 \cdot 6\text{D}_2\text{O}$ shows a rise in T_c (of about 17 K) in the mass ratio of D_2O and H_2O .⁶ All these results suggest that the structural phase transition is connected with the rearrangement of water octahedra around Co^{2+} ion with two different distortions, and can be ferroelectric in nature. In this paper, we report the results of dielectric measurements on this crystal around this temperature region.

2. Experimental Details

Dielectric constant (ϵ') and dielectric loss ($\tan \delta$) were measured with GR-716 capacitance bridge at

room temperature in the frequency range 100 Hz-0.1 MHz. Measurement at 0.1 MHz frequency was done with Marcony circuit magnification meter type TF329G, using the resonance curve principle. The frequency dependence of the dielectric properties of the crystal appears to be very sensitive to moisture, cracks and overall handling. More or less reproducible results were obtained by drying the crystals at about 50°C for some time. The accuracy of measurement is 2% for ϵ' and about 5% for $\tan \delta$.

The temperature dependence of the dielectric properties was measured at two fixed frequencies, 1 kHz and 10 kHz, by an LCR bridge in a cryostat which can control temperatures, within $\pm 1^\circ$ up to 100 K. The accuracy of measurement is 2% for ϵ' , and about 5% for $\tan \delta$. Graphite solution was used as contact material with copper electrodes. Measurements were done in the direction perpendicular to the plane containing C-axis of the crystal.

3. Results and Discussion

Fig. 1 shows the variation of ϵ' , $\tan \delta$ and ac conductivity (σ) of CFSH with frequency (ω). The increase in ϵ' and $\tan \delta$ at lower frequency (< 1 kHz) indicates the existence of space charge polarization within the crystal. The dc electrical conductivity also shows a nonlinear V - I characteristic and ageing effect indicating space charge polarization at room temperature.⁷ Values of ϵ' and $\tan \delta$ show typical

dipolar characteristics in the frequency region 1 kHz–1 MHz. The relaxation time at room temperature is 1.5×10^{-5} sec. The $\log \sigma$ vs $\log \omega$ curve shows a linear characteristic in the same region.

Figs. 2 and 3 indicate the temperature variation of ϵ' and $\tan \delta$ at frequencies 1 kHz and 10 kHz. Both ϵ' and $\tan \delta$ increase abruptly at the transition temperature and fall off gradually below T_c . The height and spread of the anomaly are found to be frequency dependent. The jump height decreases with higher frequency. The ac conductivities calculated from the dielectric constants and dielectric losses also show maxima at T_c and a linear curve

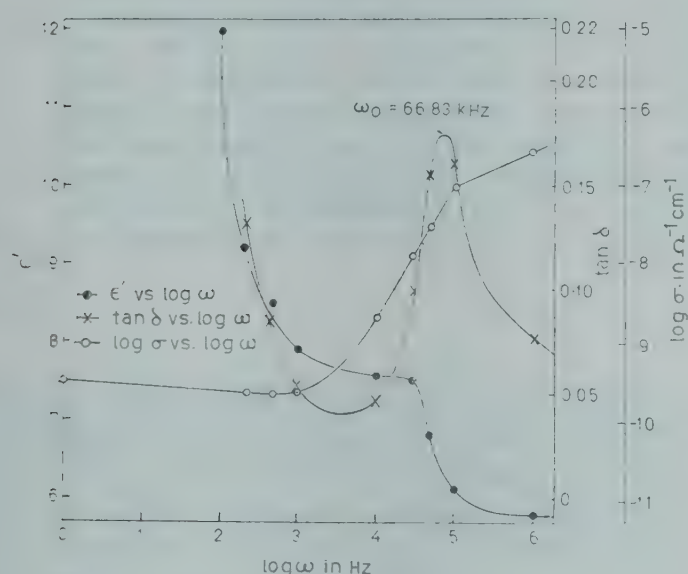


Fig. 1—Frequency variation of ϵ' , $\tan \delta$ and ac conductivity for $\text{CoSiF}_6 \cdot 6\text{H}_2\text{O}$ at room temperature

for $\log \sigma$ vs $1/T$ above T_c similar to that obtained in dc conductivity measurements (Fig. 4). But the jump heights and activation energies are smaller for the ac conductivities. Activation energy for dc measurement and at 1 kHz and 10 kHz are 0.64, 0.37 and 0.49 eV respectively. The hysteresis in T_c is obtained in the heating cycle as shown in Figs. 2 and 3, confirming the earlier thermal, magnetic and other measurements. During heating, ϵ' and $\tan \delta$ show much greater base value above T_c . The single crystals of CFSH crack at the transition point due to anomalous thermal expansion. Therefore, a second run was taken, results of which are shown in Figs. 2 and 3. It can be seen that the anomaly near the transition has become much smaller in the second run with a general increase in the base value. The jump in ϵ' and $\tan \delta$ also appears to occur slightly below T_c . This kind of behaviour was also noticed in the dc conductivity measurements.

The abrupt jump in ϵ' and $\tan \delta$ for CFSH is unlike other ferroelectric crystals like alum.⁸ Instead, it has some similarity with the behaviour of such crystals as $(\text{NH}_4)_2\text{SO}_4$ analyzed by Ohshima and Nakamura⁹ which according to them indicates that the long range order develops suddenly at T_c without increase in the local order in parallel alignment of the dipoles. The decrease in anomaly in the second run can be attributed to the sputtering within the crystal at T_c .

Further experimentation is necessary to confirm the onset of spontaneous polarization and polariza-

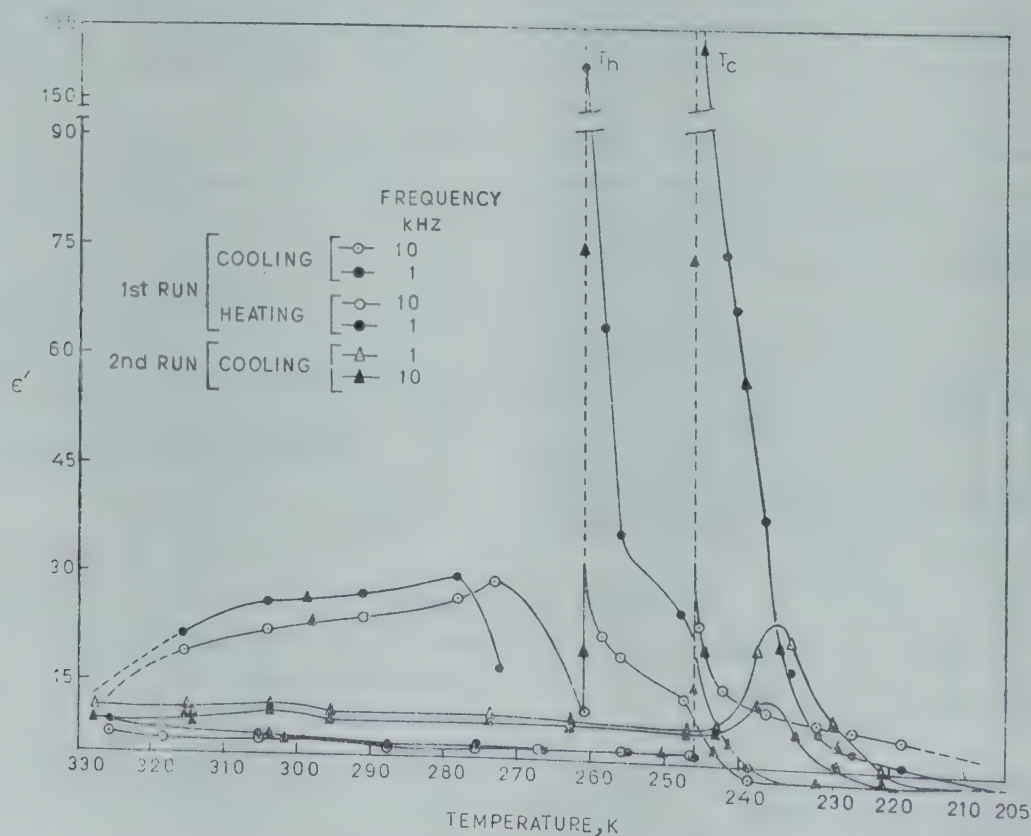


Fig. 2—Temperature variation of ϵ' for $\text{CoSiF}_6 \cdot 6\text{H}_2\text{O}$

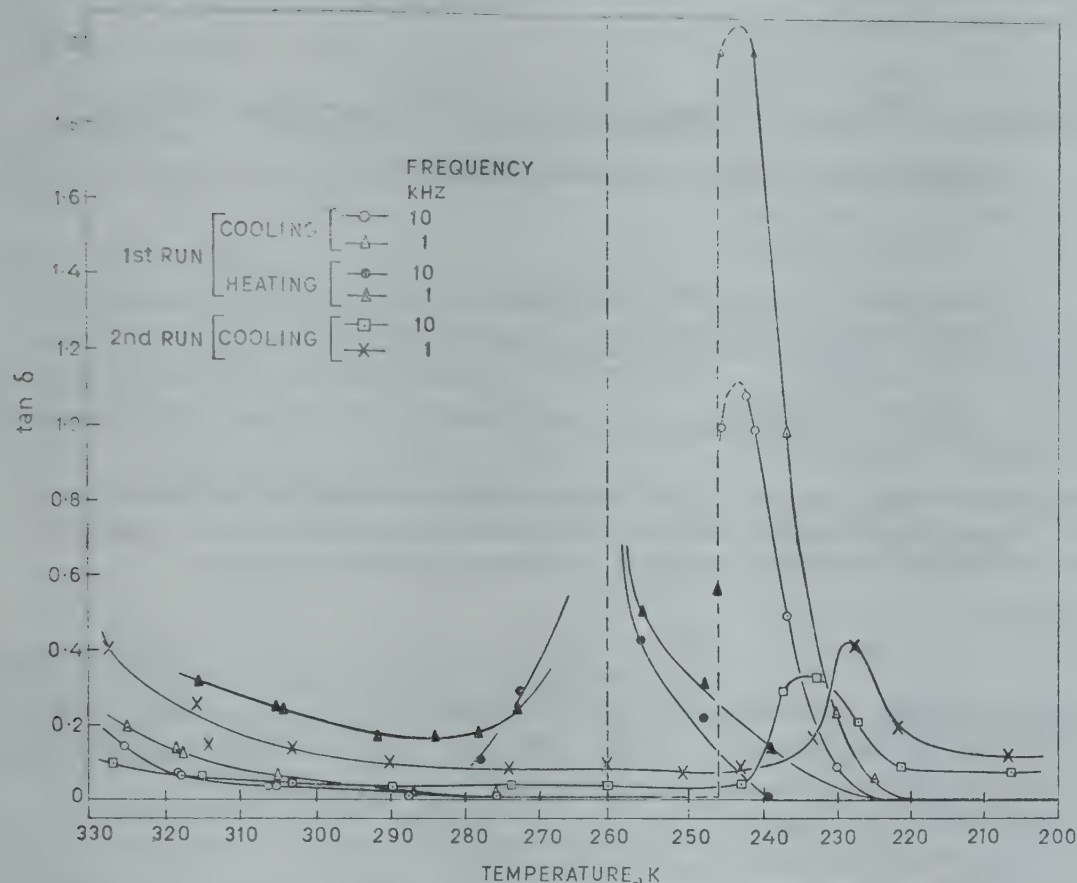


Fig. 3—Temperature variation of $\tan \delta$ for $\text{CoSiF}_6 \cdot 6\text{H}_2\text{O}$

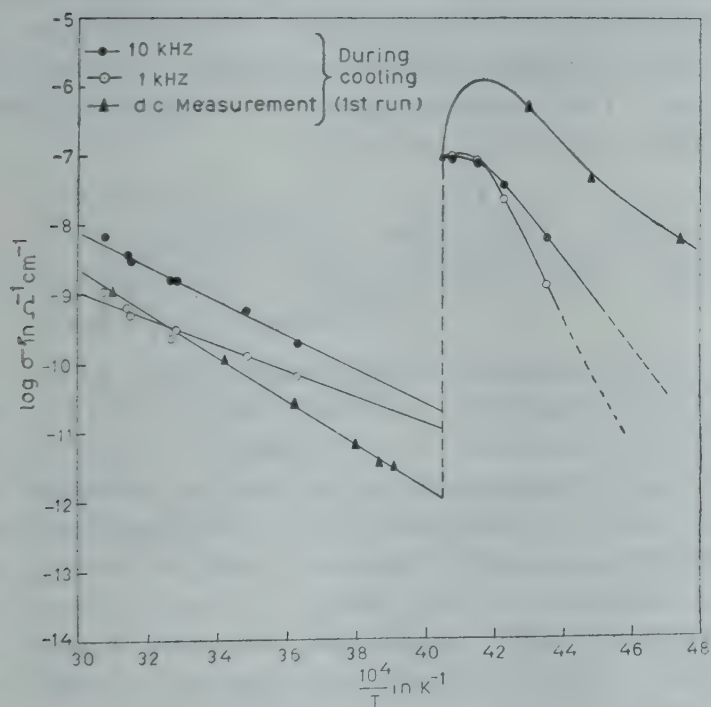


Fig. 4—Temperature variation of ac and dc electrical conductivity for $\text{CoSiF}_6 \cdot 6\text{H}_2\text{O}$

tion reversal before inferring about the nature of this dielectric anomaly.

References

1. Majumdar M & Dutta S K, *J. chem. Phys.*, **42** (1965), 418.
2. Dutta Roy S K & Ghosh B, *J. Phys. Chem. Solids*, **26** (1968), 1511.
3. Ray S, Zalkin A & Templeton D H, *Acta Crystallogr.*, **B**, **29** (1973), 2741.
4. Yablokov Yu V, Zampov V, Zeatdinov M M & Davidovitch R L, *Chem. Phys. Lett.*, **48** (1977), 443.
5. Watanabe T, *J. phys. Soc. Japan*, **20** (1972), 1443.
6. Ghosh B, Chatterjee N, Das A N, Dutta Roy S K & Pal Amitava, *J. Phys. C*, **10** (1977), 1257.
7. Mitra S S, Ghorai S K & Dutta Roy S K (communicated).
8. Makita Y & Sumita M, *J. phys. Soc. Japan*, **31** (1971),
9. Ohshima H & Nakamura E, *J. Phys. Chem. Solids*, **27** (1966), 481.

Prediction of Effective Thermal Conductivity of Two-phase Porous Materials Using Resistor Model

VEERENDRA KUMAR & D R CHAUDHARY

Department of Physics, University of Rajasthan, Jaipur-4

Received 19 July 1979; accepted 3 March 1980

A formula based on resistor model is proposed for the calculation of effective thermal conductivity of a two-phase porous medium. Using three parameters, viz. values of the thermal conductivities of the constituent materials and the porosity, the effective thermal conductivity of a two-phase medium is evaluated.

1. Introduction

The prediction of the effective thermal conductivity of a two-phase medium is of great importance in industry, agriculture and research. Many attempts have been made to obtain relations for the effective thermal conductivity of a two-phase medium; some of the relations are based on rigid mathematical considerations¹ and some are empirical.² Our approach in deriving an expression for predicting the effective thermal conductivity of a two-phase system is based on resistor model.

2. Derivation of Expressions

Consider a two-phase medium made of a solid material (subscript s) and a fluid (subscript f) filling the pore space. The effective thermal conductivity of such a two-phase system will depend upon the thermal conductivities of the constituent material denoted by K_s , K_f , the porosity ϕ , and the volume fraction occupied by the solid $(1-\phi)$. The whole system is assumed to be formed by the columns of solid and fluid in such a way that on fixing the direction of heat flow we obtain the maximum ($K_{||}$) and the minimum (K_{\perp}) values of the effective thermal conductivity. The maximum and minimum values are weighted arithmetic and weighted harmonic mean of constituent phases respectively.

$$K = \phi K_f + (1-\phi) K_s \quad \dots(1)$$

$$K = \left[\frac{\phi}{K_f} + \frac{(1-\phi)}{K_s} \right]^{-1} \quad \dots(2)$$

It is obvious that the effective thermal conductivity of a two-phase system must lie between these two extreme values. An intermediate relation³ corresponds to a weighted geometric mean of K_s and K_f .

$$K = K_f^{\phi} K_s^{(1-\phi)} \quad \dots(3)$$

As this relation does not predict the effective thermal conductivity of a two-phase medium correctly, a different kind of weighted geometric mean was proposed.⁴ This relation is

$$K = K_{||}^n K_{\perp}^{(1-n)} \quad \dots(4)$$

In Eq. (4) it is assumed that n th fraction of the system behaves as if oriented in the direction of the heat flow and the remaining $(1-n)$ th fraction is oriented perpendicular to the direction of the heat flow. The weightage factor n is obtained on substituting $K_{||}$ and K_{\perp} in Eq. (4),

$$n = \frac{\ln \left[\phi \frac{K}{K_f} + (1-\phi) \frac{K}{K_s} \right]}{\ln \left[1 + \phi (1-\phi) \left\{ \frac{K_f}{K_s} + \frac{K_s}{K_f} - 2 \right\} \right]} \quad \dots(5)$$

The maximum and minimum values of n are 1 and 0 respectively. Further letting $\phi \rightarrow 0$ ($K = K_s$ for $n = 1$) and $\phi \rightarrow 1$ ($K = K_f$ for $n = 1$) in Eq. (5) we see that extreme values of n are not obtained as in both the cases the expression becomes divergent. Therefore, using L' Hospital's rule, we obtain a set of conditions in the form of linear differential equations with appropriate boundary conditions (given in parenthesis for each equation) corresponding to the maximum and minimum values of n . These equations are:

$$\frac{K_f}{K_s} = 1 + \frac{1}{K} \frac{\partial K}{\partial \phi} ; \left\{ \begin{array}{l} n = 1 \\ \phi = 0 \\ K = K_s \end{array} \right\} \quad \dots(6)$$

$$\frac{K_s}{K_f} = 1 - \frac{1}{K} \frac{\partial K}{\partial \phi} ; \left\{ \begin{array}{l} n = 1 \\ \phi = 1 \\ K = K_f \end{array} \right\} \quad \dots(7)$$

$$\frac{K_s}{K_f} = 1 - \frac{1}{K} \frac{\partial K}{\partial \phi} ; \left\{ \begin{array}{l} n = 0 \\ \phi = 0 \\ K = K_s \end{array} \right\} \quad \dots(8)$$

$$\frac{K_f}{K_s} = 1 + \frac{1}{K} \frac{\partial K}{\partial \phi} ; \left\{ \begin{array}{l} n = 0 \\ \phi = 1 \\ K = K_f \end{array} \right\} \quad \dots(9)$$

These differential equations can be arranged in two pairs depending upon the K_s/K_f ratio.

2.1. Case (i) : $K_f > K_s$

If the conductivity of the fluid is more than the conductivity of the solid, then Eqs. (7) and (8) are applicable. Using boundary conditions we obtain the following solutions of Eqs. (7) and (8):

$$K_L = K_s e^{\alpha\phi}, \text{ where } \alpha = \left(1 - \frac{K_s}{K_f} \right), \text{ and} \quad \dots(10)$$

$$K_H = K_f e^{-\alpha(1-\phi)} \quad \dots(11)$$

The subscripts L and H are used to demonstrate that Eq. (10) represents the lower value of K and Eq. (11) gives the higher value of K . When ϕ is small, Eq. (10) and when $(1-\phi)$ is less, Eq. (11) reproduce experimental results agreeably. But for a two-phase mixture (where ϕ is between 0.2 and 0.8) a linear combination of K_H and K_L with proper weightage appears to predict K values.

$$K = (1-\phi) K_L + \phi K_H \quad \dots(12)$$

It can be seen that as $\phi \rightarrow 0$, $K \rightarrow K_L$ and similarly as $\phi \rightarrow 1$, $K \rightarrow K_H$.

2.2 Case (ii): $K_s > K_f$

The corresponding differential equations are Eqs. (6) and (9). Under the appropriate boundary conditions the solutions are :

$$K_H = K_s e^{\beta\phi}; \text{ where } \beta = \left(\frac{K_f}{K_s} - 1 \right) \quad \dots(13)$$

$$\text{and } K_L = K_f e^{-\beta(1-\phi)} \quad \dots(14)$$

For a natural two-phase mixture a linear combination of Eqs. (13) and (14) should predict the effective thermal conductivity:

$$K = (1-\phi) K_H + \phi K_L \quad \dots(15)$$

Eqs. (13), (14) and (15) can also be obtained on interchanging ϕ and $(1-\phi)$, and K_s and K_f respectively in Eqs. (10), (11) and (12).

2.3 Woodside-Messmer Condition

Woodside and Messmer⁵ have shown that any relation based on Ohm's law model should satisfy the following condition:

$$\left(\frac{dK}{dK_s} \right)_{K_s=K_f} = (1-\phi) \quad \dots(16)$$

It can be easily seen that Eqs. (10), (11), (13) and (14) along with Eqs. (12) and (15) satisfy the condition.⁵

3. Reproduction of Basic Extremum Relations

Any relation based on resistor model must be capable of reproducing the basic extremum Eqs. (1) and (2). If we expand exponential terms treating α and β as small quantities and neglect second- and higher-order terms, then extremum relations are obtained. It can easily be checked that in both the cases $K_H \rightarrow K_{H1}$ and $K_L \rightarrow K_{L1}$. The intermediate relation [Eq. (3)] is obtained through approximation from any of the four Eqs. (10), (11), (13) and (14).

We have pointed out earlier that K_L and K_H predict only low and high values of K under the extreme conditions $\phi \rightarrow 0$ and $\phi \rightarrow 1$. In order to obtain a formula which remains valid for the entire range of porosity we match the logarithmic derivatives of K_L and K_H . By doing this, we obtain

$$\alpha = \beta = -\ln(K_s/K_f) \quad \dots(17)$$

Table 1 — Calculated and Experimental⁷ Thermal Conductivities of Blood

24°C					37°C				
ϕ	K_{exp} (W/m K)	K_{calc} (W/m K)	% deviation	Average % deviation	ϕ	K_{exp} (W/m K)	K_{calc} (W/m K)	% deviation	Average % deviation
0.97	0.567	0.567	0.00		0.97	0.596	0.596	0.00	
0.92	0.563	0.561	0.36		0.93	0.592	0.591	0.18	
0.89	0.559	0.557	0.34		0.88	0.588	0.586	0.34	
0.82	0.546	0.549	0.54	0.36	0.79	0.580	0.573	1.21	0.5
0.74	0.538	0.539	0.18		0.68	0.567	0.559	1.40	
0.65	0.533	0.529	0.75		0.59	0.546	0.547	0.19	
—	—	—	—		0.56	0.542	0.543	0.19	

Substituting this value of α and β in Eqs. (10) to (15) we find that all these equations reproduce the intermediate relation [Eq. (3)].

4. High K_s/K_f Ratio

For high K_s/K_f ratio, a comparison between values calculated using Eq.(15) and measured values show that the latter are lower than the former. This suggests that in order to get an extrapolation formula for high K_s/K_f ratio we should also have a superposition term obtained by multiplying K_L and K_H . The appropriately weighted root of this term is added or subtracted from Eq. (15). This yields a set of bounds⁶ on higher and lower value of K . For high K_s/K_f ratio, we thus obtain a relation

$$K = (1-\phi)K_H + \phi K_L \pm \phi(1-\phi) \sqrt{K_L K_H} \quad \dots(18)$$

5. Comparison with Experimental Values

Blood is a system for which $K_f/K_s \approx 2$ ($K_f > K_s$). The experimentally measured thermal conductivity data over a wide porosity range at two different temperatures (24°C and 37°C) are available.⁷

Using Eq. (12), we have calculated the thermal conductivity, and the computed values along with experimental values are listed in Table 1. The differences between the calculated and experimentally measured value are not statistically significant.

In Table 2 we have compared the calculated thermal conductivity of copper-solder system using Eqs. (14) and (15) with measured values.⁸ It is clear that when $(1-\phi)$ is small Eq. (14) gives better results than Eq. (15). This should be expected as Eq. (14) is derived for the case $\phi \rightarrow 1$. With increasing $(1-\phi)$ values, the linear combination of K_H and

K_L [Eq. (15)] appears to be giving comparable results with measured values.

We have calculated K of several other two-phase systems using the present formula [Eqs. (12) and (15)]. These K values are listed in Table 3. Comparison of calculated results with measured values indicates that for low K_s/K_f , expressions derived in the present study work reasonably well. With increasing K_s/K_f ratio, computed values are found to deviate from the actual values. Calculated data further show that for low dispersion [for low values of ϕ and $(1-\phi)$] Eq. (13) and Eq. (14) appear to predict K quite satisfactorily even for high K_s/K_f ratio.

In Table 4 we have compared computed thermal conductivity of Rajasthan desert sand using Eq. (18) and measured¹² values. In these calculations we have used the values of α and β given by Eq. (17).

Table 2—Calculated and Measured⁸ Thermal Conductivities of Copper-Solder System ($K_s / K_f = 5.096$)

Porosity ϕ	$K_{exp} (\times 10^2$ W/m K)	$K_{calc} (\times 10^2$ W/m K) using Eq. (14)	$K_{calc} (\times 10^2$ W/m K) using Eq. (15)	% Deviation of K_{calc} using Eq. (15)
0.9876	0.788	0.789	0.801	1.65
0.9864	0.788	0.790	0.813	3.17
0.9714	0.817	0.799	0.828	1.35
0.9493	0.837	0.810	0.863	3.10
0.9004	0.954	0.846	0.954	0.00
0.9805	0.790	0.793	0.813	2.90
0.9737	0.811	0.798	0.825	1.73
0.9714	0.826	0.799	0.828	0.24
0.8971	0.950	0.848	0.960	1.05
0.7623	1.192	0.954	1.233	3.36

Table 3—Comparison of K Values Calculated using Eqs. (12) and (15) with Experimental Data for Two-Phase Systems

System	ϕ	K_s / K_f	W/m °C		% Deviation
			K_{exp}	K_{calc}	
Foresterite/magnesia ⁹	0.868	0.163	2.479	2.479	0.0
Water/petrol solvent ¹⁰	0.8	3.323	0.267	0.276	+3.4
	0.8	3.830	0.205	0.218	-1.1
Water/mineral oil ¹⁰	0.8	4.098	0.234	0.205	-12.4
	0.6	4.098	0.293	0.276	-5.7
Cellosize/flexol plasticizer ¹¹	0.9	3.318	0.191	0.190	-0.5
	0.7	3.318	0.236	0.245	+3.9
	0.9	3.022	0.210	0.215	+2.4
	0.7	3.022	0.257	0.271	+5.7
Cellosize polypropylene glycol ¹¹	0.9	3.735	0.182	0.175	-4.2
	0.7	3.735	0.234	0.231	-1.4
	0.9	3.738	0.180	0.179	-0.66

Table 4—Comparison of the Computed Values with Measured Values of Thermal Conductivity of Rajasthan Desert Sand¹² [$K_s / K_f = 126.98$]

ϕ	K_{exp} (W/m °C)	K_{calc} (W/m °C) using Eq. (18)	% Deviation
0.3850	0.387	0.403	4.1
0.3876	0.375	0.391	4.3
0.4052	0.336	0.357	5.9
0.4297	0.302	0.316	4.4
0.4394	0.312	0.301	3.5
0.4502	0.289	0.285	1.4
0.4600	0.274	0.278	1.4

Mean deviation = 3.6%

The superposition term with negative sign gives good agreement between calculated and measured values. It is in accordance with expectation for the experimental values of this type of disperse material fall on lower bound.

6. Summary of Results

The proposed relations are simple and are more rigorous. For low K_s/K_f ratio, these expressions predict the effective thermal conductivity of a two-phase medium reasonably well. As the ratio K_s/K_f increases, the predicted values are found to deviate from the measured values. When the ratio K_s/K_f increases it is found that for low values of ϕ and $(1-\phi)$ the limiting values K_L and K_H reproduce the measured

values with reasonable accuracy, but the values predicted by a linear combination of K_L and K_H are found to depart from the measured values. However, by adding or subtracting a superposition term, constructed by multiplying K_L and K_H , a set of bounds is obtained even for high K_s/K_f ratio. The experimental values are found to lie between these bounds.

Acknowledgement

The authors are thankful to Prof. R C Bhandari for discussions and encouragement.

References

1. Powers A E, *Res. Dev. Rep.* KAPL-2145 Knolls Atomic Power Laboratory, March 6, 1961.
2. Sugawara A & Yoshizawa Y, *Aust. J. Phys.*, **14** (1961), 469.
3. Litchnecker K, *Phys. Z.*, **27** (1926), 115.
4. Chaudhary D R & Bhandari R C, *J. Phys. D*, (ser 2) **1** (1968), 815.
5. Woodside W & Messmer J M, *J. appl. Phys.*, **32** (1961), 1688.
6. Johansen S, Frost I & Jord N R, **16** (1975), 13.
7. Ahuja A S, *J. appl. Physiol.*, **37** (1974), 765.
8. Lee H J & Taylor R E, *J. appl. Phys.*, **47** (1976), 148.
9. Kingrey W D, *J. Am. ceram. Soc.*, **42** (1959), 617.
10. Knudson J G & Wand R H, *Ind. Engng. Chem.*, **50** (1958), 1667.
11. Nahas N C & Couper J R, *Res. Rep. ser. No. 7*, University of Arkansas, Arkansas, 1966.
12. Chaudhary D R, Agrawal M P & Bhandari R C, *Indian J. pure appl. Phys.*, **7** (1969), 252.

Reduction & Second Quantization of Generalized Electromagnetic Fields for Non-zero Mass System

D C JOSHI & B S RAJPUT

Department of Physics, Garhwal University, Srinagar (Garhwal) U P

Received 1 January 1979; accepted 21 May 1980

Reduction and second quantization of electromagnetic fields associated with spin-1/2 non-zero mass particles carrying electric and magnetic charges have been carried out in terms of Foldy-Shirokov realizations of Poincare group and the expression for field Hamiltonian has been derived.

1. Introduction

Schwinger¹⁻² constructed the quantum field theory of spin- $\frac{1}{2}$ magnetic charge, which is relativistically invariant in consequence of Dirac's³ quantization condition. Zwanziger^{4,5} extended this theory to the fields associated with particles carrying simultaneously the electric and magnetic charges but assumed the existence of controversial⁶ string variables. His theory also does not show the rotational invariance when the gauge field is massive. We^{7,8} have developed in purely group theoretical manner, a gauge invariant and Lorentz covariant quantum field theory for the fields associated with spin-1 particles carrying electric and magnetic charges by assuming the generalized charge on each particle as a complex quantity, the real and imaginary parts of which are the electric and magnetic charges respectively. In the present paper we have extended this work to the reduction and second quantization of generalized electromagnetic fields which consist of a spin-1 transverse field and a longitudinal field produced by spin-1/2 particles of non-zero mass carrying the electric and magnetic charges. Reduced expansions of transverse electromagnetic fields in terms of Foldy⁹-Shirokov¹⁰ realizations of the irreducible representations of the Poincare group have been expressed in terms of two vector potentials and those of longitudinal fields have been expressed in terms of two scalar potentials, the reduced expansions for which have been derived in terms of a wavefunction which transforms as Dirac spinor. Second quantization of generalized electric and magnetic fields has been done in purely relativistic, group theoretical, Lorentz covariant and gauge invariant manner by replacing the amplitudes and their complex conjugates by annihilation and creation operators respectively. Local commutation rules for the transverse and

longitudinal fields and potential operators have been derived. The total field Hamiltonian has also been calculated.

2. Reduction of Generalized Fields in Presence of Non-zero Mass Spin-1/2 Particles

Generalized electric and magnetic fields for non-zero mass system produced by spin- $\frac{1}{2}$ particles carrying generalized charge

$$q = e - ig, \quad \dots(1)$$

where e and g are fundamental electric and magnetic charges, may be considered as consisting of transverse and longitudinal parts in the following manner:

$$\mathbf{E} = \mathbf{E}^T + \mathbf{E}^L \quad \dots(3)$$

and

$$\mathbf{H} = \mathbf{H}^T + \mathbf{H}^L \quad \dots(4)$$

Reduced expansions of \mathbf{E}^T and \mathbf{H}^T in terms of Foldy⁹-Shirokov¹⁰ realizations of irreducible representations of Poincare group have already been derived¹¹ in the following form:

$$\mathbf{E}^T(x) = \frac{i}{4\pi^{3/2}m} \sum_{\epsilon=\pm 1} \epsilon \int d\mathbf{p} [m\mathbf{f}(\epsilon, \mathbf{p})] \exp\{i(\mathbf{p}\cdot\mathbf{x} - \epsilon\omega t)\} \quad \dots(4)$$

and

$$\mathbf{H}^T(x) = \frac{i}{4\pi^{3/2}m} \sum_{\epsilon=\pm 1} m \int \frac{d\mathbf{p}}{\omega(m, \mathbf{p})} \left\{ \mathbf{p} \times \mathbf{f}(\epsilon, \mathbf{p}) \right\} \exp\left\{ i(\mathbf{p}\cdot\mathbf{x} - \epsilon\omega t) \right\} \quad \dots(5)$$

where $\mathbf{f}(m, \mathbf{p})$ is the representation of wavefunction of particle of mass m and spin-1 in the basis characterized by the Hilbert space on which the generators of inhomogeneous Lorentz group operate;

$\hbar(m, \mathbf{p}) = \mathbf{f}^*(m - \mathbf{p})$; $x = (\mathbf{x}, t)$; $c = \hbar = 1$; and $\omega(m, \mathbf{p}) = \omega = (m^2 + p^2)^{1/2}$ and ϵ is the sign of energy. These reductions of fields mean their expansions in terms of complex functions $\mathbf{f}(\epsilon, \mathbf{p})$ belonging to various values of ϵ , where the momentum vector \mathbf{p} has the components p_i ($i = 1, 2, 3$) each of which takes on the values from $-\infty$ to ∞ . Such reductions are based on the observation that infinitesimal generators associated with the transformations of wavefunction describing the fields satisfy the same commutation rules as satisfied by the infinitesimal generators of proper, orthochronous, inhomogeneous Lorentz group. Reduced expansions (4) and (5) are conveniently derived in the linear momentum basis in which the components of linear momentum operator are diagonal. In general, the set of functions $\mathbf{f}(\epsilon, \mathbf{p}, \lambda)$, where λ , the discrete variable runs through $(2s + 1)$ values (s being the spin of particle of mass m), constitutes the representation of the states of a Hilbert space. The linear product of two states

$|\psi\rangle$ and $|\psi^1\rangle$ of this space is defined as

$$\langle \psi^1 | \psi \rangle = \sum_{\lambda} \int \mathbf{f}^{1*}(\mathbf{p}, \lambda) \cdot \mathbf{f}(\mathbf{p}, \lambda) \frac{d\mathbf{p}}{\omega(\mathbf{p})} \quad \dots(6)$$

and the state $A|\psi\rangle$ is represented by

$$(A\mathbf{f})(\mathbf{p}, \lambda) = \tilde{A}\mathbf{f}(\mathbf{p}, \lambda) \quad \dots(7)$$

where A is any infinitesimal generator of inhomogeneous Lorentz group and \tilde{A} is the corresponding infinitesimal generator in the basis characterized by the space of the function in Hilbert space.

The transverse parts \mathbf{E}^T and \mathbf{H}^T satisfy the ordinary Maxwell's equations in presence of electric current density $\mathbf{j}_1(x)^{11}$, which we call the intrinsic current. Vanishing of charge source density in Maxwell's equations for transverse fields leads to the condition

$$\mathbf{p} \cdot \mathbf{f}(\epsilon, \mathbf{p}) = 0 \quad \dots(8)$$

Longitudinal parts \mathbf{E}^L and \mathbf{H}^L of the generalized fields may be written in the following form in terms of electric and magnetic scalar potentials ϕ_e and ϕ_g respectively:

$$\mathbf{E}^L = -\nabla \phi_e \quad \dots(9)$$

and

$$\mathbf{H}^L = -\nabla \phi_g \quad \dots(10)$$

The potentials ϕ_e and ϕ_g may be written in terms of four-component Dirac field $\psi_{1/2}$ produced by spin- $\frac{1}{2}$ particles carrying electric and magnetic charges:

$$\phi_e(\mathbf{x}) = e \int D(\mathbf{x} - \mathbf{x}') \bar{\psi}_{1/2}(\mathbf{x}') \gamma_4 \psi_{1/2}(\mathbf{x}') d\mathbf{x}' \quad \dots(11)$$

and

$$\phi_g(\mathbf{x}) = g \int D(\mathbf{x} - \mathbf{x}') \bar{\psi}_{1/2}(\mathbf{x}') \gamma_4 \psi_{1/2}(\mathbf{x}') d\mathbf{x}' \quad \dots(12)$$

where γ_4 is the fourth Dirac matrix, bar denotes adjoint and the function $D(\mathbf{x} - \mathbf{x}')$ is given by

$$D(\mathbf{x} - \mathbf{x}') = \frac{1}{(2\pi)^3} \int \frac{d\mathbf{p}}{\omega'^2} \exp\{i\mathbf{p} \cdot (\mathbf{x} - \mathbf{x}')\} \quad \dots(13)$$

Using the reduced expansions¹¹ for $\psi_{1/2}(\mathbf{x})$ in terms of irreducible representations of Poincare group, we get following reductions for the scalar potentials:

$$\begin{aligned} \phi_e(x) = & \frac{e}{(2\pi)^3} \int \frac{d\mathbf{p}}{\omega'^3} [f(m', \mathbf{p}) \exp\{i(\mathbf{p} \cdot \mathbf{x} - \omega' t)\} \\ & + h^*(m', \mathbf{p}) \exp\{-i(\mathbf{p} \cdot \mathbf{x} - \omega' t)\}] \end{aligned} \quad \dots(14)$$

and

$$\begin{aligned} \phi_g(x) = & \frac{g}{(2\pi)^3} \int \frac{d\mathbf{p}}{\omega'^3} [f(m', \mathbf{p}) \exp\{i(\mathbf{p} \cdot \mathbf{x} - \omega' t)\} \\ & + h^*(m', \mathbf{p}) \exp\{-i(\mathbf{p} \cdot \mathbf{x} - \omega' t)\}] \end{aligned} \quad \dots(15)$$

where m' is the mass of spin- $\frac{1}{2}$ particle, $\omega' = (m'^2 + p^2)^{1/2}$. In Eqs. (14) and (15), $f(m', \mathbf{p})$ and $h^*(m', \mathbf{p})$ are the representations of wavefunctions of scalar fields (for both the signs of energy) in the space upon which the infinitesimal generators of inhomogeneous Lorentz group operate. Substituting Eqs. (14) and (15) into Eqs. (9) and (10) respectively, we get the following reduced expansions for \mathbf{E}^L and \mathbf{H}^L :

$$\begin{aligned} \mathbf{E}^L(\mathbf{x}) = & -\frac{ie}{8\pi^3} \int \frac{d\mathbf{p}}{\omega'^3} \mathbf{p} [f(m', \mathbf{p}) \\ & \exp\{i(\mathbf{p} \cdot \mathbf{x} - \omega' t)\} - h^*(m', \mathbf{p}) \exp\{-i(\mathbf{p} \cdot \mathbf{x} - \omega' t)\}] \end{aligned} \quad \dots(16)$$

and

$$\begin{aligned} \mathbf{H}^L(\mathbf{x}) = & -\frac{ig}{8\pi^3} \int \frac{d\mathbf{p}}{\omega'^3} \mathbf{p} [f(m', \mathbf{p}) \exp\{i(\mathbf{p} \cdot \mathbf{x} - \omega' t)\} \\ & - h^*(m', \mathbf{p}) \exp\{-i(\mathbf{p} \cdot \mathbf{x} - \omega' t)\}] \end{aligned} \quad \dots(17)$$

from which it is obvious that longitudinal fields \mathbf{E}^L and \mathbf{H}^L are proportional to e and g respectively and in the absence of electric and magnetic charges corresponding longitudinal field vanishes.

The transverse parts of the electromagnetic fields may also be written in the following manner in terms of transverse vector potentials \mathbf{A}^T and \mathbf{B}^T :

$$\mathbf{H}^T = \nabla \times \mathbf{A}^T \quad \dots(18)$$

and

$$\mathbf{E}^T = -\nabla \times \mathbf{B}^T \quad \dots(19)$$

Using the Eqs. (4), (5) and (8) the reduced expansions for \mathbf{A}^T and \mathbf{B}^T may be written as follows:

$$\begin{aligned} \mathbf{A}^T(\mathbf{x}) = & \frac{1}{4\pi^{3/2}} \int \frac{d\mathbf{p}}{\omega} [\mathbf{f}(\mathbf{p}) \exp\{i(\mathbf{p} \cdot \mathbf{x} - \omega t)\} \\ & + \mathbf{h}^*(\mathbf{p}) \exp\{-i(\mathbf{p} \cdot \mathbf{x} - \omega t)\}] \end{aligned} \quad \dots(20)$$

and

$$B^T(\mathbf{x}) = \frac{1}{4\pi^{3/2}} \int \frac{d\mathbf{p}}{p^2} [\{\mathbf{p} \times \mathbf{f}(\mathbf{p})\} \exp \{i(\mathbf{p} \cdot \mathbf{x} - \omega t)\} + \{\mathbf{p} \times \mathbf{h}^*(\mathbf{p})\} \exp \{-i(\mathbf{p} \cdot \mathbf{x} - \omega t)\}] \quad \dots(21)$$

The generalized electric field $\mathbf{E}(\mathbf{x})$ and generalized magnetic field $\mathbf{H}(\mathbf{x})$, may therefore, be described by the two four-potentials $\{B_\mu\} = \{B^T, i\phi_e\}$ and $\{A_\mu\} = \{A^T, i\phi_g\}$ respectively.

The components of generalized electric and magnetic four-currents j_μ and k_μ associated with spin- $\frac{1}{2}$ particles carrying electric and magnetic charges may be written as

$$j_\mu = e \bar{\psi}_{1/2}(\mathbf{x}) \gamma_\mu \psi_{1/2}(\mathbf{x}) \quad (22)$$

and

$$k_\mu = g \bar{\psi}_{1/2}(\mathbf{x}) \gamma_\mu \psi_{1/2}(\mathbf{x}) \quad \dots(23)$$

respectively. Using the reduction of $\psi_{1/2}(\mathbf{x})$ ¹² in these equations, we get the following reduced expansions for electromagnetic charge and current source densities:

$$j_0(\mathbf{x}) = \frac{e}{(2\pi)^3} \int \frac{d\mathbf{p}}{\omega'} [f(m', \mathbf{p}) \exp \{i(\mathbf{p} \cdot \mathbf{x} - \omega' t)\} + h^*(m', \mathbf{p}) \exp \{-i(\mathbf{p} \cdot \mathbf{x} - \omega' t)\}] \quad (24)$$

and

$$\mathbf{j}(\mathbf{x}) = \frac{e}{(2\pi)^3} \int \frac{d\mathbf{p}}{\omega'^2} \mathbf{p} [f(m', \mathbf{p}) \exp \{i(\mathbf{p} \cdot \mathbf{x} - \omega' t)\} + h^*(m', \mathbf{p}) \exp \{i(\mathbf{p} \cdot \mathbf{x} - \omega' t)\}] \quad \dots(25)$$

and similar expressions for $k_0(\mathbf{x})$ and $\mathbf{k}(\mathbf{x})$ with e replaced by g .

For Eqs. (24) and (25) we can readily verify the equation of continuity

$$\partial_\mu j_\mu = 0 \text{ and } \partial_\mu k_\mu = 0 \quad \dots(26)$$

From Eqs. (24) and (25) we can observe the proportionality of charge and current source densities with fundamental electric and magnetic charges respectively.

Maxwell's field equations for generalized electric and magnetic fields for non-zero mass system in the presence of electric and magnetic four-currents j_μ and k_μ may be written in the following forms:

$$\nabla \cdot \mathbf{E} = j_0, \nabla \times \mathbf{E} = -\frac{\partial \mathbf{H}}{\partial t} - \mathbf{k} \quad \dots(27)$$

and

$$\nabla \cdot \mathbf{H} = k_0, \nabla \times \mathbf{H} = -\frac{\partial \mathbf{E}}{\partial t} - \mathbf{j} - \mathbf{j}_1 \quad \dots(28)$$

where $\mathbf{j}_1(\mathbf{x})$ is the intrinsic current density, inclusion of which is necessary¹¹ for the reduction of electromagnetic fields for non-zero mass system. Its reduced expansion has been derived¹¹ in the following form:

$$\mathbf{j}_1(\mathbf{x}) = -\frac{m^2}{4\pi^{3/2}} \left[\int \frac{d\mathbf{p}}{\omega} \left\{ \mathbf{f}(\mathbf{p}) \exp \{i(\mathbf{p} \cdot \mathbf{x} - \omega t)\} + h^*(\mathbf{p}) \exp \left\{ -i(\mathbf{p} \cdot \mathbf{x} - \omega t) \right\} \right\} \right] \quad \dots(29)$$

3. Second Quantization

We get the second quantized reduced expansions for the transverse operators of fields and potentials by replacing the function $\mathbf{f}(\mathbf{p})$ and $\mathbf{h}^*(\mathbf{p})$ in the reduced expansions (4), (5), (20), (21) by annihilation and creation operators of spin-1 particles with non-zero mass. Similarly replacing the functions $f(m', \mathbf{p})$ and $h(m', \mathbf{p})$ in equations (16), (17) by annihilation operators and their complex conjugates by creation operators of positive and negative energy particles in scalar field, the second quantized reduced expansions for longitudinal field and potential operators may be obtained. The second quantized expansions for field and potential operators are Lorentz covariant¹³ and gauge invariant because, for non zero mass system, the requirement of reduction of wavefunction associated with the field under consideration is that one gets the expansions for $A\psi(\mathbf{x})$ on replacing every $\mathbf{f}(\mathbf{p})$ by $\tilde{A}\mathbf{f}(\mathbf{p})$ in the reduced expansion where \tilde{A} is any infinitesimal generator of inhomogeneous

Lorentz group and \tilde{A} is the corresponding infinitesimal generator in the basis characterizing the Hilbert space. Further, we may have second quantized operators $[A]$ corresponding to any infinitesimal generator \tilde{A} for the reduced expansions of field and potential operators and it may be shown that these second-quantized operators also constitute a representation of infinitesimal generators of inhomogeneous Lorentz group in the second quantized theory.

Using the second-quantized reduced expansions and assuming the Bose statistics for the annihilation and creation operators $\hat{f}(\mathbf{p})$, $\hat{h}^*(\mathbf{p})$ associated with spin-1 particles and $\hat{f}(m', \mathbf{p})$, $\hat{h}^*(m', \mathbf{p})$ associated with scalar field, the following equal time commutation relations may be obtained:

$$\begin{aligned} [\hat{A}_i^T(\mathbf{x}), \hat{B}_j^T(\mathbf{x}')] &= [\hat{B}_j^T(\mathbf{x}), \hat{B}_j^T(\mathbf{x}')] \\ &= [\hat{A}_i^T(\mathbf{x}), \hat{B}_j^{T*}(\mathbf{x}')] = [\hat{B}_i^T(\mathbf{x}), \hat{B}_j^{T*}(\mathbf{x}')] \\ &= [\hat{B}_i^{T*}(\mathbf{x}), \hat{B}_j^{T*}(\mathbf{x}')] = 0 \end{aligned} \quad \dots(30a)$$

$$[\hat{E}_i^T(\mathbf{x}), \hat{H}_j^T(\mathbf{x}')] = [\hat{E}_i^T(\mathbf{x}), \hat{E}_j^T(\mathbf{x}')] = 0 \quad \dots(30b)$$

$$\left[\hat{E}_i^T(\mathbf{x}), \hat{E}_j^{T*}(\mathbf{x}') \right] i \omega^2 \Delta(\mathbf{x} - \mathbf{x}') \quad \dots(30c)$$

$$\left[\hat{E}_i^T(\mathbf{x}), \hat{B}_j^{T*}(\mathbf{x}') \right] = 0 \quad \dots(30d)$$

$$\left[\hat{E}_i^T(\mathbf{x}), \hat{A}_j^{T*}(\mathbf{x}') \right] = i \delta_{ij} \delta(\mathbf{x} - \mathbf{x}') \quad \dots(30e)$$

$$\left[\hat{E}_i^L(\mathbf{x}), \hat{E}_j^L(\mathbf{x}') \right] = \left[\hat{H}_i^L(\mathbf{x}), \hat{H}_j^L(\mathbf{x}') \right] = 0 \quad \dots(30f)$$

$$\left[\hat{E}_i^L(\mathbf{x}), \hat{E}_j^{L*}(\mathbf{x}') \right] = -\frac{ie}{4\pi^3} \frac{\nabla_i \nabla_j}{\omega^4} \Delta(\mathbf{x} - \mathbf{x}') \delta_{ij} \quad \dots(30g)$$

and

$$\left[\hat{H}_i^L(\mathbf{x}), \hat{H}_j^{L*}(\mathbf{x}') \right] = -\frac{ig}{4\pi^3} \frac{\nabla_i \nabla_j}{\omega^4} \Delta(\mathbf{x} - \mathbf{x}') \delta_{ij} \quad \dots(30h)$$

where

$$\Delta(\mathbf{x} - \mathbf{x}') = \frac{1}{(2\pi)^3} \int \frac{d\mathbf{p}}{\omega} \sin \mathbf{p} \cdot (\mathbf{x} - \mathbf{x}')$$

and other symbols have their usual meanings.

The Hamiltonian density $H(\mathbf{x})$ of the second-quantized generalized electromagnetic field may be written as follows¹³ in terms of the components of generalized four-potential operator,

$$V_\mu = A_\mu - iB_\mu = \{A^T - iB^T, i(\phi_e - i\phi_g)\};$$

$$H(\mathbf{x}) = \frac{1}{2} \left[\sum_{\mu=0}^3 \left\{ \hat{V}_\mu^{\mu*}(\mathbf{x}) \cdot \hat{V}_\mu(\mathbf{x}) + \nabla \hat{V}_\mu^{\mu*}(\mathbf{x}) \cdot \nabla \hat{V}_\mu(\mathbf{x}) \right\} + \sum_{j=1}^3 m^2 \hat{V}_j^{\mu*}(\mathbf{x}) \hat{V}_j(\mathbf{x}) + m'^2 \hat{V}_0^{\mu*}(\mathbf{x}) \hat{V}_0(\mathbf{x}) \right] \quad \dots(31)$$

Using the Eqs. (14), (15), (20), (21) and (31) and carrying out the volume integration, we get the following expression for total field Hamiltonian:

$$\mathcal{H} = \frac{q^* q}{8\pi^3} \int \frac{d\mathbf{p}}{\omega'^4} \left[\mathbf{f}^*(m', \mathbf{p}) \cdot \mathbf{f}(m', \mathbf{p}) + h(m', \mathbf{p}) \cdot h^*(m', \mathbf{p}) \right] + \int \frac{d\mathbf{p}}{2p^2} (\omega^2 + p^2) \left[\mathbf{f}^*(m, \mathbf{p}) \cdot \mathbf{f}(m, \mathbf{p}) + \mathbf{h}(m, \mathbf{p}) \cdot \mathbf{h}^*(m, \mathbf{p}) \right] \quad \dots(32)$$

which may also be written as

$$\mathcal{H} = \mathcal{H}_\gamma + \mathcal{H}_I$$

where \mathcal{H}_γ , the free field Hamiltonian is given by

$$\mathcal{H}_\gamma = \int d\mathbf{p} [\mathbf{f}^*(m, \mathbf{p}) \cdot \mathbf{f}(m, \mathbf{p}) + \mathbf{h}(m, \mathbf{p}) \cdot \mathbf{h}^*(m, \mathbf{p})] \quad \dots(33)$$

and \mathcal{H}_I is the interaction Hamiltonian,

$$\mathcal{H}_I = \frac{q^* q}{8\pi^3} \int \frac{d\mathbf{p}}{\omega'^4} \left[\mathbf{f}^*(m', \mathbf{p}) \cdot \mathbf{f}(m', \mathbf{p}) + h(m', \mathbf{p}) \cdot h^*(m', \mathbf{p}) \right] + \frac{m^2}{2} \int \frac{d\mathbf{p}}{p^2} \left[\mathbf{f}^*(m, \mathbf{p}) \cdot \mathbf{f}(m, \mathbf{p}) + \mathbf{h}(m, \mathbf{p}) \cdot \mathbf{h}^*(m, \mathbf{p}) \right] \quad \dots(34)$$

The expression for interaction Hamiltonian given by Eq. (34), may also be obtained by using the following Hamiltonian density:

$$H_I(\mathbf{x}) = J_\mu \cdot V_\mu^* \quad \dots(35)$$

where the components of generalized four-current vector $J_\mu(\mathbf{x})$ are given by

$$J_0(\mathbf{x}) = j_0 - i k_0$$

and

$$\mathbf{J}(\mathbf{x}) = \mathbf{j} + \mathbf{j}_1 - i \mathbf{k} \quad \dots(36)$$

Using the second-quantized reduced expansions of V_μ and J_μ and carrying out the volume integration, Hamiltonian density given by Eq. (35) leads to the expression (34) for interaction Hamiltonian.

4. Discussion

Reduced expansions (16), (17) show the symmetry between the longitudinal components of generalized electric and magnetic fields, either of which is zero only when corresponding charge on the particles vanishes. It has been shown by Eqs. (9), (10), (18) and (19) that two, four-potentials are needed to describe the generalized electromagnetic fields produced by the particles carrying generalized charges. The proportionality of longitudinal components of these potentials with electric and magnetic charge and current source densities has been shown by Eqs. (14), (15), (24) and (25) in terms of electric and magnetic charges.

Purely group theoretical method has been used for the second quantization of the generalized electromagnetic fields in terms of physical annihilation and creation operators and nowhere any hypothetical superposition of states has been used. It is noteworthy that if any of the reduced expansions given by Eqs. (4), (5); (14), (15); (16), (17) and (20), (21); are operated by any operator \hat{A} out of the infinitesimal generators of Poincare group, we get a similar expansion except that $\mathbf{f}(\mathbf{p})$ and $\mathbf{h}(\mathbf{p})$ are replaced by $\tilde{A} \mathbf{f}(\mathbf{p})$ and $\tilde{A} \mathbf{h}(\mathbf{p})$, where \tilde{A} is the finite, spin infinitesimal generator of unitary ray representation of Poincare group and therefore no gauge term appears in these operations. It shows

that the theory of second quantization developed here is gauge invariant. Commutation rules derived here for the transverse fields are local ones, contrary to those derived by Zwanziger.⁴

The expression for Hamiltonian \mathcal{H}_γ given by Eq. (33) is the usual one derived earlier,¹³ for the free electromagnetic fields for non-zero mass system. The interaction Hamiltonian given by Eq. (34) has been shown to be derivable from Eq. (35), which shows that there is interaction of intrinsic current $\mathbf{j}_1(x)$ with the vector potentials, while the interaction of \mathbf{j}_μ with vector potentials is vanishing. Thus due to the presence of intrinsic current in non-zero mass case the interaction Hamiltonian does not vanish even if the charges are zero. This behaviour is contrary to the zero mass case,¹⁴ where no intrinsic current or charge source density was essential for the reduction of electromagnetic field.

References

1. Schwinger J, *Phys. Rev.*, **144** (1966), 1087.
2. Schwinger J, *Phys. Rev.*, **151** (1966), 1048.
3. Dirac P A M, *Proc. R. Soc.*, **A133** (1931), 60.
4. Zwanziger D, *Phys. Rev.*, **176** (1968), 1489.
5. Zwanziger D, *Phys. Rev.*, **D3** (1971), 880.
6. Peres A, *Phys. Rev.*, **167** (1968), 1449.
7. Rajput B S & Prakash Om, *Indian J. Phys.*, **50** (1976), 929.
8. Rajput B S & Prakash Om, *Indian J. pure appl. Phys.*, **16** (1978), 593.
9. Foldy L L, *Phys. Rev.*, **102** (1956), 568.
10. Shirokov Yu M, *Soviet Phys. JETP*, **13** (1961), 240.
11. Rajput B S, *Nuovo Cim. Lett.*, **2** (1971), 712.
12. Moses H E, *J. math. Phys.*, **8** (1967), 1134.
13. Rajput B S & Prakash Om, *Indian. J. Phys.*, **48** (1974), 215.
14. Joshi D C & Rajput B S, *Indian J. Phys.*, (1978), in press.

An Investigation of the Electron Cyclotron Resonance Line Shape in Transient Afterglow Plasmas of Neon & Argon

A P KABILAN*

Plasma Physics Laboratory, Patrice Lumumba University, Moscow W-302, USSR

Received 27 October 1979

Variations of the electron-atom collision frequency and the electron density with time in neon and argon afterglow plasmas have been deduced from the measurements of the height and the width of electron cyclotron resonance lines in the time interval of 20-300 μ sec after discharge cut-off. The time dependence curves of the electron temperature in the afterglows have been obtained from the experimental variations of the collision frequency.

1. Introduction

The obtaining of a weakly ionized gas with electron temperature less than 1000 K (down to cryogenic temperatures) is of much interest for electron-atom interaction studies at energies lower than 0.1 eV. An afterglow plasma, in which the electron temperature rapidly relaxes to the neutral temperature and the electron density falls relatively slowly, could be a suitable object for these purposes. However, the processes of relaxation and deionization in a decaying plasma have not been studied thoroughly. The present paper reports measurements of the rates of cooling of electrons and deionization in transient afterglow plasmas of neon and argon by studying the electron cyclotron resonance (ECR) line shape.

2. Theory

Let us consider a weakly ionized gas in a dc magnetic field and a perpendicular high-frequency electric field with amplitude E and angular frequency ω . The average power (\bar{P}) absorbed by the electrons from the microwave in the case of constant mean free time has been calculated by Kelly *et al.*¹ as:

$$\bar{P} = \frac{ne^2E^2}{m} \left[\frac{\nu_c}{\nu_c^2 + (\omega - \omega_B)^2} + \frac{\nu_c}{\nu_c^2 + (\omega + \omega_B)^2} \right] \quad \dots(1)$$

where n is the electron density, e , m are the electron charge and mass respectively ν_c the electron-atom collision frequency and ω_B the Larmor frequency. The usual assumption for cyclotron resonance $\omega_B \gg \nu_c$ simplifies Eq. (1) to:

$$\bar{P} = \frac{ne^2E^2}{m} \frac{\nu_c}{\nu_c^2 + (\omega - \omega_B)^2} \quad \dots(2)$$

From Eq. (2) it follows that \bar{P} as a function of ω has a half-width $\Delta\omega$ equal to ν_c . Experimental results in support of this have been reported by Kelly *et al.*¹ for the case of hydrogen at average electron-energies above 3-4 eV, when the collision frequency is practically independent of the electron velocity. It has also been found by Kelly *et al.*³ that the ECR line shape is not very sensitive to the velocity dependence of the collision frequency and that the equality of $\Delta\omega = \nu$ is practically valid even in this case. The validity of Eq. (2) is enhanced considerably, if the electron velocity distribution function is Maxwellian, as is the case when the cyclotron heating of the electrons is insignificant. This can easily be seen from the derivation leading to Eq. (32) in the work of Kelly *et al.*¹ or Eq. (1) of the present study. The half-width of the absorption line in this case gives a direct measure of the effective collision frequency.

The power absorbed at resonance $\omega = \omega_B$, follows from Eq. (2), as

$$\bar{P}_r = \frac{ne^2E^2}{m} \frac{1}{\nu} \quad \dots(3)$$

It can be easily seen that the normalized electron density may be deduced from the measurement of the height and the width of the ECR lines:

$$\frac{n}{n_0} = \frac{\bar{P}_r}{\bar{P}_{r0}} \frac{\nu}{\nu_0} \quad \dots(4)$$

3. Apparatus and Procedure

The general arrangement of the experimental system is sketched in Fig. 1. The discharge was powered by a pulsed ($\tau_d = 40 \mu$ sec) 40 MHz-40 W oscillator

*Present address: 1114 Ponnappillai Lane, East Street, Thanjavur, Tamil Nadu.

through two symmetrical external ring electrodes. The discharge tube 15mm in diameter intersected the waveguide, placed between the magnet poles 8 cm in diameter. The gap between the poles was adjustable and the magnetic field could be varied by upto ± 100 gauss around the resonance value 1080 gauss. The waveguide assembly was made up of standard S-band waveguides 72×34 mm. In order to provide enough space for the manipulation of the magnet poles and ensure reasonable field homogeneity along the plasma sample, the working section of the waveguide was narrowed to 52×20 mm and filled with a dielectric so that the impedance was restored to the original value. The estimated field non-homogeneity was about 0.5%. The sensing microwave was generated by a pulsed ($\tau_s = 0.2 \mu\text{sec}$) 3GHz-10 mW clystron. A standing wave was formed in the line in such a way that the sample was located in the region of maximum electric field. The delay of the sensing microwave pulse with respect to the discharge pulse was varied between 20 and 300 μsec and each time the ECR line was registered by varying the magnetic field.

During the interaction of the sensing microwave with plasma, the electron temperature could safely be considered to be constant. From previous studies² it is known that after a lapse of 15-20 μsec from the moment of discharge cut-off, the electron velocity distribution function becomes Maxwellian excepting in a small velocity interval $0-V_0$, where V_0 corresponds to the maximum of the distribution function. The power of the sensing wave (E) was chosen such that the following condition was fulfilled.³

$$E^2 \ll \frac{2 m W_m}{c^2 \tau_s \nu} \frac{[(\omega - \omega_B)^2 + \nu^2]}{\omega^2 + \omega_B^2 + \nu^2} \quad (5)$$

where W_m is the average electron energy. This means that the increment of average electron energy due to the cyclotron heating is not considerable and hence

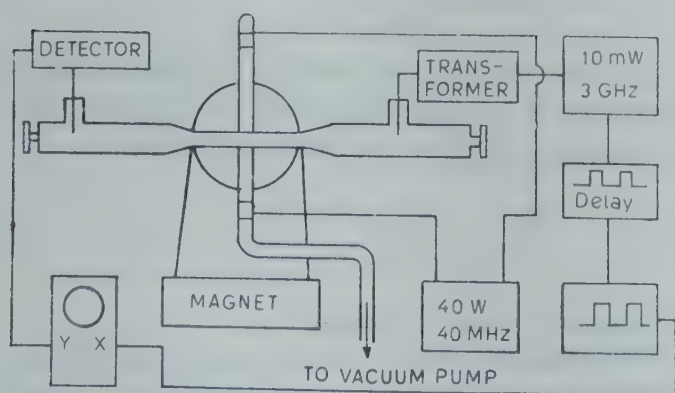


Fig. 1—Experimental set-up

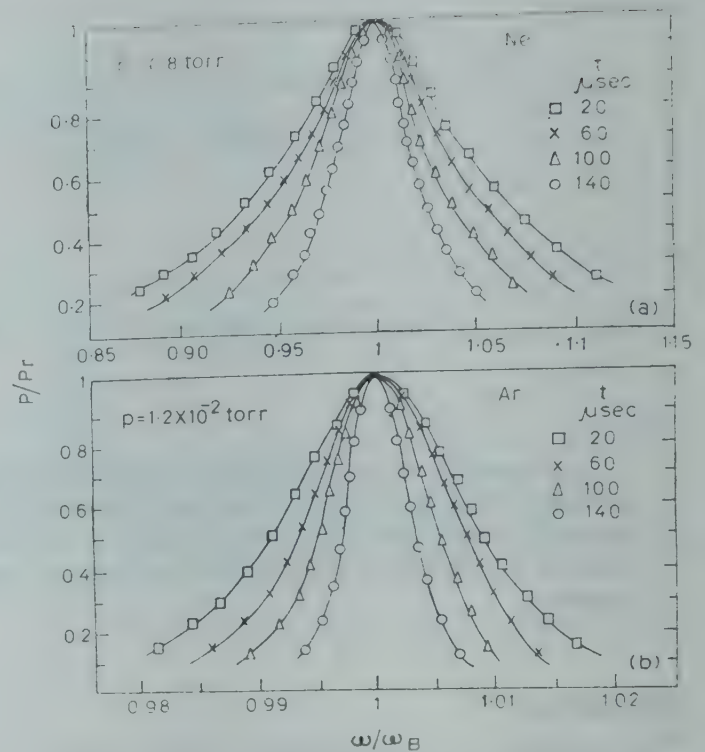


Fig. 2—Evolution of ECR lines in a neon afterglow (a) and in an argon afterglow (b)

does not alter the electron velocity distribution. Thus the experimental conditions were chosen so as to ensure a Maxwellian electron velocity distribution function.

4. Results

Figs. 2(a) and (b) show the ECR lines registered at various moments after the discharge cut-off in neon and argon. It can be noted that the cyclotron absorption curve narrows with time. This testifies to the monotonical decrease of the effective collision frequency as the electron temperature falls (in the temperature range investigated). As was assumed, every ECR line is governed by Eq. (2). Fig. 3(a) shows the time dependence of the effective electron-neutral collision frequency (ν_{eff}) in the neon afterglow, deduced from the measurements of the half-width of ECR lines. Similar results for argon are presented in Fig. 3(b). It can be seen that in both the cases, at higher pressures, ν_{eff} falls approximately exponentially and at lower pressures, a sharp fall is noted first, after which ν_{eff} decreases relatively slowly. Comparison of these results with the available experimental data³ on temperature dependence of ν_{eff} shows that the rapid fall corresponds to the temperature interval 10-4 eV in the case of neon and 9-2 eV in the case of argon. At these energies, considerable role is played by inelastic collisions and diffusion loss of fast electrons and hence the average electron energy falls rapidly.

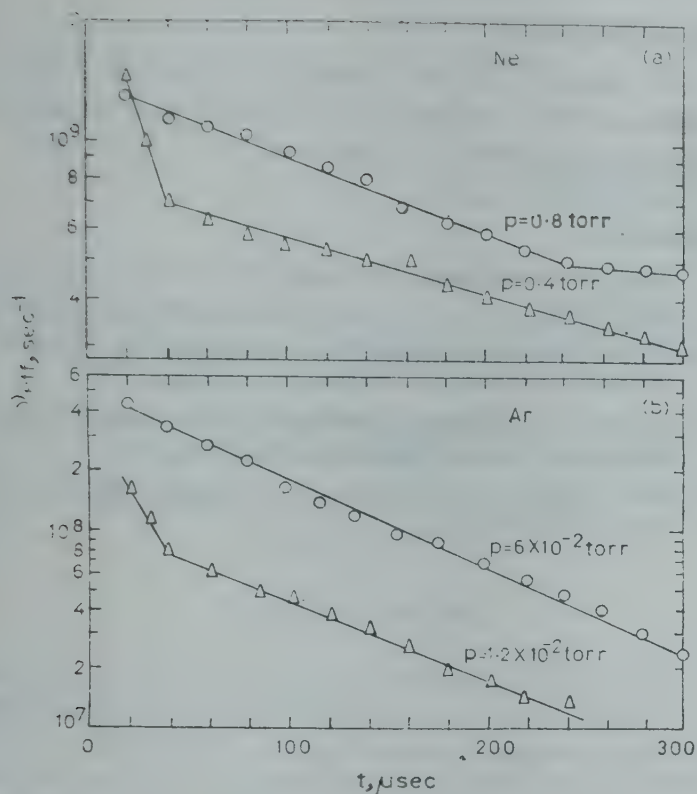


Fig. 3—Experimental variations of the effective collision frequency (ν_{eff}) with time, deduced from ECR line width at various moments in the neon afterglows (a) and in the argon afterglows (b)

The balance equation for electron temperature is as known

$$\frac{\partial T_e}{\partial t} = -x \nu_{\text{eff}} (T_e - T_a) \quad \dots (6)$$

where T_a is the neutral particle temperature and x denotes the fraction of energy transferred during one collision. In the case of purely elastic collisions; $x = 2m/M$, where M is the heavy particle mass. Integrating Eq. (6) with ν_{eff} as the function of time, we get

$$T_e = T_a + (T_{e0} - T_a) \exp \left[- \int_0^t x \nu_{\text{eff}}(t) dt \right] \quad \dots (7)$$

where T_{e0} is the initial electron temperature. Thus measurements of ν_{eff} as a function of time would enable us to determine the time dependence of the normalized electron temperature $[T_e(t) - T_a / T_{e0} - T_a]$. Measuring the initial temperature T_{e0} , we can evaluate $T_e(t)$. Combining now $\nu_{\text{eff}}(t)$ and $T_e(t)$ we can get the temperature dependence of the collision frequency $\nu_{\text{eff}}(T_e)$. Figs. 4(a) and (b) depict the electron temperature variations with time, calculated by the above mentioned method for neon and argon respectively. In the present study, the initial temperatures were not measured; instead their values were determined from the available $\nu_{\text{eff}}(T_e)$ data.

The variations of the normalized electron density with time, deduced from the measurements of the height and the width of ECR lines using formula (4), are presented in Fig. 5.

Conclusion

The ECR method, adopted in this work may be used for studies of decaying plasmas as well as for

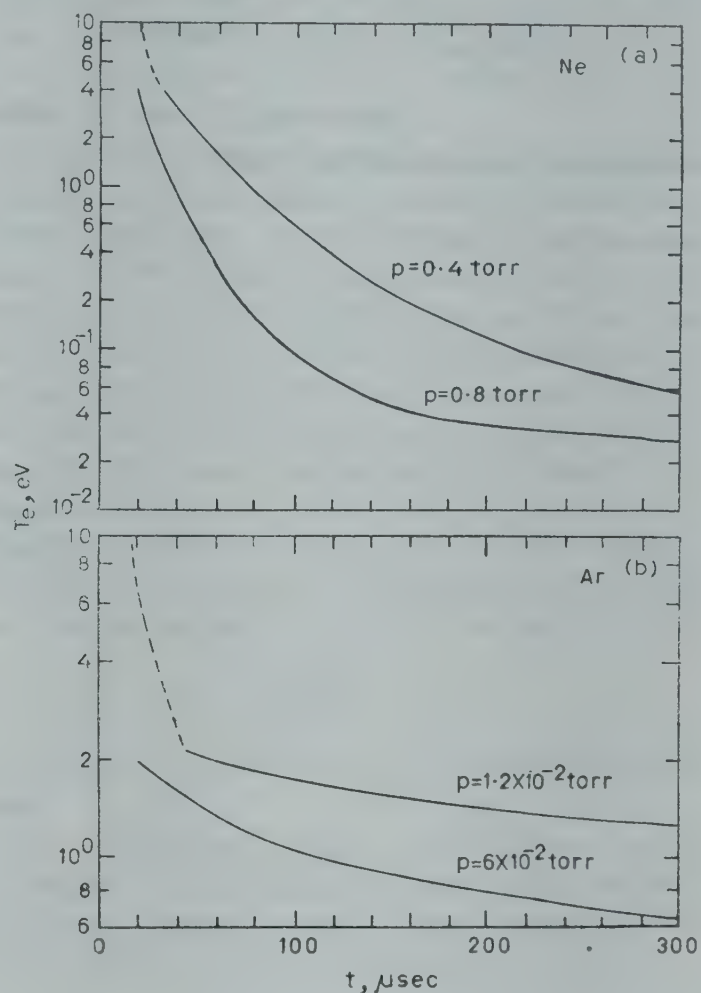


Fig. 4—Time dependence of electron temperature (T_e) calculated from the experimental variations of the effective collision frequency with time [$\nu_{\text{eff}}(t)$] in the neon afterglows (a) and in the argon afterglows (b). The curves represented by broken lines are those obtained by direct comparison of $\nu_{\text{eff}}(t)$ with $\nu_{\text{eff}}(T_e)$ data

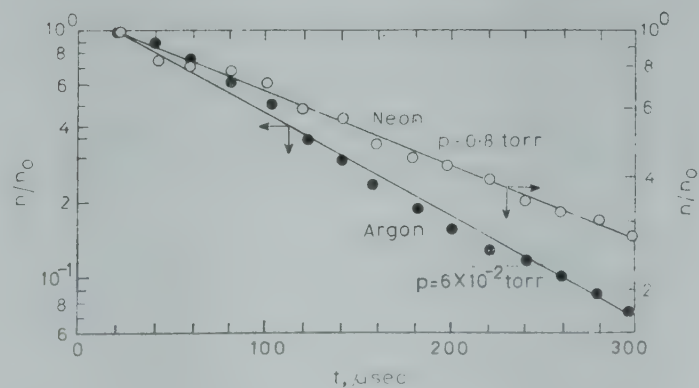


Fig. 5—Plot of normalized electron density vs time, deduced from the ECR line width and height in the neon afterglow (a) and in the argon afterglow (b)

measurements of electron-neutral collision cross-sections at very low energies. From the measurements of the initial temperature and the width of ECR lines in an afterglow plasma, one can deduce $\nu_{\text{eff}}(T_e)$ for low temperatures (down to cryogenic temperatures). Momentum-transfer cross-section (σ_{MT}) can be computed by inverting the following equation:

$$\nu_{\text{eff}} = \frac{4}{3} \pi^{1/2} \left(\frac{2}{m} \right)^{1/2} \frac{1}{(k T_e)^{5/2}} \int_0^{\infty} \sigma_{MT}(u) u^2 \exp(-U/kT_e) du \quad \dots(8)$$

as is done for example, by Sol *et al.*⁴

Acknowledgement

The author is very grateful to Prof. K S Golovanivsky, who suggested this work and rendered guidance in carrying out the work.

References

1. Kelly D C, Margenau H, Brown S C, *Phys. Rev.*, 108 (1957), 1367.
2. Malkin O A, *Pulsed currents and relaxation in gases* (Russian) ('Atomizdat' Publishers, Moscow), 1974.
3. Golant V E, *Microwave methods of plasma diagnostics* (Russian) ('Nauka' Publishers, Moscow), 1968.
4. Sol C, Devos F & Gauthier J C, *Phys. Rev. A*, 12 (No. 2), (1975), 502.

Communications

Broad Line Proton Magnetic Resonance Investigations on Solid Semi-carbazide Hydrochloride

PUSHPA KHARE, S S ASHUTOSH MISHRA, PURNIMA BHARTI
& R C GUPTA

Department of Physics, Lucknow University
Lucknow 226 007

Received 21 April 1980

Broad line NMR investigations of solid semi-carbazide hydrochloride $[\text{CO}(\text{NH}_2)\text{NHNH}_3\text{Cl}]$ was made from 77 to 373 K. The second moment (mean square width) of the spectra at 77 K at which the lattice is effectively rigid is consistent with the assumed model, thereby giving an NMR check of the molecular structure of the sample. As the temperature is raised, the NH_2 group starts rotating and at 323 K, there is a simultaneous rotation of NH_2 and NH-NH_3 groups. Beyond 348 K, an unusual increase in the second moment and unusual broadening of the line width was observed, which has been explained on the basis of the distortion in the crystal structure of the sample. The activation energy has also been calculated.

Proton magnetic resonance study of semi-carbazide hydrochloride, important for its electrochemical characteristics, has been carried out to gain information concerning the molecular structure and motions of the molecules.

The crystal structure of the title compound was previously determined by Mario Na delli *et al.*¹ The organic ion is non-planar. The NH_3 group is 0.44 Å from the plane of the other heavy atoms. The nitrogen atoms are numbered as follows:



N(3) is the proton acceptor atom as can be deduced from its environment and from the value of the distance N(2)-N(3) (1.411 ± 0.014). The chloride ions form nearly equilateral triangles containing the Z_1 axis and N(3) H_3 groups face these triangles. Because the N(2)-N(3) bond is inclined to these triangles, only two hydrogen bonds to chloride ions are possible. The coordinates of H(4), H(5), H(6) were deduced assuming a tetrahedral environment of N(3) with the distance $\text{N}-\text{H} = 1.03$ Å and using the best orientation for hydrogen bonding to chloride ions. The coordinates of H(1) and H(2) were calculated assuming a trigonal configuration for N(1). The coordinates of H(3) were determined

assuming this atom to be in the plane OC N(1) N(2). The crystals were orthorhombic, having four molecules per unit cell. Unit cell dimensions are $a = 7.51 \pm 0.01$ Å, $b = 13.13 \pm 0.01$ Å, $c = 4.64 \pm 0.01$ Å, and $v = 457.8$ Å³.

The PMR spectra were recorded by us at the Tata Institute of Fundamental Research, Bombay, on a Varian Associates variable frequency spectrometer using V-4340 variable probe assembly and a 12 in. magnet system. The resonance frequency was kept at 7.5 MHz. The temperature was varied by controlling the flow of the heated or cooled nitrogen gas over the sample. The accuracy of the measurement of the proton second moment is about ± 1.0 gauss².

Calculations—The experimental value of proton second moment has been calculated from the derivative curves using the trapezium rule² which yields:

$$S = \frac{\sum h^3 f(h)}{3 \sum h f(h)}$$

The values were corrected for the modulation amplitude.³

The theoretical value of the proton second moment of a polycrystalline sample may be obtained from Van Vleck's theory.³ The expression for proton second moment as given by Van Vleck is

$$S_1 = \frac{715.9}{N} \sum_{j>k} r_{jk}^{-6}$$

Where r_{jk} is the interproton distance between j th and k th protons and N is the number of protons over which the sum is taken. The calculation of r_{jk} has been done by taking the positional coordinates of protons given by Mario Na-delli *et al.*¹ S_1 consists of the contribution of the protons of the same molecule (intramolecular). The value of intramolecular contribution came out to be 28.60 gauss².

For estimating S , one should also consider the contribution due to the protons of the different molecules (of the same compound) interacting with each other (intermolecular). The estimation of intermolecular contribution (S_2) to the proton second moment involves the construction of a carefully scaled model of the crystal lattice and thereby measurement of the distances between the various

protons positioned at different lattice sites. However, it can be calculated to a great accuracy (when the lattice constants are known) by Smiths approximation formula which is as follows:

$$S_2 = 358.1 \times 4\pi \times N_p \times (3M^3V)^{-1}, M = R$$

where N_p is the number of protons per unit cell, V the unit cell volume in \AA^3 , M the cut-off radius and R the proton radius. $N_p = 24$, $V = 457.8 \text{ \AA}^3$, $R = 3.7 \text{ \AA}$ and the value of S_2 came out to be 2.88 gauss^2 . Hence the total $S = 31.48 \text{ gauss}^2$.

Activation energy—The expression connecting line width and the correlation frequency was given by Bloembergen *et al.*⁵ and was subsequently modified by Gutowsky and Pake⁶ and by Kubo and Tomita.⁷ The modified expression is

$$2\pi\nu_c = \alpha\gamma\delta H [\tan\{\pi(\delta H^2 - B^2)/2(C^2 - B^2)\}]^{-1}$$

where $\alpha = (8 \times 0.6931)^{-1}$, γ is the gyromagnetic ratio, δH the line width in the transition region, B the line width at temperature higher than the transition region and C the line width at temperature lower than the transition region. The correlation frequencies are assumed to fit an Arrhenius equation:

$$\nu_c = \nu_0 \exp\left[\frac{-E_R}{RT}\right]$$

where E_R is the activation energy for the reorientation of the molecule. A graph plotted between $\log \nu_c$

and $1/T$ is linear with a slope $\left(\frac{-E_R}{R}\right)$. Thus this

slope multiplied by the gas constant R will give the value of activation energy E_R . The values of ν_c used for plotting ν_c versus $1/T$ are given in Table 1. The value of E_R calculated is 23.99 kcal/mole .

Discussion—The variation of second moment as a function of temperature for semi-carbazide hydrochloride is shown in Fig. 1. At the temperature 77K , the mean value of experimental second moment

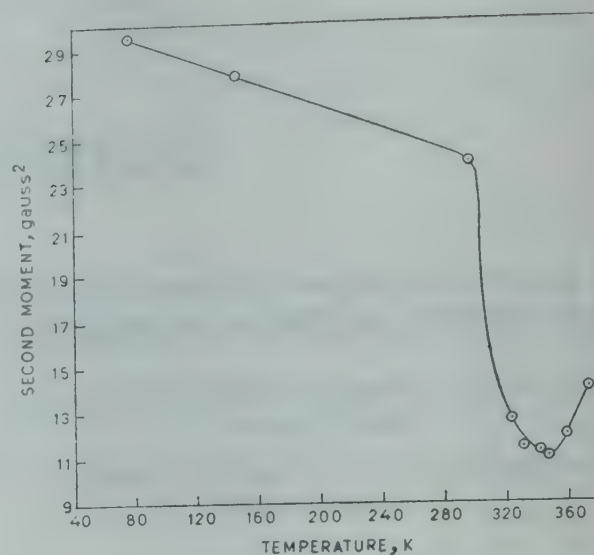


Fig. 1—Variation of second moment as a function of temperature

is about $29.6 \pm 1.0 \text{ gauss}^2$ which appears to be in agreement with the theoretically calculated value of second moment (31.48 gauss^2). This shows that the lattice is effectively rigid at lower temperatures when all the molecular motions may be considered to be frozen. Thus we see that our second moment data are consistent with the previous X-ray study and support our assumed model of crystal structure.

The fall in the value of second moment after 77K , indicates some kind of motions inside the lattice. In case of a group rotation, the intramolecular contribution is reduced by a factor $1/4 (3 \cos^2 \gamma_{jk} - 1)^2$ (Gutowsky and Pake⁶) where γ_{jk} is the angle made by the line joining the j th and k th protons with the axis of rotation. A small reduction in the value of second moment was observed between 77 and 298 K . This fall in the value of second moment can be attributed to the motion of the NH_2 group which is also supported by the fact that in this compound, $\text{N}(1)$ forms a weak hydrogen bond.¹ Following the arguments given in a previous publication,⁸ the reduction in the value of the intramolecular second moment due to the rotation of NH_2 group taking the N—H bond length as 1.03 \AA come to be 2.16 gauss^2 . To find the reduction in S_2 , Smith⁴ has given a reduction factor in the range of 0.65 – 0.50 for stationary rotatory interaction. From this, the reduction in S_2 has been calculated to be 1.44 – 1.87 and reduction in S , 3.60 – 4.03 . The reduced value of the second moment due to the rotation of NH_2 group should, therefore, be in the range 27.88 – 27.45 gauss^2 . The experimental value 27.75 gauss^2 at 146 K , thus confirms the rotation of NH_2 group. Further reduction in second moment is probably due to the continuance of the rotation of NH_2 group.

Table 1—Molecular Reorientation Frequencies (ν_c) for Semi-carbazide Hydrochloride at Different Temperatures

Temp. K	$\nu_c \text{ } 10^5 \text{ Hz}$
300	0.008128
305	0.009307
310	0.016343
315	0.023639
320	0.036181
325	0.04388
330	0.053688
335	0.078394
340	0.11793

After 298 K, there is a steep drop in the proton second moment value (10.72 ± 1 gauss²). The narrowing of the absorption line between 298 and 323 K may be due to the simultaneous rotation of NH₂ and NH—NH₃ groups about their respective axes. The rigid lattice intramolecular second moment for isolated NH₃ group is 51.42 gauss². The change when this rotates about C—N axis is $\frac{3}{4} \times 51.42$, i.e. 37.58 gauss². Since NH₃ group contains 3 protons out of the total 6 protons present in the molecule, the calculated change in S_1 , due to NH₃ group rotation is, therefore, $\frac{3}{6} \times 37.58$, i.e. 18.79 gauss². The change in S_1 due to NH group rotation has been calculated to be 0.1088 gauss². Therefore, the total change in S_1 , due to NH₂, NH—NH₃ groups would be $2.16 + 18.79 + 0.1088$, i.e. 21.0588 gauss². For the calculation of change in S_2 , Smith has given a reduction factor in the range 0.42–0.25 for rotating-rotating interactions. Thus, using this factor, the change in S_2 , for simultaneous rotation of these groups has been calculated to be in the range 1.21–0.718 gauss². Therefore, the change in total second moment should be in the range 22.27–21.78 gauss² and the reduced value of second moment would be in the range, 9.21–9.70 gauss². The experimental value of the second moment E 323 K comes out as 10.70 ± 1 gauss², thus confirming our hypothesis of simultaneous rotation of NH₂ and NH—NH₃ groups. The rotation of NH₃ group at 323 K is also supported by the fact that the chloro addition occurs by strong links^{9,10} and hence the rotation of NH₃ group which exists in bound conditions does not appear to be reasonable at lower temperatures. The infrared study¹¹ of semi-carbazide hydrochloride gives characteristic absorptions at about 3460, 3370–2800 and 7670 cm⁻¹, which are assigned to NH stretching and rocking modes. A further slight reduction in S at 348 K may perhaps be due to the continuance of the rotation of the above groups.

Beyond 348 K, there appears a definite increase in the value of second moment and the line width also unusually broadens. This may be explained on the basis of the distortion in the crystal structure, accounted for by the interaction of chloride ions with NH₃⁺. These views on the distortion of semi-carbazide ion are supposed by the fact that semi-carbazide is planer in bis semicarbazide copper (II) and bis semicarbazide-zinc chloride. It is quite possible that the crystal symmetry may change at the transition temperature. This new structure will be of higher symmetry than the lower temperature modification and the centre of gravity of the mole-

cules will probably be closer together. Thus the second moment although still decreasing with increase in temperature, will suddenly jump to a higher absolute value. Such an unusual increase in the value of second moment has also been observed by Agarwal and Gupta¹² in 1,5-dimethyl-naphthalene.

The authors wish to express their thanks to Prof. R Vijayaraghavan and his NMR group at TIFR, Bombay, for providing experimental facilities. Thanks are also due to Prof. B G Gokhale, Head of the Physics Department, Lucknow University, Lucknow, for his kind interest throughout the work. One of the authors (PK) is also thankful to CSIR, New Delhi, for the award of a research fellowship.

References

1. Na-delli, Mario, Fava, Giovanna & Grimaldi, Griulia, *Acta Crystallogr.*, 19 (6) (1965), 1038.
2. Van Vleck J H, *Phys. Rev.*, 74 (1948), 1168.
3. Andrew E R, *Phys. Rev.*, 91 (1953), 425.
4. Smith G W, *J. chem. Phys.*, 42 (1965), 4299.
5. Bloembergen N, Purcell E M & Pound R V, *Phys. Rev.*, 73 (1948), 162.
6. Gutowsky H S & Pake G E., *J. chem. Phys.*, 18 (1950), 162.
7. Kubo R & Tomita K, *J. phys. Soc. Japan*, 9 (1954), 888.
8. Banerjee A K, Agarwal V D & Gupta R C, *Z. Phys. Chem.*, 8 (1973), 37.
9. Brewster R Q & McEwen W E, *Organic chemistry* (Prentice Hall of India, New Delhi), 1969, 46, 114, 507.
10. Dyer John R, *Application of absorption spectroscopy of organic compounds* (Prentice-Hall of India, New Delhi), 9 (1971), 91.
11. Davison W H J & Christie P E, *J. chem. Soc.*, (1955), 3389.
12. Agarwal V D & Gupta R C, *Indian J. pure Phys.*, 7 (1969), 740.

Pulse Height Analyzer for High Counting Rate in Mössbauer Work

ANJALI KRISHNAMURTHY, RAMESH CHANDRA &
S LOKANATHAN

Department of Physics, University of Rajasthan
Jaipur 302 004

Received 3 October 1979

An additional coincidence in usual pulse height analyzer has been designed and its performance in Mössbauer gamma detection has been tested. The energy resolution in the detection of 14.4 keV Mössbauer gamma gets improved at high counting rates and thereby the Mössbauer absorption enhances.

Base line fluctuations in pulse height analyzers impose a limit on the counting rate that can be handled in Mössbauer spectroscopy. Thus, although the output of the preamplifier-amplifier system may

be quite fast with a width of say $1\ \mu\text{sec}$ or less, the ac coupling of the amplifier to the pulse height analyzer (PHA) does not allow restoration of the base line in the PHA to zero volts. The output of the amplifier system, here, is a train of either unipolar or bipolar pulses. Various sophisticated base line restorers are discussed in the literature.¹⁻⁵ Ideally, for bipolar shaped pulses of short width, there is no need of base line restoration for RC coupling with a large RC time-constant. But in practice, the output of the amplifier often contains slowly varying voltages which may be from several sources, such as the 50 Hz ripple, drifts and long pulse tails from imperfect pole zero cancellation. This, together with statistical fluctuations arising from the random nature of the input signals, results in base line fluctuations. These fluctuations ultimately reduce the percentage of Mössbauer absorption observed at high counting rates.

In this communication, a simple circuit is described (Fig. 1) which overcomes this difficulty upto a reasonable extent. Here we have used to advantage the feature that in Mössbauer spectroscopy, linearity is not really important for pulse height analysis. Thus, this circuit differs from the analyzers with the

usual base line restorers in that its operation is limited to inputs within the range 1.7 to 5 V. This requires the gain of the amplifier to be set so that the pulses corresponding to the 14.4 keV gammas (or any others of interest in the particular experiment) lie within about 2 to 4 V.

The output of the amplifier is fed to two comparators 710 acting as lower level and upper level discriminators (LLD and ULD). The trailing edges of LLD and ULD are used to trigger two 74121 monostables, M_L and M_U , which generate outputs corresponding to LLD and ULD of widths 0.5 and $1.0\ \mu\text{sec}$. The negative output of the monostable corresponding to ULD and the positive corresponding to LLD are connected to two inputs of 7413(b) NAND gate. This part of the circuit constitutes an ordinary PHA with trailing edge triggering.

The output of the amplifier is also used to trigger a 7413(a) NAND gate (with Schmitt trigger) as an inverter. The inputs of 7413 has 0.8 V hysteresis, i.e. its output state changes only when the input rises above 1.7 V for positive going signals and falls below 0.9 V for negative going signals. The trailing edge of 7413(a) output triggers the third monostable M_C . The presence of the output of this monostable

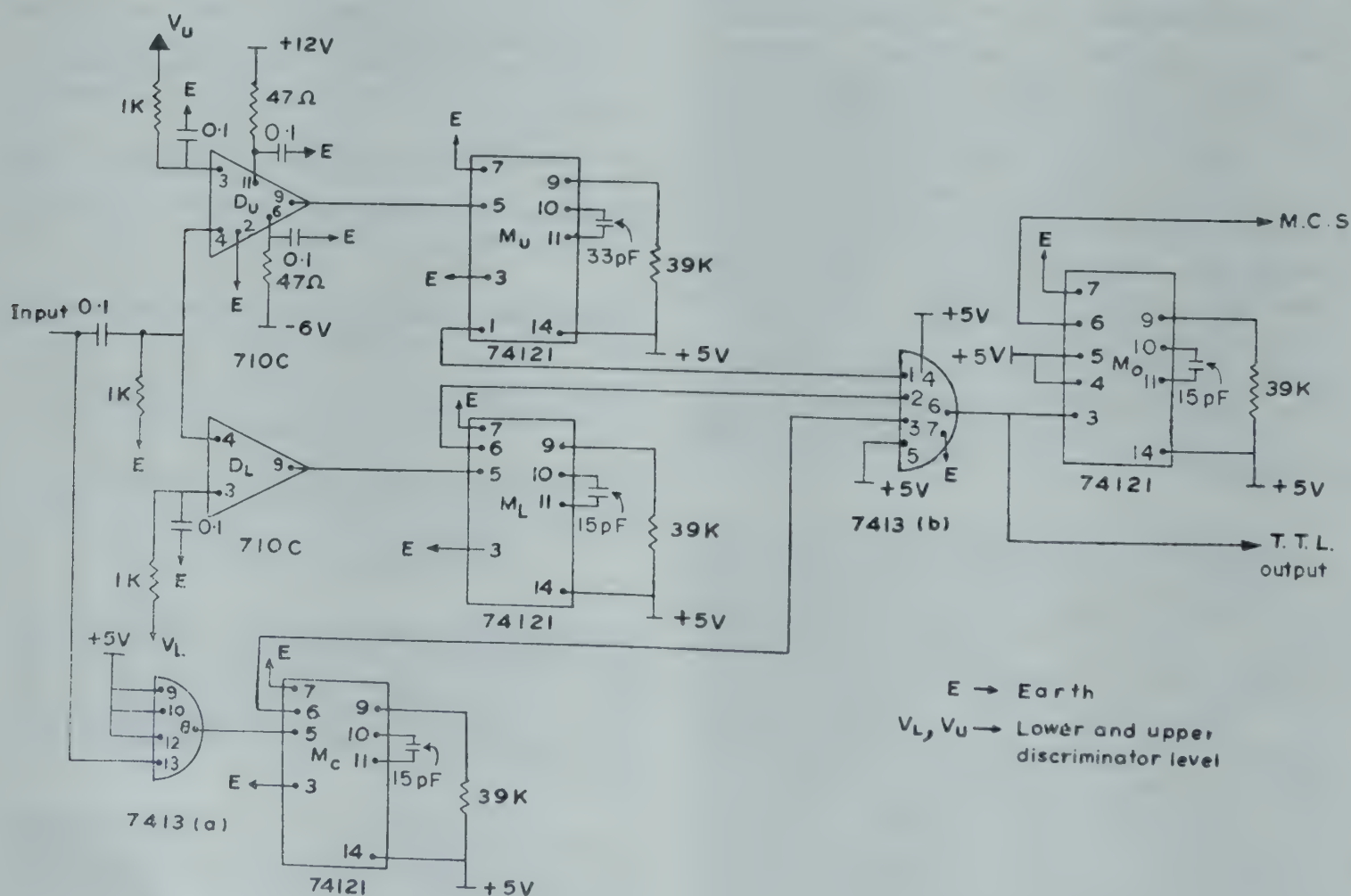


Fig. 1—Modified circuit of pulse height analyzer for fast counting rate

Mo along with the output corresponding to LLD changes the output state of 7413(b) in the absence of any inhibit output from the monostable M_U corresponding to ULD. Either the TTL output of 7413(b) can be directly coupled to any scaler or in case the input to the scalar needs any specific width (as in the case of ND 1100 multichannel analyzer), it can be adjusted with the help of an additional monostable M_o . It will be appropriate to re-emphasize that this PHA is not suitable for usual pulse height analysis, because it will not analyze below 1.7 V inputs. Thus, the fact that the linearity of pulse height analysis of the detection system is not of much importance for Mössbauer studies, is used here, in increasing the speed of the detection system.

In order to see the effect of increasing counting rate we have plotted, in Fig. 2, pulse height spectra for the ^{50}Co source at two positions, 7 cm and 3 cm apart, from the detector, using this analyzer. The effect of this additional coincidence can be removed if the III input of 7413(b) is connected to +5V and then it behaves as an ordinary analyzer. The pulse height spectra using the ordinary analyzer, at these positions with 7 and 3 cm distance between source and detector, are also shown in Fig. 2. The effect of additional coincidence in spectrum I clearly indicates the improvement in the 14.4 keV peak in terms of its width and peak-to-valley ratio. There is improvement in spectrum II as well, which is for a lower counting rate.

The ultimate effect of any modification for high counting rates should appear in larger Mössbauer absorption. To ascertain this, Mössbauer spectra of stainless steel with and without this additional coincidence were taken at a rate of 50,000 gammas per sec after PHA. The baseline or the background and the height of peak for both the spectra is given in Table 1. To observe the improvement, the time required for collecting 1% statistics at the absorption peak, which means that the value of standard deviation is 1% of the peak height, was calculated and is shown in column 5 of Table 1.

From col. 5 of Table 1, it is clear that there is a saving of about 15% time using this additional coincidence. This improvement is observed at the counting rate of 14.4 keV around 50,000 per sec after PHA. However, at still higher counting rates with a

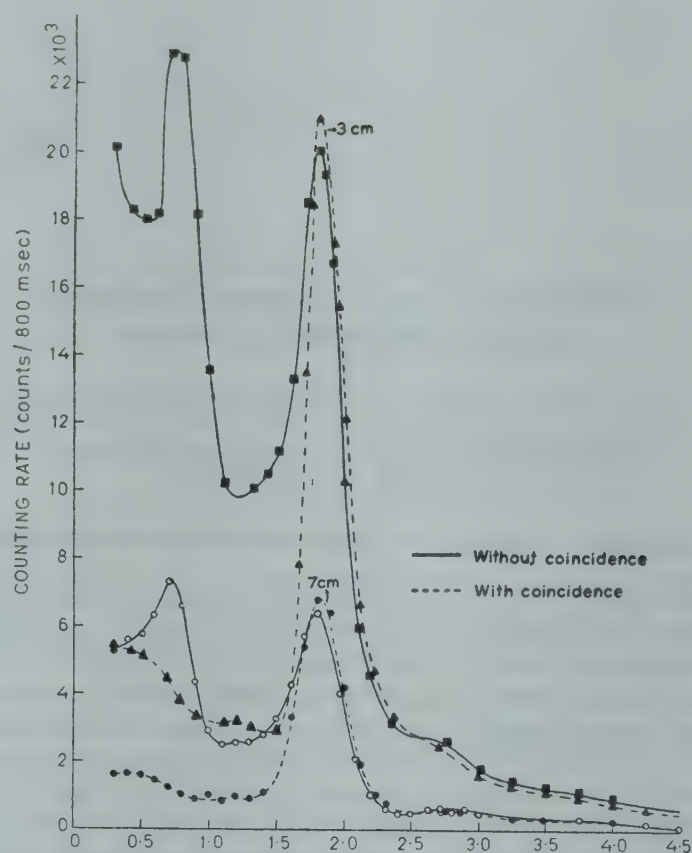


Fig. 2—Pulse height spectra for the source at two positions from the detector using with coincidence and without coincidence circuits

Table 1—Effect of Additional Coincidence.

Mössbauer parameters	Back-ground counts	Counts at the peak	Absorption at peak in counts	Time for 1% statistics
With additional coincidence	88,000	57,000	$31,000 \pm 381$	1.4 hr
Without such coincidence	113,700	78,500	$35,200 \pm 438$	1.6 hr

stronger source (which is not available with us) one would expect a further improvement.

The authors wish to express their gratefulness to Prof. B Saraf and Dr Y S Shishodia for many helpful discussions.

References

1. Robinson L B, *Rev. Scient. Instrum.*, **32** (1961) 1057.
2. Chase R L & Poulo L R, *IEEE Trans.*, NS14 (No. 1), (1967), 83.
3. Williams C W, *IEEE Trans.*, NS15 (No. 1), (1968), 297.
4. Bertolaccini & Bussolati C, *Nucl. Instrum. Meth.*, **100** (1972), 349.
5. Radeka V, *Rev. Scient. Instrum.*, **38** (1967), 1397.

Notes

After-effect of Heat & Magnetic Field on the Dielectric Permittivity of Sulphur

VIJAY K. SHRIVASTAVA, M L KHARE & C S BHATNAGAR

Department of Physics, Maulana Azad College of Technology, Bhopal 462 007

Received 13 August 1979; revised received 10 December 1979

Permittivity study has been made in sulphur, treated thermally in presence of magnetic field. Samples have been prepared at different temperatures from 60° to 100°C (at intervals of 10°C) using different magnetic fields. A small increase in permittivity at low forming temperatures (T_f) has been explained on the basis of transfer of electrons from electrodes to the dielectric. Macroscopic field distortion takes place because of the trapping of these electrons, increasing the permittivity of the sample. Decrease in permittivity at higher T_f has been ascribed to the trapping of $4p$ electrons at structural defects. The effect of the magnetic field is to enhance the temperature effect by creating some additional impurity bands. The electrons may get trapped in trap sites located in these bands giving a decrease in permittivity.

Permittivity of some dielectric materials usually undergoes a change on electret formation. However, Gerson and Rohrbaugh¹ did not observe any such change, but Chatterjee and Bhadra² found an increase in dielectric constant on electret formation. Bhadra³ also reported an increase in permittivity along the direction of polarizing electric field and a corresponding decrease perpendicular to it. In case of a magnetoelectret (ME), Qureshi and Bhatnagar⁴ observed a slight increase ($< 1\%$) in permittivity in perspex samples that were formed at lower temperatures ($T_f < T_g$, where T_f is forming temperature and T_g is glass transition temperature). But in samples having $T_f > T_g$ they observed about 5% decrease in permittivity. A similar decrease has also been observed by Deshpande and Khare⁵ and by Quamara *et al.*⁶ in PVC.

This study has now been extended to sulphur, which is also an electret-forming material. Thermo-electrets of sulphur were first prepared by Johnson and Carr.⁷ Nadzhakov⁸ studied photo-electrets of sulphur while Sharma and Bhatnagar⁹ have investigated its ME properties. This paper deals with the change in permittivity of sulphur as observed after its ME formation.

Experimental details—Sulphur sublimate (E-Merck), which is polycrystalline in nature, was used for the

preparation of samples. MEs (discs of 4 cm diameter and 1 mm thickness) were made by the method reported earlier.¹⁰ Samples were prepared for different values of T_f (60, 70, 80, 90 and 100°C.). For each T_f , different samples were made using magnetic field strength (H_f) of 2.5, 4.5, 6.5, 8.5, 10.5, 12 and 14 kOe. Blank samples (at zero magnetic field) were also made at different T_f to distinguish the effect of magnetic field from that of the effect of temperature.

Permittivity (ϵ) was determined by using a universal bridge (Marconi TF 2700). Measurement on each sample was done before, and five minutes after, its ME formation at a fixed frequency of 1 kHz. In order to record the recovery, measurements were made every day following the sample preparation and were continued up to one month. A slight recovery in the induced change has been observed, as found in other cases.^{4,5}

Since sulphur is photo-sensitive, its ME state gets destroyed by day light.^{9,10} Therefore experimentation was done in darkness (i.e. during night) while measurements were made in red light as done earlier.⁹⁻¹¹ The samples were stored in a blackened desiccator.

Results—Percentage change in permittivity ($\Delta\epsilon$) for samples prepared at different T_f and H_f is shown in Fig. 1. For samples having $T_f = 60$ and 70°C, there is a slight increase in ϵ (Figs. 1a and 1b), which seems to be more or less independent of the strength of magnetic field. In 80°C-samples (Fig. 1c) the change is positive at lower fields but it gradually decreases on increasing the field strength and at 12 kOe it becomes negative. The negative $\Delta\epsilon$ then increases with magnetic field. In 90°C-samples (Fig. 1d) the changeover from positive to negative takes place at a lower field strength and in 100°C-samples $\Delta\epsilon$ is negative for all values of magnetic field (Fig. 1e). The general trend of variation of $\Delta\epsilon$ with magnetic field is that $\Delta\epsilon$ decreases on increasing the magnetic field (Fig. 1). The dotted curves in Fig. 1 show the variation of $\Delta\epsilon$ after one month. These curves show that there is partial recovery in $\Delta\epsilon$, but its variation with T_f and H_f is similar to that observed in freshly prepared samples.

In Fig. 2, the effect of T_f on $\Delta\epsilon$ is shown in samples prepared at a constant magnetic field. At lower temperatures, $\Delta\epsilon$ is positive but becomes

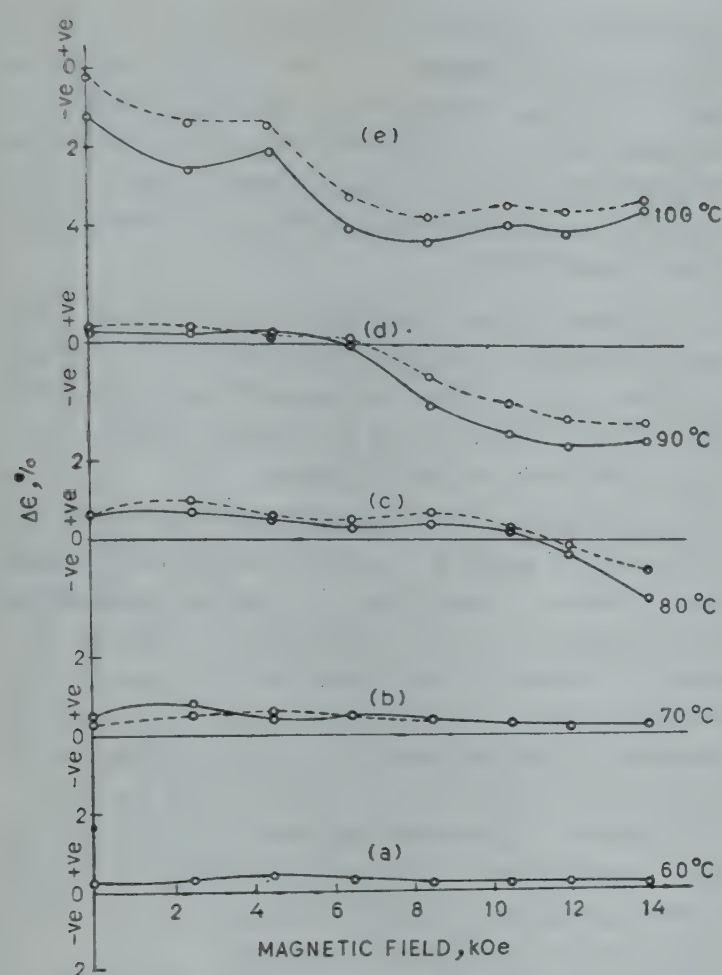


Fig. 1—Percentage change in $\Delta\epsilon$ for samples prepared at different T_f and H_f

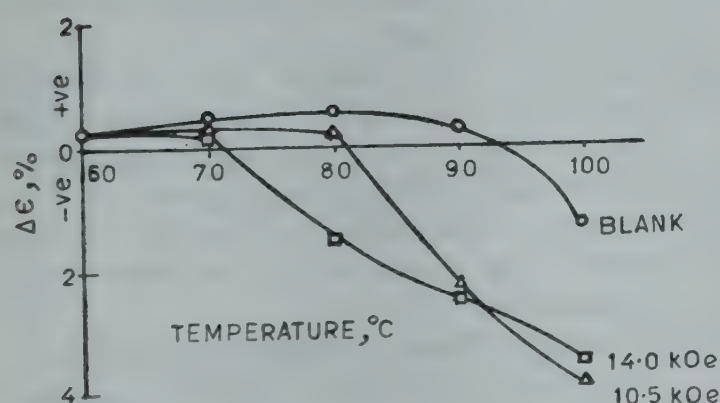


Fig. 2—Effect of T_f on $\Delta\epsilon$ at constant magnetic field

negative as T_f is increased. The effect of magnetic field is to lower the value of the temperature at which $\Delta\epsilon$ becomes negative

The recovery of $\Delta\epsilon$ with time is shown in Fig. 3. The recovery is quite slow, and even after a month there is not much change in the value of $\Delta\epsilon$.

Discussion—The slight increase in $\Delta\epsilon$ at lower forming temperatures may be due to electron transfer from metal to the dielectric surface. During sample formation, the two sides of the sulphur disc remain in contact with tin foils and, therefore, some electrons are likely to be transferred from the foil to sulphur. These electrons might get trapped in surface states.

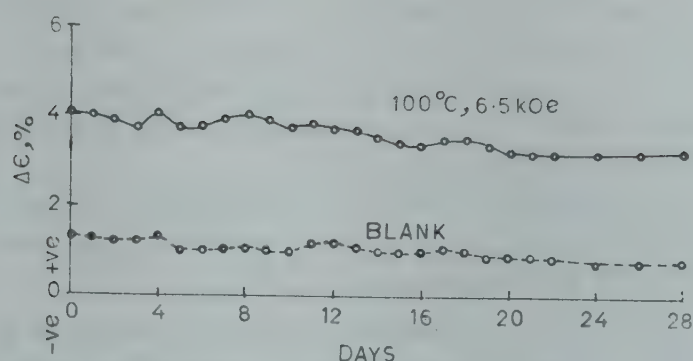


Fig. 3—Recovery of $\Delta\epsilon$ with time for sample prepared at 100°C with zero (blank) and 6.5 kOe magnetic field

This would result in negative iso charge.¹² This is in accordance with charge measurement study reported earlier.¹¹ The trapped negative charge would be loosely bound to the dielectric and would lead to macroscopic field distortion. This would increase the polarizability of the dielectric and result in a small increase in $\Delta\epsilon$. (Ref. 13).

Superimposed over this there would be a volume effect. As T_f is increased, a large number of charge carriers (electrons) are liberated within the dielectric due to thermal excitation. These liberated electrons move about within the dielectric. Simultaneously there would be generation of trap sites due to the increased number of structural defects. During gradual cooling, the electrons would get trapped in these structural defects and might virtually get frozen in. Thus the after effect of this heat treatment, even without any magnetic field, would be that a good number of electrons, being dislodged from their atoms, get trapped in structural defects. These electrons are the outermost 4p electrons of sulphur. As sulphur atoms lose their outermost electrons, their electronic polarizability considerably decreases. The trapped electrons, no doubt, would produce some distortion causing slight increase in $\Delta\epsilon$, but at 1 kHz, the decrease in electronic polarizability would contribute more than the increase due to field distortion. Hence a simple heat treatment results in decrease of permittivity.

It is clear from the curves in Figs. 1 and 2 that magnetic field enhances the temperature effect. The decrease observed in zero-field samples at higher T_f is seen to occur at lower temperatures when the samples cool down in magnetic field. According to Hasegawa,¹⁴ when dielectrics are slowly cooled in strong magnetic fields, some additional impurity bands are created. The electrons may be visualized to get trapped in trap sites located in these bands. Thus the decrease in $\Delta\epsilon$ is expected to be more pronounced in magnetically treated samples. Another possibility, though very small, for accounting for

the decrease in permittivity, is that S-8 rings (sulphur molecules is made up of 8 atoms in closed-ring form) may orient in a direction perpendicular to the magnetic field¹⁵ causing a decrease in the direction parallel to the magnetic field.

The decrease in permittivity seems to be primarily an after-effect of heat treatment, which gets enhanced due to the presence of magnetic field.

The authors are thankful to the Principal, M A College of Technology, Bhopal, for providing necessary facilities. Thanks are due to (Km) Malini Variyar and Meenakshi Gopalan for their help rendered during the work. One of the authors is thankful to CSIR New Delhi for the award of a senior research fellowship. Thanks are also due to the National Science Foundation of USA for providing some equipment.

References

1. Gerson R & Rohrbaugh J H, *J. chem. Phys.*, **23** (1955), 2381.
2. Chatterjee S D & Bhadra T C, *Phys. Rev.*, **98** (1955), 1728.
3. Bhadra T C, *Indian J. Phys.*, **32** (1952), 281.
4. Qureshi M S & Bhatnagar C S, *Indian J. pure appl. Phys.*, **13** (1975), 797.
5. Deshpande (Mrs) G K & Khare M L, *Indian J. pure appl. Phys.*, **15** (1977), 692.
6. Quamara J K, Khare M L & Bhatnagar C S, *Indian J. pure appl. Phys.*, **15** (1977), 617.
7. Johnson O J & Carr P H, *Phys. Rev.*, **42** (1932), 912.
8. Nadzhakov G & Godishnik, *Fiz. Mat. Sof. Universitet*, **33** (1936-37), 409.
9. Sharma L N & Bhatnagar C S, *Indian J. pure appl. Phys.*, **8** (1970), 500.
10. Sharma L N & Bhatnagar C S, *Indian J. pure appl. Phys.*, **9** (1971), 240.
11. Shrivastava V K, Qureshi M S & Bhatnagar C S, *Indian J. pure appl. Phys.*, **17** (1979), 4.
12. Khare M L & Bhatnagar C S, *Indian J. pure appl. Phys.*, **8** (1970), 700.
13. Von Hippel A R, *Dielectrics & waves*, (John Wiley, New York), 1959.
14. Hasegawa H, *Physics of solids in intense magnetic fields* (Plenum Press, New York), 1969, 247.
15. Mc Mahon W, *J. Am. chem. Soc.*, **78** (1956), 3290.

Variable Frequency Interference Filter*

J ASHOK & D VASANTHA

Applied Physics Department, Andhra University
Waltair 530 003

Received 24 December 1979; revised received 30 May 1980

The fabrication technique of an interference filter having different pass frequencies at different points along its length is described. The technique utilizes rotating baffle mechanism used in parabolization techniques, modified to the present application.

* Presented at the "National Symposium of Science & Technology of Vacuum, Surfaces, Thin films", 21st-24th, December, 1979, Indian Institute of Technology Delhi.

Interference filters made of thin films have several major advantages over other types of wave-length selecting devices like gratings, prisms or absorption filters. A variable frequency interference filter with separate pass bands along regions across its length has also its own advantages in several types of instrumentation.

In an interference filter, the wavelength of maximum transmission is a direct function of the spacer layer thickness. Thus an interference filter with variable pass band along its length should have a spacer layer with graded thickness.

A continuous variation of pass wavelength can be obtained by using a continuously graded spacer layer. This can be achieved by proper positioning of substrate with respect to the vapour source. The extent of variation achievable by this method is, however, limited. On the other hand, any type of gradation can be obtained by using a rotating baffle such as the one used in parabolization of mirrors.¹

To obtain an interference filter, a baffle having seven separate pass wavelengths along its length has been designed. Each centimetre length of the filter transmits a different wavelength.

The major steps in the design of the baffle are:

- (i) Calculation of thickness that is required at various points along the substrate, since the spacer layer should have an optical thickness of half a wavelength.
- (ii) Calculation of thickness that is actually coated² along the length of the substrate without any baffle. One end of the specimen is assumed to receive maximum vapour.
- (iii) Calculation of difference between the thickness needed as per step (i) and the thickness coated as per step (ii).
- (iv) Calculation of angular closing at each point as a fraction of full closing, taken in this case as $(3/2)\pi$.

A typical calculation to obtain the angular closing, at each point of the substrate to allow the necessary vapour is given in the following.

The thickness required is less than the thickness coated without baffle, as per calculations. So the baffle should decrease the condensation up to the requirement, by cutting off a portion of the vapour. For this, the maximum angular closing, 270° should correspond to a maximum thickness difference, $=938.87 \text{ \AA}$ at a particular point, $\delta = 5 \text{ cm}$; with $T_0 = 2725 \text{ \AA}$. For minimum thickness difference, the angular closing is to be minimum and can be calculated from above values as there exists a direct relation between the thickness difference and the



Fig. 1—(a) The baffle; (b) front view of the baffle: S, source, AB, baffle, CD, substrate holder and EF, substrate.

angular closing. Similarly, the remaining values are calculated.

A polar graph is plotted for thickness difference versus angular closing. An aluminium sheet is cut in the profile of the graph which gives the required baffle [Fig. 1 (a)]. The baffle is placed between the vapour source and the substrate, and the front view is shown in [Fig. 1 (b)].

The junior author (D V) is grateful to CSIR, New Delhi for financial assistance.

References

1. Strong J, Neher H V, Whitford A E, Cartwright C H, Hayword R, *Procedures in Experimental Physics*, (Prentice-Hall Inc., Engle Wood Cliffs, N J), p 180.
2. Holland L, *Vacuum deposition of thickness*, (Chapman & Hall, London), 1958, 145.

90° Growth Twins in Float-Zone Silicon Crystals

R K BAGAI & W N BORLE

Solid State Physics Laboratory, Delhi 110 007

Received 3 October 1979

Formation of 90° twins in float-zone silicon crystals is reported. The origin and interaction of stacking faults after 90° twin are discussed. A cellular structure is found to exist beyond the twin boundary rather than a dendritic structure as reported in the case of crystals grown by the Czochralski pulling method.

A 90° twin is formed in a growing crystal whenever the twin plane is perpendicular to the growth

direction. Such twinning has been observed in silicon crystals grown along $\langle 111 \rangle$ direction by Czochralski (CZ) pulling method.^{1,2} The twin plane is formed spontaneously all over the solid-liquid interface and the twin plane or boundary thus formed is referred also as $(111) \parallel (\bar{1}\bar{1}\bar{1})$ boundary because changes the original (111) growth plane to a new $(\bar{1}\bar{1}\bar{1})$ growth plane. Some interesting features of this boundary in CZ crystals have been reported earlier.^{3,4} However, the occurrence of 90° twins in float-zone silicon crystals has not been known so far. During the present investigation, it is observed that this type of twinning occurs quite frequently while growing dislocation-free float zone (FZ) silicon crystals along $\langle 111 \rangle$ direction. The nature of such twinning in FZ silicon crystals is being reported in this note. The intention is to understand more clearly about the growth conditions giving rise to this type of twinning and to study the structural phenomena taking place at this boundary.

All the crystals are grown in vacuum using internal work-coil type float zoner. The experimental details regarding the growth of dislocation-free FZ crystals have already been reported.⁵ Preferential etching, optical photomicrographic and X-ray topographic techniques are used for studying the structural defects.

It has been noticed that the twins are usually formed at the shoulder region of the growing crystal where there is a higher probability of some growth disturbance to occur due to changes in the growth conditions. However, it is observed that under similar conditions of growth, if the initial growth is not dislocation-free, the probability for the appearance of twins is less. The probable mechanism for the formation of 90° twin can be explained on the basis of the following observations.

It is known that during the growth of dislocation-free silicon crystals, solid-liquid interface is expected to be flat and coincident with (111) plane if the growth is along $\langle 111 \rangle$ direction. The growing (111) plane being the low energy (smooth) plane, considerable amount of supercooling in the melt adjacent to solid-liquid interface is necessary for further growth. Under such conditions, the mechanism of growth is two-dimensional nucleation and growth.² The growth takes place by the formation of two-dimensional nucleus which requires the formation of critically-sized, two-dimensional cluster of atoms, which is three atoms situated at 60° from each other for silicon lattice. At this stage, if any growth accident takes place involving some

element of torque it is more likely that the two-dimensional nucleus cluster of atoms gets oriented through 60° , thereby giving rise to 90° twin.

After etching with boiling NaOH solution, a sharp line demarcating the two grains is clearly seen. Presence of stacking faults has been observed in the $\langle \bar{1}\bar{1}\bar{1} \rangle$ lattice grown beyond the 90° twin. As the growth proceeds, stacking faults disappear slowly. The crystal can be grown to a considerable length even after twinning and does not become polycrystalline within a short distance of the twin as in CZ crystals.

The origin of the stacking faults and the nature of their interaction is discussed in the following.

Usually no stacking fault is produced in bulk FZ crystals grown under normal conditions of growth but whenever the growing crystal twins perpendicular to the growth direction these faults are created in the twinned region. They originate mostly at the interface of the original (111) lattice and the $(\bar{1}\bar{1}\bar{1})$ twinned lattice of the crystal. As the crystal grows, these faults also grow along the {111} planes. As they are growing, these faults interact with each other and give rise to figures of various shapes. No fault cuts across other faults.

Equilateral triangular faults characteristic of the silicon epitaxial films^{6,7} are not observed in these crystals. However, sometimes triangular shapes are formed due to the intersection of these faults. The shapes formed by the intersection may expand

or may reduce in further growth of the crystal, e.g. as in Figs. 1 (a) and (b). This depends upon the direction in which the intersecting faults move in the (111) growth plane during the growth. To find out the direction of movement, a technique of repeated etching is used. It has also been found that the figures formed by parallel faults remain constant as the crystal grows further. This is illustrated in Figs. 2 (a) and (b). These are the etch patterns in sequence in a particular region of the growing surface at increasing distance from the twin plane. It is further found that while sweeping across the growth surface these line faults serve as sinks for the dislocations in the crystal. It can be seen that the region bounded by the line faults contains either no dislocation etch pits or only a few etch pits as compared to the outside region.

Various attempts have been made to explain the origin of stacking faults. For the epitaxial layer,⁸ stacking faults were thought to originate from collapsed sheet of vacancies. Chemical contamination⁹ of the substrate surface by oxygen and carbon might also be expected to lead to their generation. Ravi and Varker¹⁰ concluded that nucleation sites for these defects during oxidation are related to swirl defect. In the recent model put forward by Mahajan *et al.*¹¹ to account for oxidation-induced stacking faults or stacking faults formed during aging, it is said that the first stage in the origin of stacking faults is envisaged to involve the formation of silicon-oxygen clusters on the {111} planes.

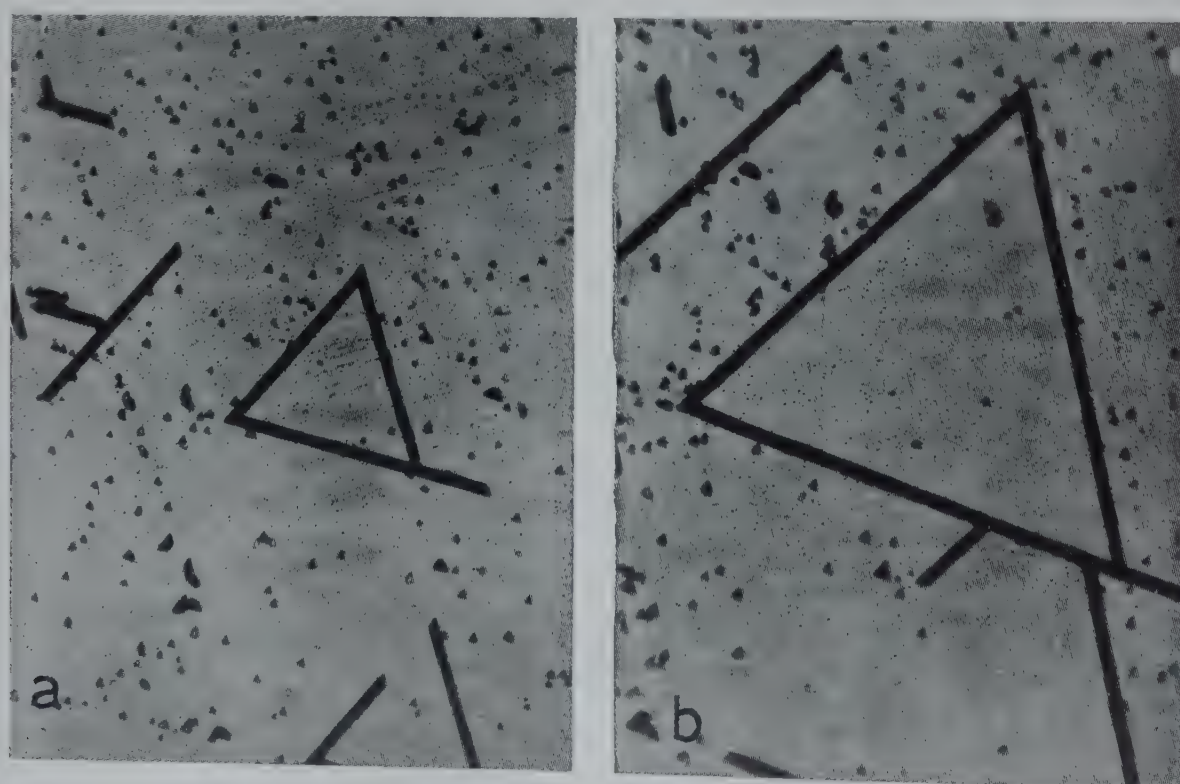


Fig. 1—Photomicrograph revealing the figures formed by the intersection of stacking faults on (111) plane ($\times 80$) [(a) near the twin plane, (b) at increasing distance from twin plane (expanding figures)]

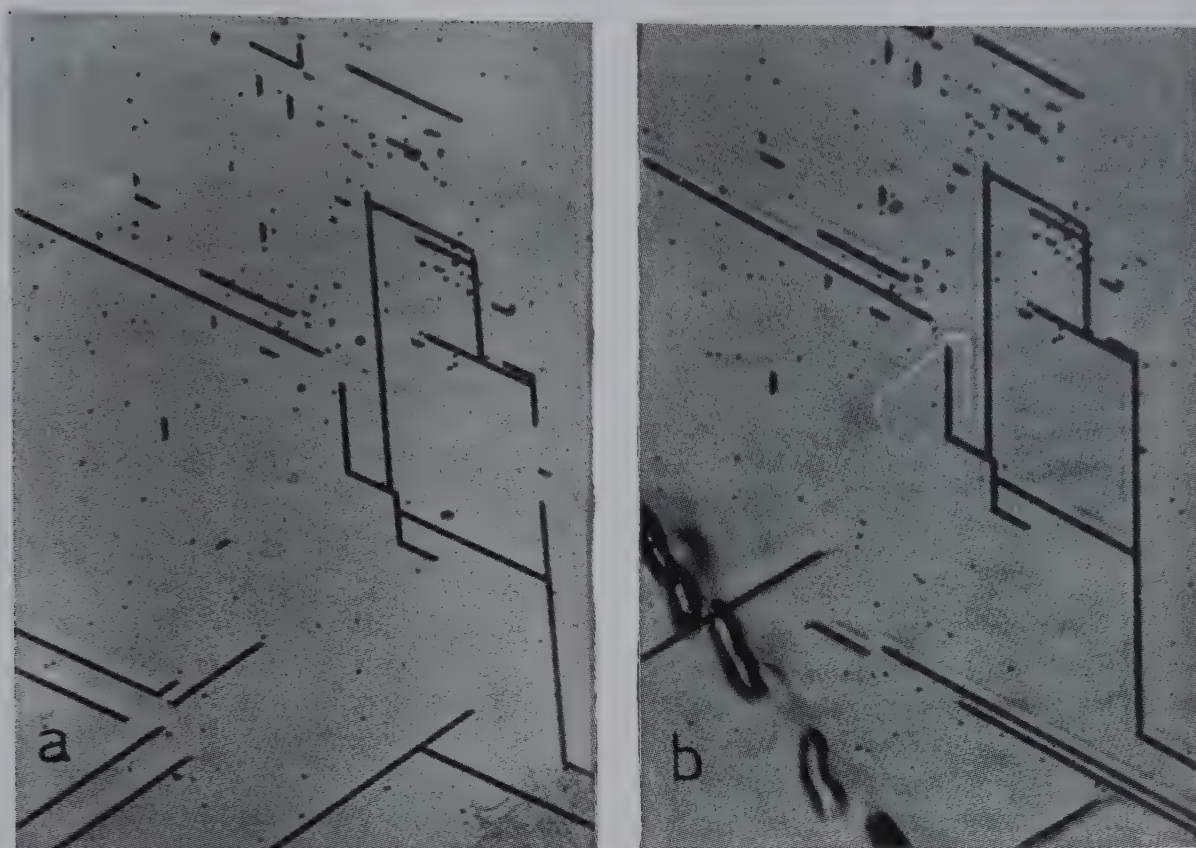


Fig. 2—Photomicrograph showing the figures formed by parallel stacking faults at different distances from the twin plane. Faint and dark lines in (b) are due to double etching and indicate the direction of movement of faults ($\times 80$).

However, for the stacking faults observed in the bulk crystals grown by CZ or FZ methods their origin can easily be related to the formation of 90° twins. The content of oxygen in FZ silicon crystals grown in vacuum is quite less ($<10^{16}$ atoms/cc) as compared to CZ crystals or oxidized slices, and still the stacking faults are formed, indicating thereby that the presence of oxygen may not be playing a bigger role in the formation of stacking faults. However, the dislocation-free FZ crystals are always supersaturated with point defects¹²⁻¹⁴ (vacancies or self-interstitials). Thus it is likely that the point defect clusters alone in the presence of thermal and crystallographic conditions available at the 90° twins are sufficient to nucleate stacking faults.

It has been earlier reported¹ that dendritic structure appears near $(111) \parallel (\bar{1}\bar{1}\bar{1})$ boundary after which the crystal usually became polycrystalline. However, in the present case the growing FZ crystal does not become polycrystalline after 90° twin and, in fact, single crystal growth can continue for sufficiently longer lengths. Dendritic structure is also not observed in such crystals. But a cell-like structure¹⁵ [Fig. 3] is found by reflection topographs taken on wafers near the boundary and at a certain distance away from the boundary. This type of cellular structure is observed so clearly for the first time in silicon crystals. It is thus possible that under the present conditions of growth the supercooling is

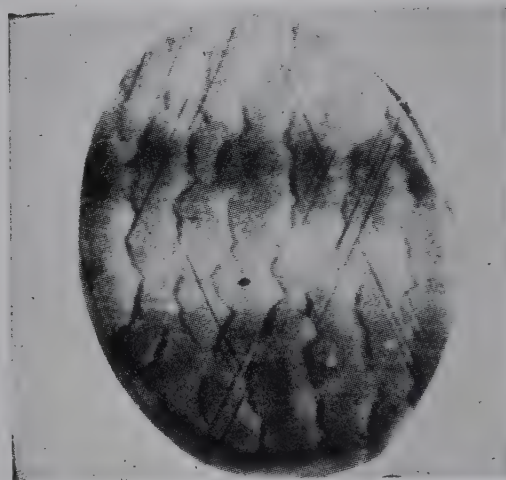


Fig. 3—The (111) reflection topograph showing cell-like structure

not high enough for the dendritic structure to occur. The continuation of crystal growth after twinning without becoming polycrystalline, further suggests that dendritic structure should not exist in such crystals.

The authors are grateful to Prof. S C Jain, Director, Solid State Physics Laboratory, Delhi, for his encouragement and permission to publish this paper. Thanks are also due to Dr A V R Warriar and Prof. G C Trigunayat for useful discussions, to Shri B B Sharma for X-ray topographic work and to Shri M Bal and Shri O P Nangia for their help in conducting the experiments.

References

1. Turovskii B M & Lainer L V, *Soviet Phys.-Crystallogr.*, **9** (1964), 71.
2. Borle W N, *Studies on silicon crystal growth*, Ph D thesis, Nagpur University, Nagpur, 1973.
3. Borle W N, *Sci. Metall.*, **7** (1973), 267.
4. Borle W N, *Indian J. pure appl. Phys.*, **12** (1974), 848.
5. Bagai R K, Borle W N, Bal M & Nangia O P, *Indian J. pure appl. Phys.*, **18** (1980), 642.
6. Booker G R & Stickler R, *J. appl. Phys.*, **33** (1962), 3281.
7. Drum C M & Van Gelder W, *J. appl. Phys.*, **43** (1972), 4465.
8. Jaccodine R J, *Appl. Phys. Lett.*, **2** (1963), 201.
9. Finch R H, Queisser H J, Thomas G T & Washburn J, *J. appl. Phys.*, **34** (1963), 406.
10. Ravi K V & Varker C J, *J. appl. Phys.*, **45** (1974), 263.
11. Mahajan S, Rozgonyi G A & Brasen D, *Appl. Phys. Lett.*, **30** (1977), 73.
12. Plaskett T S, *Trans. metallurg. Soc.*, (AIME), **233** (1965), 809.
13. Dekock A J R, *Semiconductor silicon*, edited by H R Huff and E Sirtl, (1977), 508.
14. Bernewitz L & Mayer K R, *Phys. Status Solidi (a)*, **16** (1973), 579.
15. Hurle D T J, *Prog. mater. Sci.*, **10** (1966), 126.

Study of Surface Distortion around Dynamic Impacts on Cleavages of Sodium Bromide Single Crystals

M H ANSARI & S C DATT

Department of Postgraduate Studies & Research in Physics
University of Jabalpur, Jabalpur 482 001

Received 4 January 1980

Single crystals of sodium bromide were grown by Kyropoulos technique and freshly cleaved {100} planes were impacted by a spherical ball. The indentations caused due to these dynamic impacts were found to be surrounded by square-shaped slip lines along $\langle 100 \rangle$ directions. The surface distortions were studied by the multiple-beam interferometry. Fizeau fringe patterns show that the steps were formed at the four $\langle 110 \rangle$ corners. The white light fringes of equal chromatic order show a sinking-in along $\langle 100 \rangle$ directions and piling-up along $\langle 110 \rangle$ directions.

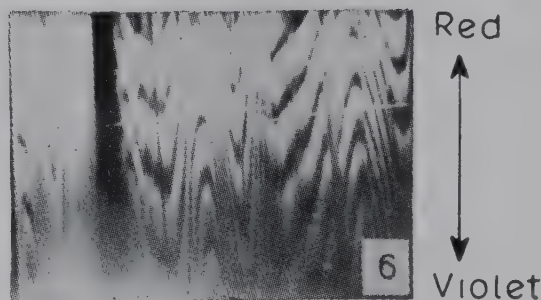
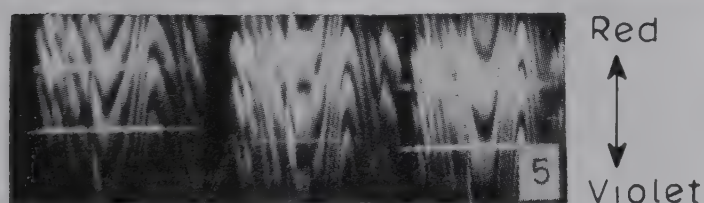
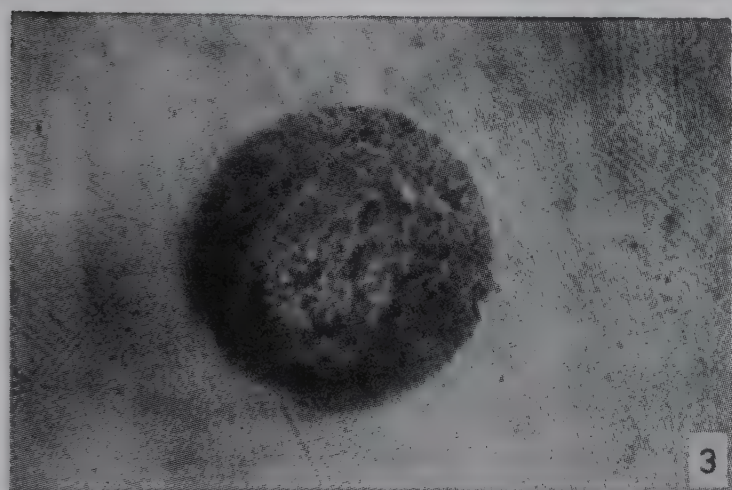
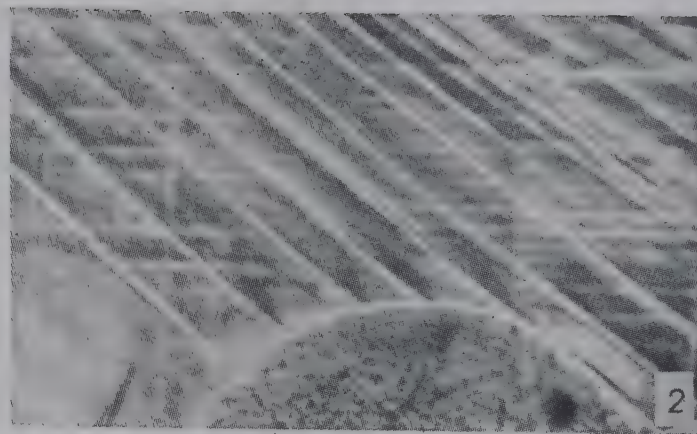
Multiple-beam interferometry has been found to be one of the powerful techniques for studying the details of the surface distortions around indentations.¹⁻⁴ Tolansky and Nichols⁵⁻⁷ used this technique to study the distortions around the hardness test indentations on several metals. The pressure crack figures on diamond faces, tin, silicon carbide and tin-nickel alloy have been studied by different workers.⁸⁻¹² This report is devoted to the study of surface distortions around percussion figures on {100} cleavage planes of sodium bromide single

crystals by the technique of multiple-beam Fizeau fringes and fringes of equal chromatic order.

Single crystals of sodium bromide were grown by Kyropoulos technique from the material of reagent grade purity. After proper annealing, the specimens of high perfection and low dislocation density having approximate dimensions $5 \times 5 \times 3 \text{ mm}^3$ with {100} planes were prepared from the central section of the crystal boule. The {100} planes of the freshly cleaved specimens were subjected to dynamic impacts by steel ball of radius 0.785 mm. The ball was released by an electromagnet and was allowed to fall under gravity through a vertical glass tube.¹³ The velocity was varied by varying the height of the falling ball. The dislocation around the indentation was studied by etching the specimen in glacial acetic acid for about 5-7 sec. For multiple-beam interferometric studies, the impacted specimen was first vacuum coated with silver and then matched against a correctly silvered plane glass plate. The monochromatic light of wavelength 5510 \AA was used for Fizeau fringes. The piling-up and sinking-in around the percussion figures were studied by fringes of equal chromatic order (FECO).⁴ These studies were made using Carl-Zeiss NU 2 universal research microscope. For all the above studies the absolute humidity was held under 8 p/m^3 .

The ball impact with velocity 170 cm/sec on (100) plane along with its phase-contrast is shown in Figs. 1 and 2. It is evident from these photographs that the indentation is surrounded by square-shaped slip lines along $\langle 100 \rangle$ corners. The slip lines are crowded near the indentation; however, the mutual separation between them increases with distance from the indentation. Fig. 3 illustrates the impression of these lines along with other details, from which it is evident that etch pits are found on the slip lines. The slip lines along $\langle 100 \rangle$ and $\langle 110 \rangle$ directions are clearly visible and that a star etch pattern is formed around the indentation. The Fizeau fringe pattern is exhibited in Fig. 4. The fringe quality shows that the cleavage planes are of optical grade and have good reflectivity. The piling-up phenomenon around the indentation is clearly revealed by the loops of the fringes which show that the surface distortion is maximum along $\langle 110 \rangle$ directions. The slip lines produced around the indentation are forming steps which are prominent at the $\langle 110 \rangle$ corners. The piling-up and sinking-in around the indentation were studied by white light fringes of equal chromatic order, which are shown in Fig. 5 (a, b and c) and Fig. 6

NOTES



(a) (b) (c)

(a) (b) (c)

Fig. 1—Ball impact due to a velocity 170 cm/sec ($\times 75$), Fig. 2—Phase-contrast of Fig. 1 ($\times 190$), Fig. 3—Etch pattern around the ball impact ($\times 95$), Fig. 4—Fizeau fringes around the ball impact for a velocity of 170 cm/sec ($\times 75$)

Fig. 5—FECO along $\langle 100 \rangle$ directions, of Fig. 4 at different slit positions, of the spectrograph

Fig. 6—FECO along $\langle 110 \rangle$ directions, of Fig. 4 at different slit positions, of the spectrograph

(a, b and c) for different positions of the slit of the spectrograph along $\langle 100 \rangle$ and $\langle 110 \rangle$ directions, respectively. These fringes show a sinking-in along $\langle 100 \rangle$ directions and a piling-up along $\langle 110 \rangle$ directions.

Sodium bromide has a cubic structure and has a slip system $\{110\} \langle 110 \rangle$. For such a system, when stress is applied on any of the $\{100\}$ planes along $[100]$ direction, the four $\{110\}$ slip planes are equally stressed and multislip occurs on these planes.

These results agree with the theoretical explanation given by Huntington *et al.*¹⁴ and Stokes *et al.*¹⁵. Also, the dislocations generated on the two intersecting slip planes (011) and (101) will pile-up along (110) plane.¹⁶

References

1. Tolansky S, *Multiple-beam interference microscopy of metals*, (Academic Press, New York), 1970.
2. Tolansky S, *Surface microtopography*, (Longmans Green, London), 1960.
3. Tolansky S, *An introduction to interferometry*, (Longmans Green, London), 1955.
4. Tolansky S, *Multiple-beam interferometry*, (Clarendon Press, Oxford), 1948.

5. Tolansky S & Nichols D G, *Phil. Mag.*, **43** (1952), 410.
6. Tolansky S & Nichols D G, *Nature, Lond.*, **164** (1949), 840.
7. Tolansky S & Nichols D G, *Nature, Lond.*, **164** (1949), 113.
8. Howes V R & Tolansky S, *Proc. R. Soc.*, **A230** (1955), 287.
9. Howes V R & Tolansky S, *Proc. R. Soc.*, **A230** (1955), 294.
10. Tolansky S & Williams A P, *Proc. phys. Soc. Lond.*, **68B** (1955), 548.
11. Murty T S, *Interferometric and hardness studies of surfaces of crystals*, Ph D thesis, University of London, London, 1962.
12. Ramanathan V R, *Indian J. pure appl. Phys.*, **13** (1975), 221.
13. Ansari M H, *Surface structural and hardness studies of some single crystals*, Ph D thesis, University of Jabalpur, Jabalpur, 1979.
14. Huntington H B, Dickey J E & Thomson R, *Phys. Rev.*, **100** (1955), 1117.
15. Stokes R J, Johnston T L & Li C H, *Phil. Mag.*, **4** (1959), 920.
16. Cottrell A H, *Trans. Am. Inst. Min. (Metall) Engrs.*, **212** (1958), 192.

Stability of Intramolecular Hydrogen Bond of 8-Hydroxy Quinoline in Different Solvents : IR Spectroscopic Study

I SURYANARAYANA & B K SAIKIA

Regional Research Laboratory, Jorhat 785 006

Received 16 July 1979; revised received 10 September 1979

8-Hydroxyquinoline exhibits a band in the 3μ region of IR spectrum in carbon tetrachloride solution at 3405 cm^{-1} which was assigned to the intramolecular hydrogen bonded OH. The hydrogen bond is stable in non-oxygenated solvents like methylene chloride, carbon disulphide, etc. In chloroform, however, a small proportion of molecules show *trans* form. In strong proton-acceptor solvents like dioxane, diethyl ether, acetone, etc. the chelation is ruptured and intermolecular hydrogen bonds are formed with the solvent molecules. From the relative intensities of the bands corresponding to the OH group of intermolecular hydrogen bonds, the relative proton-accepting abilities of these solvents have been assessed.

8-Hydroxyquinoline, an analytical reagent for the estimation of metal ions like aluminium, iron, etc. is a five-membered chelate. Chelation in this compound is between the hydroxyl group at the 8th position and the quinoline nitrogen atom. The infrared spectra were reported earlier by a number of workers.^{1,2} Mason³ has shown that it exists solely in enol form without undergoing any tautomerization. Srinivasan and Ramaiah⁴ established the presence of intramolecular hydrogen bond in this compound from the shift of the OH band.

Suryanarayana *et al.*⁵ reported the influence of solvents on the chelates of benzoin and methyl mandelate where hydrogen bonds are formed devoid of resonance stabilization. So far, no systematic study has been made on the systems having resonance stabilization, which gives rise to stronger hydrogen bonds. Hence, this study has been undertaken and the results are discussed in this note.

8-Hydroxyquinoline used in the present study is of Merck quality. All the solvents were purified by the procedures available in the literature⁶. Benzophenone, being solid, its saturated solution in carbon tetrachloride was used. The spectra were recorded in the 3μ region on Perkin-Elmer 237 B grating spectrophotometer using KBr matched cells of 0.5 mm thickness. The concentrations of the solutions used were less than 0.1 M. In the ternary mixture study, the mixture of the solvents of the same composition is placed in the reference beam to compensate the solvent absorption. The measurements were made at $37 \pm 2^\circ\text{C}$.

OH band in non-oxygenated solvents—The OH band of 8-hydroxyquinoline in non-oxygenated solvents is around 3400 cm^{-1} (Table 1). These values are slightly lower than those reported by Bellamy.² In cyclohexane, it is at 3410 cm^{-1} and is symmetrical

Table 1—Hydroxy Stretching Frequencies of 8-Hydroxyquinoline in Different Solvents

Solvent	$\nu_{\text{OH}}, \text{cm}^{-1}$	$\Delta\nu_{1/2}, \text{cm}^{-1}$
Cyclohexane	3410	30
Carbon disulphide	3400	50
Carbon tetrachloride	3405	72
Chloroform	3470 (sh)	
	3395	122
Dichloromethane	3400	100
Acetonitrile	3380	155
	3300 (sh)	
Dioxane	3300	267
Diethyl ether	3400	100
	3300 (sh)	
Anisole	3390	94
Diphenyl ether	3390	80
Acetone	3390 (sh)	
	3340	90
Acetophenone	3385	122
	3330	
Benzophenone	3400	90
sh = shoulder		

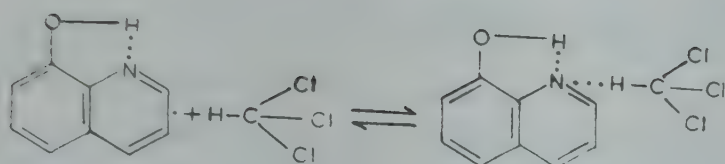


Fig. 1—Structural diagram showing the influence of chloroform on hydroxyl group

and sharp. The band shifts towards lower frequencies with an increase in the half bandwidth as the polarity of the solvent increases. The maximum shift is observed in the case of acetonitrile (30 cm^{-1}). In chloroform, the OH band is accompanied by a shoulder at 3470 cm^{-1} which may be assigned to the hydroxyl group which is under the influence of chloroform molecules trying to form a hydrogen bond with the nitrogen atom (Fig. 1). The bandwidth is greater compared to other chlorinated solvents like CCl_4 and CH_2Cl_2 . This increased bandwidth which is an indication of the presence of more than one species also supports the interaction of chloroform trying to form the hydrogen bond with the nitrogen atom forcing the OH group to take *trans* configuration.

OH band in ethereal solvents—In dioxane, the band due to the OH group is observed at 3300 cm^{-1} . The band is asymmetric and its width is very large. The position of the band is almost the same as that of phenol in dioxane, which implies that the hydroxyl group is in hydrogen bond formation with dioxane molecules. This, in turn, shows that the chelate is broken and intermolecular hydrogen bonded species (associated species) are formed. The asymmetry of the band also indicates the presence of more than one species. This is found to be true when the spectra are recorded in ternary mixtures. In a mixture of 0.1 ml of dioxane in 0.9 ml of CCl_4 , the band at 3400 cm^{-1} is the main band and the 3300 cm^{-1} band is observed only as a shoulder. With the increase in relative proportion of dioxane, the intensity of the shoulder increases. The presence of shoulder indicates the formation of associated species with dioxane molecules and their relative proportion increases in the more concentrated solutions. In anisole and diphenyl ether also the bands are observed at 3400 cm^{-1} . In anisole, however, the band is slightly asymmetric towards the lower frequency side whereas in diphenyl ether it is almost symmetrical. These observations indicate that anisole contains a small proportion of associated species and diphenyl ether contains almost the chelate species.

OH band in ketonic solvents—In acetone, the OH band at 3340 cm^{-1} is due to the associated species and the shoulder at 3390 cm^{-1} is due to the chelate

species. The band assignments have been confirmed by ternary mixture study. The intensities of the two bands indicate that acetone solution contains a small proportion of chelate species. Similarly, in acetophenone the two bands due to the chelate species and associated species are at 3385 cm^{-1} and 3330 cm^{-1} . It appears from the intensities of the two bands that the chelate and associated species are almost in equal proportion. In benzophenone solution, however, only one band is observed at 3400 cm^{-1} with a slight asymmetry towards the lower frequency side indicating the presence of a small proportion of associated species.

Relative interacting abilities of the solvents—As the associated species are formed only when the chelate is ruptured by the solvent, the proportion of the associated species gives a direct measure of the interacting abilities of the solvents.

From the results presented earlier, the proportion of associated species in different ethereal solvents is seen to be in the order dioxane > diethyl ether > anisole > diphenyl ether.

The marked decrease in the donor ability of anisole oxygen compared to that of diethyl ether is due to the involvement of the lone pair of electrons of oxygen in the mesomeric interaction with the phenyl ring. The donor ability of diphenyl ether is further reduced because of enhanced conjugation.

In different ketonic solvents, the proportion of associated species is in the order acetone > acetophenone > benzophenone. The decreasing tendency to form associated species of these ketones can be explained on the basis of steric effects even though the donating capacity of the carbonyl oxygen increases in the order benzophenone > acetophenone > acetone.

The overall interacting abilities of the solvents from the associated species formed with the chelate are in the order non-oxygenated solvents < diphenyl ether < anisole < benzophenone < diethyl ether < acetophenone < dioxane < acetone.

The authors wish to express their gratitude to Dr G Thyagarajan, Director, Regional Research Laboratory, Jorhat, for his constant encouragement.

References

1. Badger G M & Moritz A C, *J. chem. Soc.*, (1958), 3471.
2. Bellamy L J, *Trans. Faraday Soc.*, 55 (1959), 220.
3. Mason S F, *J. chem. Soc.*, (1957), 4874.
4. Ramaiah K. & Srinivasan V R, *Proc. Indian Acad. Sci.*, 55 (1962), 360.
5. Suryanarayana I, Subrahmanyam B & Subba Rao N V, *Proc. Indian Acad. Sci.*, 82A (1975), 55.
6. *Techniques of organic chemistry*, Vol. VII, edited by P P Weissberger, J R Riddick & E E Troops (Interscience, New York), 1955, 367, 372, 381, 411, 425.

Elastic Constants of Phloroglucinol Dihydrate by X-Ray Diffuse Scattering

SURESH CHANDRA

Physics Department, Allahabad University
Allahabad 211 002

Received 28 May 1979; revised received 27 October 1979

All the nine elastic constants of the molecular crystal phloroglucinol dihydrate have been determined at room temperature from a photographic study of the 400, 060, 002, 103 and 031 diffuse reflections. The values of the constants (in 10^{10} dyne/cm²) are: $C_{11} = 2.53$; $C_{22} = 2.94$; $C_{33} = 5.92$; $C_{44} = 14.16$; $C_{55} = 6.76$; $C_{66} = 4.05$; $C_{12} = 5.02$; $C_{23} = 0.34$; and $C_{13} = 1.01$. Each elastic constant has been evaluated from two directions of wave vector.

In the present investigation all the nine elastic constants of orthorhombic crystals of phloroglucinol dihydrate (PD) have been determined from a study of X-ray thermal diffuse scattering from selected planes. The photographic method of recording diffuse reflection was preferred as only small single crystals are needed; it is more suitable than other methods where large and oriented single crystals are necessary.

This method was first applied for the determination of elastic constants of cubic crystals by Ramachandran and Wooster¹ and was later extended to non-cubic crystals by many workers.²⁻⁷ A detailed account of the method applied to molecular crystal was reported by Amoros and Amoros.⁸

Theory—The ratio of the intensity of first order diffuse scattering of X-rays (I_d) from a crystal of volume δv to that of the incident beam (I_0) corresponding to a particular thermal wave vector q (where $q \rightarrow 0$) and the reciprocal lattice point hkl is given by the expression,¹

$$I_d/I_0 = \frac{\epsilon^2 k_B T}{V} F_T \delta v \frac{Q^2}{q^2} K [u v w]_{hkl} \quad \dots(1)$$

where k_B is the Boltzmann's constant, T the temperature at which observations are taken, F_T the structure factor at temperature T for the reflection hkl , Q the reciprocal lattice vector, V the volume of the unit cell, and ϵ the amplitude scattered by a free electron (given by Thomson's formula).

$$K [u v w]_{hkl} = L^2 A_{11}^{-1} + M^2 A_{22}^{-1} + N^2 A_{33}^{-1} \\ + 2 M N A_{23}^{-1} + 2 N L A_{13}^{-1} + 2 M L A_{12}^{-1} \quad \dots(2)$$

where L , M , N and u , v , w are the direction cosines of Q and q respectively with reference to the orthogonal elastic axes. A_{ij}^{-1} are the elements of the matrix A_{ij}^{-1} , which is inverse to the matrix A_{ij} given for

orthorhombic crystals by

$$\begin{Bmatrix} A_{11} \\ A_{22} \\ A_{33} \\ A_{23} \\ A_{13} \\ A_{12} \end{Bmatrix} = \begin{Bmatrix} C_{11} & C_{66} & C_{55} & 0 & 0 & 0 \\ C_{66} & C_{22} & C_{44} & 0 & 0 & 0 \\ C_{55} & C_{44} & C_{33} & 0 & 0 & 0 \\ 0 & 0 & 0 & C_{23} + C_{44} & 0 & 0 \\ 0 & 0 & 0 & 0 & C_{13} + C_{55} & 0 \\ 0 & 0 & 0 & 0 & 0 & C_{12} + C_{66} \end{Bmatrix} \begin{Bmatrix} u^2 \\ v^2 \\ w^2 \\ vw \\ uw \\ uv \end{Bmatrix} \quad \dots(3)$$

For a particular direction of propagation of thermal wave, the value of q is calculated from the known orientation of the crystal with respect to the incident beam. Hence, from the measurements of I_d and I_0 , the values of $K [u v w]_{hkl}$ can be evaluated using Eq. (1) and from it, the elastic constants can be determined.

Experimental details—Crystals of PD were obtained from a solution in alcohol and recrystallized from water at room temperature. Crystals of approximately 10^{-3} cm³ size examined by Laue photographs and polarizing microscope for any strain and defects were chosen for the study. Powder diffraction lines of aluminium on the photographs were used for the calibration of the angle of diffraction to a high degree of accuracy.

The crystal reflected monochromatic X-ray beam (Cu K α) obtained from calcite was used for final record of the diffuse reflection at the correct orientation of the crystal, known from the Laue photographs taken with white radiation. The average exposure time was 25-30 hr. The X-ray tube was operated at 20kV and 25mA to avoid higher harmonics.

Observations at different mis-settings from the Bragg position were taken. The direct beam intensity was reduced using nickel foils placed before the film. Thickness of the foils was adjusted to suit the intensity of diffuse spot. Each picture thus taken contained the diffuse reflection, the direct beam image and the powder lines of aluminium. Each photograph was developed in fresh developer along with the calibration wedge strip used for the standardization of the intensity. The intensity distribution of the diffuse reflection and intensity of the direct beam were scanned with a photometer (Moll). The intensities were computed from the ordinates of the photometric curve by calibration with the calibration wedge.

Value of I_d corresponding to a particular thermal wave vector was corrected for general or background scattering, skew, polarization and divergence. Corrections for absorption and second order scattering

were not done as these were expected to be within the limits of accuracy of the intensity measurements by photographic method.

Results and discussion—The crystals of PD are orthorhombic with cell data: $a = 6.73$; $b = 13.58$, $c = 8.09$ Å; and space group $Pnma$.⁹ Wallwork and Powell⁹ observed some interesting X-ray diffuse scattering effects due to structural disorder. Recently, Singh and Singh¹⁰ thoroughly studied the growth and disorder of PD and reported an ordered structure for the needle-shaped crystals grown from aqueous solution. X-ray thermal diffuse scattering could be studied taking needle-shaped crystals possessing no surface features and by a systematic analysis of reciprocal space.

The reciprocal lattice points used for the evaluation of the constants are of the type $h00$, $0k0$, $00l$, $0kl$ and $h0l$. The reciprocal planes studied and the values of their structure factors and Bragg angles are as follows:

Index of plane	Structure factor	Bragg angle
400	66.80	27°14'
060	50.00	19°53'
002	28.16	10°59'
031	42.48	11°14'
103	37.44	18°05'

The criterion discussed in detail by Ramachandran and Wooster¹ was used to select reflections for the present study. Elastic constants C_{11} , C_{22} , C_{33} , C_{44} , C_{55} and C_{66} were determined independently from $K[u v w]_{hkl}$ values. The remaining constants C_{12} , C_{23} and C_{13} were derived from the $K[u v w]_{hkl}$ values in specified directions, e.g. $[1/\sqrt{2} \ 0 \ 1/\sqrt{2}]$, and the independent constants C_{11} , etc.

The corrected I_d was plotted against the square of the wavelength of the corresponding thermal wave ($\lambda_t = 1/q$) for different directions of propagation vector and different reciprocal lattice points (Fig. 1).

It is evident from Eq. (1) that the plot of I_d versus λ_t^2 for a particular reciprocal lattice point and a particular direction of propagation of the thermal wave should be a straight line passing through the origin (if background is subtracted from I_d). Since the slope of the straight line gives $I_d \propto |q|^2$, and other quantities in Eq. (1) are known, values of $K[u v w]_{hkl}$ can be calculated, which in turn gives the values of elastic constants (Table 1).

The accuracy of determination of the elastic constants is primarily dependent on the accuracy of measurement of I_d/I_0 . The constants of C_{11} , C_{22} ,

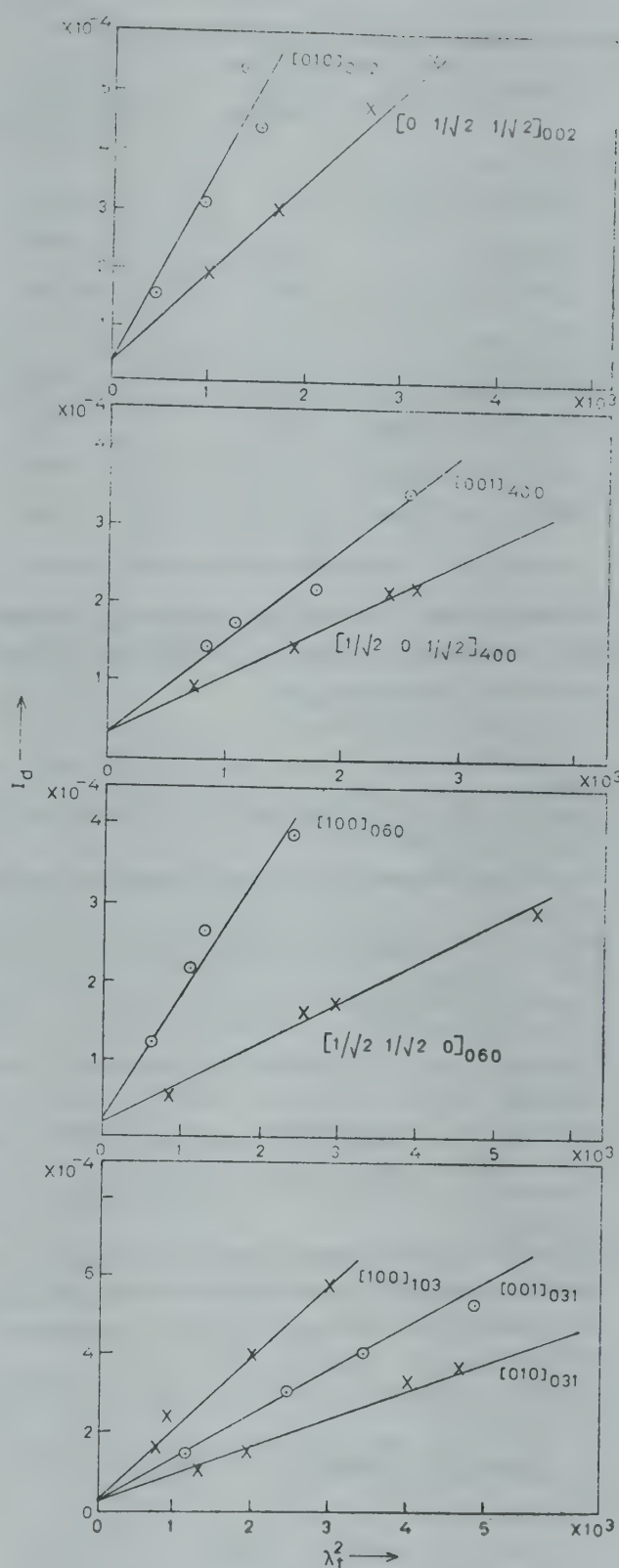


Fig. 1— I_d versus λ_t^2 of the elastic wave for various reflections and propagation vectors

C_{33} , C_{44} , C_{55} and C_{66} which depend on single $K[u v w]_{hkl}$ values are estimated to be accurate within $\pm 8\%$, whereas the accuracy of C_{12} , C_{13} and C_{23} , which depend on two K 's, is estimated to be $\pm 12\%$.

A possible correlation between elasticity data and crystal structure will be reported later.

The author is grateful to Dr M P Hemkar and Prof. Vachaspati for their encouragement and inte-

Table 1—Values of Elastic Constants

K direction	Elastic constant	Value 10^{10} dyne cm^{-2}
K[100] ₁₀₃	C_{11}	2.53
K[010] ₀₃₁	C_{22}	2.94
K[001] ₀₃₁	C_{33}	5.92
K[010] ₀₀₂	C_{44}	14.16
K[001] ₄₀₀	C_{55}	6.76
K[100] ₀₆₀	C_{66}	4.05
K[1/√2 1/√2 0] ₀₆₀	C_{12}	5.02
K[1/√2 0 1/√2] ₄₀₀	C_{13}	1.01
K[0 1/√2 1/√2] ₀₀₂	C_{23}	0.34

rest in the work. Financial assistance under the scheme of Scientists' pool of CSIR, New Delhi, is also gratefully acknowledged.

References

1. Ramachandran G N & Wooster W A, *Acta crystallogr.*, 4 (1951), 335, 431.
2. Prince E & Wooster W A, *Acta crystallogr.*, 6 (1953), 450.
3. Prasad S C & Wooster W A, *Acta crystallogr.*, 8 (1955), 614.
4. Prasad S C & Wooster W A, *Acta crystallogr.*, 9 (1956), 35, 38, 169, 304.
5. Chakraborty S C & Sen R K, *Bull. Natl. Inst. Sci. India*, 14 (1958), 20.
6. Joshi S K & Kashyap B M S, *Acta Crystallogr.*, 17 (1964), 629.
7. Chandra S & Hemkar M P, *Acta crystallogr.*, A29 (1973), 25.
8. Amoros J L & Amoros M, *Molecular crystals: Their transforms and diffuse scattering* (John Wiley, New York).
9. Wallwork S C & Powell H M, *Acta crystallogr.*, 10 (1957), 48.
10. Singh S R & Singh G, *J. Crystal Growth*, 44 (1978), 58.

Sputtered Molybdenum Film Resistors

AWATAR SINGH

Solid State Devices Division, Central Electronics
Engineering Research Institute, Pilani 333 031

Received 31 December 1979

Sputtered molybdenum film resistors have been fabricated on oxidized silicon wafers and 7059 glass substrates. The sheet resistance in the range 100-1000 ohm/sq has been obtained. The temperature coefficient of resistance has been found to be negative and in the range of 200 to 1000 ppm/°C. Such a resistor can be used as thermistors.

Although molybdenum is not a new material in semiconductor technology, it has been used for years in semiconductor power devices; its self-aligning

gate feature, high melting point, high electrical and thermal conductivity and good match of thermal expansion with silicon make it ideal for use in digital VLSICs. In earlier works¹⁻⁷ the fabrication of moly gate MOSFETs and the study of its resistivity, fine line pattern ability, adhesion to various substrates and stability were described. This note reports the results of the study of sputtered molybdenum film resistors on glass and oxidized wafers.

The molybdenum film was deposited on substrates using an rf diode sputtering unit (Edwards Make No. E 12E3). The unit had a water-cooled sputtering target and 3 kVA internal power supply. A sheet of high purity 99.999% molybdenum (3 in. diameter) was used as the cathode, and the substrate was placed on an earthed anode immediately below the cathode such that the cathode-substrate spacing was 5 cm. The rf supply was obtained by modifying an old rf induction heater to obtain about 1 kV rms at a frequency of 1 MHz. A set of suitable deposition and etching conditions was found by experiments and used as standard. It was estimated that around 60 W of rf power was used for deposition and etching. The sputtering parameters were as follows:

Background vacuum	100 ⁻⁵ torr
Sputtering pressure	0.2 torr
Sputtering rate	200 Å/min
Power	60 W
Gas	99.999% argon
Film thickness of moly	100-1000 Å

The film resistors were made by depositing the aluminium film 1 µm thick on the sputtered moly film in another vacuum coater and by using sputter etching technique^{5,6} to delineate the patterns and to remove the photoresist. The wet chemical etching technique for film resistor fabrication was also tried but the former proved much better in terms of pattern delineation and reproducibility.

The sheet resistance was measured by four-point probe and the TCR was measured using a deviation bridge. The results are given in Table 1. We see that the TCR increases with sheet resistance and remains always negative. Moreover, the TCR is more negative for resistors on oxidized silicon wafers. It is because, the oxide surface is not as smooth as the glass surface.

The heat treatment given to the resistor, rendered its behaviour highly unpredictable, i.e. it made the TCR to increase/decrease irregularly. This is because the unprotected film behaves erratically. However, when some sort of film protection, i.e. photoresist layer was given, it made the film to behave

Table 1—TCR on Glass Substrate

Sheet resistance ohm/sq	7059 glass substrate	TCR in ppm/°C oxidized silicon wafer
100	-200	-300
200	-300	-300
500	-500	-600
1000	-1100	-1200

predictably. It indicates that for fabricating a useful moly film resistor, a protective layer must be applied to them.

Since the TCR of the film is high, we feel that such resistors can be used as thermistors.

References

1. Singh, A, *Instn Electron. Telecomm. Engrs. India, Students J.*, 20 (1979), 179.
2. Singh A, *Proc. IEEE*, 68 (1980), 536.
3. Singh A & Kemhadjian H A, *Microelectron & Reliab.* (1979). In press
4. Singh A, *J. Instn Electron. Telecomm. Engrs India*, 26 (1890), 299.
5. Singh A, SSD/Int. Memo/78-IV.
6. Singh A, *Micro-electronics & Reliab.*, 20 (1980), 293.
7. Singh A, *Solid St. Electron.*, (1979), In press.

Slater-Condon & Spin-Orbit Parameters for Tm^{3+} in Thulium Sulphate, Thulium Ethyl Sulphate & Zinc Sulphide

S V J LAKSHMAN & C K JAYA SANKAR

Department of Physics, S V University, Tirupati 517 502

Received 20 August 1979; revised received 31 December 1979

The partial derivatives for Tm^{3+} ion have been evaluated for the first time. The values of Slater (F_2, F_4, F_6), interelectronic repulsion and spin-orbit (ξ_{4f}) parameters have been evaluated for Tm^{3+} from the reported spectral data of $\text{Tm}_2(\text{SO}_4)_3 \cdot 8\text{H}_2\text{O}$, $\text{Tm}(\text{C}_2\text{H}_5\text{SO}_4)_3 \cdot 9\text{H}_2\text{O}$ and Tm^{3+} in ZnS crystals. The nature of the bonding is found to be ionic in thulium sulphate and covalent in thulium ethyl sulphate and zinc sulphide.

Optical absorption spectrum of thulium sulphate was studied by Bethe and Spedding.¹ Wong and Richman² reported the analysis of the absorption spectrum and Zeeman effect of thulium ethyl sulphate. Ibuki and Langer³ studied the spectrum of Tm^{3+} in ZnS. Petrov⁴ reported the spectrum of thulium perrehenate tetrahydrate. Since Racah and spin-orbit parameters are only available for thulium perrehenate tetrahydrate⁴ and not for others, the authors have taken up the present study. Partial derivatives are required, to evaluate these parameters by Taylor's series expansion method. Since they

are not readily available in literature (for Tm^{3+}), the authors have calculated them, following Wong.⁵

In the first order approximation, the energy E_J of the level J is given by

$$E_J = E_{0J} + \frac{dE_J}{dF_2} \Delta F_2 + \frac{dE_J}{dF_4} \Delta F_4 + \frac{dE_J}{dF_6} \Delta F_6 + \frac{dE_J}{d\xi_{4f}} \Delta \xi_{4f} \quad \dots(1)$$

where E_{0J} is zero order energy of the level J , and dE_J/dF_K and $dE_J/d\xi_{4f}$ are partial derivatives. Further

$$\left. \begin{aligned} \Delta F_2 &= F_2 - F_2^0 \\ \Delta F_4 &= F_4 - F_4^0 \\ \Delta F_6 &= F_6 - F_6^0 \\ \Delta \xi_{4f} &= \xi_{4f} - \xi_{4f}^0 \end{aligned} \right\} \quad \dots(2)$$

where F_2^0, F_4^0, F_6^0 and ξ_{4f}^0 are the free ion parameters and F_2, F_4, F_6 and ξ_{4f} are the parameters of the ion in the crystal.

The energy expressions inclusive of electrostatic and spin-orbit interactions for the different electronic states arising from $4f^{12}$ configuration of Tm^{3+} are taken from Dieke⁶ with the sign of ξ reversed. These expressions are solved for the free ion (F_2^0, F_4^0, F_6^0 and ξ_{4f}^0) parameters. These parameters are increased one after another by one unit and each time the energies of the levels are calculated. The respective partial derivatives dE_J/dF_K and $dE_J/d\xi_{4f}$ are thus evaluated. However, for convenience, the parameter F_6^0 was increased by 0.1 unit and the energy difference was multiplied by a factor of 10 in order to obtain dE_J/dF_6 value. These values are presented in Table 1.

Using the E_{0J} values and the partial derivatives given in Table 1 and using the experimental band position as E_J for the respective energy levels, Eq. (1) was solved by the least squares method⁷ for the evaluation of $\Delta F_2, \Delta F_4, \Delta F_6$ and $\Delta \xi_{4f}$ values. From the known free ion values, the Slater-Condon (F_2, F_4 and F_6) and spin-orbit ξ_{4f} parameters for the Tm^{3+} ion in the respective crystals are calculated.

The rms deviation is calculated from the formula

$$\sigma = \left(\frac{\sum \Delta_i^2}{N} \right)^{1/2} \quad \dots(3)$$

where Δ_i is the deviation and N is the number of energy levels fitted.

The nephelauxetic ratio β is defined as⁸

$$\beta = \nu_c/\nu_a \quad \dots(4)$$

where ν_c and ν_a refer to the energies of the corresponding transitions in the complex¹⁻³ and the aquo-ion⁹ respectively. The β values for all the observed transitions are computed and their average value $\bar{\beta}$ is used to estimate¹⁰ the parameter of bonding δ

Table 1—The Zero Order Energies and Partial Derivatives of the Energies with Respect to F_2 , F_4 , F_6 and ξ_{4f} for Tm^{3+}

Level	E_0	$\frac{dE}{dF_2}$	$\frac{dE}{dF_4}$	$\frac{dE}{dF_6}$	$\frac{dE}{d\xi_{4f}}$
$^3\text{H}_6$	0	0	0	0	0
$^3\text{H}_4$	5475.7	7.55	53.71	-146.32	-0.20
$^3\text{H}_5$	8282.0	-0.46	-0.55	-0.13	3.22
$^3\text{F}_4$	12568.7	2.92	24.73	-61.37	3.77
$^3\text{F}_3$	14243.5	14.54	17.45	-273.13	3.21
$^3\text{F}_2$	14820.0	21.71	4.75	-82.18	2.00
$^1\text{G}_4$	21258.7	-1.85	85.91	25.31	6.06
$^1\text{D}_2$	27779.0	48.52	16.82	-275.62	2.53
$^1\text{I}_6$	34011.4	49.08	58.89	13.74	2.92
$^3\text{P}_0$	35303.3	70.30	91.79	-1122.83	2.14
$^3\text{P}_1$	36102.2	69.54	83.45	-1274.13	3.21
$^3\text{P}_2$	38023.1	57.39	30.77	-461.58	5.11
$^1\text{S}_0$	77232.3	83.78	240.11	1577.57	4.28
Free ion values: $F_2 = 451.1$, $F_4 = 68.07$, $F_6 = 7.437$, $\xi_{4f} = 2656$					

Table 2—Experimental, Calculated Energy Levels and Bonding Parameters for Tm^{3+} in $\text{Tm}_2(\text{SO}_4)_3 \cdot 8\text{H}_2\text{O}$

Energy level	Aquo-Ion, cm^{-1}	E_{exp} , cm^{-1}	$E_{\text{calc.}}$, cm^{-1}	$(E_{\text{exp}} - E_{\text{calc.}})$, cm^{-1}
$^3\text{F}_4$	12700	12750	12851.6	-101.6
$^3\text{F}_3$	14500	14600	14550.2	49.8
$^3\text{F}_2$	15100	15150	15038.7	111.3
$^1\text{G}_4$	21350	21500	21475.7	24.3
$^1\text{D}_2$	28000	28000	28057.7	-57.7
rms deviation	—	—	—	76.0
$\bar{\beta}$	—	—	—	1.0042
δ (%)	—	—	—	-0.4216

(in per cent for each complex) using the relation

$$\delta = \left(\frac{1 - \bar{\beta}}{\bar{\beta}} \right) \times 100 \quad \dots(5)$$

Depending on the ligands the values of δ may be positive or negative indicating covalent or ionic bonding.

The observed and calculated energy values for Tm^{3+} in thulium sulphate, thulium ethyl sulphate and zinc sulphide are presented in Tables 2 and 3 along with the $\bar{\beta}$ and δ values. The rms deviations are also given in these Tables.

The evaluated interelectronic repulsion and spin-orbit parameters for Tm^{3+} in the three host crystals are presented in Table 4. It is interesting to note that the ratios F_4/F_2 and F_6/F_2 are each equal to

Table 3—Experimental, Calculated Energy Levels and Bonding Parameters for Tm^{3+} in $\text{Tm}(\text{C}_2\text{H}_5\text{SO}_4)_3 \cdot 9\text{H}_2\text{O}$ and ZnS

Energy level	E_{exp} , cm^{-1}	$E_{\text{calc.}}$, cm^{-1}	$(E_{\text{exp}} - E_{\text{calc.}})$, cm^{-1}
In $\text{Tm}(\text{C}_2\text{H}_5\text{SO}_4)_3 \cdot 9\text{H}_2\text{O}$			
$^3\text{F}_4$	12673	12748.5	-75.5
$^3\text{F}_3$	14446	14409.0	37.0
$^3\text{F}_2$	15092	15009.2	82.8
$^1\text{G}_4$	21276	21258.0	18.0
$^1\text{D}_2$	27926	27968.9	-42.9
rms deviation	—	—	57.0
$\bar{\beta}$	—	—	0.9975
δ (%)	—	—	0.2504
In ZnS			
$^3\text{F}_4$	12503	12612.5	-109.5
$^3\text{F}_3$	14341	14287.4	53.6
$^3\text{F}_2$	14916	14796.0	120.0
$^1\text{G}_4$	21016	20989.9	26.1
$^1\text{D}_2$	27517	27579.1	-62.1
rms deviation	—	—	82.0
$\bar{\beta}$	—	—	0.9857
δ (%)	—	—	1.4519

Table 4—Computed Values of Various Parameters of Tm^{3+} in Free ion, Sulphate, Ethyl Sulphate and Zinc Sulphide

Parameter	Thulium Free-ion cm^{-1}	$\text{Tm}^{3+}:\text{Tm}_2$ $(\text{SO}_4)_3 \cdot 8\text{H}_2\text{O}$ cm^{-1}	$\text{Tm}^{3+}:\text{Tm}$ $(\text{C}_2\text{H}_5\text{SO}_4)_3 \cdot 9\text{H}_2\text{O}$ cm^{-1}	$\text{Tm}^{3+}:\text{ZnS}$ cm^{-1}
F_2	451.1	452.21	453.53	445.02
F_4	68.07	63.53	61.66	60.51
F_6	7.437	7.273	7.618	7.198
ξ_{4f}	2656.0	2757.24	2746.74	2718.02
F_4/F_2	0.151	0.140	0.136	0.136
F_6/F_2	0.016	0.016	0.017	0.016

0.151 and 0.016 respectively for the free ion of Tm^{3+} and are almost the same for the ion in crystals.

As is seen from Tables 2 and 3 the nature of the bonding is covalent in thulium ethyl sulphate and zinc sulphide while it is ionic in thulium sulphate. The magnitude of the bonding parameter suggests greater covalency in ZnS than in ethyl sulphate.

One of the authors (CKJS) is grateful to the Department of Science and Technology, New Delhi for the grant of a junior research fellowship.

References

1. Bethe H A, Spedding F H, *Phys. Rev.*, **52** (1937), 454.
2. Wong E Y, Richman J, *J. chem. Phys.*, **34** (1961), 1182.

3. Ibuki S I & Langer D, *J. chem. Phys.*, **40** (1964), 796.
4. Petrov K I, Orlin N A & Plyshchev V E, *Optics and spectrosc.*, **27** (1969), 189.
5. Wong E Y, *J. chem. Phys.*, **35** (1961), 544.
6. Dieke G H, *Spectra and energy levels of rare earth ions in crystals* (Interscience Publishers, New York), 1968.
7. Scarborough J B, *Numerical mathematical analysis* (Oxford Publishing Co., Oxford), 1966.
8. Tandon S P & Mehta P C, *Spectrosc. Lett.*, **2** (1969), 255.
9. Carnall W T, Fiels P R & Rajanak K, *J. chem. Phys.*, **49** (1968), 4424.
10. Sinha S P, *Spectrochim. Acta*, **22** (1966), 57.

PMR Study of Intramolecular Motion in Solid 2,4-Dinitrophenyl Hydrazine

ALPANA ROY & R C GUPTA

Department of Physics, Lucknow University, Lucknow

Received 29 September 1979

NMR studies of solid 2, 4-dinitrophenyl hydrazine have been carried out in the temperature range 77-393 K. An agreement has been observed between the experimental values of the second moment obtained from the derivative curves of the PMR absorption line for the sample and the calculated value of the second moment for a rigid lattice, indicating that the lattice is rigid up to the transition temperature. The observed reduction in the value of the second moment accompanied by further narrowing of the line-width observed with rise in temperature, in the range 298-393 K, has been explained as due to rotation of NH.NH₂ group about its C—N bond as well as —NH₂ group about its N—N bond.

The NMR study of 2, 4-dinitrophenyl hydrazine has been carried out in an effort to gain information regarding the structure and molecular mobility of the NH.NH₂ group. It is interesting to note that there is no hydrogen bond which may hinder such a motion in this crystal. The molecular motion inside the crystal lattice modifies the local field to a great extent which results in the reduction of the second moment.

In the absence of any precise data regarding the molecular structure, a model of the compound assuming the standard values of the bond distances and angles was made. Structural parameters from the other molecules such as benzene derivatives and hydrazine have also been a basis of the choice. The atomic coordinates of various hydrogen positions in the molecule were calculated assuming the following data:

The ring was assumed to be unsymmetrical with bond distances C—H = 1.09 Å, C—C = 1.45 Å, C—N = 1.41 Å, ∠ NNH = 121°. The N—H bond connecting the —NH.NH₂ group was assumed to be 1.02 Å. The NH.NH₂ group is assumed to be in

the plane of the ring and the molecular model is shown in Fig. 1.

Wide-line PMR experiments were done at TIFR, Bombay, on Varian Associate frequency spectrometer and an associated nuclear induction probe with 12 in. magnet system. The derivative tracings were recorded at 7.5 MHz.

The experimental values of the second moment for 2, 4-dinitrophenyl hydrazine at various temperatures were calculated from the derivative curves obtained at these temperatures. Calculations were done by making use of the trapezium rule which gives the value of second moment as

$$S_2 = \frac{\sum h^3 f(h)}{3 \sum h f(h)}$$

The value of the second moment at 77 K thus calculated was found to be 16.72 gauss².

Theoretical rigid lattice value of the second moment calculated from the expression based on Van Vleck's¹ theory for a polycrystalline sample consists of two parts, viz. intramolecular (*S*₁) and intermolecular (*S*₂).

*S*₁ of 2, 4-dinitrophenyl hydrazine has been calculated using Bearden and Watt's² values of physical constants using the relation.

$$S_1 = \frac{715.9}{N} \sum_{j \neq K} \gamma_{jK}^{-6}$$

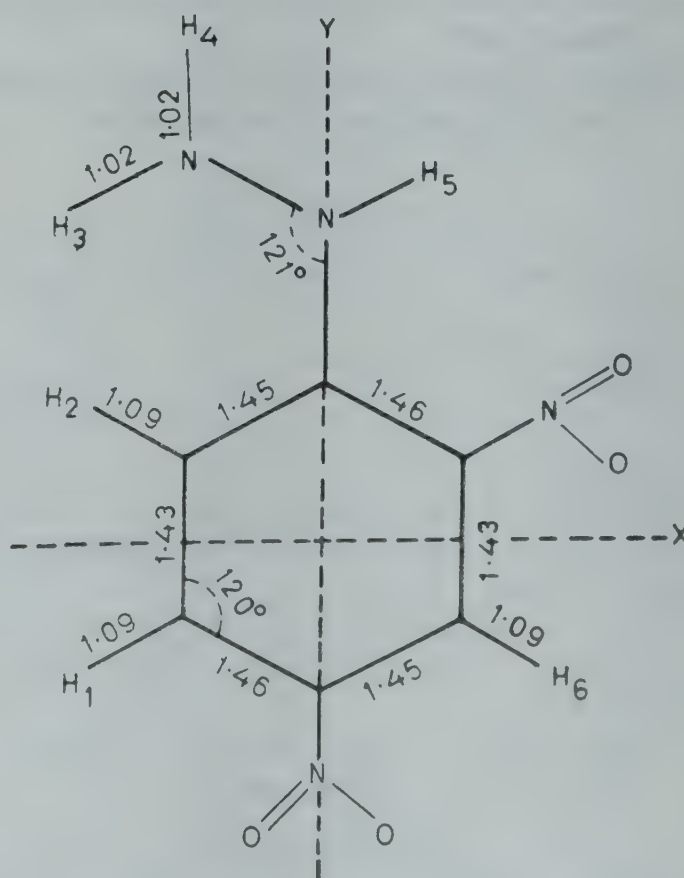


Fig. 1—Structural formula of 2, 4-dinitrophenyl hydrazine molecule

where, N is the number of magnetic nuclei over which the sum is taken. The value of S_1 is found to be 15.52 gauss^2 . The S_2 for 2, 4-dinitrophenyl hydrazine is calculated following the method adopted by Andrew and Eades³. Its value is found to be 1.57 gauss^2 . The theoretical rigid lattice value of second moment ($S_1 + S_2$) hence is 17.09 gauss^2 .

Thus at 77 K the experimental mean value of the second moment 16.72 gauss^2 appears to be in satisfactory agreement with the theoretically calculated value of 17.09 gauss^2 , for rigid lattice configuration. This implies that the lattice is effectively rigid at lower temperature, when all the molecular motions are considered to be frozen. The second moment data are thus consistent with our assumed model of 2,4-dinitrophenyl hydrazine. From Fig. 2 we observe that between 77 and 298 K, the second moment versus temperature curve possesses a slight downward slope. This slope may be assigned to the torsional oscillations of the $-\text{NH.NH}_2$ group which are capable of occurring at such low temperatures. Beyond 298 K, there is a rapid fall in the value of the second moment and also in the line-width (Fig. 2) indicating the onset of molecular motion in the crystal lattice. The molecular motion can take place by only imparting sufficient energy (in our case thermal energy) to enable the molecule to surmount the potential barrier hindering the motion. Two distinct possibilities arise:

- (i) The molecule may rotate about one of its symmetry axes.
- (ii) The $-\text{NH.NH}_2$ group may rotate about the C—N bond joining it to the phenyl ring.

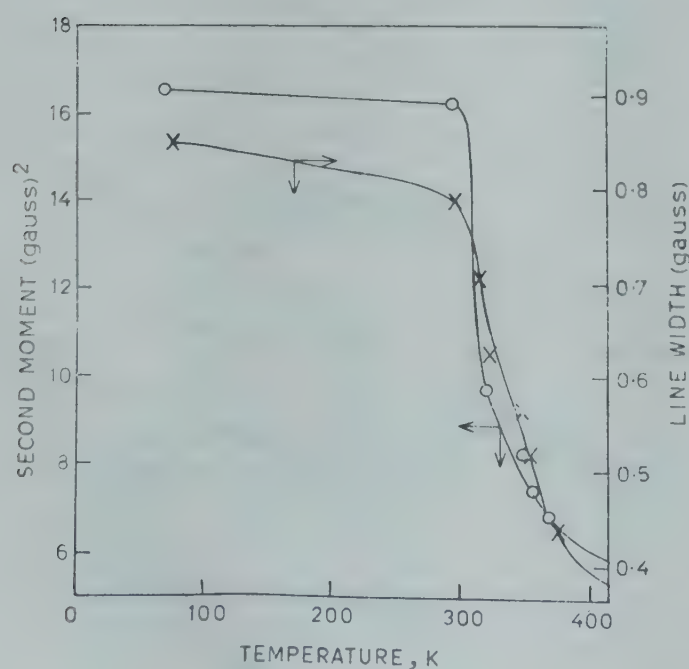


Fig. 2—Plot of temperature versus second moment and line width of 2, 4-dinitrophenyl hydrazine molecule

The possibility of molecular reorientation about its symmetry axis is completely ruled out, because by the addition of two nitro groups to the phenyl hydrazine molecule, its molecular size will increase producing greater internal friction. Molecular reorientation also does not agree with the theory given by Gutowsky and Pake.⁴

The reduction in the second moment and line-width at higher temperatures may be accounted for by the rotational motion of the side chain group. It is interesting to note that $-\text{NH.NH}_2$ group is not only capable of intramolecular rotation around its C—N bond but the $-\text{NH}_2$ group is capable of rotating around its N—N bond which has also been supported by Ulich *et al.*⁵ So it is evident that the addition of one more rotating group in the molecule increases the contribution of intramolecular rotation. This contribution appears to have produced a greater effect in reducing the value of the second moment at higher temperatures. The effect of group rotation on second moment can be easily calculated with the help of a theory adopted by Kromhout and Moulton.⁶ The rigid lattice second moment of the isolated $-\text{NH.NH}_2$ group is found to be 25.77 gauss^2 . If this group rotates around the C—N axis, the change would be 19.32 gauss^2 . Since the $-\text{NH.NH}_2$ group includes 2 protons out of the total 6 protons present in the molecule, the calculated change in the second moment of the molecule for this motion is $19.32 \times 3/6 = 9.66 \text{ gauss}^2$. The final reduced value is $17.09 - 9.66 = 7.43 \text{ gauss}^2$ approximately the same as the experimentally observed value (6.81 ± 1) gauss^2 at 373 K. The difference between the theoretical and experimental values, lies within the experimental error, thereby, confirming the validity of our assumption, viz. that the $-\text{NH.NH}_2$ group rotates around its bond.

The authors are indebted to Prof. B G Gokhle, Head of the Department of Physics, for his interest and encouragement throughout the work. Thanks are also due to Prof. R Vijayaraghavan and his NMR group for their generous help in providing experimental facilities at TIFR, Bombay.

References

1. Van Vleck J H, *Phys. Rev.*, **74** (1948), 1168.
2. Bearden J A & Watts H M, *Phys. Rev.*, **81** (1951), 73.
3. Andrew E R & Eades R G, *Proc. phys. Soc. Lond.*, **A66** (1953), 415.
4. Gutowsky H S & Pake G E, *J. chem. Phys.*, **18** (1950), 162.
5. Ulich H, Peisker H & Andrieth L F, *J. Am. chem. Soc.*, **55** (1933), 673.
6. Kromhout R A & Moulton W G, *J. chem. Phys.*, **23** (1955), 1673.

Relative Permittivity of the Acetates of Potassium, Lithium, Rubidium & Cesium*

J HATIBARUA

Department of Physics, Gauhati University, Gauhati 14

Received 12 July 1979; revised received 5 November 1979

The variation of the complex relative permittivity of the acetates of potassium, lithium and rubidium, as functions of frequency and temperature and that of the acetate of cesium as a function of temperature at a fixed frequency are reported. The small rise in the ϵ' values for potassium acetate near the transition II→I (155°C) and the rapid rise in both ϵ' and ϵ'' for all acetates from about 100°C upwards are attributed to the orientational effect of the acetate ions and thermal activation of the cations respectively. The activation energies obtained are 17.4, 20.0 and 25.4 kcal/mole for Li, K and Rb acetates respectively.

Following the discovery of anomalous thermal expansion of potassium acetate by Hazlewood *et al.*¹ at three temperatures, 80, 160 and 230°C, a study of the thermal behaviour by X-ray diffraction and some physical methods has been undertaken.² The crystallographic data of potassium acetate along with those of rubidium and cesium acetates have already been reported.³ The thermal expansion results have also been published.⁴ In the present note, the results of measurement of the complex dielectric constants are reported. The dielectric measurements were done in order to detect any ferro \rightleftharpoons para electric transition, as transition of such a nature has been hinted in the study of Hazlewood *et al.*¹ The present study has not found any evidence of such a transition. Results of the dielectric measurements on the acetates of Li, Rb and Cs have also been described for comparison.

Several dielectric cells of pyrex glass with electrodes of different metals and of different geometry have been fabricated. The results from different cells have not differed significantly. From initial experiments it has been concluded, in the case of potassium acetate, that the measured value should not be affected, if the sample has been continuously dried for at least 72 hr, subjecting it to rapid thermal cycles through the transition II→I (155°C). The sample was always heated in moderately high vacuum ($\sim 10^{-4}$ torr) to exclude atmospheric oxygen so that decomposition would not occur by electron transfer.¹ The cell with the polycrystalline (fused) sample has been kept immersed in an oil bath, the temperature of which has been controlled to $\pm 0.5^\circ\text{C}$. A commercial ac bridge

(Wayne Kerr, B221) has been used for the measurement of capacitance and conductance at 1592 Hz. The same bridge with an external oscillator and a detector has been used for other frequencies. The experimental procedure for the other acetates has been similar.

The graphs of ϵ' and ϵ'' versus temperature for a fixed frequency for all the acetates and against frequency for a few high temperatures for potassium acetate are shown in Figs. 1 and 2 respectively. The real part ϵ' shows two effects as the temperature is increased. First, there is an increase in the ϵ' values as the transition II→I is approached ($T_c = 155^\circ\text{C}$). The increase in ϵ'' at the transition, if there be any, has not been detected, as these values from room temperature to T_c are found to be too small for measurement. The second effect is common to both the values of ϵ' and ϵ'' , i.e. the values show rapid rise from about 100°C to the highest temperature of measurement. This effect is evident for all the frequencies and for all the acetates. Again, at a particular temperature, both ϵ' and ϵ'' increased

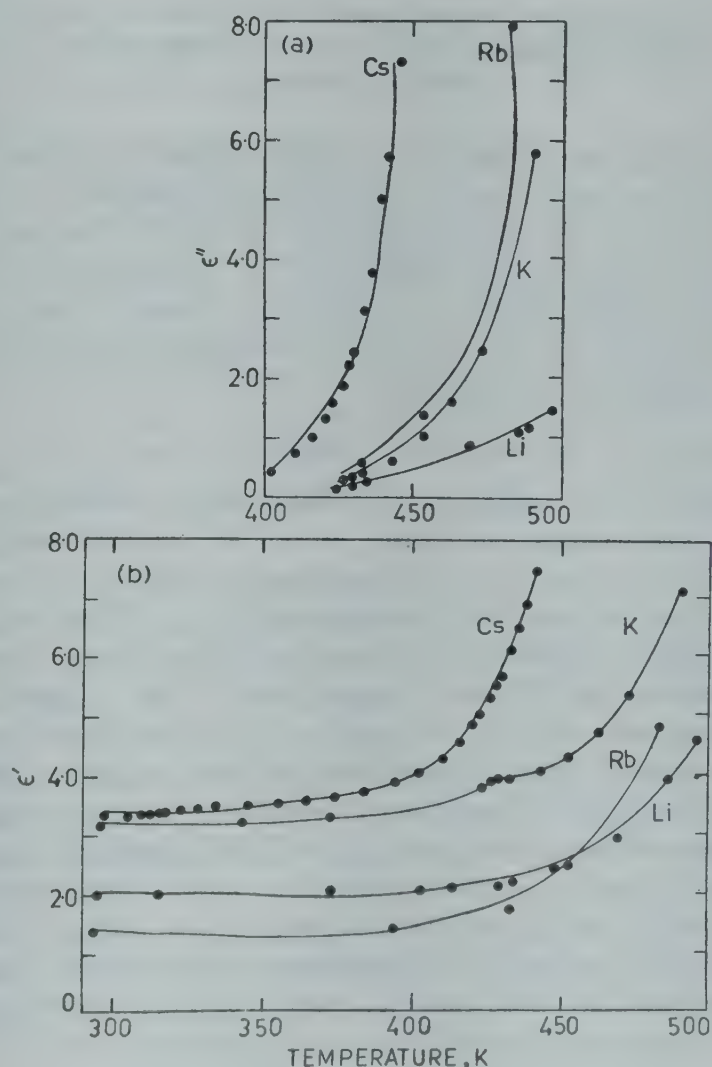


Fig. 1—Plots of ϵ' and ϵ'' versus temperature at 1592 Hz for the acetates of lithium (anhydrous), potassium and cesium and at 1 kHz for rubidium acetate

*Based on the Ph.D. thesis of the author (London University London, 1968).

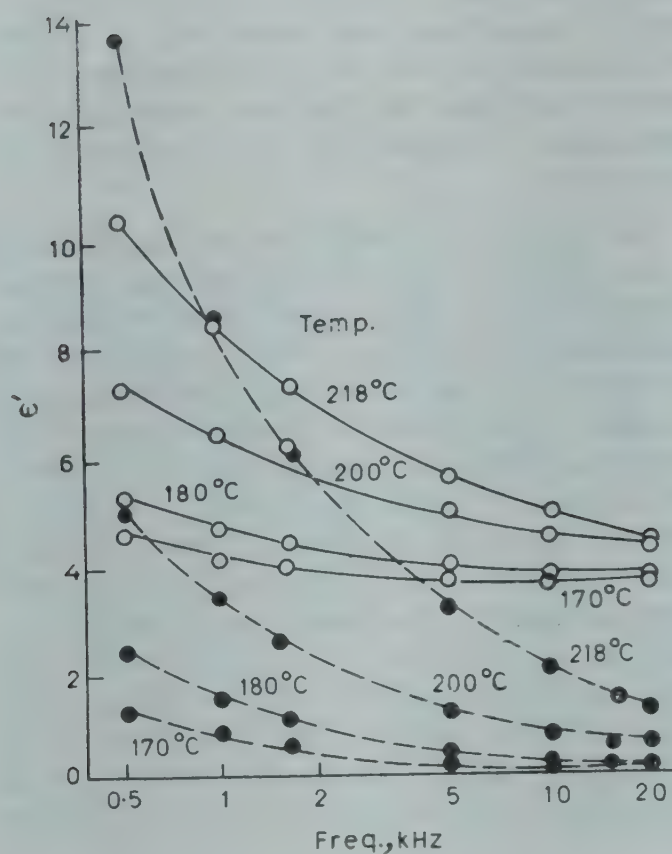


Fig. 2—Complex dielectric constants of potassium acetate plotted against frequency [\circ — \circ , real and \bullet — \bullet , the imaginary part]

with decreasing frequency. Thus dielectric response as a function of frequency closely resembles that of a medium of hopping charge carriers.⁵ This has been taken as the mechanism of producing the second effect. In these acetates, the charge carriers are likely to be the cations. As conductivity and diffusion are closely related

$$\epsilon'' = A \exp(-E/RT)$$

where A is a coefficient, E is the energy of activation of the carriers in calories, $R = 1.987$ cal/deg/mole. To test the validity of the above argument, graphs of $\log \epsilon''$ versus $1/T$ are drawn (Fig. 3). These are straight lines and for the same sample, all these are parallel for different frequencies. This suggests that processes with constant activation energies are involved. The activation energies are: acetates of lithium: 16; potassium: 17; rubidium: 19 kcal/mole (estimated uncertainty: 20%, 14%, 30% respectively). It appears that the increase in energy may have some relation with the increase in the cation size. This is proposed as an evidence that the charge carriers are the cations and that their activation leads to the second effect.

The crystallographic study of Hatibarua² reveals that as the transition temperature 155°C is approached, the acetate ions begin to librate between

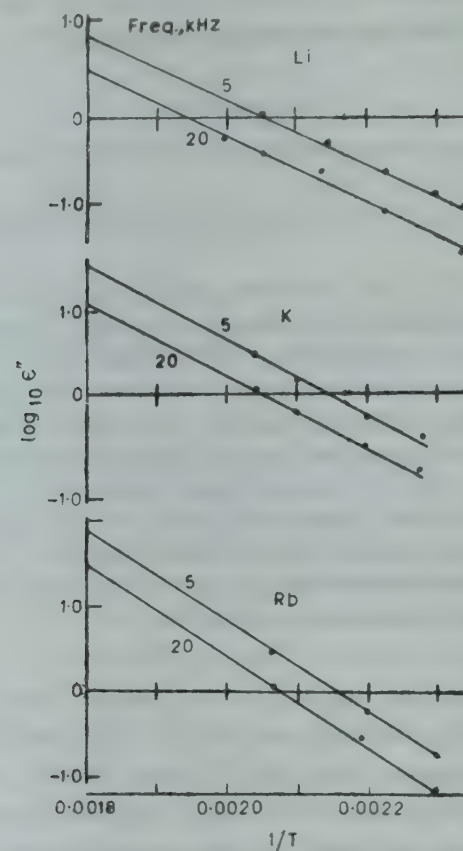


Fig. 3—Graphs of $\log \epsilon''$ versus $1/T$ for the acetates of Li, K and Rb at frequencies 20 and 5 kHz

two equivalent sites. These two alternative sites are represented by the two twin orientations of the low temperature monoclinic phase. As the temperature is increased, more and more acetate ions switch between the two sites (or obverse and reverse configurations) until both orientations are statistically equally populated. It is thus a 'displacive transformation'.^{6,7} The increase in the dielectric constant near the transition has therefore been attributed to ionic orientational effect.

The author wishes to express his gratefulness to his supervisor Dr G S Parry for his inspiring guidance. It is also a pleasure to thank Prof. A R Ubbelohde, FRS, for his continued interest.

References

1. Hazlewood F J, Rhodes E & Ubbelohde A R, *Trans. Faraday Soc.*, 62 (1966), 3101.
2. Hatibarua J, *An investigation of the thermal behaviour of some ionic compounds by crystallographic & Physical methods* Ph D thesis, London University, 1968.
3. Hatibarua J & Parry G S, *Acta crystallogr.*, B28 (1972), 3099.
4. Hatibarua J, *Curr. Sci.*, 47 (1978), 719.
5. Jonscher A K, *Thin Solid Films*, 50 (1978), 187.
6. Buerger M J, *Amer. Miner.*, 30 (1945), 469.
7. Buerger M J, *Phase transformations in solids* (John Wiley, New York), 1951, 183.

Influence of Dielectric Constant on Cationic Mobilities of Electrolytic Solutions in Relation to Eigen Mechanism

V BRAHMAJI RAO**

Department of Physics, Siddartha Engineering College
Vijayawada 520 010
and

T SATYANARAYANA RAO & N CHOWDARY BABU

Department of Physics, Siddartha College
Vijayawada 520 010

Received 28 November 1978; revised received
18 March 1980

The dielectric data obtained experimentally using resonance method have been applied to the expressions for cationic mobilities of transition metal cations of chosen bi-bi valent electrolytes. The results are presented as plots of cationic mobilities versus square root of concentration. These plots indicate the process of ion pair formation of the three types as envisaged by Eigen. The results are discussed in terms of the size of ionic atmosphere, the charge distribution on it and the variation of electrophoretic and the relaxation force.

Debye and Hückel¹ deduced a set of equations (using Poisson-Boltzmann expressions) which lead to expectations for ionic mobilities of cations that differ seriously from the corresponding experimental values.² Modifications to the expressions for activity coefficients³ were deduced on the basis of Glueckauf's model⁴ for the depression of dielectric constants of electrolytic solutions and these expressions were in a better conformity with experimental observations for the respective parameters.⁵ The present note attempts to apply the data of lowering of dielectric constant of electrolytes to the transport parameters of ionic mobility.

Further, adopting the resonance method used by Lefevre *et al.*⁶ the dielectric data of the chosen electrolytes in water-solvent system are obtained. The resonance method essentially consists of an oscillator of Franklin type incorporating the dielectric cell of the type designed by Sayce and Brisco,⁷ and modified by Sugden,⁸ in the tank circuit. A digital frequency meter with a high degree of accuracy of the order of one part per million is used to determine the frequency of the oscillator/whence the value of the dielectric constant is deduced. The chemicals used are purified according to standard chemical method of Weissberger.⁹ Thus initially theoretical and experimental values of the dielectric constant are compared, and the agreement is found to be satisfactory. A similar set of results for a

different set of electrolytes were already published earlier.¹⁰

At the second stage the dielectric data are applied to the expressions for ionic mobilities as presented by Bockris and Reddy.¹¹ We have

$$u = u^0 - \left[\frac{Ze}{6\pi\eta} + \frac{300\mu^0 e^2 W}{6DkT} \right] \frac{K}{300} \quad \dots(1)$$

where

$$u^0 = \frac{1}{300} \cdot \frac{Ze_0}{6\pi r \eta}$$

$$\text{and } W = (Z_+ \cdot Z_-) \left(\frac{2q}{1 + \sqrt{q}} \right) \quad \dots(2)$$

where

$$q = \left[(Z_+ \cdot Z_-) / (Z_+ + Z_-) \right] \left[\frac{\lambda_+ + \lambda_-}{Z_+ \cdot \lambda_+ + Z_- \cdot \lambda_-} \right] \quad \dots(3)$$

For symmetrical electrolytes $Z = Z_+ = Z_-$ and all the parameters bear their usual significance (vide Ref. 10) and K is given by the expression

$$K^2 = \left[\frac{4\pi N e^2}{1000 DkT} \right] \left[\sum_i C_i Z_i^2 \right] \quad \dots(4)$$

and is equal to the reciprocal of the thickness of ionic atmosphere and $\sum_i C_i Z_i^2 = f(I)$ where I is the ionic concentration and λ_+ and λ_- are the ionic conductances of the ions.

The dielectric data determined and deduced above are used in the above equations for ionic mobilities, treating the value of D as a variable depending on the concentration (C) of the electrolyte in the solvent. The data are computed on the IBM 1130. The results are presented as plots of cationic mobility, the relaxation component and electrophoretic components versus \sqrt{C} in Figs. 1, 2 and 3 respectively.

If the dielectric constant is to be treated as a constant independent of the variation of C , then the equation for ionic mobility (u), relaxation term (RT) and the electrophoretic term (EPT) imply linear plots with \sqrt{C} as abscissa. But it is observed that this proportional relationship fails the moment D is considered to be a variable. Further, the plots exhibit three kinks, or a gradient change with reckonable alteration of the linearity at these concentrations. The gradient changes are attributed to the three stages of formation of ion pairs envisaged by 'Eigen' mechanism.¹² For a 'Smenocolytic' solvent like water with large dielectric constant, the electrolytic potential energy (PE) of two ions in contact is of the order of kT (or even less at lower C). The electrostatic PE, (e^2/aD) of a pair of ions assumes a

** Present Address: Dr V Brahmaji Rao, Department of Physics, Sri Venkateswara College, (University of Delhi), Dhaura Kuan, New Delhi 110 021.

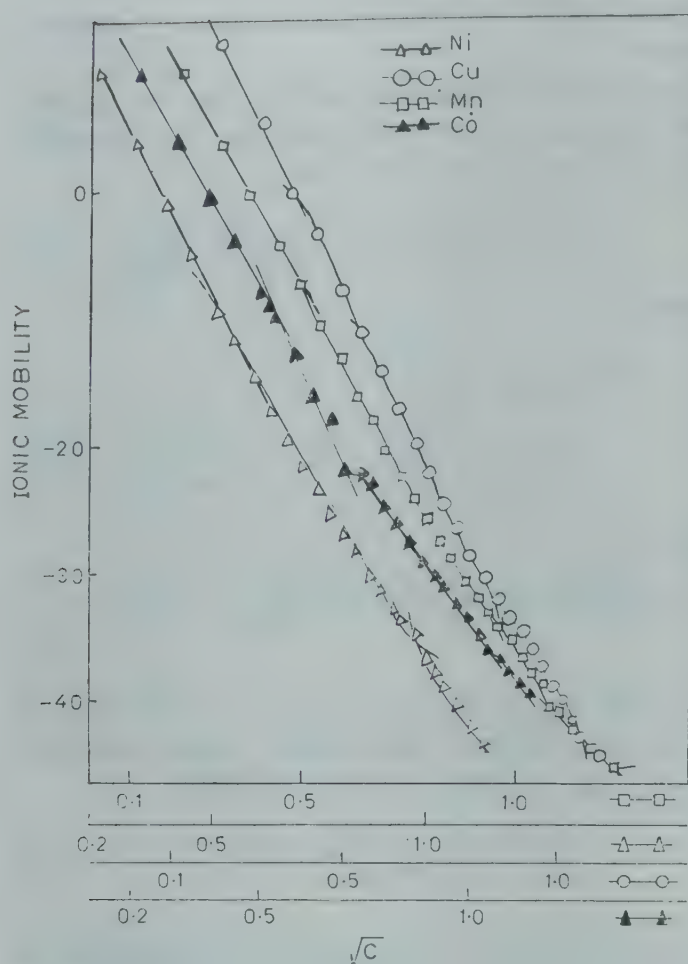


Fig. 1—Ionic mobility versus \sqrt{C} for various sulphates studied

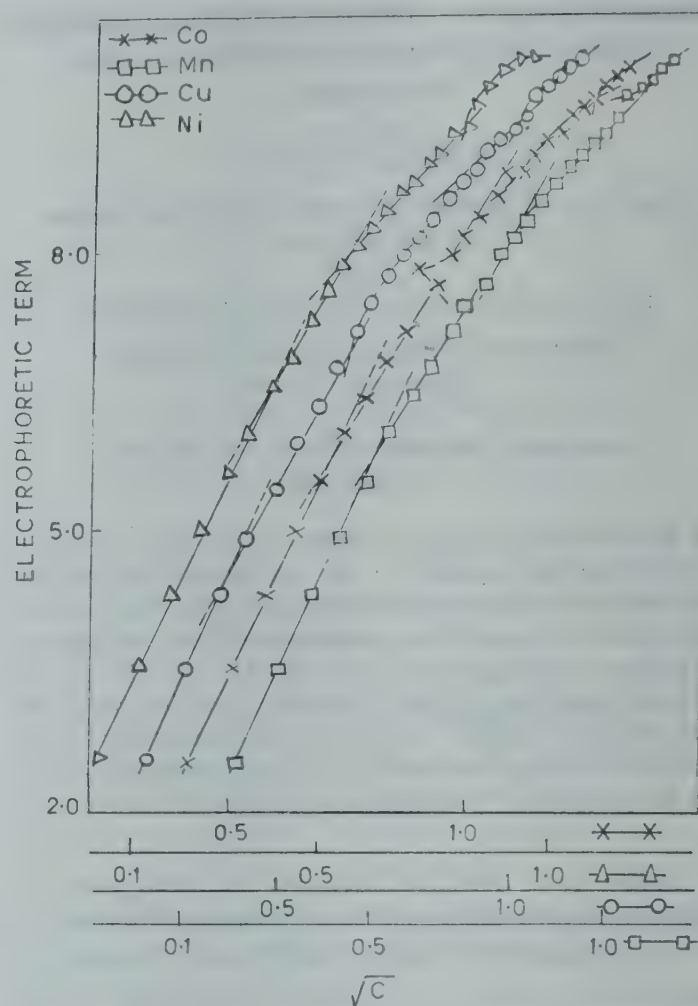


Fig. 3—Electrophoretic term versus \sqrt{C} for the sulphates studied

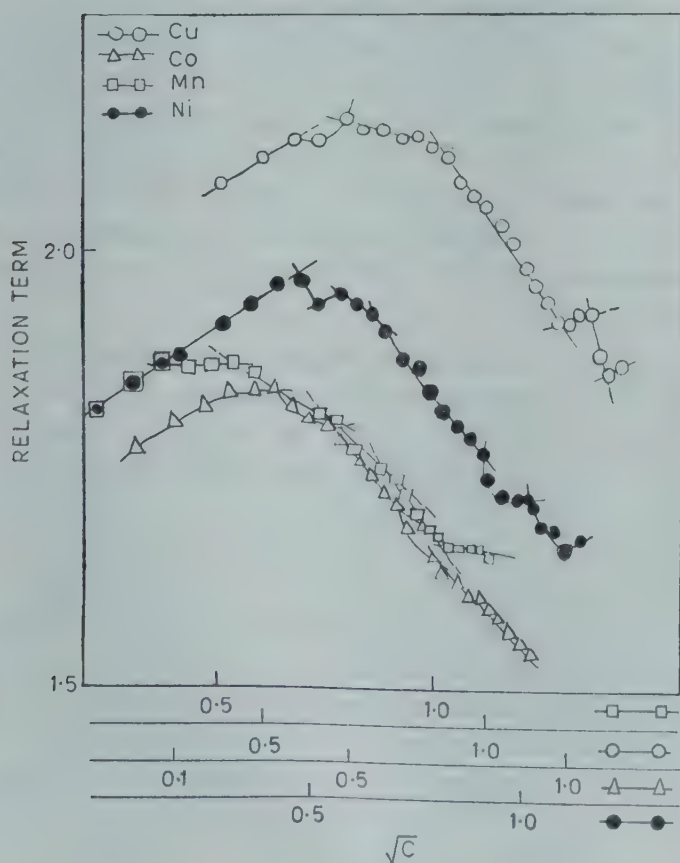


Fig. 2—Relaxation term versus \sqrt{C} for various sulphates studied

greater value than kT as C is increased, (consequently reducing D). Hence the pair of ions becomes relatively more stable against thermal decomposition. Thus the ions tend to form an ion pair which behaves like a dipole in an external field, and neither of the ions of the pair can contribute for the transport of charge, resulting in a consequent decrease in the number of carriers. These ion pairs differ from neutral molecules of an ionogen¹⁰ in the sense that the latter are aggregates of atoms held together by covalent electronic bonds, whereas in the former the cation and anion retain their identity.¹³ All the graphs taking \sqrt{C} as the abscissa and (u) and the EPT as ordinates (Figs. 1 and 3) showed that ionic mobility is inversely proportional to \sqrt{C} and the EPT is directly proportional to \sqrt{C} broadly.

But the plots of RT versus \sqrt{C} (Fig. 2) have a nonlinear shape. As is observable, the RT increases with C initially and later records a fall. As C increases, the viscous force acting on the ionic atmosphere, at the time of its drift records an increase, and hence the EPT records an increase with C . But at the points where the graphs show a kink, obviously the rate of growth of EPT changes. A reduction in the gradient implies a formation of ion

NOTES

pair (which, in turn reduces the free ions available in solution) which reduces the rate of growth of viscous force.

But the plot of RT (Fig. 2) shows deviation from linearity because this term depends on two parameters namely dielectric-constant (D) and viscosity (η). At lower C values, the variations in the D , being substantial, predominate over the variations in the viscous force and hence the plot records a growth up to a marginal concentration. But beyond this value of C , D shows very little variation compared to the variation of the viscous force. Further, a reduction in D of the solvent increases the thickness of the ionic atmosphere (IA). This enhances the electrophoretic effect and reduces the relaxation effect. These are the reasons which produce the change in the gradients in the plots. The above plots record a kink where the rate of decrement in the thickness of the IA decreases with C implying a decrement in the rate of increase of the value of K , the reciprocal of the thickness of the IA. Hence at the points where the solvent separated, solvent shared, and contact ion pairs are formed, the rate of increase of electrophoretic force is suddenly reduced. Because when the resistance due to the moving IA on the ion pair becomes more compared to the resistance on the single central ion, an effective reduction in the electrophoretic force is caused. Similarly the rate of increase of relaxation force is suddenly reduced when the retardation of the central ion due to the presence of the excess of the charge of the opposite sign behind the moving ion is lesser than the retardation produced in the case of ion pair formation resulting in the reduction of the relaxation force.¹⁴

Similar observations in the studies of ultrasonic relaxation by a number of other workers¹⁵⁻²² were also explained successfully on the basis of 'Eigen mechanism'.

The authors acknowledge with thanks the University Grants Commission, New Delhi for the financial assistance, and Dr JVG Krishna Moorthy, Head, Department of Chemistry, Siddartha Engineering College, Vijayawada for his valuable suggestions.

References

1. Debye P & Huckel E, *Phys. Z.*, 24 (1923), 185, 305; 25 (1924), 145.
2. Falkenhagen H, *Electrolytes* (Clarendon Press, Oxford), 1934.
3. Brahmaji Rao V, *Influence of dielectric constant on the activity coefficients, conductance and compressibility of electrolytic solutions-Ion pair formation*, Ph D thesis, Andhra University, Waltair 1977.
4. Glueckauf E H, *Trans. Faraday. Soc.*, 60 (1964), 1637, 572.

5. Brahmaji Rao V *et al.*, *Trans. Saest*, 14 (No 2), (1979), 53.
6. Lefevre C P, *et al.*, *J. chem. Soc.*, (1950), 768.
7. Sayce J, Brisco *et al.*, *J. chem. Soc.*, (1925), 315.
8. Sugden S, *J. chem. Soc.*, (1933), 768.
9. Weissberger A, *Physical methods of organic chemistry* Vol. VII (Interscience, New York).
10. Brahmaji Rao V, *Indian J. pure appl. Phys.*, 14 (1976), 643.
11. Bockris J O M & Reddy K A N, *Modern aspects of electro chemistry* (Plenum press, New York).
12. Eigen M, *Z. Phys. Chem. Frankfurt*, 1 (1954), 176.
13. Eigen M, *Discuss Faraday. Soc.*, 24 (1957), 25.
14. Eigen M & De Maeyer, *Investigation of rates and mechanism of reactions—The techniques of organic chemistry*, Vol. VIII Part 2, chapter 18 (Interscience, New York), 1963.
15. Fuoss R M & Accasina F A, *Electrolytic conductance* (Interscience, New York) 1959, 208.
16. Blandamer M J, *Introduction to chemical ultrasonics* (Academic Press, London) 1973, 71.
17. Atkinson G, in *Hydrogen bonded solvent system*, edited by Convinton and Jones (Taylor and Francis, London) 1968, 161.
18. Blandamer M J, *Q. Rev.*, 24 (1970), P 169.
19. Hammes P, *Acustica*, 21 (1969), 228.
20. Yeager E, *J. phys. Chem.*, 70 (1966), 313.
21. Petrucci S, *J. phys. Chem.*, 71 (1967), 1181, 308.
22. Kor S K, *J. phys. Chem.* 70 (1966), 314.

Temperature Dependence of Pressure-broadened Microwave Line-widths of Some Rotational Lines of Carbonyl Sulphide

G K JOHRI, S GUPTA, B CHANDRA & R P RISHISHWAR
Physics Department, DAV College, Kanpur 208 001

Received 12 July 1979; accepted 24 December 1979

The calculations of line-width parameters at various temperatures and for $J = 0 \rightarrow 1$, $J = 1 \rightarrow 2$ and $J = 2 \rightarrow 3$ transitions have been done for self broadening of OCS by using a new interruption function formulated by Jahri and Srivastava [*Chem. Phys. Lett.*, 45 (1977), 364]. The new function gives temperature variation of line-width in agreement with the measured values.

The importance of temperature and state dependence of pressure broadened spectral line widths was discussed by several workers.¹⁻³ This note presents the results of our study on the temperature variation and the J dependence of the line-width parameters ($\Delta\nu/p$) using a new interruption function formulated by Johri and Srivastava.⁴ The calculations of $\Delta\nu/P$, at various temperatures and for $J = 0 \rightarrow 1$, $J = 1 \rightarrow 2$ and $J = 2 \rightarrow 3$ transitions have been done for the self broadening of carbonyl sulphide (OCS) molecule. The results obtained have been compared with experimental and theoretical values of other workers.⁵⁻¹⁴ Least square fit method has been used to obtain the

parameter (β) which explains the temperature dependence of the line-width parameters. The line-width parameters at 300 K have also been calculated using least square fit method.

The expression for the line-width parameter of microwave transition from initial state i to final state f is given as

$$\Delta\nu = N \sum_{J_2} \rho_{J_2} \int_0^\infty b db \int_0^\infty dv v F(v) \left[P_i(b, v) + P_f(b, v) \right] \quad \dots(1)$$

where b is the impact parameter; v relative velocity; $F(v)$ the Maxwell Boltzmann distribution function; ρ_{J_2} the fraction of the colliding molecules in state J_2 ; N the total number of colliding molecules. P_a ($a = i, f$) is the transition probability of leaving the initial state a . The transition probability under the Anderson's theory¹⁵ is given as

$$P_a^A(b, v) = \sum_{m_a m_2} \frac{\langle J_a m_a J_2 m_2 | p^2 | J_a m_a J_2 m_2 \rangle}{(2J_a + 1)(2J_2 + 1)} \quad \dots(2)$$

where the symbols have their usual significance.¹⁵

Johri and Srivastava⁴ formulated the following collision interruption function under the Anderson's theory.¹⁵

$$P(b, v) = 1 - \exp \left[-\frac{F_i^A}{2} - \frac{P_f^A}{2} \right] \quad \dots(3)$$

The collision interruption function as formulated by Mehrotra and Boggs⁵ is

$$P^{MEB}(b, v) = 1 - \exp \left[-\frac{P_{MEB}^i}{2} - \frac{P_{MEB}^f}{2} \right] \cos(S_{if}^{MEB}) \quad \dots(4)$$

$$\text{where } S_{if}^{MEB} = \frac{1}{\hbar} \int_{-\infty}^{\infty} (V_i - V_f) dt - (\phi_i - \phi_f) \quad \dots(5)$$

P_a^A is the transition probability under the Anderson's theory; P_{MEB}^A the transition probability under the Mehrotra and Boggs theory.

Anderson¹¹ found an empirical equation for temperature dependence of OCS line-width as

$$(\Delta\nu/p) = \frac{1815}{T} + 0.00321 T^{1/2} (J+1)^{1/2} \exp \left[-\frac{h B J(J+1)}{kT} \right] \quad \dots(6)$$

The experimental results of Feeny *et al.*² for self broadening of $J = 1 \rightarrow 2$ OCS line show a temperature dependence as

$$(\Delta\nu/p) = \frac{1850}{T} + 0.01 T^{1/2} \quad \dots(7)$$

Recently Luijendijk¹³ and, Wensink and Dijkerman¹⁴ assumed the following relation

$$\Delta\nu(T)/p = \left[\Delta\nu(T_0)/p \right] \left[\frac{T}{T_0} \right]^\beta \quad \dots(8)$$

We can compute β and $\Delta\nu(T_0)/p$ by means of a least square fit of $\log \Delta\nu(T_0)/p$ against $\log(T/T_0)$. In the computation it was assumed that error in the temperature measurement was negligible.

The calculations of line-width parameters at various temperatures and for $J = 0 \rightarrow 1$, $J = 1 \rightarrow 2$ and $J = 2 \rightarrow 3$ transitions have been done for self broadening of OCS by using a new interruption function formulated by Johri and Srivastava⁴ (JS). The interactions considered are dipole-dipole, dipole-quadrupole, quadrupole-dipole, quadrupole-quadrupole and dispersion forces. The parameters used are the same as used by Murphy and Boggs.¹⁶ The line-width parameters calculated by using JS, Anderson's empirical relation¹¹ and the relation of Feeny *et al.*¹² are compared with the observed⁶⁻⁹ line-widths in Table 1.

From Table 1 it can be seen that $\Delta\nu/p$ values of JS are in close agreement with the experimental values compared to those of others. Feeny's value is 17.3% more and that due to Anderson's empirical relation is 14.1% more than the measured value for $J = 0 \rightarrow 1$ transition.

From the temperature variation study for $J = 0 \rightarrow 1$, $J = 1 \rightarrow 2$ and $J = 2 \rightarrow 3$ lines it is clear that the line-width parameter decreases as the temperature increases. It is interesting to note that as the temperature increases in a particular J -state, the deviation from the measured values decreases. The deviation around 300 K of $\Delta\nu/p$ calculated by using JS from the measured widths are within the experimental uncertainties.

Table 2 gives the values of the parameter β and $(\Delta\nu/p)$ at 300 K obtained by least square fit method using Eq. (8). Table 2 clearly shows that the interruption function used by JS gives β and $\Delta\nu/p$ values in agreement with the measured ones. Hence it is concluded that the new interruption function formulated by JS⁴ gives results in agreement with the measured values in respect of temperature variation and the J dependence. The MEB theory, important for the line-shift calculations also gives almost the same results as obtained in the present calculations. Further, all the interactions are to be included in theoretical values to make the agreement close to the temperature variation of the measured line-widths.

The authors are grateful to Prof. Krishnaji and Dr S L Srivastava, Allahabad University, Allahabad

NOTES

Table 1—Calculated Line-width Parameters ($\Delta\nu/P$ MHz Torr⁻¹) Using New Interruption Function of Johri and Srivastava (J S) compared with that of others at 3 Different Transitions

Temp., K	Exptl. values	Mehrotra & Boggs relation Ref. (5)	JS	Anderson's empirical relation (Ref. 11)	Feeny <i>et al.</i> , relation (Ref. 12)
$J = 0 \rightarrow 1$					
185.80	8.60(01)*	9.23	8.88	9.81	10.09
273.70	5.50(01)*	6.75	6.47	6.68	6.92
$J = 1 \rightarrow 2$					
140.00	11.00(06)*	11.49	11.06	13.02	13.33
196.50	8.43(06)*	8.75	8.41	9.30	9.55
245.80	6.92(07)*	7.31	7.02	7.45	7.68
297.00	6.02(05)*	6.26	—	6.19	6.40
300.00	6.15(31)**	6.21	5.98	6.13	6.34
300.00	6.06(21)†	6.21	5.98	6.13	6.34
300.00	6.35(25)†	6.21	5.98	6.13	6.34
347.70	5.22(04)*	5.53	5.32	5.30	5.50
$J = 2 \rightarrow 3$					
136.40	11.45(17)*	11.92	11.38	13.37	13.68
192.10	8.60(06)*	9.01	8.46	9.52	9.77
230.50	7.36(03)*	7.77	7.32	7.96	8.18
273.80	6.39(04)*	6.76	6.39	6.72	6.92
299.30	5.92(02)*	6.29	5.93	6.16	6.35
337.90	5.48(05)*	5.71	5.41	5.47	5.66

* From Refs. 6 and 7; † From Ref. 9 and 10.

** From Ref. 8.

Table 2—Values of β and $\Delta\nu/P$ [at 300 K] as Obtained by Least Square Fit Method for 3 Transitions of OCS

Transition	β			$(\Delta\nu/P)$, MHz Torr ⁻¹		
	Measured	MEB	JS	Measured	MEB	JS
$J = 0 \rightarrow 1$	-0.72	-0.80	-0.82	6.08	6.28	6.00
$J = 1 \rightarrow 2$	-0.82	-0.78	-0.81	5.92	6.26	5.96
$J = 2 \rightarrow 3$	-0.84	-0.94	-0.84	5.95	5.88	5.92

and to Prof. D Ramachandra Rao, Physics Department, Indian Institute of Technology, Kanpur for constant encouragement during the present work. The authors G K J and RPR are thankful to the University Grants Commission, New Delhi for financial support.

References

1. Krishnaji, *J. scient. Ind. Res.*, **32** (1973), 168.
2. Birnbaum G, *Adv. chem. Phys.*, **XII**, (1967), 487.
3. Rabitz H, *Ann. Rev. Phys. Chem.*, **25** (1974), 155.
4. Johri G K & Srivastava S L, *Chem. Phys. Lett.*, **45** (1977), 364.
5. Mehrotra S C & Boggs J E, *J. chem. Phys.*, **66** (1977), 5306.
6. McGurk J C, Schmalz T C & Flygare W H, *Adv. chem. Phys.*, **25** (1974), 1.
7. Luijendijk S C M, Ph D dissertation, University of Utrecht, The Netherlands, December 1973.
8. Battaglia A, Cattani M & Torrini O, *Nuovo Cim.*, **61** (1969), 193.
9. Johri G K, Prakash V & Srivastava S L, *Indian J. Phys.*, **51B** (1977), 23.
10. Johri G K & Srivastava S L, *Proc. natn. Acad. Sci., India*, **48** (1978), (A, I).
11. Anderson R S, *Phys. Rev.*, **97** (1955) 1654.
12. Feeny H, Lackner H A, Moser P & Smith W V, *J. chem. Phys.*, **22** (1974), 79.
13. Luijendijk S C M, *J. Phys. B*, **10** (1977), 1741.
14. Wensink W A & Dijkerman H A, *J. Phys. B*, **10** (1977), 663.
15. Anderson P W, *Phys. Rev.*, **76** (1949), 647.
16. Murphy J S & Boggs J E, *J. chem. Phys.*, **47** (1967), 691.

An Assembly for Measuring the dc Conductivity of Organic Solids

S C DATT

Department of Postgraduate Studies and Research in Physics, University of Jabalpur, Jabalpur 482 001

Received 19 April 1979; revised received 8 August 1979

An assembly for measuring the dc conductivity of organic crystals, and other high resistivity materials, in the temperature range 25-200°C has been described. Resistivity of the order of 10^{19} ohm-cm has been measured with an estimated accuracy of 5%. A vibrating reed electrometer is used, together with a special sample holder. The latter has provision for temperature measurement and control and maintaining the specimen in vacuum or in an inert atmosphere. Contact pressure between the sample electrodes and the low impedance electrode connector of fixture is achieved by gravity. The microphonic noise was controlled by providing sufficient rigidity to the lead wires attached to high and low impedance electrode connectors. The electrostatic shielding was provided by the outer brass cylinder, encasing the high impedance part of the circuit. Provision for the easy mounting and removal of the sample has also been made.

The choice of apparatus to be used in making resistivity measurements depends on the resistance of the sample and the accuracy desired. The ac techniques using combination of voltmeter, ammeter and the conductivity bridge are considered to be sufficient when no great accuracy is desired and resistivity is less than 10^{11} ohm-cm. However, these methods are inadequate for the much higher resistivities of organic molecular crystals like naphthalene, anthracene, etc. The dc instrumentation developed in the present case and described in the present note extends the limit of measurement to the order of 10^{19} ohm-cm and is suitable for making the measurement of dark conduction in an inert atmosphere as well as in vacuum of 10^{-5} torr.

Instrumentation—A simplified block diagram of the electrical measuring system is shown in Fig. 1. The principal measuring instrument is an electrometer amplifier, Type EA 815 (ECIL, India). A simplified cross-section of the sample holder is shown in Fig. 2 which is self-explanatory as regards the different constructional details. The sample holder can be successfully used for sample temperatures as high as 200°C, with water cooling of the top.

The sample crystal together with the electrode arrangement was mounted on a 1-cm thick bottom teflon disc. This teflon disc was supported from the covering teflon disc at the top by means of three rods made of german silver — a material with a very low thermal conductivity — to keep the flow of heat

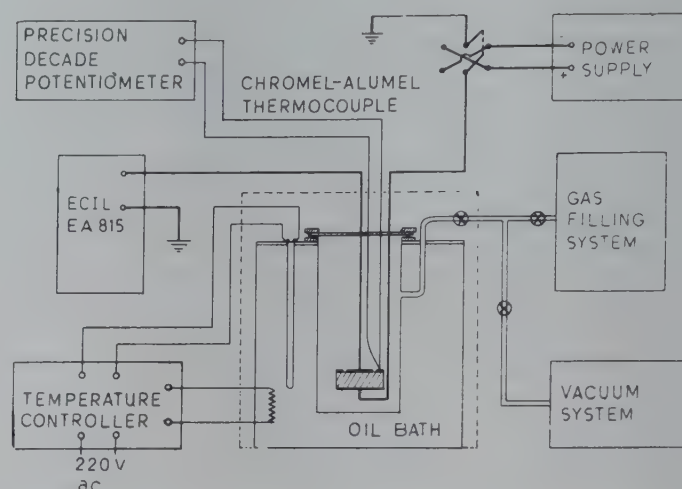


Fig. 1—Block diagram of resistivity measuring system

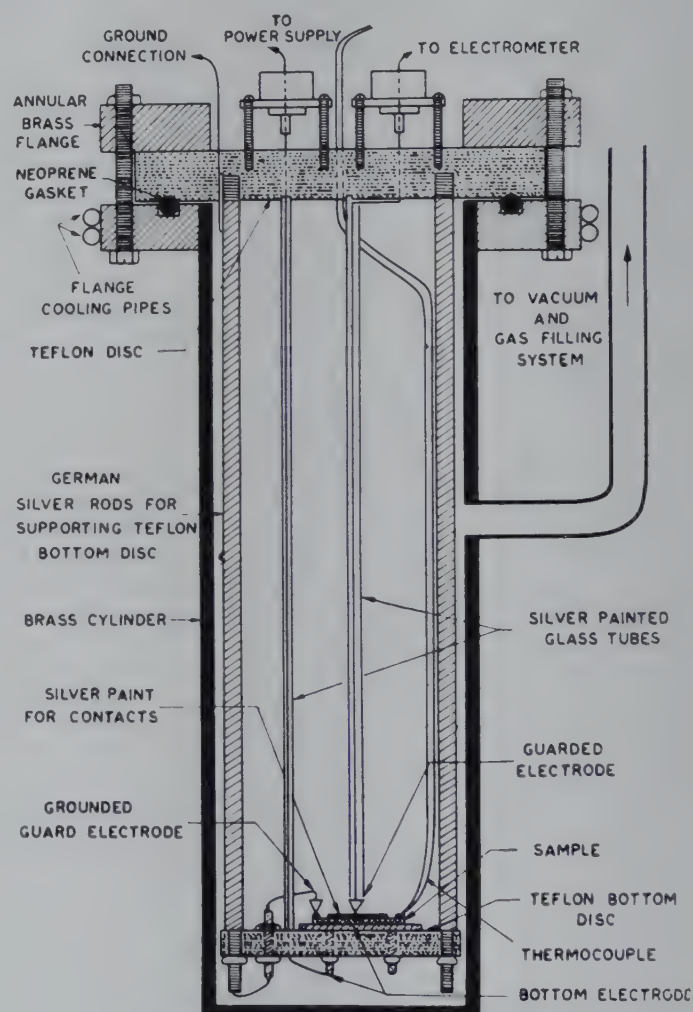


Fig. 2—Sample holder

from the bottom of the sample holder to the top as small as possible. The sample mounting arrangement thus forms an integral part of the top teflon disc. Fig. 3 illustrates the enlarged view of the electrode arrangement on the bottom teflon disc. The problem of making good electrical contact to the crystal sample usually presents many complications due to temperature and high insulation resistance required. Spring contacts were avoided as they were not found suitable at higher temperature ranges. An alternative

NOTES

and a novel solution was the use of gravity to provide contact pressure. All sample electrodes, including the guard ring, were made by vapour-depositing silver or by hand painting with silver paint. The bottom or high impedance electrode was a rectangular plate which was securely fastened to the teflon disc. The low impedance electrode connector which connects the guarded electrode to the electrical circuit, as well as the guard ring connector were of sufficient mass and of such shapes (Fig. 3) that the total weight falls at the point of contact. This provides adequate contact pressure, and since the influence of gravity is independent of temperature, a constant contact pressure is maintained throughout. Both the guard and guarded electrode connectors were allowed sufficient vertical motion. This arrangement was necessary since it was found to be almost impossible to maintain the guarded and guard electrode connectors in the same plane during temperature cycling of the system if both were firmly attached to the teflon disc. The guard ring was grounded through the german silver rod. This reduces the effect of surface leakage and conduction through the insulation of test fixture.

In order to control microphonic noise, the lead wires attached to high and low impedance electrode connectors were kept rigid. This rigidity was derived chiefly from the top teflon disc which was kept in a fixed position by bottom and top annular flanges. The lead wires were also sufficiently thick and they were kept straight and tight inside the sample holder. As the two lead wires were nearly parallel, one at high potential and the other at nearly earth potential, even a small mechanical shock to the apparatus could produce large capacitatively converted noise voltage to the electrometer. To keep off such

troubles, the lead wires were shielded by silver-painted glass tubes. The outer jacket-brass cylinder of the sample holder also formed an electrostatic shield for the inner, high impedance portion of the circuit.

Three copper lead wires of 20 gauge — meant for providing voltage to the sample, connection to the electrometer and ground path to the guard electrode — were taken out through the top teflon disc. Chromel-alumel thermocouple wires for measuring the temperature of the sample were also taken out through this teflon disc. All these wires were taken out through tight fitting holes drilled in the teflon disc and these positions were made vacuum tight by using Araldite Powder AT 1 (CIBA Ltd, Basle, Switzerland).

In order to measure the temperature of the crystal, two thermocouples were mounted, one at the top and the other at the bottom surface of the 'dummy' crystal of equal size and thickness which was placed adjacent to the crystal being measured. The mean of these two thermocouple readings was taken as the effective temperature of the crystal.

A significant point in the design of any sample holder is the ease with which samples may be changed when measurements are being taken on many different crystals. Removal of crystals from our sample holder was extremely simple and hardly took a few minutes. The outer jacket of the sample holder was fixed rigidly and was kept immersed in an oil bath. For changing the samples, all that was needed was to remove the top teflon disc which accommodated the crystal mounting arrangement.

Performance—Conductivity measurements on three naphthalene single crystals, prepared from naphthalene,¹⁻³ which was zone-refined⁴ 50 times, were made using an electrometer amplifier, type EA 815 (ECIL, India).⁵ The results are shown in Fig. 4.

The reproducibility of the results indicates the capability of the test fixture for accurate measurement of high resistivities of organic solids. The accuracy achieved with this system is estimated to be $\pm 3\%$ in the measurement of conductance, $\pm 5\%$ in the measurement of conductivity and $\pm 1\%$ in the measurement of sample temperature. The lowest current measured with this accuracy is of the order of 10^{-15} A. Leakage current across the test fixture was not observable in the background noise of the system. It is worth mentioning that the order of the current of most of the semiconductors is higher than that reported here which evidently justifies the successful use of the sample holder for various organic semiconductors.

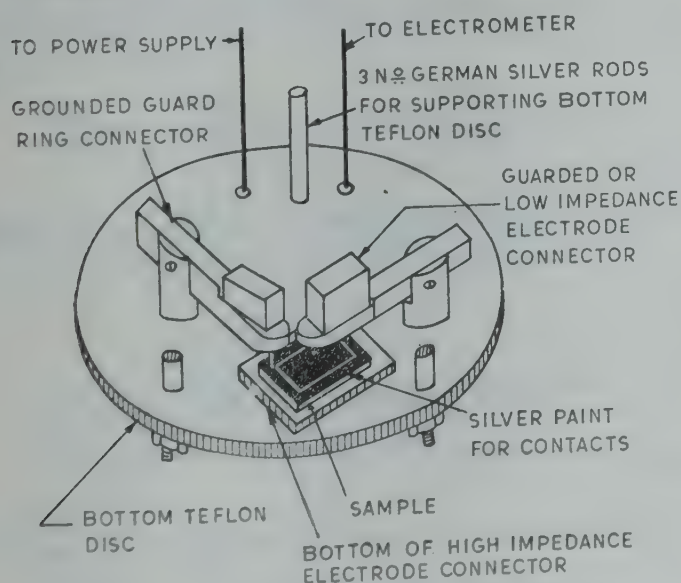


Fig. 3—Enlarged view of the electrode arrangement on the bottom teflon disc

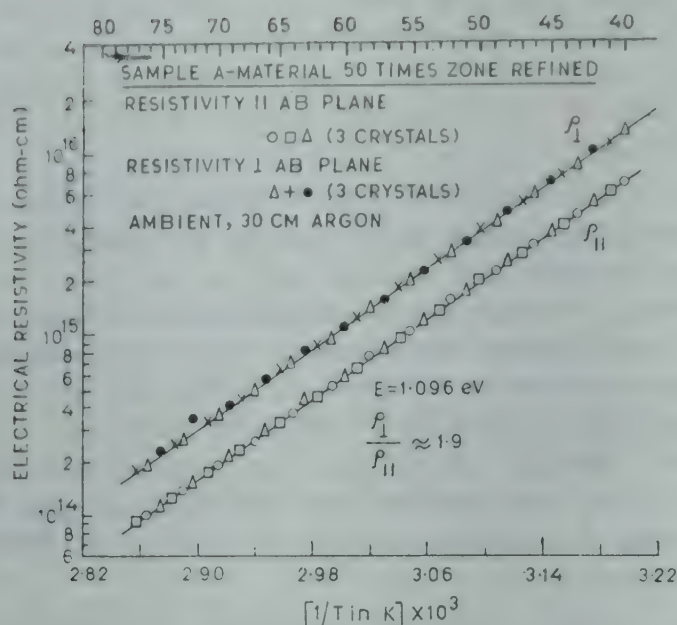


Fig. 4—Electrical resistivity as a function of temperature

The author is grateful to Profs. B D Nag and J K D Verma, Saha Institute of Nuclear Physics, Calcutta, for discussions on various design considerations. He is also thankful to Dr Ranjit Singh for the help rendered in the preparation of the manuscript.

References

1. Datt S C, Verma J K D & Nag B D, *Indian J. Phys.*, 41 (1967), 739.
2. Datt S C & Verma J K D, *Indian J. pure appl. Phys.*, 6 (1968), 96.
3. Datt S C & Verma J K D, *J. scient. ind. Res.*, 27 (1968), 11.
4. Datt S C, Verma J K D & Nag B D, *J. scient. ind. Res.*, 25 (1966), 455.
5. Datt S C & Singh R, *J. Phys. Soc. Japan*, to be published.

Motional Impedance of a Rigid, Conducting, Diamagnetic Prolate Plasma Spheroid

B N MARIHAL & B G JYOTI

Post-graduate Department of Studies in Physics
Karnatak University, Dharwad 580 003

Received 22 March 1979; revised received 25 September 1979

Considering the motion of rigid, infinitely conducting, diamagnetic prolate plasma spheroid by a magnetic field, an expression for the motional impedance has been evaluated. With an illustrative example, it has been shown that the motional impedance is of the order of a milliohm.

Many research programmes in plasma physics are mainly concerned with fast acceleration processes, such as exploding wires, plasma injection, shock tubes, plasma propulsion, etc. An interesting approach to accelerate plasmoids as a function of

time is made¹ by hydromagnetic consideration. However, this cannot be used in many cases due to its geometrical difficulty. Acceleration of plasmoids is made² ignoring fluid aspect of plasma behaviour and taking into account the electro-magnetic behaviour alone. It is shown³ that a moving body alters the impedance of an electric circuit and leads to the concept of motional impedance. Therefore, it is proposed in this communication to evaluate the motional impedance of a prolate spheroid which moves under the influence of a magnetic field produced by a truncated conical coil.

To evaluate the expression for motional impedance we consider a prolate plasma spheroid of semi-axes α and β ($\alpha > \beta$) moving under the influence of a magnetic field due to a truncated conical coil (Fig. 1). The total current $i = -dq/dt$ to the coil, being supplied by the discharge of a condenser of capacity c . Let R and r be the radii of mouth and back-end of the truncated cone of length $l = (z_1 - z_0)$. Then, the force acting on the spheroid is given by²

$$F_x(x) = \Lambda \mu_0 i^2 \left\{ \frac{2(1-e^2)\alpha^3 x}{(x^2 - \alpha^2)} + (e^2 - 3/4) \lambda \log_e \left(\frac{x+\alpha}{x-\alpha} \right) - (e^2 - 1/2) \frac{\lambda}{2} \log_e \left[\frac{\alpha^2 - e^2(x+\alpha)^2}{\alpha^2 - e^2(x-\alpha)^2} \right] \right\} \quad \dots (1)$$

where

$$\Lambda = -\frac{\pi}{2} \frac{z_1^4}{(z_1 - z_0)^2 \alpha^2} g^2(\eta, \nu) (1 - e^2) \quad \dots (2)$$

$$g(\eta, \nu) = -\frac{\eta}{1+\eta^2} + \frac{1 - (1 - \eta^2)\nu}{(1 + \eta^2)(1 - \nu)^2 + \eta^2 \nu^2} + \frac{\eta^2 \Omega}{(1 + \eta^2)^{3/2}} \quad \dots (3)$$

$$\Omega = \left[\sinh \eta^{-1} + \sinh^{-1} \left(\frac{1 - (1 + \eta^2)\nu}{\eta} \right) \right] \quad \dots (4)$$

$$\lambda = \left[1 + \frac{k-1}{2} \left(\frac{1-e^2}{e^2} \right) \left\{ \frac{1}{e} \log_e \left(\frac{1+e}{1-e} \right) - 2 \right\} \right]^{-1} \quad \dots (5)$$

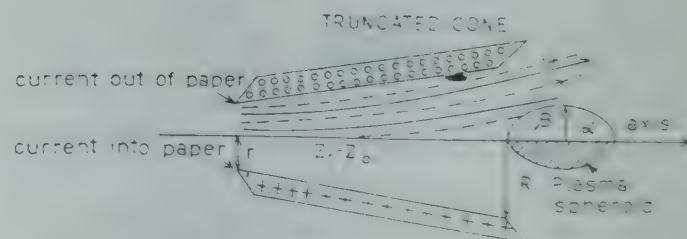


Fig. 1—Spheroidal configuration [Dotted lines indicate unperturbed field due to coils alone; solid lines indicate perturbed lines around spheroid]

$$e = (1 - \beta^2/\alpha^2)^{1/2} \quad \dots(6)$$

$$v = z_0/z_1 \quad \dots(7)$$

and

$$\eta = R/z_1 \quad \dots(8)$$

Applying Newton's second law, the equation of motion for the system can be written as

$$F(x) = m \frac{d^2 x}{dt^2} = Ai^2$$

$$\text{or} \quad \frac{dv}{dt} = \frac{A}{m} \left(\frac{dq}{dt} \right)^2 \quad \dots(9)$$

where

$$A = \Lambda \mu_0 \left\{ \frac{2(1-\lambda)\alpha^3 x}{(x^2 - \alpha^2)^2} + \left(e^2 - \frac{3}{4} \right) \lambda \log \left(\frac{x+\alpha}{x-\alpha} \right) - (e^2 - \frac{1}{2}) \frac{\lambda}{2} \log \left[\frac{\alpha^2 - e^2(x+\alpha)^2}{\alpha^2 - e^2(x-\alpha)^2} \right] \right\} \quad \dots(10)$$

The plasma present in the acceleration processes is usually a very high temperature plasma. It offers negligible resistance to electric currents and hence resistive losses in the plasma can be neglected. Therefore, considering plasma as an ideal conductor (i.e. plasma of infinite conductivity) the energy equation governing the system is given by

$$L \left(\frac{dq}{dt} \right)^2 + \frac{1}{2} m v^2 + \int_0^t R \left(\frac{dq}{dt} \right)^2 dt' + \frac{q^2 - q_0^2}{2c} = 0 \quad \dots(11)$$

where the terms in Eq. (11) represent respectively (term by term) the stored magnetic energy, the kinetic energy acquired by the plasmoid, the energy lost due to joule heating in the circuit, and the energy stored in the capacitors. Since the inductance L depends on the position of the plasmoid it is an implicit function of time t .

Differentiating and then substituting for dv/dt , Eq. (11) becomes

$$L \frac{d^2 q}{dt^2} + \left[\left(\frac{1}{2} \frac{\partial L}{\partial x} + A \right) v + R \right] \frac{dq}{dt} + \frac{q}{c} = 0 \quad \dots(12)$$

The value of $\frac{1}{2} \partial L / \partial x$ is evaluated by making use of the relation between force and inductance.⁴

$$F_x(x) = \frac{1}{2} i^2 \frac{\partial L}{\partial x} \quad \dots(13)$$

Comparing Eqs. (9) and (13), we find

$$A = \frac{1}{2} \frac{\partial L}{\partial x} \quad \dots(14)$$

Substituting the value of $\frac{1}{2} \partial L / \partial x$ in Eq. (12), we get

$$L \frac{d^2 q}{dt^2} + (2Av + R) \frac{dq}{dt} + \frac{q}{c} = 0$$

$$\text{or} \quad L \frac{di}{dt} + (2Av + R) i + \int_0^t \frac{idt}{c} = 0 \quad \dots(15)$$

which represents the emf equation for a damped R - L - C circuit. The term

$$R_m = 2Av \quad \dots(16)$$

has the dimensions of impedance and is due to motion of the spheroid. Therefore, R_m is the motional impedance of the plasma spheroid. Since, the resistive losses in the plasma are neglected, the present work holds good only for an ideal case of infinite conductivity plasma. Physically, motional impedance gives rise to an instantaneous mechanical power appearing in a moving spheroid.

Illustrative example—Consider an elongated prolate spheroid with semiaxes $\alpha = 1$ cm and $\beta = 0.2$ cm. Let $v = 200$ km/sec be its velocity. The parameters defined by Eqs. (6) and (5) are, $e = 0.98$ and $\lambda = 1.05$ respectively. If we consider a cone of length 18 cm, with radii $r = 1$ cm, and $R = 4$ cm, then $z_0 = 6$ cm, $z_1 = 24$ cm, and $\eta = 1/6$, $v = 1/4$, $g(\eta, v) = 1.78$. Finally, assuming that the plasma is injected at a point 6 cm from the smaller end of the cone and 12 cm from the larger end of the cone, we see, that, the initial position of the plasmoid is at $x = 12$ cm. On substituting these numerical values in Eq. (16), the value of the motional impedance (R_m) comes out to be $\cong 3.7$ m Ω .

Financial support of the University Grants Commission, New Delhi, in the form of a fellowship is gratefully acknowledged.

References

1. Rosenbluth M, *Los Alamos Rep* LA 1850, Los Alamos, New Mexico, 1954.
2. Ayres R V, *J. appl. Phys.*, **32** (1961), 1549.
3. Everitt W L, *Communication engineering* (McGraw Hill, New York), 2nd Edn, 1937, 687-689.
4. Abraham M & Becker R, *Classical electricity and magnetism* (Hafner Publishing, New York), 1932, 162.

X-ray K Absorption Discontinuity in Crystalline & Amorphous Arsenic

Y L RAO & C MANDE

Department of Physics, Nagpur University, Nagpur 440 010

Received 5 July 1979

The shape of the X-ray K absorption discontinuity of arsenic in the crystalline and amorphous varieties has been studied, using a Cauchois type bent crystal spectograph of 100 cm diameter. The splitting of the main K absorption discontinuity of arsenic has been observed for the first time.

It is well known that the K absorption discontinuities of the elements of the first transition metal ($3d$) series are split into two components, K_1 and K_2 .^{1,2} Recent work has shown that the K absorption discontinuities of the second transition metal ($4d$) series have a similar shape.³ In a recent investigation carried out in our laboratory, we have shown for the first time, that the K absorption edge of selenium is split into two components, K_1 and K_2 .⁴ In this note we report the study of the K absorption discontinuity of arsenic, both in crystalline and amorphous varieties.

A 100-cm Cauchois type X-ray spectrograph, equipped with a mica crystal oriented to reflect from the (201) planes, was employed for recording the absorption spectra. Many spectra were obtained for each sample under appropriate conditions. Microphotometer traces of the spectra were obtained with magnification $\times 100$ on the Spectroline Scanner fabricated by M/s Applied Research Laboratories, California. The crystalline arsenic powder used was 99.9% pure. Amorphous arsenic was prepared by heating the arsenic powder in evacuated sealed silica ampoules followed by rapid quenching in water. The nature of the samples was controlled by studying their X-ray diffraction patterns. Further details of the experimental technique can be found in the earlier publications from this laboratory.^{5,6}

The shapes of the K absorption discontinuity of arsenic in crystalline and amorphous forms are shown in Fig. 1. These curves drawn after averaging the results from a number of microphotometer

records, represent the variation of transmitted intensity as a function of energy and consequently the maxima and minima in these curves correspond to the minima and maxima respectively in the values of the absorption coefficient. We have observed, for the first time, that the main K absorption edge of arsenic is split into two components K_1 and K_2 in both the varieties.

Arsenic may be regarded as a semiconductor with electronic configuration $4s^2 4p^3$. The three p electrons are located in the valence band, while the empty p orbitals form the conduction band.

Fig. 1 can be thought as being composed of two component absorption curves, in which the points 'a' and 'b' represent maxima of absorption. We can attribute the first absorption component K_1 with maximum at 'a' to the transition of the $1s$ electron to the top of the valence band. Normally there are no vacancies in this band for the transition to take place. However, Mande and Patil⁷ showed that such a transition can take place because of various processes which create sizable number of holes located preferentially at the top of the valence band. The first X-ray absorption is then on account of these empty levels. The component K_2 of which the absorption maximum corresponds to the point 'b' can be attributed to the transition of the $1s$ electron into the conduction band. The conduction band consists of the vacant p orbitals as mentioned earlier, and it is because of this that the K_2 component is stronger.

It is known⁸ that no major difference exists in the band structure of elemental and simple amorphous semiconductors. Hence one can expect an overall similarity in the shapes of the absorption edges of the two forms of arsenic.

One of the authors (YLR) is indebted to CSIR, New Delhi, for financial support during the course of this work.

References

1. Cauchois Y, *Les Spectres de rayons X et la structure électronique de la matiere* (Gauthier-Villars, Paris), 1948.
2. Sandström A E, cited in *Encyclopedia of physics*, Vol. 30, edited by S Flugge (Springer-Verlag, Berlin), 1957, 227.
3. Kostroun V O, Fairchild R W, Kukkonen C A & Wilkins J W, *Phys. Rev.*, B13 (1975), 3268.
4. Rao Y L & Mandé C, *Phys. Status Solidi* (b), 92 (1979), K61.
5. Sapre V B & Mandé C, *J. Phys. C*, 5 (1972), 793.
6. Pendharkar A V & Mandé C, *Physica*, 66 (1973), 204.
7. Mandé C & Patil R N, *Indian J. pure appl. Phys.*, 1 (1963), 435.
8. Stuke J, *Festkorperprobleme*, 9 (1969), 46.

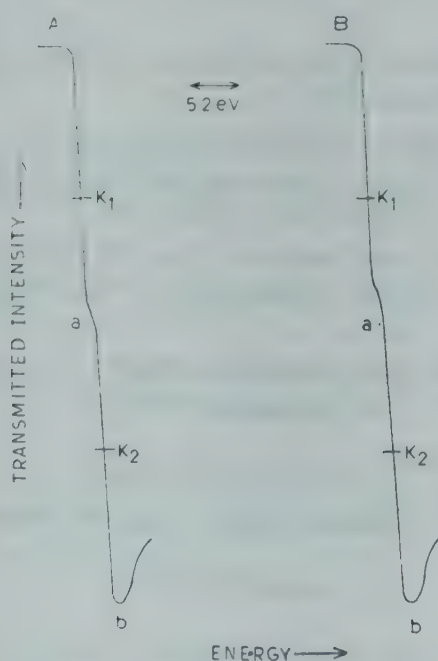


Fig. 1—Shapes of K absorption discontinuity of arsenic in crystalline and amorphous forms [A, Crystalline arsenic; B, amorphous arsenic]

Electronic Simulation of Acoustic Emission

SANJEEV CHADDA & S P MALLIKARJUN RAO

Physics Department, College of Science, Osmania University
Hyderabad 500 007

Received 16 April 1979; revised received 7 July 1979

A simple electronic circuit, which simulates the burst type of acoustic emission, is described. Random pulses of exponentially decaying nature, of different signal frequencies (100 kHz to 2 MHz) can be generated with a randomness in amplitude, pulse width and pulse repetition time periods. This arrangement is extremely useful in checking the electronic system of an actual acoustic emission test set-up.

Acoustic emission occurs in materials undergoing stress.¹ This subject has gained immense importance due to its non-destructive testing capabilities.^{1,2} Acoustic emission is of two kinds: continuous emission—with a high frequency and low amplitude, and burst emission—with a high amplitude and low repetition rate. The burst type of emission, with which we are concerned in the present communication, occurs at random with repetition

rates ranging from about 100 to 3000 bursts/sec. The signal frequency inside the burst remains essentially the transducer resonance frequency. The amplitudes of the bursts as received by the transducer, are usually of the order of few hundred microvolts.

To obtain useful information from the burst type of emission, different parameters of the signal observed, like the number of bursts per second, total number of bursts, number of counts in a single burst, count rate, total count over a length of time, the energy in a burst, maximum amplitude in a burst and amplitude distribution of the signal received, are studied.^{1,2} Hence, the authors designed a circuit that is capable of simulating the burst type of emission.

The circuit shown in Fig. 1, is capable of giving randomly varying, exponentially decaying pulses at the frequencies of interest. The randomness is obtained in amplitude, repetition rate and the burst duration. This randomness is essentially obtained by the white noise produced by a Zener diode working in avalanche breakdown region. The above random

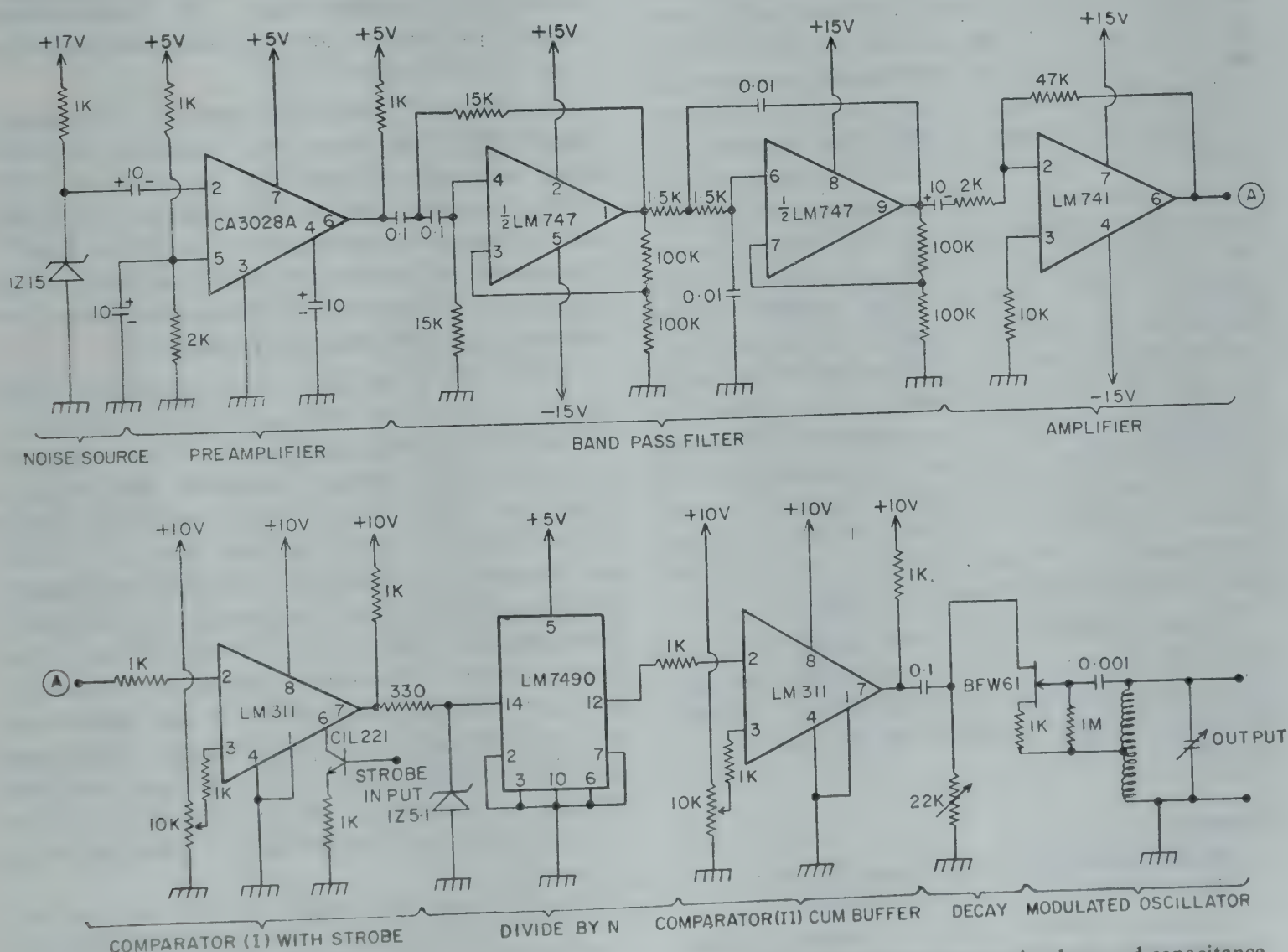


Fig. 1—Circuit diagram of the electronic simulator of acoustic emission [Resistance values are in ohms and capacitance values are in microfarads.]

signal is used to generate random pulses, which are, in turn, used to modulate an oscillator to obtain the random bursts at the frequency of interest.

White noise generated by a Zener diode in its breakdown region, is first amplified by a pre-amplifier (CA 3028) and is filtered by the bandpass filter (LM 747) to obtain lower frequencies from the noise. The voltage waveform obtained varies randomly with time—both in amplitude and frequency. This waveform is now compared with a dc reference voltage by the comparator (LM 311). Since the input to the comparator is random, at its output we get pulses of random pulse width occurring at random periods. However, the amplitude of these pulses is same due to the comparator action. A divide-by-two circuit (LM 7490) is now used to increase the pulse width of the random pulses (a single LM 7490 can be used as divide-by-five or divide-by-ten circuit also for larger pulse widths). The output of this is given again to an LM 311, now used as a buffer, at the output of which a proper resistor-capacitor combination is introduced to give suitable decay constant. This exponentially decaying output has random amplitude, random duration and random repetition rate. The randomness in amplitude is obtained because of the randomness in pulse width of the input waveform and because of the fact that the maximum voltage to which the capacitor (used at the output of the buffer—LM 311) charges, varies with the pulse width. This random, decaying waveform is given as supply voltage to a Hartley oscillator (FET-BFW 61), oscillating in the frequency range 100 kHz to 2 MHz. The oscillator is thus modulated and random bursts at the frequency of interest are produced. Finally these bursts are passed through a frequency-compensated rf-attenuator (Radart make, model 723) to give a variable output amplitude, whose value can be varied from a few tens of microvolts to a few volts. The circuit constructed is capable of generating decaying pulses of approximately 5-10 μ sec duration, with repetition periods ranging from 10 μ sec to 1 msec.

The above electronic simulator circuit will be of great help to an acoustic emission engineer, as he can use this to check his acoustic emission electronic system—either constructed by him or purchased off the shelf.

References

1. *Acoustic Emission*, American Society for Testing and Materials Special Technical Publication 505, 1972.
2. *Monitoring structural integrity by acoustic emission*, American Society for Testing Materials Special Technical Publication, 571, 1975.

Infrared Spectra of the Biological Molecule 4,6-Dihydroxy-2-Methyl Pyrimidine*

NITISH K SANYAL

Department of Physics, University of Gorakhpur
Gorakhpur 273 001

and

R K GOEL†, K P KANSAL‡ & S N SHARMA@
Department of Physics, D N College Meerut 250 002

Received 10 April 1979; revised received 8 October 1979

The infrared absorption spectra of 4,6-dihydroxy-2-methyl pyrimidine have been recorded on Perkin-Elmer-521 spectrophotometer in the region 250-4000 cm^{-1} using KBr and nujol mull techniques. The spectra have been analyzed assuming C_{2v} point group symmetry for the molecule. The assignments have been proposed and discussed. Tautomeric behaviour of the molecule has also been discussed.

Though pyrimidine, cytosine, thymine, uracil and their derivatives are of great biological importance, very few spectroscopic studies are reported for these molecules in literature.¹⁻¹² The present note reports the vibrational (hereafter referred to simply as 4,6-DH-2-MP) spectral study of 4,6-dihydroxy-2-methyl pyrimidine and the tautomeric behaviour caused by OH groups.

The infrared absorption spectra of chemically pure 4,6-DH-2-MP have been recorded on Perkin-Elmer spectrophotometer-521 in the region 250-4000 cm^{-1} in solid phase. The observed bands and their proposed assignments are given in Table 1. The analysis of the observed bands and their assignments to probable modes of vibration have been done assuming C_{2v} point group for the molecule.

The C—H stretching mode lies between 3000-3100 cm^{-1} .¹³ In view of this, the band observed at 3077 cm^{-1} has been assigned to C—H stretching mode ν_{20a} in the present molecule. According to Kletz and Price,¹⁴ the C—OH stretching occurs around 1300 cm^{-1} in substituted phenols. Mecke and Rossmly¹⁵ have suggested that OH deformation mode appears at a lower frequency near 1200 cm^{-1} . Thus the bands observed at 1305 and 1332 cm^{-1} have been assigned to X-sensitive stretching vibration ν_{13} and ν_{7b} respectively, due to OH groups substitution at 4 and 6 positions in the present case. Wilmshurst and Bernstein¹⁶ and Mooney¹⁷ have shown that there appears a strong band around 1200 cm^{-1} which involves C—CH₃ valence oscillation. Thus the strong

*Part of this work was presented at the IX All India Biophysics Symposium, held at Gorakhpur in March 1979.

†To whom all correspondence should be made.

‡Department of Physics, S S V College, Hapur, U P.

@Analytical Physics Section, I.I.P., Dehra Dun 248 005.

Table 1—Assignments of Fundamental Frequencies of
4,6-Dihydroxy-2-Methyl Pyrimidine*
(All values in cm^{-1})

Sym- metry species	Vibra- tion number	Observed band position along with intensity*	Assignment
A_1	20a	3077m	C—H stretching
	2	1220s	C—CH ₃ stretching, OH ipb
	13	1305ms	C—OH stretching
	8a	1585m	Ring stretching
	19a	1385m	Ring stretching
	9a	635s	C—OH ipb
	12	987vs	Ring ipb
	1	825vvs	Ring stretch, Ring breathing, Ring in-plane bend
	6a	537vs	
B_2	7b	1332s	C—OH stretching
	8b	1617vw	Ring stretching
	19b	1485m	Ring stretching
	14	1355sb	Ring stretching
	3	370m	C—CH ₃ ipb
	15	940vs	C—H ipb
	18b	545 (nujol) vs	C—OH ipb
A_2	6b	657vs	Ring planar deformation
	16a	412mw	Ring-non-planar defor.
	17a	295mw	C—OH, opb
B_1	5	32ms	C—OH, opb
	11	848ms	C—H, opb
	10b	315ms	C—CH ₃ , opb
	4	695m	Ring opb
	16b	340s	Ring opb
Group Vib.	OH group	3705mw	O—H stretching
		3680m	O—H stretching
		1280s	O—H ipb
		1220s	O—H ipb
		355s	O—H opb
		345s	O—H opb
	CH ₃ group	1290mw	C—H asym. stretching
		1500w	CH ₃ asym def
		1470mw	CH ₃ asym def
		1460mw	CH ₃ sym def
		1140ms	CH ₃ rocking
		1050vvs	CH ₃ rocking
	Others	388ms	C=O out-of-phase bend.
		545vs	C=O in-phase bend.
		1663m	6 C=O stretching
		1683m	4 C=O stretching

*ipb, in-plane bending; opb, out-of-plane bending;
 β -ipb; s, strong; vs, very strong; vvs, very very strong;
 m, medium; mw, medium weak, ms, medium strong;
 w, weak; vw, very weak; sb, strong and broad.

band observed at 1220 cm^{-1} has been assigned to X-sensitive vibration ν_2 due to substitution of CH₃ group at 2nd position to the ring in the present molecule. This also finds support from literature.^{7,9,11} However, as stated above, this mode may have contribution from O—H in-plane bending vibration also. The other O—H in-plane bending has been identified at 1280 cm^{-1} .

In the spectra of pyrimidine-4,6- d_2^6 , the pair of bands at $1398, 1466\text{ cm}^{-1}$ and at $1564, 1568\text{ cm}^{-1}$ have been observed which are analogous to the pair of bands originating from e_{1u} (1485) and e_{2g} (1595) vibration of benzene respectively, observed in substituted benzenes. Thus the pair of bands at 1385 cm^{-1} (ν_{19a}), 1485 cm^{-1} (ν_{19b}) and 1585 cm^{-1} (ν_{8a}), 1617 cm^{-1} (ν_{8b}), observed in analogy to substituted benzenes, have been assigned to coupled C—C and C—N vibrations in the present case. This also finds support from the literature.^{5,7,9,11} In substituted benzenes, the frequency of one of the two ring modes ν_1 and ν_{12} decreases to 820 cm^{-1} while the other remains at $\sim 1000\text{ cm}^{-1}$. Thus the bands observed at 825 and 987 cm^{-1} in 4,6-DH-2-MP have been assigned to ν_1 and ν_{12} modes respectively. These assignments are in close agreement with those made by Job and Kartha⁹ and Goel *et al.*⁷ in case of substituted pyrimidines.

For molecules containing OH group, the O—H valence vibration appears in the range $3500\text{--}3700\text{ cm}^{-1}$. In phenol, the O—H valence oscillation was observed at 3628 cm^{-1} .¹⁸ In view of this, the two O—H valence modes have been identified at 3680 and 3705 cm^{-1} in the present case. Green *et al.*¹⁹ have assigned the O—H out-of-plane vibration at $400, 366$ and 312 cm^{-1} in three dichlorophenols. Thus the bands observed at 345 and 355 cm^{-1} have been assigned to this mode in the case of the title compound.

Three C—H stretching vibrations (two asymmetric and one symmetric) are expected due to CH₃ group in the region $2800\text{--}3000\text{ cm}^{-1}$. Only one band has been observed in this region at 2990 cm^{-1} and thus has been assigned to this mode in the present molecule. This finds support from literature.^{9,11} In toluene, Wilmschurst and Bernstein¹⁶ have assigned the two CH₃ rocking modes at 1040 and 1080 cm^{-1} . These modes have been assigned at 1050 and 1140 cm^{-1} in the title compound and find support from the work of Job and Kartha.⁹

Apart from other vibrations, it is interesting to note that the bands with medium intensity at 1683 and 1663 have been observed in C=O region and thus have been assigned to 4 C=O and 6 C=O

stretching mode respectively. One C=O in-plane has been identified at 545 and one C=O out-of-phase (it may have contribution from C—H in-plane bending modes also) at 388 cm^{-1} in the present molecule. These find support from the work of Sanyal *et al.*¹¹ But no N—H frequency has been observed in their respective regions. Thus in this molecule, the migration of proton from OH group to the N of the ring cannot be taken conclusively. It is also in agreement with the spectral analysis of 4,6-dihydroxy pyrimidine.¹⁰

One of the authors (RKG) is thankful to the University Grants Commission, New Delhi, for financial assistance.

References

1. Itto M, Shimada R, Kuraishi T & Mizushima W, *J. Chem Phys.*, **25** (1956), 597.
2. Lord R C, Marson A J & Miller F A, *Spectrochim. Acta*, **9** (1957), 113.
3. Simmons J D & Innes K K, *J. Molec. Spectrosc.*, **13** (1964), 435.
4. Sbrana G, Adembri G & Califano S, *Spectrochim. Acta*, **22** (1966), 1831.
5. Sarma Y A, *Spectrochim. Acta*, **30A** (1974), 1801.
6. Nejad F M & Stidham H D, *Spectrochim. Acta*, **31A** (1975), 1433.
7. Goel R K, Sanyal Nitish K & Srivastava S L, *Indian J. Pure & appl. Phys.*, **14** (1976), 842.
8. Allenstein E, Kiemle P, Weldin J & Podszun W, *Spectrochim. Acta*, **33A** (1977), 189.
9. Job V A & Kartha S B, *Proc. Indian Acad. Sci.*, **85A** (1977), 476.
10. Goel R K & Sharma S N, *Proc. Natn. Acad. Sci. India*, communicated.
11. Sanyal Nitish K, Srivastava S L & Goel R K, *Indian J. Phys.*, **51B** (1977), 108.
12. Srivastava S L, Goel R K & Rohitashava, *J. Chim. Phys.*, **75** (1978), 1091.
13. Bellamy L J, *The infrared spectra of complex molecules*, (Chapman & Hall, London), 1975.
14. Kletz T A & Price W C, *J. Chem. Soc.*, (1947), 644.
15. Mecke & Rossmly, *Z. Electrochem.*, **59** (1955), 866.
16. Wilmshurst J K & Bernstein H J, *Can. J. Chem.*, **35** (1957), 911.
17. Mooney E F, *Spectrochim. Acta*, **20** (1964), 1343.
18. Evans J C, *Spectrochim. Acta*, **16** (1960), 1382.
19. Green J H S, Harrison D J & Kynaston W, *Spectrochim. Acta*, **28A** (1972), 33.

INSTRUCTIONS TO CONTRIBUTORS

Manuscripts should be typewritten in double space and on *only one side* of good quality paper; the original and *one carbon copy are to be submitted*.

Papers must be written in clear and concise English. Good attention to spelling and grammar should be given. Long introductions should be avoided. Standard international nomenclature should be followed in giving names of chemical compounds. Standard abbreviations for units of measurement should be used in the text, tables and illustrations. The abbreviations should be used without fullstops.

Title—The title should be neither too brief/general nor unnecessarily long. It should reflect the content of the paper so as to derive the maximum advantage in indexing and information retrieval. A short title for use as running title should also be supplied. If a paper forms part of a series, a subtitle indicating the aspects of the work covered in the paper should be provided.

Abstract—The abstract should indicate the scope of the work and the principal findings of the paper. It should not exceed 3% of the length of the paper and, barring exceptional cases, it should not exceed 200 words. The abstract should be prepared in such a form that abstracting periodicals can use it without modification.

Data—Only such primary data as are essential for understanding the discussion and the main conclusions emerging from the study should be included. All such secondary data as are of interest to a specific category of readership may, if necessary, be deposited in the editorial office (or retained by the authors) for supply on demand. A footnote to this effect may be inserted at a suitable place in the paper.

Mathematical portions—Special attention should be given to the mathematical portions of the paper. Equations must be well separated from the text and written clearly with good separation between the successive lines. The usual norms of breaking long mathematical expressions may be adhered to. Equations should be numbered consecutively in Arabic numerals with the number in parentheses near the right hand margin. Superscripts and subscripts should be clearly indicated in pencil by V and \wedge sign respectively. Capital and small letters, particularly of the same letter when both occur, as well as letters or symbols likely to be confused one for the other, should be clearly distinguished. Special characters (e.g. Greek, script, vector, tensor, matrix, etc.) required must be indicated by marginal notes. Letters and symbols which should appear in bold face must be clearly indicated. To simplify typesetting: (i) long and complicated mathematical expressions which are frequently repeated should be replaced with single letter/symbol, without clashing with the others used in the paper; (ii) the "exp" form of complex expon-

ential functions should be used; and (iii) to simplify fractions, the solidus (/) is to be used and fractional exponents are to be used instead of root signs, e.g.

$$\text{write } \left(4\omega_{pl} K_{3\lambda}^2 / \omega K_D^2 \right)^{1/2} \text{ and not } \sqrt{4 \frac{\omega_{pl} K_{3\lambda}^2}{\omega K_D^2}}$$

$$\text{write } \exp \{ -i\omega_0 (t_1 - t_2)/2 \} \text{ and not } e^{-i\omega_0 (t_1 - t_2)/2}$$

Tables—Tables should be typed on separate sheets of paper without any text matter on the page. They should be numbered consecutively in Arabic numerals and should bear brief titles. *Column headings should be brief*. Units of measurements should be abbreviated and placed below the headings. Nil results should be indicated and distinguished clearly from absence of data. Graphs as well as tables, both representing the same set of data, must be strictly avoided. Inclusion of structural formulae inside the tables should be avoided as far as possible. Tables should be referred to in the text by numbers and not by terms like 'above', 'below', 'preceding' or 'following'.

Illustrations—All illustrations should be numbered consecutively in Arabic numerals. Captions and legends to the figures should be self-explanatory and should be typed on a separate sheet of paper and attached at the end of the manuscript. Line drawings should be made with Indian ink on white drawing paper (preferably Bristol board), cellophane sheet or tracing cloth. In addition to the originals, a set of blue-prints or photostat copies should be sent. For satisfactory reproduction, the graphs and line drawings should be drawn to approximately twice the printed size.

The lettering should be uniform, preferably in stencil, so as to be *not less than 2 mm after reduction* widthwise to 3" or 6" as required. The size of geometrical shapes (used to distinguish different graphs), dot, lines, etc. should be sufficiently large to permit the necessary reduction without loss of detail. In the case of *photographs*, prints must be on glossy paper and contrasty. If an illustration is taken from another publication, reference to the source should be given and prior permission secured. Illustrations should be protected by thick cardboard packing against creases, folds and broken corners during transit. Illustrations should be referred to in the text by numbers and not by terms like 'above', 'below', 'preceding' or 'following'.

Infrared, ultraviolet, NMR and other spectra, DTA curves, etc. should be included only if they pertain to new compounds and/or are essential to the discussion; otherwise only significant numerical data should be included in the text.

References—The list of references should be prepared strictly in accordance with the style

in the Journal. In the text, references to literature should be numbered consecutively, in the order of their first occurrence, and should be indicated by superscripts at the relevant places; as far as possible the placement of references on numerals or other symbols should be avoided; in such cases the reference may be given in parenthesis in running text, e.g. "this yielded for n a value of 2.3 (Ref. 5)". Full bibliographic details for all the references mentioned in the text should be listed in serial order at the end of the paper.

In citing references to research papers, names and initials of authors should be followed, in order, by the title of the periodical in the abbreviated form (underlined), the volume number (two lines underneath), the year within circular brackets and the page reference [e.g. Venkatesh, H G & Guha Sarkar, G, *Indian J. Pure Appl. Phys.*, **12** (1974), 502]. For names of periodicals, the standard abbreviations followed by the *Physics Abstracts* should be used. If the reference is to an article published without any authorship in a periodical, the title of the article takes the place of the author in the citation [e.g. The content, influence and value of scientific conference papers and proceedings. *Unesco Bull. Libr.*, **16** (1952), 113-26.]. If a paper has been accepted for publication, the names of the authors and the journals should be given followed by the words "in press" within circular brackets [e.g. Sastry, B. A. & Sastry, G. S., *Physica*, (Netherlands) (in press).].

In the list of references, unpublished work, accepted papers in press and personal communications should be clearly distinguished.

Even if a reference contains more than two authors, the names of all the authors with their respective initials should be given. The abbreviations *et al.*, *idem* and *ibid* should be avoided.

Reference to a book should include details in the following order: names and initials of authors, the title of the book (underlined), name of publisher and place of publication within circular brackets and year [e.g. Herzberg, G, *Spectra of diatomic molecules* (D Van Nostrand & Co. Inc., New Jersey), 2nd Edn, 1950, 31.]. If the reference is to the work of an author published in a book by a different author or edited by a different person, the fact that it is cited from the source book should be clearly indicated [e.g. Garlick, G F J, cited in *Encyclopedia of Physics*, Vol. 26—*Light and matter II*, edited by S Flugge (Springer Verlag, Berlin), 1958, 1.].

Proceedings of conferences and symposia should be treated in the same manner as books. Reference to a paper presented at a conference, the proceedings of which are not published, should include, in the

following order, names and initials of authors, title of the paper (underlined), name of the conference, place where the conference was held and date (Deekshitulu, B L, *Design and fabrication of drum scanner for picture processing*, paper presented in the Symposium on Applied Optics, Indian Institute of Science, Bangalore, 28-30 Nov. 1974).

Reference to a thesis should include the name of the author, title of the thesis (underlined), university or institution to which it was submitted and year of submission (e.g. Chandrasekaran, K S., *Studies on crystal structure and absolute configuration of crystals*, Ph. D. thesis, Madras University, 1956).

Reference to a patent should include names of patentees, country of origin (underlined) and patent number, the organization to which the patent has been assigned within circular brackets, data of acceptance of the patent and reference to an abstracting periodical where available [Trepagnier, J H, *US Pat.* 2,463,219 (to E I du Pont de Nemours & Co.), 1 March 1949, *Chem. Abstr.*, **43** (1949), 7258.].

Abbreviations and symbols—Abbreviations used should conform to the style of the journals. The following prefixes to units of measurements may be used for expressing submultiples and multiples.

Submultiples	Abbreviation	Multiples	Abbreviation
Deci- ($=10^{-1}$)	deci	deca- ($=10^1$)	deca-
centi- ($=10^{-2}$)	c	hecto- (10^2)	hecto
milli- (10^{-3})	m	kilo- ($=10^3$)	k
micro- ($=10^{-6}$)	μ	mega- ($=10^6$)	M
nano- ($=10^{-9}$)	n	giga- ($=10^9$)	G
pico- ($=10^{-12}$)	p	tera- ($=10^{12}$)	T
femto- ($=10^{-15}$)	f		
atto- ($=10^{-18}$)	at		

Frequently repeating combinations of words, e.g. electric field gradient (EFG), junction field effect transistor (JFET), stimulated Raman emission (SRE), should be abbreviated subsequently, indicating the abbreviated form in parentheses, as shown, at the place of their first occurrence.

Nomenclature—Where too many symbols are used in the text, a section entitled "Nomenclature", explaining the significance of the various symbols, may be given and placed just above the Acknowledgement section.

Acknowledgement—Acknowledgements should not be exuberant and must be made only to real assistance rendered in connection with the work reported in the paper.

Appendixes—Appendixes, typed on separate sheets, should be numbered consecutively, in Arabic numerals, in the order of their occurrence in the text, and should be placed at the very end of the paper.